VARIATIONS IN THE PARTICULATE FLUX OF ^{230}TH AND ^{231}PA AND PALEOCEANOGRAPHIC APPLICATIONS OF THE ^{231}PA/^{230}TH RATIO

by

Ein-Fen Yu
B.S., Marine Sciences, Chinese Culture University, 1983
M.S., Oceanography, National Taiwan University, 1985

Submitted in partial fulfillment of the requirements for the degree of
Doctor of Philosophy

at the
MASSACHUSETTS INSTITUTE OF TECHNOLOGY
and the
WOODS HOLE OCEANOGRAPHIC INSTITUTION

May, 1994

Copyright Ein-Fen Yu 1994. All rights reserved.

The author hereby grants to MIT and WHOI permission to reproduce and distribute copies of this thesis document in whole or in part.

Signature of author _____
Joint Program in Oceanography
Massachusetts Institute of Technology/
Woods Hole Oceanographic Institution

Certified by _____
Dr. Michael P. Bacon
Thesis Supervisor

Accepted by _____
Dr. Daniel J. Repeta
Chair
Joint Committee for Chemical Oceanography

MASSACHUSETTS INSTITUTE
OF TECHNOLOGY

JUN 01 1994

LIBRARIES

ARCHIVES

VARIATIONS IN THE PARTICULATE FLUX OF ^{230}TH AND ^{231}PA AND PALEOCEANOGRAPHIC APPLICATIONS OF THE ^{231}PA/^{230}TH RATIO

by

Ein-Fen Yu

ABSTRACT

Fractionation between ^{230}Th ($t_{1/2}$ = 7.5x10^{4}yr) and ^{231}Pa ($t_{1/2}$ = 3.2x10^{4}yr), the two longest-lived radionuclides produced from the decay of natural uranium, is found widely within the oceans. This large scale fractionation was investigated in samples of sinking particulate matter collected with sediment traps and in deep-sea sediment cores. New analytical methods for uranium, thorium, and protactinium isotopes by Inductively-Coupled Plasma Spectrometry (ICP-MS) with a conventional Meinhard concentric glass nebulizer were developed. Composite samples from sediment traps deployed a year or longer in diverse geographic regions of the ocean were analyzed to examine assumptions underlying the use of the ^{230}Th-normalized flux method and the ^{231}Pa/^{230}Th ratio for reconstruction of the fluxes of sedimentary components in the present and past ocean. The compiled results demonstrated that over most of the ocean, the flux of ^{230}Th into the sediments balances approximately its production rate in the overlying water column, with an accuracy better than 30%; whereas ^{231}Pa tends to migrate towards the margins or other regions of high particle flux. Thus the ^{231}Pa/^{230}Th ratio is sensitive to regional differences in the scavenging intensity. In addition to this, the influence of particle composition on the ^{231}Pa/^{230}Th ratio was investigated, but it was not possible to reach a definitive conclusion. The thesis describes aspects of the large scale geochemical fractionation between the two elements within the Atlantic Ocean during the Holocene and the Last Glacial Maximum and attempts to answer questions concerning the causes of the large scale fractionation resulting from a differential partitioning of the two elements between a vertical flux with sinking particles and a horizontal flux to boundaries due to ocean circulation. A quantification of the influence on the fractionation of the two nuclides by advection resulting from the thermohaline circulation was made, and it is shown that almost half of the ^{231}Pa production in the water column is exported from the Atlantic Ocean to the Southern Ocean. This export is important in the budget of ^{231}Pa in deep-sea sediments of the Southern Ocean. This suggests that the variations in ^{231}Pa/^{230}Th ratio reflect variations not only in particle flux, but also in the intensity or pattern of the thermohaline circulation. Reconstruction of the ^{230}Th-normalized biogenic opal and carbonate paleo-fluxes suggests no significant changes in surface production in the southern Indian Ocean between the Last Glacial Maximum and the Holocene period.

Acknowledgments

This work would not be complete without support and aid from numerous people. I would especially like to thank to my thesis advisor, Dr. Mike Bacon, for his constant advice, guidance, support, encouragement, patience, and understanding throughout my years in the Joint Program. Dr. Roger Francois also contributed greatly throughout this work. I would also like to thank the other members of my thesis committee, Drs. Ed. Boyle and Bill Curry, for their generous offering of their expertise and scientific advice throughout this thesis work.

I would like to thank Alan Fleer in particular for teaching all he knows about deep-sea sediment sample preparation procedures, and his constant assistance in the lab. Terry for assistance in problem shooting of counting system is also appreciated. I am grateful to Dr. Ron Pflaum for his regular assistance in setting up the ICP-MS at Harvard, Prof. Stein Jacobsen for providing access to the instrument. I am grateful to Tim Shaw, Debbie Colodner, Rob Sherrell, and Keily Falkner for teaching me about ICP-MS during the beginning stage of my development of analytical techniques by ICP-MS.

A special thanks to Dr. Ken Buesseler, who has kindly allowed me to use one of his counting systems while the major counter system in Mike's lab was out of order. Mary Hartman offered help in routine changing my samples. Special thanks go to Drs. Bill Curry and Mark Altabet for their kindness to allow me to use equipments in their lab.

This work benefitted from the supplies of year or longer collections of sediment trap materials that were kindly provided by Dr. Susumu Honjo and his colleague Dr. Steve Manganini. Appreciation goes to Steve who assisted in splitting all sediment trap materials.

This work also benefitted greatly from the supplies of deep-sea sediments from the Deep-Sea Sample Repository in Lamont-Doherty Earth Observatory (LDEO) (Supported by National Science Foundation through Grant OCE91-01689 and the Office of Naval research through Grant N00014-90-J-1060), Antarctic Research Facility of Florida State University, and Deep-Sea Sample repository in Woods Hole Oceanographic Institution. Thanks to Ms. Rusty Lotti in LDEO and Mr. Dennis Cassidy in Antarctic Research Facility for their continuous aid in sampling. Sample materials of a downcore from the Southern Indian Ocean

were kindly provided by Dr. Laurent D. Labeyrie at Gif-sur-Yvette, France. The Holocene and Last Glacial Maximum sections of three cores in the North Atlantic Ocean were kindly provided by Dr. Eystein Jansen through the connection of Dr. Delia Oppo.

I would like to acknowledge MIT Research Reactor which is supported from the U. S. DOE Reactor Sharing Grant No. DE-FG07-80ER 10770. A015 for providing facilities to make ^{233}Pa tracer.

Special thanks go to Greg Ravizza. I learned a great deal from his always bright questions or comments. He continuously offered encouragement and help in many ways, and shared his tremendous experiences.

I am also indebted to my other two pre-general examine committee, Drs. Ed. Sholkovitz and Phil. Gschwend along with Mike for their guidance in taking courses and encouragement throughout my first two most difficult years in the Joint Program. I also want to thank Dr. Mark Kurz who generously offered me an opportunity to learn some about mass spectrometry.

Many thanks go to Marcia Davis for improving my writing in English for years, and her great favor in editing. Thanks to Ms. Laura Praderio for her very efficient helps in editing this thesis as well.

Thanks to my friends and colleagues during these academia years in the Joint Progam, Nathalie Waser, Debbie Colodner, Jenny Lee, Greg Ravizza, Catherine Goyet, Frank Yang, Ed. Brook, and Mike DeGrandpre. I am especially grateful to Nancy Hayward for her warm heart in smoothing and comforting my difficult life in a foreign country.

Finally, I wish to thank my family for supporting me through this crazy endeavor.

Funding for this research was provided by the National Science Foundation (Grants OCE-8817836, OCE-8922707, OCE-9016494, and OCE-9200780). Funds from the Woods Hole Oceanographic Institution and from the Gordon Research Conferences for travel to scientific meetings are also gratefully acknowledged.

Table of Contents

Title page ---- 1
Abstract ---- 3
Acknowledgments ---- 4
Table of contents ---- 6
List of figures ---- 11
List of tables ---- 14

Chapter 1 Introduction ---- 17
1.1 Background ---- 17
1.1.1 *In situ* production of ^{231}Pa and ^{230}Th in sea water ---- 17
1.1.2 Large-scale fractionation of ^{231}Pa and ^{230}Th ---- 17
1.2 Goals of the thesis ---- 19
1.3 Outline of the thesis ---- 20
Chapter 2 The new methods for uranium, thorium, and protactinium isotopes by inductively coupled plasma-mass spectrometry --- 23
2.1 Introduction ---- 23
2.2 Apparatus ---- 24
2.3 Reagents, spikes, and working references ---- 26
2.4 Radiochemical techniques ---- 28
2.4.1 Sample preparation---- 29
2.4.2 Sample dissolution ---- 29
2.4.3 Subsampling for ^{238}U and ^{232}Th ---- 32
2.4.4 Coprecipitation with Fe and Al hydroxides ---- 33
2.4.5 Ion exchange procedure for separation and purification of U, Th and Pa ---- 33
2.4.6 Chemical yield determination of Pa ---- 34
2.4.7 Final analyte preparation for ICP-MS ---- 35
2.5 ICP-MS analysis ---- 35
2.5.1 ICP-MS operation parameters ---- 35
2.5.1-a Sample introduction ---- 35
2.5.1-b Optimized conditions and features for Pa, U and Th isotopes analysis ---- 36
2.5.1-c Resolution, sensitivity and stability ---- 36
2.5.1-d Background, memory effect, and detection limits --- 41

2.5.1-e Linearity and dynamic: range ---------- 42
2.5.2 Analytical procedures ---------- 43
2.6 Determination of ^{231}Pa by ICP-MS ---------- 44
2.6.1 Degree of ionization of ^{231}Pa ---------- 44
2.6.2 Abundance sensitivity ---------- 44
2.6.3 Quantitative analysis of $^{231}Pa/\ ^{230}Th$ isotope ratio and instrument fractionation ---------- 45
2.6.4 Matrix effects ---------- 47
2.6.5 Precision and accuracy ---------- 55
2.7 Simultaneous determination of $^{230}Th+^{234}U+^{235}U$, and $^{232}Th+^{238}U$ by isotope dilution-ICPMS ---------- 59
2.7.1 Abundance sensitivity ---------- 59
2.7.2 Mass fractionation ---------- 59
2.7.3 Precision and accuracy ---------- 60
2.8 Calculations ---------- 60
2.8.1 Isotope dilution calculation ---------- 60
2.8.1-a Background correction ---------- 63
2.8.1-b Blank correction ---------- 66
2.8.1-c Contribution from spikes ---------- 66
2.8.2 Sources of error ---------- 67
2.9 Conclusions ---------- 68

Chapter 3 Fractionation between ^{231}Pa and ^{230}Th in the settling particles: Can we use both as tools for reconstruction of paleo-particle flux ---------- 71
3.1 Introduction ---------- 71
3.1.1 Background ---------- 71
3.1.2 Questions and aims ---------- 76
3.2 Sampling strategy ---------- 77
3.3 Sample collection, handling and distribution ---------- 78
3.3.1 NABE ---------- 78
3.3.2 Arabian sea ---------- 81
3.3.3 PAPA ---------- 81
3.4 Methods ---------- 82
3.4.1 Preparation of composite sediment trap samples ---------- 82
3.4.2 Radiochemical procedures ---------- 83

3.4.3 Carbonate content ---------- 83
3.4.4 Data processing ---------- 84
3.5 Results ---------- 84
3.5.1 Unsupported isotope activities ---------- 86
3.5.2 Authigenic uranium and particulate uranium ---------- 90
3.6 Discussion ---------- 91
3.6.1 Quantification of sediment trap efficiency with ^{231}Pa and ^{230}Th ---------- 95
3.6.2 Quantification of particulate radioisotope flux ---------- 104
3.6.2-a The value of V/P for ^{230}Th ---------- 105
3.6.2-b Is ^{230}Th flux constant ---------- 107
3.6.2-c The V/P values for ^{231}Pa ---------- 111
3.6.3 Particulate $^{231}Pa_{ex}$/ $^{230}Th_{ex}$ ratios in sediment traps ---- 112
3.6.4 Does the composition of particles affect the relationship between particle flux and the $^{231}Pa_{ex}$/ $^{230}Th_{ex}$ ratio?-- 114
3.6.5 Implications for the ^{230}Th-normalized flux method ---- 124
3.6.5-a The method and its assumptions ---------- 124
3.6.5-b Advantages and problems ---------- 125
3.7 Conclusions and Future Study ---------- 129

Chapter 4 Basin-wide variations in chemical scavenging of ^{231}Pa and ^{230}Th within the Atlantic Ocean since the Last Glacial Maximum ---------- 131
4.1 Introduction ---------- 131
4.2 Methods ---------- 133
4.3 Results ---------- 134
4.4 Discussion ---------- 141
4.4.1 Chemical fractionation between ^{231}Pa and ^{230}Th in the Holocene Atlantic sediments ---------- 141
4.4.2 Export of ^{231}Pa and ^{230}Th from the North Atlantic across 25°N ---------- 154
4.4.3 The mass balance of ^{231}Pa in Holocene Antarctic sediments ---------- 164
4.4.4 LGM/Holocene changes in the Pa/Th distribution in Atlantic sediments ---------- 167

4.4.5 Changes in the flux of sedimentary components between LGM and Holocene ---------- 179
4.5 Conclusions ---------- 188

Chapter 5 Variations in ^{231}Pa, ^{230}Th and sediment fluxes across the frontal zones in the southern Indian Ocean and changes since the Last Glacial Maximum ---------- 191
5.1 Introduction ---------- 191
5.1.1 Why do we care to reconstruct past changes in particle fluxes in the Southern Ocean? ---------- 191
5.1.2 Why do ^{231}Pa, ^{230}Th, $(^{231}Pa/\ ^{230}Th)_{ex}{}^{o}$ measurements? ---------- 192
5.2 Deep-sea sediment samples ---------- 193
5.2.1 Core locations and physical setting in the region ---------- 194
5.2.2 Stratigraphy and sample selection ---------- 197
5.2.3 Downcore profile on the APF in the southeastern Indian Ocean ---------- 197
5.3 Results ---------- 199
5.3.1 Uranium contents of the transect samples ---------- 199
5.3.2 Unsupported activities of ^{231}Pa and ^{230}Th of the transect samples ---------- 207
5.3.3 Radionuclide results from MD88-773 ---------- 208
5.4 Discussion ---------- 208
5.4.1 ^{230}Th-normalized paleoflux ---------- 208
5.4.1-a The ^{230}Th-normalized total flux for the Holocene transect samples ---------- 210
5.4.1-b The changes in the ^{230}Th-normalized total flux between the Holocene and the LGM of the transect samples ---------- 214
5.4.1-c The latitudinal variations in extent of sediment focusing ---------- 214
5.4.1-d Change in the focusing factor with time ---------- 219
5.4.2 Variations in $(^{231}Pa/\ ^{230}Th)_{ex}{}^{o}$ ratio ---------- 220
5.4.2-a Latitudinal variations in $(^{231}Pa/\ ^{230}Th)_{ex}{}^{o}$ ratios from the Holocene sections of the transect sediments - 222

5.4.2-b The causes for the latitudinal variations in $(^{231}Pa/\ ^{230}Th)_{ex}{}^{o}$ ratio of the Holocene transect samples ---------- 225
5.4.2-c A downcore profile of $(^{231}Pa/\ ^{230}Th)_{ex}{}^{o}$ ratios and particle fluxes south of the APF ---------- 230
5.4.3 Interpretation of the latitudinal variations in ^{230}Th-normalized opal flux ---------- 232
5.4.3-a Latitudinal distribution patterns of opal content and ^{230}Th-normalized opal flux during the Holocene - 233
5.4.3-b The conditions and processes responsible for the latitudinal distribution patterns of opal ---------- 236
5.4.3-c Interpretation of ^{230}Th-normalized opal flux changes between the LGM and the Holocene ---------- 238
5.4.3-d Impact of APF northward migration on the latitudinal distribution and magnitude of changes in chemical properties and particle flux ---------- 241
5.4.3-e Did biological production change during the LGM? 243
5.4.4 Interpretation of ^{230}Th-normalized carbonate flux ------- 245
5.4.4-a Latitudinal variations of carbonate record, and changes between the LGM and the Holocene ---------- 245
5.4.4-b MD88-773 carbonate profiles provide evidence of carbonate production changes ---------- 248
5.4.4-c The effect of $CaCO_3$: C_{org} rain ratio on the interpretation of carbonate records ---------- 250
References ---------- 253

List of Figures

Figure 2.1 A schematic flow chart for separation and purification of U, Th, and Pa isotopes for ICP-MS analysis ---------- 30
Figure 2.2 Variations of instrument tuning sensitivity over a long time period ---------- 38
Figure 2.3 An example of medium-term stability of the instrument --- 40
Figure 2.4 Example of sample matrix effect on a ^{231}Pa standard analyte 49
Figure 2.5 Extent of matrix effect ---------- 50
Figure 2.6 Example of reduction in sample matrix effect on the ^{231}Pa signal ---------- 54
Figure 3.1 Comparison of estimated mean annual flux ($g/m^2/y$)------- 94
Figure 3.2 Summary of some available $^{230}Th/^{231}Pa$ activity ratios measured in the water column ---------- 99
Figure 3.3 The estimated trapping efficiency [E(230Th)] versus trap depth---------- 102
Figure 3.4 $(V/P)^{230}Th$ and $(V/P)^{231}Pa$ versus trap efficiency-corrected mass flux; $(F/P)^{230}Th$ and $(F/P)^{231}Pa$ versus mass flux ------ 108
Figure 3.5 (Pa/Th)/0.093 vs. trap efficiency-corrected mass flux---------- 113
Figure 3.6 The vertical flux/production ratio of ^{230}Th and ^{231}Pa versus trap efficiency-corrected flux ---------- 117
Figure 3.7 The $^{231}Pa/^{230}Th$ activity ratio versus trap efficiency-corrected flux ---------- 119
Figure 3.8 Deviation of the $^{231}Pa/^{230}Th$ ratio over 0.093 versus %opal, %carbonate, $\%C_{org}$ and %terrigenous material ------- 120
Figure 4.1 The map of selected cores of the Atlantic Ocean ---------- 135
Figure 4.2 The map of decay-corrected unsupported $^{231}Pa/^{230}Th$ of the Holocene Atlantic Ocean ---------- 142
Figure 4.3 Summary of unsupported $^{231}Pa/^{230}Th$ ratios in the Holocene Atlantic sediments ---------- 147
Figure 4.4 ^{230}Th distributions measured in ocean-water profiles by alpha-counting ---------- 157
Figure 4.5 ^{231}Pa distributions measured in ocean-water profiles by alpha-counting ---------- 158
Figure 4.6 Diagram of the mass balance of ^{231}Pa in the Holocene Southern Ocean---------- 166

Figure 4.7 The map of decay-corrected unsupported $^{231}Pa/^{230}Th$ of the LGM Atlantic Ocean ---------- 172
Figure 4.8 Summary of unsupported $^{231}Pa/^{230}Th$ ratios in the LGM Atlantic sediments ---------- 174
Figure 4.9 The map of LGM/Holocene ratio of the decay-corrected unsupported $^{231}Pa/^{230}Th$ ratios ($Pa/Th_{ex}{}^{o}$) in the Atlantic Ocean ---------- 177
Figure 4.10 Diagram of the mass balance of 231Pa in the LGM Southern Ocean ---------- 178
Figure 4.11 Carbonate (%) for both the LGM and Holocene in the Atlantic sediments ---------- 181
Figure 4.12 Non-carbonate (%) for both the LGM and Holocene in the Atlantic sediments ---------- 182
Figure 4.13 The LGM/Holocene ratio of the 230Th-normalized carbonate and non-carbonate flux for the Atlantic sediments ---------- 183
Figure 5.1 Map of selected cores in the southern Indian Ocean ---------- 196
Figure 5.2 Oxygen isotope chronology of core MD88-773 ---------- 198
Figure 5.3 Total uranium and authigenic uranium versus age in core MD88-773 ---------- 209
Figure 5.4 ^{230}Th-normalized total flux of the Holocene section -------- 211
Figure 5.5 LGM/Holocene ratio of ^{230}Th-normalized total flux versus latitude for the transect samples in the southern Indian Ocean ---------- 216
Figure 5.6 Comparison between the ^{230}Th-normalized total flux and the sediment accumulation rate for the Holocene transect samples in the southern Indian Ocean ---------- 218
Figure 5.7 The $(^{231}Pa/^{230}Th)_{ex}{}^{o}$ activity ratio of the Holocene sections and LGM sections of the transect sediments from the southern Indian Ocean ---------- 223
Figure 5.8 %Opal and %carbonate versus latitude for the Holocene transect sections in the southern Indian Ocean---------- 227
Figure 5.9 ^{230}Th-normalized opal and carbonate flux for the Holocene transect sections in the southern Indian Ocean---------- 228
Figure 5.10 $(^{231}Pa/^{230}Th)_{ex}o$ and ^{230}Th-normalized total flux versus age in core MD88-773 ---------- 231

Figure 5.11 LGM/Holocene ratios of ^{230}Th-normalized opal flux, carbonate flux, and $(^{231}Pa/^{230}Th)_{exo}$ versus latitude for the transect samples in the southern Indian Ocean---------- 239
Figure 5.12 The water depth and %carbonate (both the LGM and the Holocene) of the transect cores in the southern Indian Ocean-246
Figure 5.13 The water depth and carbonate flux (both the LGM and the Holocene) of the transect cores in the southern Indian Ocean-249
Figure 5.14 ^{230}Th-normalized carbonate and non-carbonate flux versus age in core MD88-773 ---------- 251

List of Tables

Table 2.1 Information on the production of ^{233}Pa by neutron activation of ^{232}Th ---------- 27
Table 2.2 ICP-MS operation conditions ---------- 39
Table 2.3 Example of background levels (in ACPS) for Th, Pa, and U isotopes ---------- 41
Table 2.4 Abundance sensitivity for ^{231}Pa ---------- 45
Table 2.5 Example of calibration for quantitative analysis of $^{231}Pa/^{229}Th$ ratio ---------- 46
Table 2.6 Examples of instrument stability on $^{231}Pa/^{229}Th$ atom ratio and instrument mass fractionation ---------- 47
Table 2.7 The experimental results of matrix effects on the measurement of $^{231}Pa/^{229}Th$ ratio ---------- 52
Table 2.8 Precision and accuracy of $^{231}Pa/^{229}Th$ measurement by ICP-MS ---------- 58
Table 2.9 Comparison of ICP-MS to α-spectrometry for ^{231}Pa measurements---------- 58
Table 2.10 Examples of stabilities on isotope ratio and the instrumental mass fractionation ---------- 61
Table 2.11 Reproducibility of Th, U isotope measurement on a uraninite standard ---------- 62
Table 2.12 Comparison of α-spectrometry results and ICP-MS results for Th and U isotopes in marine sediments ---------- 64
Table 2.13 Examples of procedural blanks ---------- 66

Table 3.1 Locations and collection information of the compiled sediment trap samples---------- 79
Table 3.2 Analytical results of radionuclides for sediment trap samples ---------- 85
Table 3.3 Calculated results of radionuclides for sediment trap samples ---------- 87
Table 3.4 Complied data for sediment trap samples ---------- 93
Table 3.5 Model results of the sediment trap efficiency ---------- 100
Table 3.6 Concentration and flux of components for sediment trap samples ---------- 116

Table 4.1 Locations of select sediment cores in the Atlantic Ocean ------ 136
Table 4.2 Analytical results of radionuclides for the Holocene Atlantic sediments ---------- 137
Table 4.3 Analytical results of radio-isotopes for the LGM Atlantic sediments ---------- 138
Table 4.4 Unsupported initial radionuclide activities for the Holocene Atlantic sediments ---------- 139
Table 4.5 Complied data of Pa/Th ratio for the Holocene Atlantic sediment ---------- 143
Table 4.6 Statistics of the $^{231}Pa/^{230}Th$ ratio of the Holocene Atlantic sediments ---------- 146
Table 4.7 Sediment composition, ^{230}Th-normalized paleoflux, and $(Pa/Th)_{exo}/0.093$ ratio for the Atlantic sediments ---------- 150
Table 4.8 Summary results of the mean Atlantic Ocean volume from AVS program ---------- 159
Table 4.9 The simple mass balance model of ^{231}Pa and ^{230}Th in the Atlantic Ocean ---------- 162
Table 4.10 Unsupported initial radionuclide activities of the LGM Atlantic sediments ---------- 170
Table 4.11 LGM/Holocene changes in ^{230}Th-normalized paleoflux and $(Pa/Th)_{exo}$ ratio of the Atlantic sediments ---------- 171
Table 4.12 Statistics of the $^{231}Pa/^{230}Th$ ratio of the LGM Atlantic sediments ---------- 173
Table 5.1 Locations and stratigraphy of cores ---------- 195
Table 5.2 Measured radioisotopes of the Holocene transect sections from the southern Indian Ocean ---------- 200
Table 5.3 Measured radioisotopes of the LGM transect sections from the southern Indian Ocean ---------- 201
Table 5.4 Analytical results of radionuclides in core MD88-773 --------- 202
Table 5.5 Calculated data of the radioisotopes for the Holocene and the LGM transect samples ---------- 203
Table 5.6 Calculated results of radionuclides and measured components results in MD88-773 core ---------- 205
Table 5.7 Contents and ^{230}Th-normalized fluxes of sediment components of transect samples ---------- 212

Table 5.8 Changes of composition and ^{230}Th-normalized fluxes between Holocene and LGM of transect section -------- 215
Table 5.9 Calculation of focusing factor for core MD88-773 ---------- 221
Table 5.10 Average values of ^{230}Th-normalized total flux and $(^{231}Pa/^{230}Th)_{ex}{}^{o}$ ratio for transect samples ---------- 224
Table 5.11 Estimations of the biogenic opal flux---------- 235

CHAPTER 1

INTRODUCTION

1.1 BACKGROUND

1.1.1. *In situ* production of ^{231}Pa and ^{230}Th in sea water

Naturally occurring protactinium-231 ($t_{1/2} = 3.2\times10^4$yr) and thorium-230 ($t_{1/2} = 7.5\times10^4$yr) have *in-situ* sources in sea water resulting from the decay of uranium. ^{231}Pa is the alpha decay daughter of ^{235}U, and ^{230}Th is the alpha decay daughter of ^{234}U. In the open ocean, uranium is essentially conservative, its concentration varies only with salinity (Cochran, 1992). Since the residence time of uranium is much longer (approximately 4.5×10^5yr, Chen *et al.*, 1986) than the stirring time of the oceans (approximately 1×10^3yr; Broecker and Peng, 1982), the distribution of uranium in the ocean is essentially uniform. Consequently, ^{231}Pa and ^{230}Th are produced at a constant rate throughout the ocean, and their rates of supply to the sediment are directly proportional to the depth of the water column. Once produced, both ^{231}Pa and ^{230}Th are removed rapidly to the sediment on a time scale of ~40 to 200 yr (Anderson *et al.*, 1983a and b) and ~20 to 40 yr (Moore and Sackett, 1964; Bhat *et al.*, 1969; Matsumoto, 1975; Brewer *et al.*, 1980; Li *et al.*, 1980; Anderson *et al.*, 1983a and b), respectively; ^{231}Pa and ^{230}Th will be removed to sediments by a rigidly fixed $^{231}Pa/^{230}Th$ activity ratio of 0.093 (or 10.8 if $^{230}Th/^{231}Pa$ activity ratio is used) determined by the $^{235}U/^{234}U$ ratio in seawater, if there is no fractionation between the two nuclides (Anderson *et al.*, 1983a). Actual measurements in the ocean, however, give results that diverge considerably from this value.

1.1.2 Large-scale fractionation of ^{231}Pa and ^{230}Th

Depth profiles of ^{230}Th in seawater often show a linearly increasing trend as expected from the *in situ* production from uranium and reversible uptake by

sinking particles (Bacon and Anderson, 1982; Anderson *et al.*, 1983a; Nozaki and Nakanishi, 1985; Cochran *et al.*, 1987; Nozaki *et al.*, 1987; Bacon, unpublished data). In comparison with the profiles of ^{230}Th in the open ocean, ^{231}Pa shows a very different pattern with increasing in total ^{231}Pa aoncentration to a mid-depth maximum, and decreasing concentration toward the bottom (Nozaki and Nakanishi, 1985). In consequence, the activity ratio ^{230}Th/^{231}Pa obtained from open-ocean water shows an increasing trend toward the bottom, and the activity ratio of ^{230}Th/^{231}Pa is generally less than the supply rate ratio which is 10.8. This implies that a large fraction of ^{231}Pa relative to ^{230}Th is transported a longer distance away from its source. The capability of large horizontal transport of Pa results from its longer residence time relative to that ^{230}Th.

Studies of sinking particles with sediment traps provide important information about the fractionation between ^{231}Pa and ^{230}Th. The works of Anderson *et al.* (1983) and later Lao (1991) confirmed that the ^{230}Th/^{231}Pa activity ratio is fractionated with values higher than 10.8 at the mid-ocean sites, and lower than 10.8 at the ocean margins. The significant horizontal ^{231}Pa concentration gradients from the mid-ocean sites toward the margins clearly indicate a net transport of ^{231}Pa (Anderson *et al.*, 1983 a and b). Many investigations of surface sediment have also shown an ocean basin scale fractionation between ^{231}Pa and ^{230}Th. Surface sediments around the margins of the ocean tend to have higher ^{231}Pa/^{230}Th ratio than the production rate ratio of 0.093, in contrast with the abyssal sediments underlying the interior regions. This is found to be commonly in the Pacific Ocean (DeMaster, 1981; Yang *et al.*, 1986; Shimmield et al., 1986; Anderson *et al.*, 1990; Lao, 1991). However, it is not true for the Atlantic Ocean, as will be shown in this thesis.

Important information regarding the large-scale fractionation of scavenged elements like ^{231}Pa and ^{230}Th has been reviewed with box models (Bacon, 1988). As Bacon pointed out, the large fractionation between ^{230}Th and ^{231}Pa within a basin comes about because of the partitioning of the two elements between two transport pathways, i.e., vertical scavenging or horizontal transport, for removal. On one hand ^{230}Th, because of its high particle reactivity and short residence time, is predominately removed with the downward flux of particles. On the other hand ^{231}Pa, which is relatively less particle-reactive, with a residence time about 2 to 3 times longer than that of ^{230}Th, can be laterally

transported longer distances away from its production site before it is removed. Consequently, over most of the ocean, the flux of ^{230}Th into the sediments balances approximately its production rate in the overlying water column; whereas ^{231}Pa tends to migrate towards the margins or regions of high particle flux. As a result, competition between vertical scavenging and horizontal transport determines the fractionation between the two elements. Thus, regional differences in the scavenging intensity and the ocean mixing rate will influence the distribution of ^{231}Pa and ^{230}Th on a basin-wide scale. The differential chemical reactivity of ^{231}Pa and ^{230}Th on different particle surfaces is another factor that can modify the fractionation between the two elements.

1.2 GOALS OF THE THESIS

In this thesis, the goal is to examine all those factors (particle scavenging intensity, particle reactivities, and ocean mixing rate) as described above for causing the large-scale fractionation of scavenged elements like ^{231}Pa and ^{230}Th. Such examination has included investigations of sediment trap samples and deep-sea sediments. Then I pursue applications based on the fractionation between the two elements in the ocean. Such applications have been included in this thesis for studies of paleoceanography, boundary scavenging, and ocean mixing.

In these areas, I can pursue two lines of investigation. First, the nearly uniform deposition of ^{230}Th over the whole seafloor can allow us to predict ^{230}Th flux, which is nearly equal to the rate of production from the decay of uranium in the water column. This allows us to use decay-corrected excess ^{230}Th activity in sediments as a reference against which variations in the flux of other sediments can be evaluated. This is the so called "^{230}Th-normalized flux method", an idea first proposed by Bacon (1984). I can apply this idea to examine the variations in sedimentary flux between the LGM and the Holocene.

The second area of research is based on the ratio of ^{231}Pa/^{230}Th. The scavenging efficiency of these nuclides and the fractionation between the two nuclides can be an indicator of intensity of particle flux. Chemical composition of the settling particles could also influence the relative distribution of the two

nuclides. From the distribution of boundary scavenging of ^{231}Pa and ^{230}Th, we may gain insights on the distribution or flux of other reactive elements or trace metals. This is particularly focused on the distribution patterns in the Atlantic Ocean. Some questions like where the boundary scavenging of ^{231}Pa or ^{230}Th occurs in the Atlantic Ocean, what factors control the distribution patterns of chemical fractionation between ^{230}Th and ^{231}Pa in the Atlantic Ocean, and how the distribution pattern changes with time are examined in this thesis.

Besides the particle flux and chemical composition of a particle, the potential importance of the influence of advection by ocean circulation is underscored by the findings of this thesis work and opens up the possible use of ^{231}Pa and ^{230}Th as tracers for examining ocean advection.

Since a basin scale fractionation between ^{231}Pa and ^{230}Th is pursued, a large number of samples would be required to obtain complete representation of different scavenging conditions (for this thesis work, the whole Atlantic Ocean is studied). Given the limitations of time, a fast and precise analytical technique was pursued to replace the conventional α-spectrometry counting method, a precise but time consuming technique. Inductively-Coupled Plasma Spectrometry (ICP-MS) was initially pursued for this purpose. Methods by Inductively-Coupled Plasma Spectrometry (ICP-MS) with a conventional Meinhard concentric glass nebulizer for measuring ^{231}Pa, and simultaneous measurement of U and Th isotopes in sediment samples were developed. The technique has been used routinely for Th and U isotopes measurements for sediments; unfortunately, given the limitation of amount of sample materials, routine measurements for ^{231}Pa by this technique were not often made for this thesis work. However, I have shown that routine measurements for ^{231}Pa by this technique can be promised if a more efficient sample introduction is available.

1.3 OUTLINE OF THE THESIS

The thesis consists of five chapters. The next chapter describes the newly developed analytical methods for uranium, thorium, and protactinium isotopes by Inductively-Coupled Plasma Spectrometry (ICP-MS) with a conventional

Meinhard concentric glass nebulizer. Chapter three address the fractionation between ^{231}Pa and ^{230}Th in the settling particles (more emphasis on the influences of scavenging intensity and the particle composition on the fractionation between the two elements) and ideas to use both as tools for reconstruction of paleo-particle flux. Chapter four opens up the question of the advection by ocean circulation causing the basin wide fractionation between ^{231}Pa and ^{230}Th. Chapter five focuses on the variations in $^{231}Pa/^{230}Th$ ratio and sediment fluxes across the frontal zones in the southern Indian Ocean and changes since the Last Glacial Maximum.

CHAPTER 2

THE NEW METHODS FOR URANIUM, THORIUM, AND PROTACTINIUM ISOTOPES BY INDUCTIVELY COUPLED PLASMA-MASS SPECTROMETRY

2.1 INTRODUCTION

The potential of uranium, thorium, and protactinium isotopes as tools in geochemistry and oceanography has been appreciated for a long time. Determination of these isotopes in marine sediments has generally been performed by α-spectrometry. The method has been widely used but tends to be very time consuming or requires elaborate laboratory facilities. With recent developments in mass spectrometry, atom-based techniques have now become superior for the analysis of long-lived radionuclides in seawater, marine deposits, and deep-sea sediments. Like fixed-magnetic thermal ionization mass spectrometry (TIMS) which provides superior sensitivity and precision to counting-techniques, inductively-coupled plasma spectrometry (ICP-MS) offers several advantages over both TIMS and α-counting: superior ionization, fast analysis, multi-element capabilities, and simple sample preparation. Methods for the determination of ^{238}U (Klinkhammer and Palmer, 1991) and ^{230}Th (Shaw and Francois, 1991) by isotope- dilution ICP-MS have recently been reported. Measurement of ^{231}Pa by ICP-MS is more difficult because of the low amounts of ^{231}Pa (its concentration is about 20 times less than that of ^{230}Th in sediment samples) and because there is no suitable Pa isotope for isotope dilution. Initial work for this dissertation involved the development of techniques for quantitative measurement of

^{231}Pa in marine sediments by ICP-MS with a conventional Meinhard concentric glass nebulizer. As the work progressed, because of the multi-element capabilities of ICP-MS, methods were also developed to allow simultaneous determination of ^{230}Th, ^{234}U, and ^{235}U on the same aliquot, and simultaneous determination of ^{232}Th and ^{238}U on another aliquot by isotope dilution. Simultaneous measurements by ICP-MS provide analyses that are not only faster and less laborious but also more precise than those provided by the α-counting technique. The success of the procedure for U isotope determinations is important, because decay-correction of ^{230}Th and ^{231}Pa in sediment samples requires knowledge of ^{234}U (or ^{238}U) and ^{235}U content.

The α-spectrometry technique was also used in this thesis for sediment trap samples, spikes and working-reference calibrations for ICP-MS work and for ^{231}Pa measurement in sediments of small size or low concentration.

2.2 APPARATUS

Analyses were performed on a model VG PQ2 Plus quadrupole ICP-MS at Harvard University. ICP-MS involves the introduction of ions from an argon gas plasma through a specialized sampling interface ($\approx$ 1 mm diameter high purity Ni sampling cone and a skimmer cone with $\approx$ 0.75 mm diameter) into a high vacuum region, where a quadrupole mass analyzer separates them for detection on the basis of their charge-to-mass ratio. Sample aliquots are introduced into the plasma with a peristaltic pump (Gilson Minipuls 22) and a Meinhard concentric glass nebulizer. The sample aerosol created in the nebulizer is directed through a spray chamber, which acts as a filter allowing

aerosol droplets ≤ 10 microns in diameter to enter the plasma. Such small droplets can be efficiently desolvated, atomized and ultimately ionized in the plasma but constitute only about 1-5% of the original aerosol, with the rest of the sample directed to a waste bottle.

Chemical yield for Pa was determined by beta-counting of ^{233}Pa tracer added at the beginning of the analysis and was performed on two 2π proportional counters (Nuclear Measurements Corporation Model PCC-11T proportional counter coupled to NMC Model DS-1T decade scaler/timer/higher voltage supply). Both counters use 10% methane/90% argon as the counting gas. The operating voltage for β -counting is at 1800V. Background for β counting is 12-20 counts/min. The counting efficiency of both proportional counters is around 50%.

Chemical yield monitoring for Pa was also done with a GeLi gamma counter during the early stages of this work. The 311.89keV photopeak was used.

Three α-counting systems were used during the course of this work: Canberra Quad alpha spectrometer model 7404 with a Canberra 8180 pulse-height analyzer; EG&G Ortec 576A with a model 918A CADCAM multichannel buffer and a 476-16 multiplexer; and a 16-detector system consisting of Kicksort 504 N Quad bias supplies and 211Q Quadamps and a Northern NS-700 series (Northern Econ II Series) pulse-height analyzer. Silicon surface-barrier detectors are used in all of these systems. Energy resolution, expressed as full peak width at half-maximum height, is 20-40 keV. Counting efficiency of the detectors ranges between 25 and 35%.

Teflon lab-ware was cleaned in soap and was then boiled twice in 50% HNO3. Polyethylene and polypropylene vessels (bottles, columns, centrifigue tubes) were leached in soap and 2N HCl acid baths. The major concern is carry-over of residual ^{233}Pa from previous samples. 8-mm x 10-cm polyethylene columns with polyethylene frits were used for ion exchange chromatography. The use of any glassware was avoided to prevent adsorption of Pa (Sill, 1978; Anderson and Fleer, 1982).

2. 3 REAGENTS, SPIKES, AND WORKING REFERENCES

Reagent grade acids and distilled deionized water were used in all procedures. Dowex AG1-X8 anion exchange resin, 100-200 mesh (Bio Rad Laboratories), was used for all ion exchange columns.

Spikes of ^{236}U and ^{229}Th were calibrated against standard solutions of ^{238}U and ^{232}Th prepared from high-purity oxides: U_3O_8, NBS 950A; ThO_2, Lindsay Code 116, 99.99% minimum purity, American Potash and Chemical Co.).

Preparation of ^{233}Pa was by neutron activation of $Th(NO_3)_4 \cdot 4H_2O$ that had been deposited on a Nuclepore aerosol filter and pressed into a pellet (Anderson and Fleer, 1982). Irradiation was performed at the Massachusetts Institute of Technology nuclear reactor. Detailed information about the irradiation of ^{232}Th to produce ^{233}Pa is given in Table 2.1. After irradiation, the pellet was soaked in concentrated NH_4OH for several hours, the excess ammonia was evaporated, and the filter was destroyed by oxidation in concentrated HNO_3. ^{233}Pa tracer was separated from the ^{232}Th on a Dowex

AG1-X8 Cl- column. Solutions of ^{233}Pa were repurified periodically to remove accumulated ^{233}U decay product.

A reference solution of ^{231}Pa for establishing the analytical procedures was milked from a Harwell uraninite solution (Huh, personal communication), and calibrated with an α-counter of known efficiency and with ^{233}Pa as yield monitor. A reference solution of ^{230}Th was directly diluted from a stock standard solution (standard solution catalog #7230 from Isotope Products Laboratories) and calibrated against a weighed amount of ^{232}Th by α-counting. Stock ^{238}U solution was made gravimetrically from an oxide U_3O_8 (NBS 950A), and the working reference solution was gravimetrically diluted from it.

Table 2.1 Information on the production of ^{233}Pa by neutron activation of ^{232}Th

Chemical form	$Th(NO_3)_4 \cdot 4H_2O$, mol. wt.= 552
Physical form	Solid
Number of ^{232}Th atoms (N)	1.09×10^{18}
Production and decay processes of ^{233}Pa	$^{232}Th\ (n, \gamma)\ ^{233}Th \rightarrow\ ^{233}Pa \rightarrow\ ^{233}U$
Irradiation time (t)	8 hours
Neutron flux (F)	5×10^{13} n/cm^2.sec
Cross section of target (σ_{Th})	7.4×10^{-24} cm^2
^{233}Th half-life	22 minutes
^{233}Pa half-life	27 days= 648 hours

$$\text{Activity } (^{233}Pa) = NF(\sigma_{Th})(1-\exp(-\lambda_{Pa}t))$$
$$= (1.09 \times 10^{18})(5 \times 10^{13})(7.4 \times 10^{-24})(1-\exp(\lambda_{Pa}t))$$
$$= 92.86\ \mu Ci\ ^{233}Pa \text{ per mg of } Th(NO_3)_4.4H_2O$$

2.4 RADIOCHEMICAL TECHNIQUES

Radiochemical techniques were designed to prepare sample for two measurement techniques: one was the conventional α-spectrometry technique, and the other was the ICP-MS technique. Sediment trap samples and some sediments of small sample size or low concentration were prepared according to the standard procedure that Anderson and Fleer (1982) and Fleer and Bacon (1991) used for α-spectrometry. Sample preparation procedures for most sediment sample determinations by ICP-MS were similar to those procedures used in α-spectrometry but with some modifications. In brief, sediment samples were prepared for analysis by means of acid dissolution. Separation and purification by of Pa, Th and U fractions were done by coprecipitation with Fe and Al hydroxides and by anion exchange chromatography of the chloro-complexes and nitrate-complexes. The solvent extraction and electroplating to prepare sources for counting were omitted in the preparation for ICP-MS.

Determination of Pa, Th, and U isotopes in sediment samples by ICP-MS requires three separate runs: (1) taking small aliquots of the dissolved sample, after appropriate dilution but without chemical separation, and spiking these small aliquots with ^{236}U and ^{229}Th for isotope-dilution analysis for simultaneous measurements of ^{238}U and ^{232}Th; (2) using a two-stage spike with ^{233}Pa as a tracer for chemical yield and ^{229}Th as an internal standard for measurement of ^{231}Pa; and (3) isotope dilution analysis for simultaneous determinations of ^{234}U, ^{235}U, and ^{230}Th on the same aliquot being spiked with ^{236}U, and ^{229}Th. ^{231}Pa measurement by ICP-MS is much more difficult because of the low aboundance of ^{231}Pa in nature (its

concentration is about 20 times less than that of ^{230}Th in sediments) and because of the fact that no suitable Pa isotopes exist for the isotope-dilution procedure. For radiation safety, ^{233}Pa was avoided, because its short half-life would require very large amount of activity (> 10^6 dpm). ^{229}Th was chosen as a substitute for several reasons: (1) the activity required for isotope dilution is not high (at least four orders less radiation), (2) its mass is close to mass 231, and (3) it causes no interference with mass 231. The preparation procedure for these separation runs is outlined schematically in Figure 2.1 and is described in the following sub-sections.

2.4.1 Sample preparation

Sediment samples are dried at 110°C to a constant weight, ground with an agate mortar and pestle, and stored in air-tight vials. Before the day for weighing, the sample is heated in an oven a few hours or overnight at 60°C to remove moisture.

2.4.2 Sample dissolution

Dried sediment is weighed and placed in a Teflon FEP beaker, and ^{236}U and ^{229}Th spikes as yield monitors are added in amounts approximately equal to the expected amount of ^{235}U and ^{230}Th in the sample. The ^{233}Pa spike is added in an amount that will yield approximately 100 cpm (counts per minute). Samples are subjected to total dissolution with mixtures of

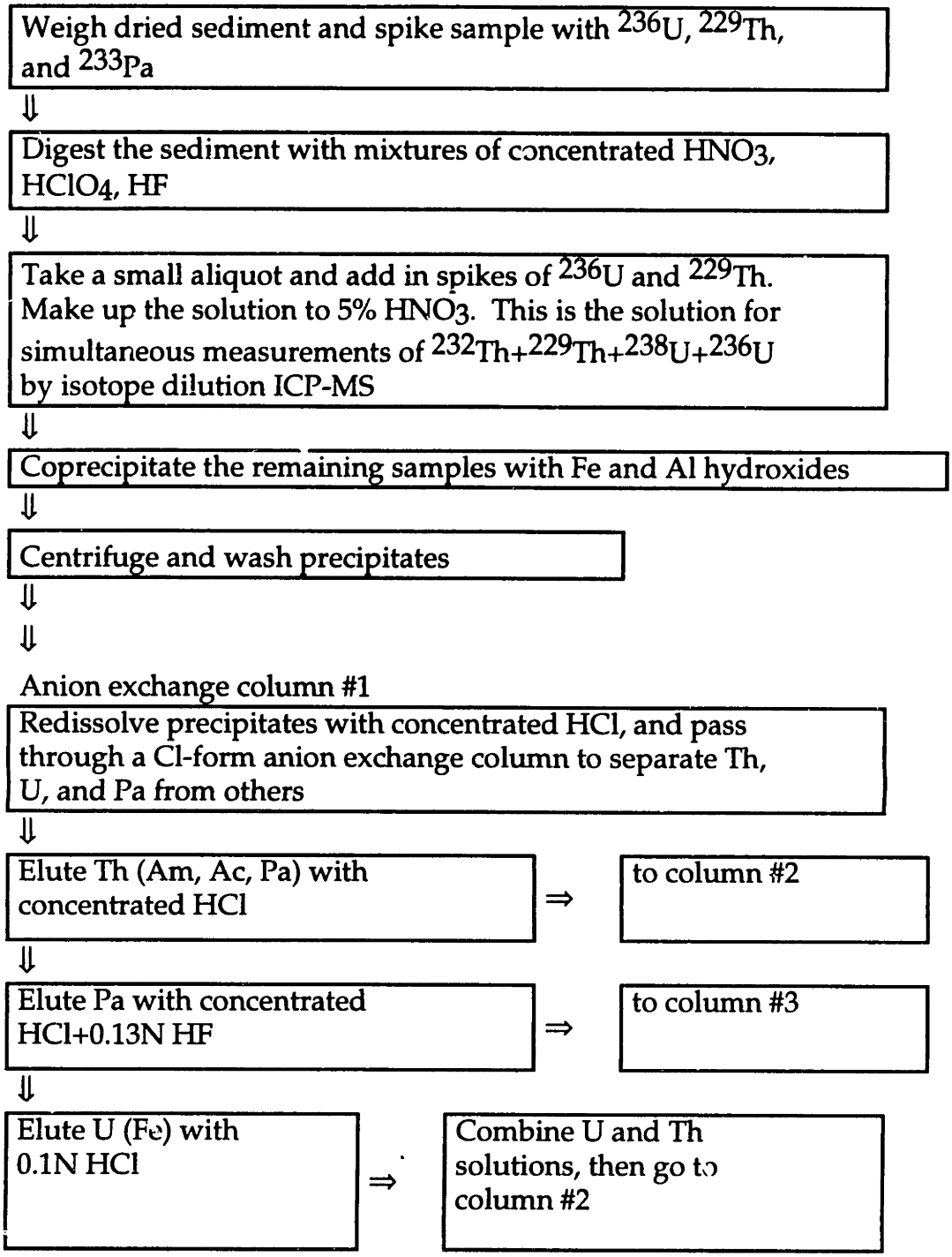

Figure 2.1 A schematic flow chart for separation and purification of U, Th, and Pa isotopes for ICP-MS analyses

Figure 2.1 (continue)

Anion exchange column #2: Nitrate-form ion exchange column for Th+U purification

Washing out most of the sample impurities with 3 column volumes of 8N HNO_3

⇓

Elute Th with 9N HCl

⇓

Elute Pa with concentrated HCl+0.13N HF, and combine it with the first Pa fraction

⇓

Elute U with 0.1N HCl

⇓

Combine U and Th fraction in a beaker, and make up to 2-2.5 ml 5% HNO_3 solution. This is the solution for simultaneous measurement of ^{230}Th+^{229}Th+^{235}U+^{234}U+^{236}U by isotope dilution-ICP-MS

Anion exchange column #3: Nitrate-form ion exchange column for Pa purification

washing out most of the sample impurities with 3 column volumes of 8N HNO_3

⇓

Elute Th with 9N HCl

⇓

Elute Pa with concentrated HCl+0.13N HF

⇓

Boil off HCl+0.1N HF solution, and convert to ~1 ml solution in 5% HNO_3

⇓

Weigh precisely both before and after taking a small aliquot (~50 µl) of Pa solution for chemical yield determination

⇓

Add the second stage of ^{229}Th into the Pa solution after yield determination, and dilute to 2-2.5 ml 5% HNO_3 solution. This is the solution for $^{231}Pa/^{229}Th$ analysis

HNO_3, HF, and $HClO_4$ along with the first set of ^{236}U, ^{229}Th, and ^{233}Pa spikes. The sample is first treated with enough 2N HCl to dissolve $CaCO_3$, then 5-15 ml 70% $HClO_4$, 1-5 ml 48% HF and 5-15 ml concentrated HNO_3 is added, and the sample is loosely covered with a lid and heated on a hotplate to break down the aluminosilicate. The sample solution is covered tightly with a lid and fuming is continued until all organic matter is destroyed by $HClO_4$. The sample is removed from the hot plate and cooled briefly, the lid is removed from the beaker, and a few more drops of 48% HF are added to the sample. Then the $HClO_4$ is allowed to fume to insure complete dissolution of floating or suspended aluminosilicate. Beaker walls are then rinsed down two or three times with concentrated HNO_3 to remove traces of HF, and the solution is further heated until it becomes a semi-solid. The trace of HF must be removed; otherwise Pa will be eluted along with Th with the 9N HCl. 2N HCl and a few ml of distilled water are then added, after which the solution is heated for few more minutes. A subsample for ^{238}U and ^{232}Th is taken at this point.

2.4.3 Subsampling for ^{238}U and ^{232}Th

After the sample is completely dissolved, the final fumed residue is taken up in 2N HCl into a pre-weighed centrifuge tube; then the digested solution, along with the tube, is weighed. A 50 µl aliquot is removed at this point, put into another pre-weighed centrifuge tube, and spiked a second time with ^{229}Th and ^{236}U for simultaneous analysis of ^{232}Th+^{229}Th+^{238}U+^{236}U by isotope dilution-ICP-MS. Spikes must be precisely weighed.

2.4.4 Coprecipitation with Fe and Al hydroxides

Dissolved sample solutions containing Th, U, and Pa are coprecipitated with Fe and Al hydroxides at a pH of 7 to 9 and centrifuged. The precipitate is washed with distilled water, centrifuged three times, then saved for purification through the ion exchange column.

2.4.5 Ion exchange procedure for separation and purification of U, Th, and Pa

The precipitate is finally redissolved in concentrated HCl and made up to a 9N HCl solution, then passed through an anion exchange column that has been preconditioned with concentrated HCl. The chloro-complexes of U and Pa are retained, and the column is washed with 9 N HCl to elute the Th. Elution of the Pa is done with concentrated HCl + 0.13N HF, and finally the U is eluted with 0.1 N HCl. The separated sample fractions containing Th, Pa, and U are heated to evaporate the HCl. Th and U fractions are recombined at this point, and the solution is converted into 8 N HNO_3. After cooling, the Th+ U solution is run through an 8N HNO_3 column to separate Th and U from the major matrix and minor interferences. Th with 9N HCl, and U with 0.1 N HCl are collected sequentially into the same beaker again. The Th+U solution is heated to boil off the HCl, then converted to nitrate; then it is evaporated to a small drop and diluted to a 2-2.5 ml solution of 5% HNO_3. This is the solution for simultaneous analysis of ^{230}Th+^{229}Th+^{235}U+^{234}U+^{236}U by ICP-MS.

The protactinium eluted from the chloride column is made up to 8 N HNO_3 solution and run through a preconditioned 8N HNO_3 column to

separate Pa from other impurities. The Pa fraction is eluted with concentrated HCl + 0.13 N HF after sequential washings with 8 N HNO_3 and 9 N HCl. The cleanup is essential to ensure a pure Pa solution and thus to avoid possible matrix effects or interferences when measuring by ICP-MS. After this final purification, the Pa fraction is converted to nitrate form by successive washings with concentrated HNO_3 followed by evaporation to ensure complete removal of HF, and it is evaporated to one small drop (~50µl) in a FEP-Teflon vial. The solution is then brought to ~ 5% HNO_3 by dilution. A small aliquot for plating on a stainless steel disc for yield determination is taken. The solution is weighed precisely both before and after taking this aliquot.

2.4.6 Chemical yield determination of Pa

Determining the chemical yield of Pa is done by β-counting the ^{233}Pa tracer. This is done by taking a subaliquot (~50 µl of ~ 2 ml) sample solution and manually plating onto a stainless steel disc. Sample solutions are weighed precisely before and after taking the subaliquot. All experiments are designed so that counts are acquired on a relative basis for a given counting geometry, negating the necessity for determining the absolute efficiencies of the detector. Several standard ^{233}Pa plates are made from each batch of ^{233}Pa working solutions. The solutions are pipetted directly into an electroplating cell and are plated. All the plates usually agree within counting statistics. Any that do not agree are discarded. Several standard ^{233}Pa plates are also plated by evaporation to compare with those are electroplated to make sure that the electroplating efficiency is 100%. The decay rate of standard ^{233}Pa is

occasionally checked to ensure that no other interferences are included in the tracer. It is desirable that enough ^{233}Pa spike for both standards and samples to obtain good precision (better than 2%) within a short time period (<20 minutes).

2.4.7 Final analyte preparation for ICP-MS

After determination of the chemical yield, a known concentration of ^{229}Th spike is added to the Pa solution. The solution is then diluted to 2-2.5 ml analyte volume and the whole analyte solution is weighed; finally, the combined solution of ^{231}Pa + ^{229}Th in 5% HNO_3 is ready for introduction into the ICP-MS. It is important to add the ^{229}Th spike after, not before, determination of chemical yield to avoid interference during the counting of ^{233}Pa from ^{229}Th and its decay products.

2. 5 ICP-MS ANALYSIS

2.5.1 ICP-MS operation parameters

Analyses were performed on a model VG PQ2 Plus quadrupole ICP-MS at Harvard University. ICP-MS operating parameters are listed in Table 2. 2.

2.5.1-a Sample introduction

All three batches (^{230}Th+^{229}Th+^{235}U+^{234}U+^{236}U; ^{231}Pa+^{229}Th; and ^{238}U+^{236}U+^{232}Th+^{229}Th) of sample in 1-5% HNO_3 are used as a final

analyte, and are separately introduced into the ICP-MS with a peristaltic pump (Gilson Minipuls 22) and a Meinhard concentric glass nebulizer. The length of the Teflon tubing between the valve and the nebulizer is minimized, and the pump is set at a constant speed. The sample volume is optimized to obtain maximum sample signal relative to background without being too high in sample viscosity. With a flow rate of 0.8 ml/min, a 48-second uptake time, and 33-second running time for each of three runs per sample, the required sample volume is 2-2.5 ml.

2.5.1-b Optimized conditions and features for Pa, U, and Th isotopes analysis

One "tuning cocktail", which contains the same concentration of different elements in the mass range from ^{9}Be to ^{238}U, is usually made up in order to optimize the operating condition of the instrument. Resolution, sensitivity, and instrument stability need to be optimized each running day; sometimes it is also necessary to adjust the instrument after a half day. Mass calibration also needs to be verified occasionally, but it is not necessary to re-calibrate it every running day.

2.5.1-c Resolution. Sensitivity, and Stability

Different resolution settings are tested to obtain one proper resolution setting without the loss of too much sensitivity. The mass spectrometer is set to provide 0.5-1.0 a.m.u. resolution over the entire mass range. 0.8 a.m.u. peak area is usually integrated. The operating conditions for the ICP-MS system are optimized by maximizing the ion intensity for ^{238}U. After tuning,

an example of the instrument mean intensity is 2.37 ± 0.03 MHz for a 50 ppb ^{238}U tuning solution. However, optimal tuning sensitivity varies from day to day. It has been recorded over a long time period (Figure 2.2). The variability in sensitivity is caused by changes in the lens voltages, the plasma operating conditions, or the flow rate of the nebulizer. Sometimes, the sensitivity loss is caused by deposition of material on the sampler or skimmer or on the orifice of the nebulizer. It is always possible to recover the original sensitivity simply by removing and cleaning these parts.

One instrument operation feature observed from Figure 2.2 is that the signal intensities fluctuated from low mass to high mass ranges on the tuning solution containing the same concentration of different elements. This feature of non-uniform elemental responses across the mass range is due to the performance of the interface. However, this feature does not affect measurements, because corrections are always made for mass fractionation with a monitor, which contains known concentrations of isotopes of interest.

The percent relative standard deviation (% RSD) is calculated for 10 successive scans in 10-20 minute intervals. Short-term stability is in the range of 1.3% RSD for a 25 ppb ^{238}U solution. For comparison, a working reference solution of ^{231}Pa with a much lower concentration (0.0155 ppb) gave a precision of 5%, which is limited mostly by counting statistics due to the low count rate. An example of a medium-term shift for a ^{231}Pa working reference is measured over 4 hours (Figure 2.3). The average difference of each run from the first run is in the range of [-(5.6 ± 2.3)]% (1σ). The medium-term stability for a standard solution of a ^{238}U or ^{230}Th is obtained as a range of <1 to 3% over 4 hours. The experiment indicates that the PQ can operate stably for a few hours but has some shift over a working day. Instability

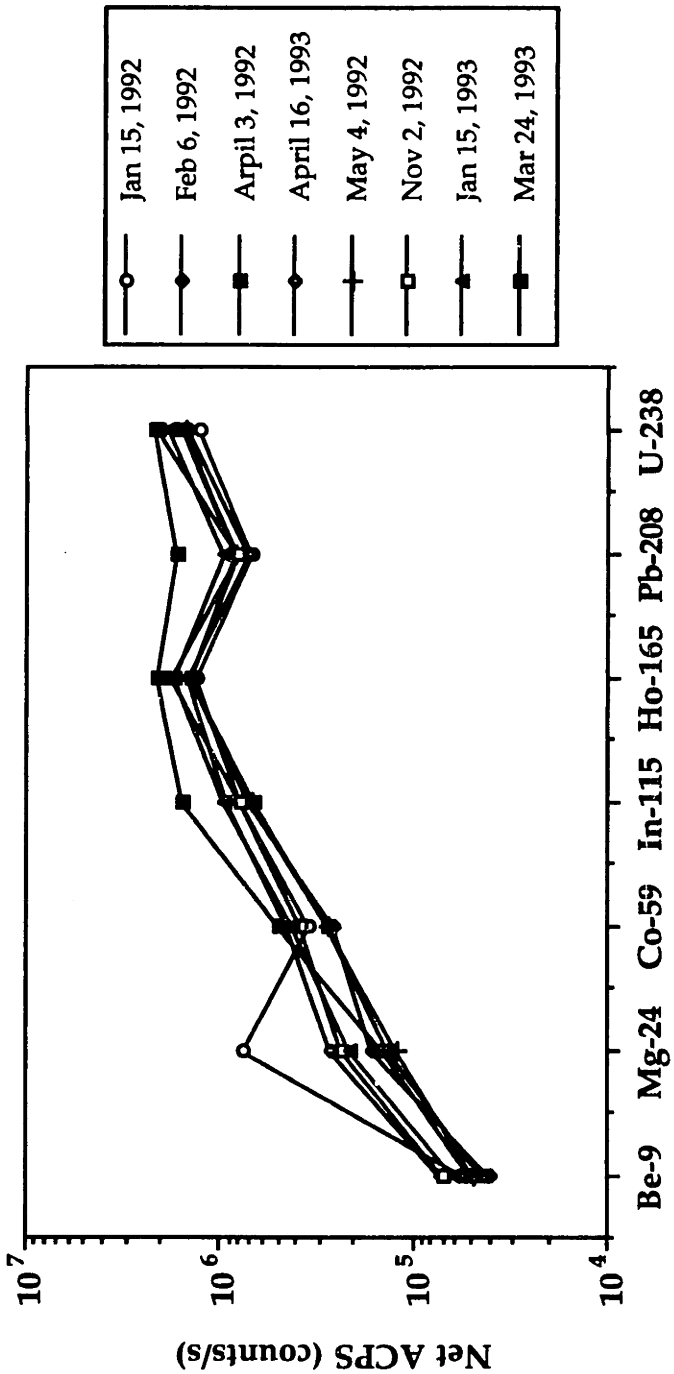

Figure 2.2 Variations of instrument tuning sensitivity over a long time period. All elements in the mass range from ^{9}Be to ^{238}U in the "tuning cocktail" are at same concentration of 25 ppb.

Table 2. 2 ICP-MS operating conditions

Instrument component	Conditions
Pneumatic Pump	Pump uptake rate: 0.8 ml/min
	Uptake time: 48 seconds
ICP unit	Forward power: 1.35 kwatt
	Reflected power: <5 watt
	Coolant Ar flow: 14.5 ml/min
	Auxiliary Ar flow: 0.6 ml/min
	Nebulizer Ar flow: 0.73 ml/min
Nebulizer	Meinhard glass concentric nebulizer
Mass spectrometer	Interface pressure: 1.5 mbar
	Quadrupole chamber pressure: 2.9×10^{-6} mbar
Analytical procedure	Analytical solution: 2-2.5 ml 5% HNO_3
	Run mode: mass scan mode
	Resolution setting: coarse scale: 5.0
	fine scale: 5.0

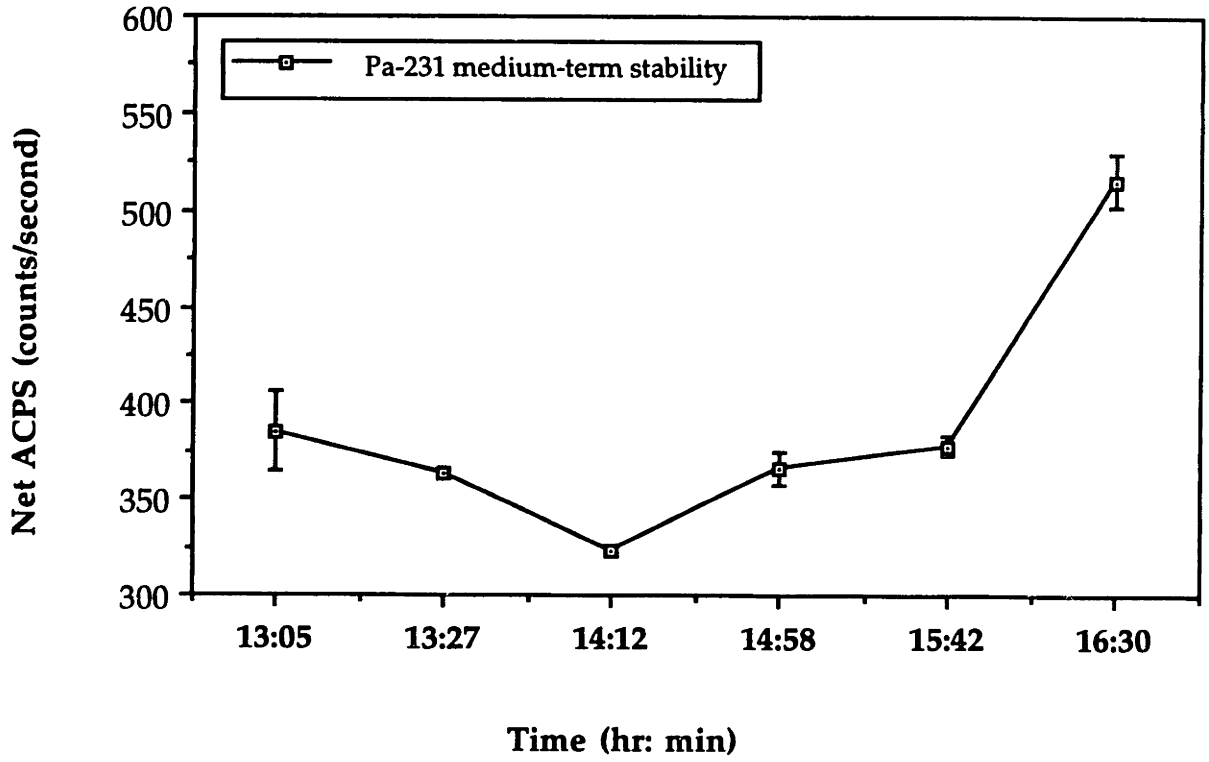

Figure 2.3 An example of medium-term stability of the instrument which is demonstrated by measuring a ^{231}Pa working solution over four hours. The concentration of the ^{231}Pa working solution is 0.0155 ppb.

manifests itself both as a gradual shift and in sporadic fluctuations. Factors that contribute to instability include a non-constant temperature in the spray chamber, inhomogeneous aerosol flow from the nebulizer, damaged or worn sampling and skimmer cones, air leakage through worn O-rings in the nebulizer mounting block, and room temperature fluctuations (Price Russ III & Bazan, 1987; Falkner, 1989, 1991). The stability of the instrument can be corrected for by periodic monitoring of a working reference solution when measurements last longer than a few hours. Therefore, the sequence of a background and a working reference interspersed with samples is applied routinely.

2.5.1-d Background, Memory Effect, and Detection Limits

Background spectra were examined for potential interferences. Deionized, distilled water, 1% and 5% HNO_3, and 2N HCl were checked, and no significant background features were observed in the mass range 228 to 240. Background levels were uniform almost all the time, and typically were in the range of 15 to 25 ACPS (counts in area peak per second) for mass 228 to 240 by mass scan mode. The average background spectra over a long period of several running days are shown in Table 2. 3. The number in parentheses is the numbers of replicate analyses.

Table 2.3 Example of background levels (in ACPS) for Th, Pa, and U isotopes

^{229}Th	^{230}Th	^{231}Pa	^{232}Th	^{234}U	^{235}U	^{236}U	^{238}U
23 ± 4	22 ± 4	25 ± 6	16 ± 2	12 ± 3	18 ± 5	16 ± 5	19 ± 1
(n=23)	(n=11)	(n=25)	(n=6)	(n=26)	(n=21)	(n=22)	(n=6)

A memory effect from previous samples can occur for high concentration runs (in particular for Th because it has a very strong tendency to adsorb on surfaces), but it can be eliminated by a combination of a one-minute rinse with deionized water and a 1.5-minute rinse with 5% HNO_3. Longer washing time may be required depending on the concentration and viscosity of the previous sample. The required washing time can be checked by continuously uptaking different washing solutions such as dilute HCl or HNO3 (1% - 5%) or deionized water and monitoring the background signal. This step is particularly necessary to insure that low concentrations of a sample will not be contaminated by a previous sample with a suspected high concentration; otherwise, the error could be significant.

The detection limit in ICP-MS is determined by the background noise and the sensitivity for the element of interest. The detection limit for ^{231}Pa is calculated by taking 3 σ of the noise in the signal against a known concentration of working reference ^{231}Pa, and its value is ~0.5 pg/g (i.e. ~ 1 x 10^9 atom/g = ~ 0.05 dpm/g) on the VG PQ2 Plus instrument. The following formula is used (Hulmston and Hutton, 1991):

$$LOD(1)\ (pg/g) = 3\sigma \times I_B/I_A \times C_A$$

where I OD = the limit of detection, I_B = integrated peak area of the blank (5.58 ACPS in this example), I_A = integrated peak area of the analyte (= 677 ACPS), and C_A = concentration of the analyte (pg/g) (= 20 pg/g = 2.093 dpm/g).

2.5.1-e Linearity and dynamic:range

The pulse counting systems that are used have an effective dynamic range of 6 to 7 orders of magnitude from 1 to 10^7 counts per second (cps) for analyte concentrations from 1 ppt to 1 ppm. The analog detector has a concentration range of 10 ppb to 100 ppm for the linear dynamic range.

2.5.2 Analytical procedures

From the results of the experiments discussed above, the following analytical procedures are used for routine analysis of Pa, Th, and U isotopes in sediments. A mass scan mode is chosen, and isotope ratios are acquired for all three separated batches of solutions containing different isotopes. Mass scan ranges are from 228.5 to 239 amu. For Pa analysis, raw data on masses 229, 231, and 232 are obtained, and the isotope ratio 231/229 is calculated. The mass 232 is included for checking the abundance sensitivity. For ^{230}Th+^{234}U+^{235}U determination, masses 231 and 237 are also acquired to check for effects of tailing or hydride formation (see below), but mass 232 is skipped to avoid detector overload. For analytical procedures of the ^{232}Th+^{238}U analysis, the masses 231, 237, and 239 are scanned to monitor the abundance sensitivity on ^{232}Th and ^{238}U spectra respectively, and possible formation of hydride. A monitor solution containing the isotopes of interest is interspersed with samples to correct for mass fractionation. All spikes and standards used for the determination of samples are examined in association with samples on each individual running day in order to make interference corrections for any contributions from spikes and standards.

2.6 DETERMINATION OF ^{231}PA BY ICP-MS

The major effort was to establish an adequate procedure for ^{231}Pa analysis using ^{229}Th as an internal standard and taking into account (1) abundance sensitivity, (2) quantitative analysis and instrumental fractionation, (3) matrix effects and matrix elimination, and (4) accuracy and reproducibility. In addition, efforts were made to establish procedures (as shown in the next section) for simultaneous isotope dilution analysis of U and Th isotopes.

2.6.1 Degree of ionization of ^{231}Pa

One advantage of ICP-MS over thermal ionization mass spectrometry (TIMS) is its superior ionization efficiency. Most elements are efficiently ionized in a high temperature range of 7500 to 8000K (Houk and Thompson, 1988). Ionization efficiency of Pa by ICP-MS has never been reported before simply because we do not know its plasma chemistry very well. It was estimated by assuming the same transport efficiency as Th, and by taking the ionization efficiency of Th which is known to be 100%. The ionization of Pa was found to be almost the same as that of Th, i.e., 100%.

2.6.2 Abundance sensitivity

Abundance sensitivity for ^{231}Pa is measured as the ratio of the areas under the peaks at masses 232 and 231. 0.8 amu (atomic mass unit), the width normally used in the data analysis, is used as the width over which the areas

are calculated between peaks 231 and 232 after correcting for background. Table 2.4 shows that even with a counting rate greater than 4 x 10^6 ACPS from a high concentration of ^{232}Th, the measured count rate on mass 231 (with net ACPS = 870) is not significantly different from the measured count rate of ^{231}Pa alone with no co-existing ^{232}Th. This indicates an abundance sensitivity of 10^6. Although a typical abundance ratio of ^{232}Th/^{231}Pa in deep-sea sediments is greater than 10^6, and overlap from the tailing of ^{232}Th would be found, I normally applied column preparation to separate Pa from Th, U, and the major cations. As a result, tailing of the mass 232 peak into the mass 231 region was never significant.

Table 2.4 Abundance sensitivity for ^{231}Pa*

^{232}Th/^{231}Pa ** (dpm/g)/(dpm/g)	^{232}Th/^{231}Pa atomic ratio (measured ratio)	Peak area counts on 231	Peak area counts on 232
4.99x10^{-4}/2.422	90 ± 1	820 ± 20	7.3 x10^3± 1.0 x10^2
4.89x10^{-3}/2.413	960 ± 30	800 ± 30	7.7x10^5 ±1.0x10^4
5.10x10^{-2}/2.490	5100 ± 220	870 ± 40	4.0x10^6±1.0x10^5

* Abundance sensitivity for ^{231}Pa is determined by measuring ratios of the areas under the peaks at masses 232 and 231; the reported data were rounded off.
** added activity ratio; i.e. (dpm/g)/(dpm/g).

2.6.3 Quantitative analysis of ^{231}Pa/^{229}Th isotope ratio and instrument fractionation

An experiment was performed by adding equal amounts of an internal standard of ^{229}Th to a series of different known amounts of a ^{231}Pa working reference. The measured ^{231}Pa/^{229}Th atom ratio was corrected for mass

fractionation using a "monitor". The results (Table 2.5) show that the calculated $^{231}Pa/^{229}Th$ ratios are identical with expected $^{231}Pa/^{229}Th$ ratios from the working references within analytical errors. These results illustrate the quantitative capabilities of $^{231}Pa/^{229}Th$ isotope ratio measurement by using ^{229}Th as an internal standard.

Table 2.5 Example of calibration for quantitative analysis of $^{231}Pa/^{229}Th$ ratio*

$^{231}Pa/^{229}Th$ Expected	$^{231}Pa/^{229}Th$ Measured	$^{231}Pa/^{229}Th$ Calculated	Measured / Expected
0.14	0.14 ± 0.01	0.15	1.00
0.20	0.22 ± 0.01	0.21	1.10
0.27	0.27 ± 0.01	0.29	1.00
0.33	0.37 ± 0.02	0.35	1.12
0.56	0.59 ± 0.03	0.60	1.05
Calibration parameters: y = mx +c			
Slope (m) = 1.069			
Intercept (c) = -3.027 E -3			
Correlation coefficient (r) = 0.997			

* atom ratio
** the measured ratio was corrected for background and for mass fractionation
*** calculated ratio was obtained with the regression line and the expected $^{231}Pa/^{229}Th$ atomic ratio

Mass fractionation corrections are required because the observed isotope ratios usually deviate from "true" values (Campana, 1980; Klinkhammer and Palmer, 1991; Shaw and Francois, 1991). Corrections are made by comparing the measured isotope ratio to a "monitor" solution

containing a known amount of ^{231}Pa and ^{229}Th. Fractionation observed on the instrument at Harvard University generally ranged from 4 to 10% (Table 2.6) between masses 231 and 229, but occasionally a higher value was observed. Some shifts in the mass fractionation effects were also found within a day's run; thus, periodic measurements of a monitor solution containing the isotopes of interest are always interspersed with sample determinations.

Table 2.6 Examples of instrument stability on $^{231}Pa/^{229}Th$ atom ratio and instrument mass fractionation

Short-term stability of $^{231}Pa/^{229}Th$	Medium-term* stability of $^{231}Pa/^{229}Th$
Expected value = 0.46 **	Expected value = 0.46 **
0.39 ± 0.02 (n=3)	0.39 ± 0.02 (n=3)
	0.43 ± 0.01 (n=3)
	0.44 ± 0.02 (n=3)
	0.42 ± 0.02 (n=3)

* medium-term stability is determined by a working solution which is measured within a half operation day.
** Expected value is atomic ratio of the working solution

2.6.4 Matrix effects

Sample matrix effects, in addition to introducing background spectral features, also induce actual changes in the analyte signal intensity. Significant signal suppression for ^{230}Th has been found in standards and samples containing high concentrations of major ions (particularly Fe) (Shaw and

Francois, 1991); in the following experiments, evidence of signal suppression for Pa is also found.

Experiment 1 Detection of matrix effects: a series of known amounts of ^{231}Pa aqueous standards (see Table 2.7) are added to several aliquots of equal amounts (Table 2.7) of sediment solution to make standards in the presence of sample matrix. Various sediments were used in order to examine effects of different kinds of sample matrix.

The data shown in Figure 2.4 illustrate how the interfering materials present in samples shift the slopes of calibration curves away from that of aqueous standards. The solid line represents a typical calibration line for a set of aqueous standards. As standard concentration increases, a linear increase in signal intensity is observed. When aliquots of a standard are added to portions of the samples, the signal intensity for all the solution still falls within the linear portion of the working curves, but because of the interference, the slopes of aqueous standards in the presence of sample matrix are different from that observed for the aqueous standards. The discrepancy between the slope of standards and the slopes of the aliquots with different kind of sediment sample matrices are decreasing 5% and 9.8% ($\pm$ 1 σ) for opaline sediment and calcareous silicate sediment respectively.

Experiment 2 Extent of matrix effect: various concentrations (Table 2.7) of one sediment (calcareous clay) matrix were added to the same amount of ^{231}Pa aqueous standard.

Figure 2.5 clearly shows that when the concentration of sample matrix is increased by 5 times, there is a suppression of signal intensity of

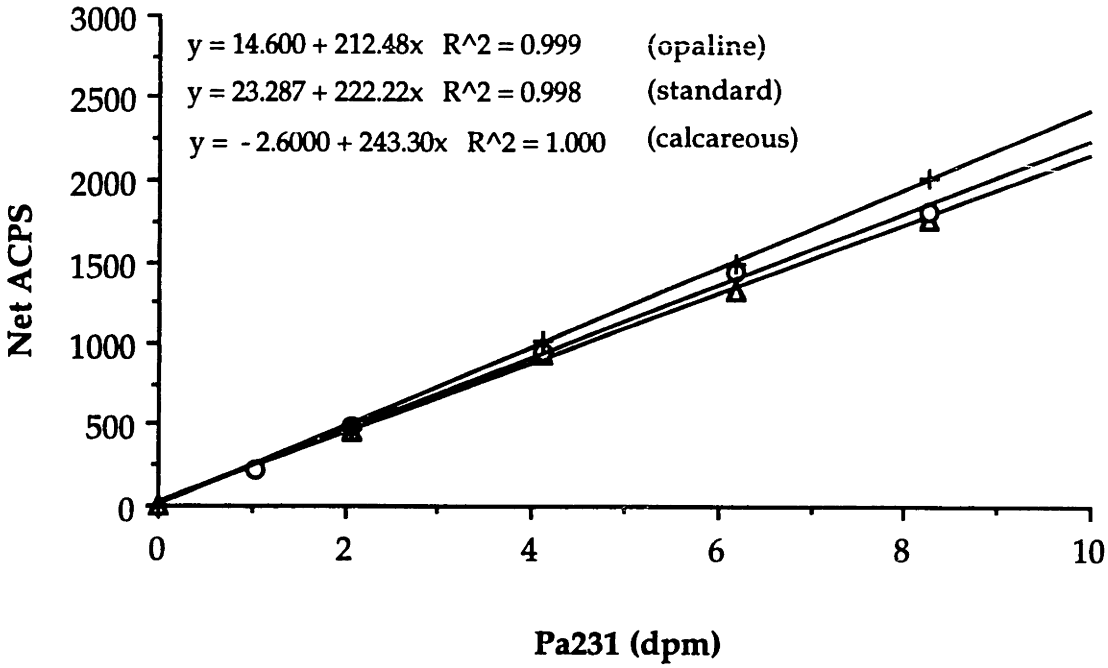

Figure 2.4 Example of sample matrix effects on a ^{231}Pa standard analyte. Circles represent standard in absence of sample matrix; triangles represent standard in presence of opaline sediment sample matrix; crosses represent standard in presence of calcareous silicate sediment sample matrix.

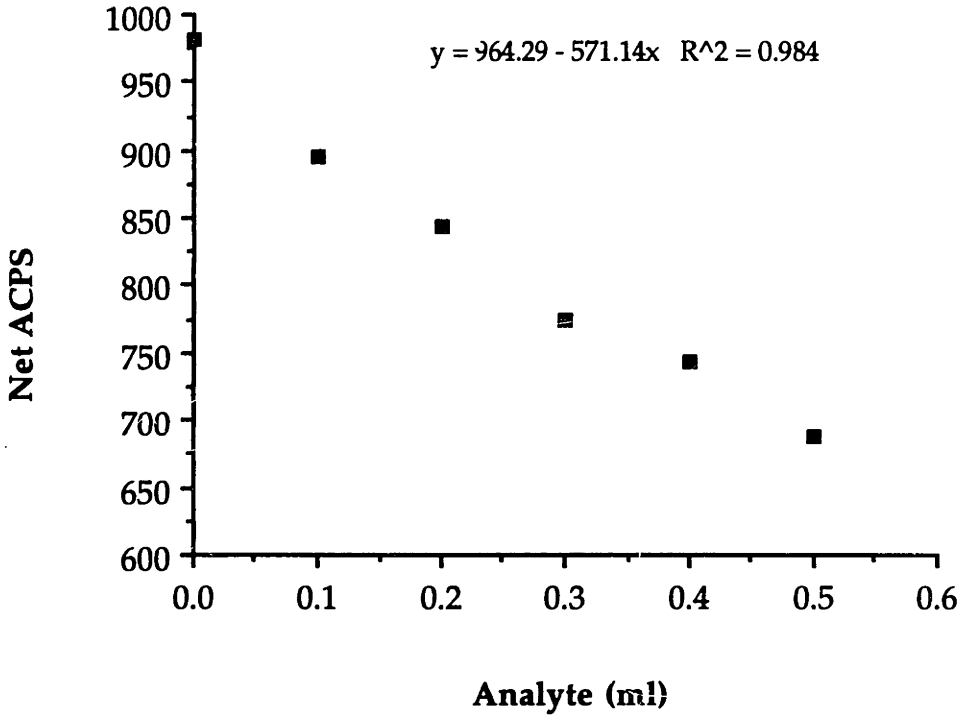

Figure 2.5 Extent of matrix effect. A set of different concentration sediment matrix with adding equal amount (2.16 dpm/g) of a ^{231}Pa working solution. The concentration of sediment is ~3g/ml.

approximately 7% to 28%. The effect is not well understood at this time; in general, a high concentration of any matrix element essentially suppresses the signal of Pa in sample analytes. Semi-quantitative scans of the sample with significant matrix effects and the sample without matrix effects were made by spiking ^{115}In as an internal standard. Results suggest that IIB and IIIB group elements in the periodic table are suspected interferences because their concentrations were 3 to 10 times higher in the sample with the matrix effects than in the ^{231}Pa standard and the sample without the matrix effects.

Spectral overlaps (*i.e.*, isobaric interferences) and/or signal intensity depression/enhancement from contained impurities in analyzing samples have also been checked for the determination of $^{231}Pa/^{229}Th$ ratio. Three sets of experiments were examined. The first set of experiments used a series of working solutions containing known amounts of both ^{231}Pa and ^{229}Th in the solution with no presence of any sediment matrix. The second set involved adding the same series of working solutions to an equal amount of a sediment matrix. The third set of experiments required addition of the same series of working solutions to different amounts of a sediment matrix. Table 2.7 shows the experimental results. The average measured $^{231}Pa/^{229}Th$ atomic ratios of the second set of experiments and the third set of experiments are 10% ± 6% and 26% ± 11% higher than the average ratio of the first set of experiments. In the third set of experiments, the average result gives a ~ 8% ± 10% higher value for a solution containing the sediment matrix than the value of a solution containing no sediment matrix (III-A solution). These results suggested that there is sample matrix effect on the measurement of the $^{231}Pa/^{229}Th$ ratio, but the measured data showed a relatively high standard deviation. The effect may not be significant if one

Table 2.7 The experimental results of matrix effects on the measurement of $^{231}Pa/^{229}Th$ ratio

Experiment #	Amount of working solution*	Initial mount of sediment matrix **	Measured atomic ratio
I-A	0/0	0/0	N.D. ***
I-B	1.03/10.30	0/0	0.40 ± 0.04
I-C	2.00/20.01	0/0	0.42 ± 0.04
I-D	3.00/29.99	0/0	0.44 ± 0.01
I-E	4.00/40.00	0/0	0.41 ± 0.01
			Average = 0.42 ± 0.01
II-A	0/0	0	N.D. ***
II-B	1.03/10.30	2g/2.5 ml	0.46 ± 0.01
II-C	2.00/20.01	2g/2.5 ml	0.42 ± 0.01
II-D	3.00/29.99	1.8g/2.5 ml	0.48 ± 0.01
II-E	4.00/40.02	2g/2.5 ml	0.47 ± 0.01
			Average = 0.46 ± 0.01
III-A	2.00/20.01	0	0.48 ± 0.01
III-B	2.00/20.01	1g/2.5 ml	0.53 ± 0.02
III-C	1.03/10.30	2g/2.5 ml	0.49 ± 0.01
III-D	1.03/10.30	3g/2.5 ml	0.63 ± 0.01
III-E	1.03/10.30	4g/2.5 ml	0.52 ± 0.01
			Average = 0.53±0.05

* the activity ratio (in unit (dpm/g)/(dpm/g)) of $^{231}Pa/^{229}Th$ in 2.5 ml weighed working solution. The expected atomic ratio of $^{231}Pa/^{229}Th$ in the working solution is ~0.45 for each individual analyte.

** the amount (in unit gram of sediment) of sediment matrix used in the analytical solution (in unit ml of analyte).

*** there is no calculation data since no significant peak area counts after subtraction from the background levels.

takes counting statistics and instrumental stability into account. Efforts were also made for reducing the matrix problem, if any, by applying ion-exchange column purification procedures, as indicated above, for the separation of Pa (and Th, U) from the major cations. The result has been observed from the data in Figure 2.6, which demonstrates that when a sample has been cleaned by an additional 8N HNO_3 column, major interference materials can be properly cleaned out, and the slope of the working curve is identical with that of the aqueous standard.

The standard addition method was thought to be a useful technique that might correct possible matrix interferences present in the sample rather than eliminating the interference itself. This method was developed for the correction of matrix effects in the beginning of this thesis; however, the method of standard addition could not be applied to many of the samples in this thesis work, since the amount of available sample material was not enough for acceptable precision by this method.

After sample purification, the final solution is introduced into ICP-MS, and as the following section shows, there is no significant matrix effect to bias the determination of the $^{231}Pa/^{229}Th$ ratio, and precise and accurate measurement for ^{231}Pa can be made by using ^{229}Th as an internal standard. The problem arising from spectral overlap is also eliminated by column-preparation. Isobaric interferences at mass 231 have never been found, since no significant background features have been observed above mass 84, and no significant MO+ or MOH forms of elements in the periodic table could interfere with the 231 and 229 mass peaks after our chemical preparation is applied. The possible chance of ^{230}ThH formation at mass 231 is also

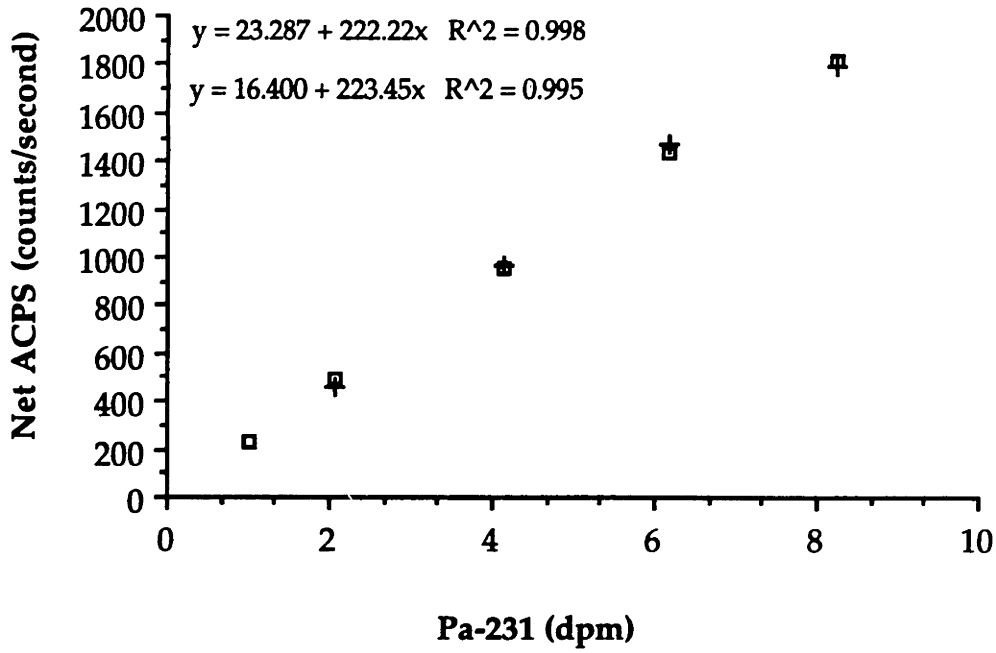

Figure 2.6 Example of reduction in sample matrix effect on the ^{231}Pa signal by applying one ion-exchange column purification. Squares represent a set of different concentration of a ^{231}Pa working solution; crosses represent the same set ^{231}Pa working solution in the presence of the sediment sample after one more step of 8N HNO_3 column purification.

unlikely to interfere significantly with the ^{231}Pa peak after column separation.

On the other hand, the "residual" of the first addition of the ^{229}Th spike might have a chance to leak into the Pa fraction during the column separation; therefore, the procedure is to add a higher amount of ^{229}Th on the second stage spike.

2.6.5 Precision and Accuracy

Precision and accuracy of ^{231}Pa determination by ICP-MS were assessed by replicate analyses of the Harwell uraninite (Congo pitchblende), which is a well-characterized reference material. It has been used for extensive inter-laboratory comparisons by α-spectrometry, and it has been shown that all uranium series isotopes approach the secular equilibrium values (a distributed note from M. Ivanovich, 1979). The equilibrium value of ^{235}U activity is proportional to ^{238}U activity (i.e., ^{235}U activity=0.046 ^{238}U activity); the equilibrium value of ^{231}Pa is thus expected to equal its parent value which is 5.56 dpm/g. Several Harwell uraninite aliquots with concentrations in the range 0.18 to 0.24 dpm per gram of solution (i.e., 0.38 dpm to 0.50 dpm of Pa from Harwell uraninite solution for a 2.1 ml analyte volume) were prepared following the same preparation procedure as for the sediment sample and with the same amount of ^{229}Th was added as an internal standard. The $^{231}Pa/^{229}Th$ ratios of the Harwell uraninite aliquots were then determined. Precision and accuracy are shown in Table 2.8. The same uraninite reference material, with a concentration in the range of 1 to 1.5 dpm of Harwell uraninite solution, was measured by α-spectrometry, and

the results are also presented on Table 2.8 for comparison. As shown in Table 2.8, the analytical results of ^{231}Pa analyses by ICP-MS are given as a mean value of 5.65 dpm/g with 4% deviation (± 1 σ), and the α-spectrometry results are given as 5.99 dpm/g with 4% deviation (± 1 σ). The standard deviation of ICP-MS results includes errors from the analytical procedure, the calibration of added spikes and working references, the chemical yield determination by beta counting, the atom ratio determination, the "monitor" solution for instrumental mass fractionation, and background subtraction of ICP-MS. The standard deviation of results by α-spectrometry includes errors from the analytical procedure, chemical yield determination by beta counting, and counting error by α-counter. Apparently, the measurements of smaller ^{231}Pa samples by ICP-MS technique have precision (0.38 dpm to 0.50 dpm of Harwell uraninite solution) comparable to that of α-spectrometry on a larger sample size (1 to 1.5 dpm), but the ICP-MS technique obtained a ^{231}Pa average value with smaller deviations from a real value (i.e., 5.56 dpm/g) of Harwell uraninite than those samples done by α-spectrometry. On the other hand, if the solutions being measured by ICP-MS have the same amount (~0.4 dpm) of analyte, days to weeks of α–counting time would be needed to obtain the same precision of ~4%.

A comparison between the internal standard-ICP-MS technique and the α--counting technique was aslo made for a series of sediment samples having a range of ^{231}Pa concentrations of ~0.29 to 1.5 dpm/g. The analytical results are shown in Table 2.9. To indicate the comparison between the two techniques, the ratio of the results of each was taken, and it shows that the correlation between the two techniques is high, with an average ratio of 0.94 ± 0.06 (1σ, n =9). The standard deviations include a partial error derived from

the α–counting technique and a partial error derived from the ICP-MS technique. The error for low concentration samples measured by ICP-MS is large because of the large background correction.

The experiments' results clearly show that the dependence of isotope ratios on the concentration or on the presence of concomitant elements existing in different type sediment samples can be eliminated by the method developed here. Apparently, from the results shown in Table 2.8 and Table 2.9, in terms of precision, accuracy, and the time requirement for obtaining a data point, the ICP-MS analytical technique of ^{231}Pa measurements, based on isotope ratios spiked with ^{229}Th as an internal standard, are preferable to the α-counting technique. The analytical method reported here for ^{231}Pa determination should be considered a stepping-stone to future advances. In future, we expect to obtain much better precision and to be able to apply the technique to a much smaller sample size using other kinds of sample introduction techniques than that with the conventional nebulizer. These sample introduction techniques may include ultrasonic-nebulizer, direct-flow injection, or electro-thermal volatilization (ETV), because it is believed that these techniques might improve sensitivity by 10 to 100-fold over that demonstrated by the conventional nebulizer.

Table 2.8 Precision and Accuracy of $^{231}Pa/^{229}Th$ measurement by ICP-MS

^{231}Pa (dpm/g) α-Spectrometry *	^{231}Pa (dpm/g) ICP-MS **
5.75 ± 0.30	5.49 ± 0.16
5.64 ± 0.32	5.74 ± 0.14
6.40 ± 0.33	5.95 ± 0.14
6.10 ± 0.06	5.91 ± 0.68
5.99 ± 0.10	5.71 ± 0.76
5.76 ± 0.10	5.59 ± 0.93
6.29 ± 0.11	5.19 ± 0.56
mean value = 5.99 ± 0.27 ***	mean value = 5.65 ± 0.24
(N=7, 1σ=4.45%)	(N=7,1σ=4.28%)

* the amount of uraninite used for the analyses is of 1.0 to 1.5 dpm.
** the amount of uraninite used for the analyses is of 0.38 dpm to 0.5 dpm.
***Average measured ^{235}U by α- spectrometry is 5.80 ± 0.12 dpm/g, (N=8, 1σ=2.10%). The reported result from inter-calibrated data of ^{231}Pa, in equlibrium with ^{235}U, is 5.51 ± 0.09 dpm/g (i.e. 0.046 * ^{238}U).

Table 2.9 Comparison of ICP-MS to α–spectrometry for ^{231}Pa measurements

Sample	α–spectrometry ^{231}Pa (dpm/g)	ICP-MS ^{231}Pa (dpm/g)	ICP-MS/ α-Spectrometry
E45-74 HL	0.91 ± 0.04	0.81 ± 0.07	0.89 ± 0.09
E48-13 HL	0.38 ± 0.02	0.29 ± 0.02	0.76 ± 0.09
E50-17 HL	1.64 ± 0.07	1.51 ± 0.22	0.92 ± 0.14
E45-27 GL	0.73 ± 0.05	0.82 ± 0.06	1.12 ± 0.11
E45-71 GL	0.44 ± 0.02	0.29 ± 0.07	0.66 ± 0.16*
E45-63 HL	1.30 ± 0.05	1.45 ± 0.13	1.11 ± 0.11
E49- 8 GL	1.08 ± 0.04	0.79 ± 0.08	0.73 ± 0.08
E50-13 GL	0.99 ± 0.02	0.73 ± 0.07	0.74 ± 0.07
E45-64 GL	0.87 ± 0.04	1.11 ± 0.13	1.27 ± 0.16
E45-79 GL	1.06 ± 0.03	0.95 ± 0.14	0.90 ± 0.14
			M=0.94 ± 0.06**

* the data is not included in the calculation for mean value
** 1 standard error of the mean

2.7 SIMULTANEOUS DETERMINATION OF $^{230}TH+^{234}U+^{235}U$, AND $^{232}TH+^{238}U$ BY ISOTOPE DILUTION-ICPMS

2.7.1 Abundance sensitivity

After optimization, coarse scale is set at 5.0 and fine scale is set at 5.0. A band of 0.6 a.m.u. is used for each peak integration, and mass-scan mode is chosen. For $^{230}Th+^{234}U+^{235}U$, isotope ratios 230/229, 234/236 and 235/236 are measured. For $^{232}Th+^{238}U$ the ratios 232/229, 238/236 are measured. Masses 231 and 237 are also scanned during $^{230}Th+^{234}U+^{235}U$ analysis to monitor any possible tailing from the ^{232}Th at mass 230 or ^{235}UH interference at mass 236. The consideration is that if ^{236}UH can interfere with mass 237, then ^{235}UH would interfere with mass 236 in the same proportion because samples are always spiked to give approximately equal amounts of ^{236}U and ^{235}U. Therefore, an approximate correction for ^{235}UH interference can be made. Usually the correction is insignificant.

2.7.2 Mass fractionation

Mass fractionations are also found in the analyses of $^{230}Th+^{234}U+^{235}U$ and $^{232}Th+^{238}U$ (Table 2.10). The mean values of the observed $^{230}Th/^{229}Th$ ratio are about 3% to 9% lower than the expected value. The $^{235}U/^{236}U$ and $^{234}U/^{236}U$

ratios are about 0.3% to 5% and 0.6% to 8% lower than the expected values. Sensitivities seem to be lower for lighter isotopes than for heavier isotopes.

Some shifts in mass fractionation were also examined with a mixture of known isotope ratio standards to monitor the stabilities within a day's run. Results show medium-term stability to be approximately in the range of 1% to 4% for 230/229, 234/236, 235/236 (Table 2.10).

No evidence that the isotopes are dependent on concentrations of sample or on the presence of concomitant elements was observed in measurements on marine sediments. Even at a solution concentration of ~ 0.2 dpm/g for ^{230}Th, it is possible to measure the isotope ratios with a precision of 2% or better by the isotope dilution technique.

2.7.3 Precision and accuracy

Reproducibility checks with uraninite reference solutions are indicated in Table 2.11. The accuracy of the isotope ratios was examined by comparing results from a variety of deep-sea samples from different sites with both isotope dilution-ICP-MS and alpha-spectrometry. Both methods give the same results (Table 2.12). For precision and speed, isotope-dilution ICP-MS analysis of ^{230}Th, ^{232}Th, ^{234}U, ^{235}U, and ^{238}U is favored over the α-counting technique.

2.8 CALCULATIONS

2.8.1 Isotope dilution calculation

Table 2.10 Examples of stabilities on isotope ratio and the instrumental mass fractionation

Isotope ratio	Short-term stability	Medium-term stability *
$^{230}Th/^{229}Th$	Expected value = 0.90 **	Expected value = 0.68 **
	0.85 ± 0.03 (n=4)	0.64 ± 0.02 (n=4)
		0.61 ± 0.04 (n=4)
		0.62 ± 0.02 (n=4)
$^{234}U/^{236}U$	Expected value = 0.78 **	Expected value = 0.78 **
	0.72 ± 0.02 (n=4)	0.72 ± 0.02 (n=4)
		0.75 ± 0.03 (n=4)
		0.78 ± 0.03 (n=4)
		0.75 ± 0.02 (n=4)
$^{235}U/^{236}U$	Expected value=103.16**	Expected value = 103.16 **
	98.14 ± 0.48 (n=4)	98.14 ± 0.48 (n=4)
		100.10 ± 0.01 (n=4)
		101.05 ± 5.81 (n=4)
		99.79 ± 3.23 (n=4)
$^{238}U/^{236}U$	Expected value = 1.56 **	Expected value = 1.56 **
	1.43 ± 0.05 (n=3)	1.43 ± 0.05 (n=3)
		1.40 ± 0.02 (n=3)
		1.48 ± 0.02 (n=3)
		1.45 ± 0.07 (n=3)
$^{232}Th/^{229}Th$	Expected value = 1.57 **	Expected value = 1.57 **
	1.68 ± 0.005 (n=3)	1.68 ± 0.005 (n=3)
		1.63 ± 0.02 (n=3)
		1.70 ± 0.06 (n=3)
		1.71 ± 0.06 (n=3)

* Medium-term stability is determined by a working solution which is measured within a half operation day.

** Expected value is atomic ratio of the working solution

Table 2.11 Reproducibility of Th, U isotope analyses of a uraninite standard

^{230}Th (dpm/g)		^{238}U (dpm/g)	$^{234}U/^{238}U$ activity ratio	^{235}U (dpm/g)	^{234}U (dpm/g)
α-counting	ICP-MS	α-counting	α-counting	ICP-MS*	ICP-MS*
128.26± 2.21	124.74± 2.10	130.55± 3.03	0.98 ± 0.02	5.67± 0.02	126.83± 3.09
125.92± 2.05	118.51± 2.57	126.89± 3.68	0.99 ± 0.02	5.79± 0.03	130.00± 4.94
124.89± 2.46	125.04± 1.50	122.53± 2.22	1.01 ± 0.02	5.72± 0.11	124.23± 6.06
126.48± 1.04	120.68± 1.24	125.35± 2.62	1.03 ± 0.02	5.64± 0.09	126.27± 12.21
127.69± 1.52			0.99 ± 0.02		
129.07± 1.13					
128.45± 1.56					
mean =	mean =	mean =	mean =	mean =	mean =
127.25 ± 1.41	122.24 ± 2.76	126.33 ± 2.89	1.00 ± 0.02	5.70 ± 0.05	126.83 ± 2.07

Radioisotope concentrations in sediments are usually reported in activity units (e.g., dpm/g). The following quantities are used to calculate the activities:

R_S=measured ratio of the sample (net ACPS ratio)

R_{mt}=measured ratio of the monitor tracer (net ACPS ratio)

R_t=known ratio of the monitor (atom ratio)

F=conversion factor, atom ratio to activity ratio

A_{spk}=activity of calibrated spike (dpm/g)

W_{spk}=weight of spike (grams)

W_S=weight of sample (grams)

Isotope ratios contain the unknown (sample) isotope in the numerator, and the known (spike) isotope in the denominator. Thus the measured ratios 230/229, 232/229, 234/236, 235/236, and 238/236 refer to ^{230}Th, ^{232}Th, ^{234}U, ^{235}U and ^{238}U in the numerators, and ^{229}Th, ^{236}U in the denominator.

One can calculate the activities of isotope compositions of interest in a sediment sample as follows:

$$A\ (dpm/g)=R_{mt}/R_t * R_s * F * A_{spk} * W_{spk} / W_s$$

2.8.1-a Background correction

During each day's run, deionized distilled water is interspersed periodically within the sequence of sample and monitor solutions, and then all the raw data from the samples and the monitor are arranged as a "blank subtraction" from the average raw data of the deionized distilled water. Background levels for deionized distilled water are usually in the same range as for 1-5% HNO_3. Background levels are average in the uniform

Table 2.12 Comparsion of α- spectrometry results and ICP-MS results for Th and U isotopes in marine sediments by ICP-MS

Table 2.12a

Sample	^{230}Th (dpm/g) α- counting	^{230}Th (dpm/g) ICP-MS	ICP-MS / α
KN64-05 GL	3.40 ± 0.10	3.52 ± 0.10	1.04
AII 107-22 HL	5.58 ± 0.22	6.00 ± 0.07	1.08
AII 107-65 HL	8.69 ± 0.44	8.45 ± 0.13	0.97
AII 107-65 GL	7.80 ± 0.42	7.82 ± 0.41	1.00
CHN 82-4 HL	6.56 ± 0.31	6.42 ± 0.10	0.98
CHN 82-11 HL	5.63 ± 0.45	5.92 ± 0.14	1.05
38 GGC GL	6.43 ± 0.32	5.79 ± 0.20	0.90
91 GGC-0	8.75 ± 0.17	8.89 ± 0.17	1.02
91 GGC 72	6.35 ± 0.19	6.12 ± 0.10	0.96
TR 163- 9.5	6.56 ± 0.23	6.42 ± 0.14	0.98
TR 163- 72	5.75 ± 0.21	5.58 ± 0.10	0.97
TR 163- 94.5	5.23 ± 0.20	5.24 ± 0.07	1.00
TR 163- 131.5	5.78 ± 0.33	5.28 ± 0.35	0.91
TR 163- 145	5.26 ± 0.20	5.71 ± 0.10	1.09
E 48-13 HL	15.10 ± 0.57	15.14 ± 0.21	1.00
E 45-74 HL	11.63 ± 0.64	11.94 ± 0.19	1.03
E 50-8 HL	4.26 ± 0.12	4.16 ± 0.09	0.98
E 45-27 GL	12.17 ± 0.36	13.27 ± 0.22	1.09
E 45-71 GL	8.38 ± 0.44	7.82 ± 0.06	0.93
E 48-27 GL	8.22 ± 0.27	7.91 ± 0.22	0.96
E 48-3 GL	3.04 ± 0.15	2.96 ± 0.07	0.97
			mean = 1.00 ± 0.05

Table 2.12b

Sample	^{234}U (dpm/g) α-counting	^{234}U (dpm/g) ICP-MS	^{234}U ICP-MS α-counting	^{235}U (dpm/g) α-counting	^{235}U (dpm/g) ICP-MS
KN64-05 GL	0.70 ± 0.04	0.63	0.90	0.03	0.031 ± 0.001
AII 107-22 HL	0.49 ± 0.03	0.41	0.84	0.02	0.029 ± 0.001
AII 107-22 GL	0.55 ± 0.03	0.57	1.04	0.03	0.029 ± 0.001
AII 107-65 HL	0.43 ± 0.02	0.43	1.00	0.02	0.019 ± 0.001
AII 107-65 GL	0.62 ± 0.02	0.69	1.11	0.03	0.032 ± 0.001
E 48-13 HL	0.24 ± 0.03	0.21	0.88		
			M=0.96±0.04		

Table 2.12c

Sample	^{232}Th (dpm/g) α-counting	^{232}Th (dpm/g) ICP-MS	^{232}Th ICP-MS α-	Sample	^{238}U (dpm/g) α-counting	^{238}U (dpm/g) ICP-MS	^{238}U ICP-MS α-
E49-29bag	1.36±0.07	1.47±0.03	1.08	CHN82-11HL	0.26±0.01	0.29±0.00	1.12
E48-11GL	0.15±0.01	0.18±0.00	1.20	29GGCHL	0.55±0.03	0.46±0.01	0.84
CHN82-11HL	0.51±0.03	0.45±0.01	0.88	55GGCHL	0.97±0.06	0.84±0.02	0.87
55GGCHL	1.55±0.09	1.80±0.01	1.16	CHN82-15HL	0.37±0.01	0.28±0.00	0.76
CHN82-15HL	0.31±0.01	0.35±0.01	1.13	38GGCGL	0.89±0.03	0.91±0.03	1.02
CHN82-11GL	1.35±0.71	1.33±0.03	0.99	55GGCGL	1.56±0.03	1.47±0.02	0.94
CHN82-15GL	1.02±0.04	1.18±0.01	1.16	82GGCGL	1.28±0.05	1.52±0.04	1.19
VM22-197-133	2.11±0.06	2.21±0.04	1.05	CHN82-15GL	0.78±0.02	0.63±0.02	0.81
			M=				M=
			1.08±0.10				0.94±0.14

range, but with a little sporadic fluctuation. For those samples with low concentrations, a factor in all of the Pa analyses in this study, the background subtraction can be significant. The effect of variable background levels can influence the precision significantly.

2.8.1-b Blank correction

Procedural blanks were occasionally run parallel to samples, and no signals significantly different from the background level were found (Table 2.13). Blank corrections are seldom more than few percent. However, count rates on the procedure blanks are subtracted from those of the samples before applying the calculation if a significant blank is found.

Table 2.13 Examples of procedural blanks (in ACPS) for ^{231}Pa and Th and U isotopes

^{231}Pa (ACPS)	^{229}Th (ACPS)	^{230}Th (ACPS)	^{232}Th (ACPS)	^{235}U (ACPS)	^{236}U (ACPS)	^{234}U (ACPS)	^{238}U (ACPS)
3 ± 3	5 ± 3	2 ± 2	10 ± 9	4 ± 0	0 ± 1	1 ± 0	4 ± 7
0 ± 0	7 ± 2	4 ± 4	4 ± 6	7 ± 6	2 ± 3	1 ± 0	4 ± 6
5 ± 5	7 ± 4	1 ± 1	1 ± 1	7 ± 4	1 ± 0	1 ± 1	1 ± 0
3 ± 3	11 ± 10	3 ± 3	1 ± 1	13 ± 1	1 ± 0	1 ± 0	3 ± 2

2.8.1-c Contribution from spikes

Contributions of the spike and working references are examined at the same time with samples on each instrument running day, and are subtracted

from all the raw data of the sample, standard, and monitor solution. A spike of ^{236}U made a 10% contribution to mass 235 (i.e., ^{235}U).

The ^{236}U spike (Oak Ridge National Laboratory) used in this work contains some impurities that have been found to interfere with peaks on masses 234 and 235. The ^{236}U contained ^{234}U in an amount equal to 12.4% of the ^{236}U activity, but this causes an atomic ratio of $^{234}U/^{236}U$ in the impurity in value equal only to 0.0013. On the other hand, the ^{236}U spike contains a significant amount of ^{235}U that is suspected to come from the residual of production process of ^{236}U by ^{235}U (n,γ) neutron irradiation. The monitoring of the ^{236}U spike by ICP-MS analyses showed that the $^{235}U/^{236}U$ ratio of impurity is 0.10 (atom ratio).

2.8.2 Sources of error

Sources of errors include the measurement of isotope ratios by ICP-MS, the calibration of spikes and working references with alpha-counting, the determination of chemical yield for Pa by beta-counting, and the weighing of the samples. Isotope ratio measurements involve precision of triplicate runs, mass fractionation correction from a monitor, and the effects of the variable background level. The accuracy of the calibrated results for all spikes and working references involve the counting statistics and the detector efficiency of the alpha counter. The latter error is only for ^{231}Pa counting since there is no other suitable α-emitting Pa isotope that can be used for isotope dilution by the alpha counting technique. The chemical yield monitor for Pa with beta-counting of a ^{233}Pa tracer involves a decay correction due to the short half-life of ^{233}Pa and the arrangement of geometric factors in counting both

the standard and the sample. Unexpected changes in the humidity of the weighing room air also cause errors in the weights of small-sized samples. Propagation of measurement errors in a derived results, f(x, y), is made by use of the following equations:

$$\sigma^2_f(x, y) = (\partial f/\partial x)^2 \sigma_x^2 + (\partial f/\partial y)^2 \sigma_y^2$$

$$\sigma_{x/y} = x/y\,(\sigma_x^2/x^2 + \sigma_y^2/y^2)^{1/2}$$

2.9 CONCLUSIONS

Methods were developed to measure ^{231}Pa and uranium and thorium isotopes in sediments by ICP-MS. The procedure involves three separate runs: (1) a two-stage spike for ^{231}Pa measurement with ^{233}Pa as a tracer for chemical yield and ^{229}Th as an internal standard; (2) isotope dilution analysis for simultaneous determinations of ^{234}U, ^{235}U, and ^{230}Th on the same aliquot with spikes of ^{236}U, and ^{229}Th; and (3) simultaneous measurements of ^{238}U and ^{232}Th by isotope-dilution analysis of a separate small aliquot removed just after sample dissolution. The precision for a ^{231}Pa measurement, at present, is ~4% on ~0.2 dpm per gram of solution. Accurate determination of the amount of ^{231}Pa in a sediment sample can be achieved at a level of greater than 0.3 dpm. The method has a detection limit of approximately 0.5 pg/g (*i.e.* , 0.05 dpm/g of solution) ^{231}Pa. In addition, accurate, simultaneous measurements of ^{230}Th, ^{234}U, and ^{235}U on one aliquot and ^{232}Th and ^{238}U on a separate aliquot by isotope dilution ICP-MS has been established for a routine sediment analysis. The whole technique

offers the following advantages when compared with α- spectrometry: (1) shorter measurement time (less than 5 minutes vs. days to weeks); (2) higher analytical precision for the same range of sample concentration (better than 5% vs. 5->10% for ^{231}Pa, and <1-3% vs. 3->10% for uranium and thorium isotopes); and (3) smaller sample size requirement for Th and U isotopes. A more efficient sample introduction method would provide a better precision and is necessary for the analysis of small samples or for samples with lower concentration such as sediment trap or water samples.

CHAPTER 3

FRACTIONATION BETWEEN ^{231}PA AND ^{230}TH IN THE SETTLING PARTICLES: CAN WE USE BOTH AS TOOLS FOR RECONSTRUCTION OF PALEO-PARTICLE FLUX?

3.1 INTRODUCTION

3.1.1 Background

Marine sediments constitute an invaluable record for the study of paleoclimatology and paleoceanography. The important task for geochemists is to unlock this history that is recorded in the sediment. The interpretation of apparent fluctuations in the sedimentary components of Quaternary sediments is a classic paleoceanographic problem (Broecker, 1971). To quantify the fluctuations, it is more meaningful to express accumulation by the mass of material rather than the thickness, i.e., in terms of gm/cm^2/ka rather than cm/ka (Broecker *et al.*, 1958).

Interest in the marine geochemistry of the radionuclides ^{230}Th and ^{231}Pa was stimulated because of their ability to be used in providing accumulation histories. Accumulation rates of deep-sea sediments can often be estimated by observing the decay of unsupported ^{230}Th or ^{231}Pa as a function of depth (Rosholt *et al.*, 1961; Ku, 1976). This method is based on the constancy of uranium-isotope concentrations in seawater and on the reactive nature of the decay products ^{230}Th and ^{231}Pa in the oceanic water column.

The estimation is based on two important assumptions: that the initial values of ^{230}Th and ^{231}Pa are constant through time, and that the sedimentation rate is constant as well. Successful examples were found in a Caribbean core (Broecker and Van Donk, 1970). However, geological processes which focus or erode material from specific sites decrease our ability to understand past variations in the sedimentation rate; thus, sediment dating using ^{230}Th and ^{231}Pa does not always provide satisfactory chronologies, because large downcore variations of initial ^{230}Th and ^{231}Pa activity in sediments can result in large uncertainties.

Two contradictory ideas have been proposed to interpret the large downcore variations of ^{230}Th activity in sediments. The debate arises from different interpretations of the relationship between unsupported ^{230}Th (the term $^{230}Th_{ex}$ will be used in the following text) flux and the overall particle flux, which is usually driven by surface ocean productivity (Fisher *et al.*, 1988; Nozaki, 1991).

In a core section with an unusually high $^{230}Th_{ex}{}^{o}$ level, one model, called the productivity model by Thomson *et. al.*, (1993), would infer unusually high production and presumably a higher overall accumulation rate, whereas the other model, called the constant $^{230}Th_{ex}$ flux model by Bacon and Rosholt (1982), would infer a period of unusually low sediment accumulation rate. Bacon and Rosholt (1982) and Bacon (1984) suggested a uniform rain rate of ^{230}Th, equal to production, occurs over the entire seafloor; thus, $^{230}Th_{ex}$ flux is independent of total mass flux. As a consequence, there is an inverse relationship between particle rain rate to the seafloor and the excess ^{230}Th activity in the settling particles. Variations in fluxes of other nuclides, trace metals, and sediment components can thus be

quantified by normalization to $^{230}Th_{ex}$ flux. This is the so-called "^{230}Th-normalized flux method".

In contrast, a production model has been proposed in several workers (Mangini and Diester-Haass, 1983; Yang *et al.*, 1990; Shimmield *et al.*, 1986; Scholten *et al.*, 1990) to interpret large variations in the sediment profiles as showing much larger departure from a vertical flux balance than is likely to occur. It was argued, however, that in their conclusion they have not considered the possibility of variable sediment focusing (Bacon, 1984; Suman and Bacon, 1989; Francois *et. al.*, 1990; Francois and Bacon, 1991). The constant $^{230}Th_{ex}$ flux model suggests that variability in sediment redistribution rates could be removed by normalizing all component fluxes to that of $^{230}Th_{ex}$. The magnitude of sediment redistribution is then just a factor adjusting the expected production in the water column to observed ^{230}Th concentrations. To illuminate the debate between the two concepts, I carried out sediment trap studies to examine the dependence of the scavenging efficiency of ^{230}Th (and ^{231}Pa) on the particle rain rates, and to examine the crucial hypothesis of constant $^{230}Th_{ex}{}^{o}$ flux in the ^{230}Th-normalized flux method in the thesis.

Besides using the ^{230}Th-normalized flux model, I propose in this thesis to use decay-corrected unsupported $^{231}Pa/^{230}Th$ ratio (the term $(^{231}Pa/^{230}Th)_{ex}{}^{o}$ will be used in the following text) as an index of particle flux in the present ocean and past time, which I call the "$(^{231}Pa/^{230}Th)_{ex}{}^{o}$ ratio index".

Uranium decay supplies ^{231}Pa and ^{230}Th in the ocean at a fixed ratio of 0.093 if there is no fractionation between the two isotopes. Many

observations of water columns, sediment traps, and sediments from previous works have shown that fractionation between ^{230}Th and ^{231}Pa occurs everywhere within an ocean basin (DeMaster, 1981; Anderson *et al.*, 1983 a&b; Bacon *et al.*, 1985; Yang *et al.*, 1986; Taguchi *et al.*, 1989; Francois *et. al.*, 1990; Francois and Bacon, 1991; Anderson *et al.*, 1991; Lao, 1991; Rutgers Van Der Loeff and Berger, 1993).

Evidence shows that a region with a removal ratio of $(^{231}Pa/^{230}Th)_{ex}{}^{o}$ that is greater than the value of 0.093 represents a preferential scavenging of ^{231}Pa. Such evidence comes from the Antarctic and the margins of the Pacific (i.e., the Panama Basin, Guatemala Basin, the northern North Pacific; Anderson *et al.*, 1983b, 1990; Yang *et al.*, 1986; Taguchi *et al.*, 1989; Lao *et al.*, 1992; DeMaster, 1979; Rutgers Van Der Loeff and Berger, 1993). Conversely, a region with a ratio of less than 0.093 represents a preferential lateral transport of a portion of ^{231}Pa to somewhere else. Such regions can be seen in the open ocean (Anderson *et al.*, 1983a; Bacon *et al.*, 1989; Lao *et al.*, 1992; Chapter 4 of this thesis).

The large fractionation between ^{230}Th and ^{231}Pa within a basin comes about because of the partitioning of the two elements between two transport pathways, i.e., vertical scavenging or horizontal transport, for removal. The differential partitioning is caused by differences in reactivity between the two elements. On one hand ^{230}Th, due to its high particle reactivity with a range of residence time between 10 and 40 years (Nozaki *et al.*, 1981; Anderson *et al.*, 1983a&b), is predominately removed with the downward flux of particles. On the other hand, ^{231}Pa is less particle-reactive, with a residence time about 2 to 3 times longer than that for ^{230}Th (Anderson et al., 1983a&b), and can be laterally transported longer distances away from its

production site before it is removed. As a result, over most of the ocean the flux of ^{230}Th into the sediments approximately balances its production rate in the overlying water column, whereas ^{231}Pa tends to migrate towards the margins or regions of high particle flux. Consequently, the $(^{231}Pa/^{230}Th)_{ex}{}^{o}$ ratio of the material falling to the seafloor reflects the particle rain rate of the overlying water column. A high value of the $(^{231}Pa/^{230}Th)_{ex}{}^{o}$ ratio reflects higher particle fluxes in a region, and a lower value reflects lower particle flux in a region. By further extrapolation of the concept into the past ocean, one expects that the variations of the $(^{231}Pa/^{230}Th)_{ex}{}^{o}$ ratio in a down-core sediment profile would reflect the fluctuations of the particle rain rate in the overlying water column. The advantage of this approach is that since the ^{231}Pa content is normalized to the ^{230}Th content, the bias of sediment redistribution processes can be removed. In addition, most biogenic particulate carriers are easily degraded by diagenesis and reminerization processes in sediments, but both ^{231}Pa and ^{230}Th, which are adsorbed onto the particles, are not significantly affected by these processes. Thus, even though particles have suffered from dissolution, both ^{231}Pa and ^{230}Th should still faithfully record the fluxes of their particulate carriers. A higher $(^{231}Pa/^{230}Th)_{ex}{}^{o}$ ratio thus confirms a higher flux based on the ^{230}Th-normalized flux method and reflects a higher particle rain or higher production from the overlying water column.

The idea of using the $(^{231}Pa/^{230}Th)_{ex}{}^{o}$ ratio as a tool for reconstruction of particle flux in the present and past ocean comes from the strong ratio-dependence on the particle flux. The idea can be proved straightforwardly by performing analyses of both isotopes on material collected in sediment traps. Spatial variations in the $(^{231}Pa/^{230}Th)_{ex}{}^{o}$ ratio

would reflect contrasts in the different flux of regions, and the temporal variations in the $(^{231}Pa/^{230}Th)_{ex}{}^{o}$ ratio at a site would reflect changes in the relative flux intensity in the region.

A particle reactive chemical substance is introduced into the ocean in dissolved form, and it is partitioned by particle dynamic processes that include adsorption, complexation and biological uptake (Anderson *et al.*, 1991) during the chemical substance's scavenging pathway through the water column. While the flux of particulate matter through the water column seems to be the principle factor regulating the overall intensity of scavenging, it may not be the unique process responsible for the phenomenon of fractionation between ^{230}Th and ^{231}Pa. The fractionation might arise from the differential particle composition, or "quality" of particle changes in different regions as well (Anderson *et al.*, 1983a&b; Anderson *et al.*, 1990 and 1991; Taguchi *et al.*, 1989; Lao, 1991; Anderson *et al.*, 1992). To examine whether the particle composition controls the fractionation of ^{231}Pa and ^{230}Th, I added the analyses of bulk particle compositions in sediment trap materials to this study in addition to the ^{230}Th and ^{231}Pa analyses.

3.1.2 Questions and Aims

The tasks of the sediment trap studies as indicated above are to examine (1) whether the assumption of a constant ^{230}Th flux holds for the ^{230}Th-normalization flux method; (2) whether the fractionation between ^{231}Pa and ^{230}Th depends predominately on total particle flux, i.e., the scavenging rate; (3) whether particle compositions affect the relationships between particle flux and the nuclide fluxes; (4) whether we can apply both

the "^{230}Th-normalized flux method" and the "$(^{231}Pa/^{230}Th)_{ex}{}^{o}$ ratio index" to infer the geographic variability of particle flux and the way it varies with time; and (5) whether we are able to apply ^{230}Th and ^{231}Pa as tools for reconstruction of particle flux in the past ocean. The task, in essence, will be to examine the relationships between particle flux and the various indicators.

3.2 SAMPLING STRATEGY

The aims of this study are (1) to determine whether the ^{230}Th flux is constant, (2) whether the $(^{231}Pa/^{230}Th)_{ex}{}^{o}$ ratio is a function of total particle flux, and (3) how particle composition would control the relationship between nuclide fluxes and particle flux. This work was done by carrying out radiochemical analyses of composited material from sediment traps that were deployed for approximately a year or longer. Seasonal variations in the flux of ^{230}Th collected in sediment traps have been observed in the Sargasso Sea (Bacon, *et. al.*, 1985). The variations are correlated with variations in particle flux and are due to short-term, local departures from a steady state. The variations in the upper water column were found to be rapidly reflected in the deeper water column. The purpose of this study is to better understand the processes in today's ocean so that we may then begin to develop an understanding of the processes in the past ocean. Records of one year or longer of sediment trap samples have thus been chosen to remove any short-period unsteady condition and to average over the annual cycle of mass flux. The sediment trap materials were kindly provided by S. Honjo and his coworkers of the Woods Hole Oceanographic Institution.

While several oceanic sites were sampled and analyzed in this work, there were also several years-long data sets available in the literature that I include in the discussion of the relationship between the ^{231}Pa and ^{230}Th flux and particle flux to make the geographic coverage as wide as possible. Once the relations between isotopes and flux of particulate materials are established, I hope to be able to state some fundamental principles about the scavenging of ^{231}Pa and ^{230}Th for paleoceanography applications.

3.3 SAMPLE COLLECTION, HANDLING AND DISTRIBUTION

The samples used in this study were collected with a large, conical sediment trap of the PARFLUX design (Honjo, 1980). Upon recovery, the samples were washed through stainless-steel sieves to separate particles into the following size fractions: >1 mm, 63 μm ~ 1 mm, and <63 μm. The radionuclide analyses were done on the <1 mm fractions. Table 3.1 gives detailed information on mooring locations, trap depths, and trap types. The following details about trap deployments and sample handling at each individual site are largely drawn from technical reports of Honjo and his coworkers (Honjo *et al.*, 1989; Takahashi *et al.*, 1989; Honjo and Manganini, 1992; Nair *et al.*, unpublished).

3.3.1 NABE

Automated, time-series sediment traps were deployed at three bathypelagic depths on bottom-tethered arrays in the North Atlantic at 34°N 21°W and 48°N 21°W for about a year (spring 1989-1990). The arrays were

Table 3.1 Locations and collection information of the compiled sediment trap samples

Trap Sample	Latitude (N)	Longitude	Trap depth (m)	Deployed days (days)	Total flux (g/cm2/ka)	References
NABE 34-1000	33.49 N	21.02 W	1159	358/302	1.83	this study
NABE 34-2000	33.49 N	21.02 W	1981	358/358	2.39	this study
NABE 34-4000	33.49 N	21.02 W	4478	358/330	2.14	this study
NABE 48-1000	47.43 N	20.52 W	1110	358/358	1.93	this study
NABE 48-4000	47.43 N	20.52 W	3734	358/358	2.52	this study
PAPA 6-deep	50.00 N	145.00 W	3800	143	0.72	this study
PAPA 7-deep	49.57 N	144.59 W	3800	168	3.08	this study
PAPA^ 6/7-deep	49.57 N	145.00 W	3800	311	2.00	this study
WAST-shallow	16.19 N	60.28 E	1085	162	6.69	this study
WAST-deep	16.19 N	60.28 E	3033	162	6.61	this study
CAST-shallow	14.29 N	64.46 E	1000	169	4.03	this study
CAST-deep	14.29 N	64.46 E	2400	169	3.47	this study
EAST-shallow	15.27 N	68.44 E	1705	162	3.26	this study
EAST-deep	15.27 N	68.44 E	2773	162	3.91	this study
Sargasso Sea	32.05 N	64.15 W	3200		0.99	Bacon et al.,1985
Lofoten Basin	69.30 N	10.00 E	2761	293	2.12	Bacon, unpublished
PAPA1-3 deep	50.00 N	145.00 W	3800	560	4.60	Bacon, unpublished
Panama Basin	05.22 N	85.35 W		360	9.60	Bacon, unpublished
Califonia-near shore 500	42.05 N	125.46 W	500	360	9.50	Lao, 1991
Califonia-near shore 1000	42.05 N	125.46 W	1000	360	12.80	Lao, 1991
Califonia-near shore 2329	42.05 N	125.46 W	2329	352	16.10	Lao, 1991
Califonia-midway 500	42.11 N	127.35 W	500	325	1.77	Lao, 1991
Califonia-midway 1750	42.11 N	127.35 W	1750	352	4.90	Lao, 1991
Califonia-midway 2330	42.11 N	127.35 W	2330	360	4.30	Lao, 1991
Bransfield Strait	62.15 S	57.31 W	1588		11.00	Rutgers van Der Loeff & Berger, 1993
Nares Abys. Plain-deep	23.16 N	63.55 W	4832		1.12	Fisher et al., 1988

deployed in March and April 1989, recovered and redeployed in September 1989, and totally recovered in April 1990. The total deployment time for the sediment traps was 378 days, including a 20-day hiatus in the middle. The 34°N station is in the North Atlantic Subtropical Zone whereas the 48°N station is in the North Atlantic Transition Zone (Honjo and Manganini, 1992); thus the two stations represent different physical and biogeographic areas. This trap experiment included synchronization of the open/close timing of all six traps, thus providing a time-space matrix in depth (1, 2, and 4.5 or 5 km) and latitude (1,256 km apart). Current meters and thermistors that were deployed 1.2 m below each of the three sediment traps at the 48°N 21°W station recorded no significant turbulence, and the currents were generally less than 5 cm/sec throughout the year-long deployment.

Each sediment trap was deployed with 13 rotary collectors. Each trap was opened and closed 26 times, providing continuous time-series sampling at 14-day intervals, except for two periods. An independent monitoring mechanism installed with each trap (Honjo and Doherty, 1988) confirmed that the entire program was executed correctly and on schedule. Before the deployment of a trap, analytical grade formalin was added to the sample containers to make a 3% solution buffered with 0.1% sodium borate. After recovery of the traps, no swimmers were identified in any samples.

Particle samples were wet-sieved through a 1-mm Nitex mesh. This was necessary to maintain precision during splitting of the major portion of the sediment, which was <1 mm. Common particles in the >1-mm fraction were large aggregates and fragmented gelatinous zooplankton.

3.3.2 Arabian Sea

Three moored arrays consisting of a total of six time-series sediment traps were continuously deployed at locations in the western (16°15N, 60°28E), central (14°29N, 64°46E), and eastern (15°28N, 68°45E) part of the northern Arabian Sea. Each mooring system consisted of two time-series sediment traps: one 1000 m below the surface and the other 1000 m above sea bottom. Prior to deployment, collecting cups were poisoned with mercuric chloride. The sediment traps were programmed to measure the flux of sinking particles at intervals of 12 to 13 days over a duration of six months per deployment. The traps were recovered and redeployed three times betwen May 1986 and 1987. Upon recovery of the traps, the samples were wet-sieved and split using a precise rotary splitter. One quarter of the <1 mm size fraction was filtered through preweighed Nuclepore filters (0.4 micron) and dried at 40°C.

3.3.3 PAPA

PARFLUX Mark 5, time-series sediment traps (Honjo and Doherty, 1988) were moored at 1000 m and 3800 m at station PAPA (50°N, 145°W; water depth 4200 m) over a four-year period from September 1982 to August 1986. The sediment traps were deployed, recovered, and redeployed about every six months. Twelve cups located in a rotating carousel provided time-series sampling during trap deployments. Sampling intervals were 12 to 14.5 days. Samples were wet-sieved through 1-mm and 63-micron stainless steel screens. The greater than 1-mm size fraction contained a negligible amount of siliceous phytoplankton.

The sediment trap samples from the PAPA site used for this study were from the traps deployed from December 3, 1984, to April 20, 1985 (PAPA6); and from May 10, 1985, to October 11, 1985 (PAPA7), almost a complete annual cycle of seasonal flux changes.

Collection cups were filled prior to deployment with 10% sodium azide to retard bacterial decomposition. Procedures for handling samples at sea and for processing samples in the lab are described in detail elsewhere (Honjo and Manganini, 1992; Nair *et al.*, unpublished; and Takahashi *et al.*, 1989).

Because of the need to avoid any seasonal bias, time-series samples were combined, using amounts of material from each sample proportional to the mass flux during the collection interval, to produce composite samples. Composite samples were then analyzed for radionuclides following the procedure described in Chapter 2. Sediment trap samples were analyzed for major sedimentary components such as carbonate, biogenic opal, and the rest of each sample was assumed to be the terrigenous fraction.

3.4 METHODS

3.4.1 Preparation of Composite Sediment Trap Samples

The procedure I used to prepare the composited sediment trap material for analysis involved the following: preparation of 20 ml scintillation vials for use in precise rotary splitting by soaking vials and rinsing them in acid, then distilled deionized water; use of a precise rotary splitter to split the materials; use of a washing solution during splitting of 3% formaldehyde +

0.1% sodium borate in ESL seawater (treated for 1-2 days with 3% formaldehyde + 0.1% sodium borate and then filtered).

Samples were filtered on 0.45 μm Nuclepore filters, rinsed with deionized, distilled water three times, then dried for 24 hours at 50°C. The dried samples were cooled in a desiccator and weighed. After cooling, the dried samples were peeled from the filters, and ground with an agate mortar pestle; then the samples were stored in plastic vials in desiccators.

3.4.2. Radiochemical Procedures

Aliquots of <200 to 500 mg of dried sediment trap material were used for radiochemical analyses. All samples were subjected to total dissolution with mixtures of HNO_3, HF, and $HClO_4$ in the presence of ^{236}U, ^{229}Th, and ^{233}Pa added as yield monitors. The radiochemical analysis procedures were followed in a sequence as shown in Figure 2.1, which included separation, purification, and electroplating. Th, U and Pa isotopes were determined by counting alpha-emitted particles with silicon surface-barrier detectors. The yields of the beta-emitting ^{233}Pa tracer were measured with a windowless 2-π proportional counter.

3.4.3 Carbonate Content

Carbonate content was determined by a method based on a vacuum-gasometric technique which was reported by Ostermann, *et al.* (1990). A preweighed sample was introduced into a sealed reaction vessel containing

concentrated phosphate acid. The pressure due to the evolution of CO_2 gas is proportional to the carbonate content when calibrated with an appropriate standard and was recorded by a transducer. The results were calculated and reported as carbonate percent in the total sample.

3.4.4 Data processing

Most of the radiochemical analyses were performed on the <1-mm size fraction, which is close to the total sample weight. The analytical results are shown in Table 3.2. Radionuclide fluxes in the <1-mm fraction were calculated, and total flux was taken on the <1-mm fraction as shown in Table 3.3. For convenient comparison of the measured fluxes with longer-term averages, I use mean annual flux units in the tables and figures. The formulae for calculation of the flux are as follows:

1. Average flux ($mg/m^2/day$) =

Total weight (mg)/(sample collection time x aperture of trap (0.5 m^2))

2. Average annual total flux ($g/m^2/y$) =

Σ Average flux * open days of each cup*365/[(total open days)*1000]

3.5 RESULTS

Analytical results of radionuclides are shown in Table 3.2. All analyses were performed on the < 1 mm size fraction except the PAPA6 deep trap. Pa and Th isotopes were measured by the alpha-counting technique. Except for

Table 3.2: Analytical results of radionuclides for sediment trap samples

Trap Sample depth (cm)	Trap depth (m)	230Th dpm/g	std.dev.	232Th dpm/g	std.dev.	231Pa dpm/g	std.dev.	238U dpm/g	std.dev.	234U dpm/g	std.dev.	235U dpm/g	std.dev.
NABE 34-1000	1159	1.21	0.04	0.29	0.017	0.041	0.005	0.47	0.02	0.51	0.02		
NABE 34-2000	1981	2.15	0.06	0.44	0.022	0.082	0.005	0.47	0.02	0.51	0.02		
NABE 34-4000	4478	5.35	0.16	0.51	0.04	0.154	0.009	0.47	0.05	0.47	0.06		
NABE 48-1000	1110	0.64	0.019	0.15	0.008	0.033	0.004	0.34	0.02	0.34	0.03		
NABE 48-4000	3734	2.58	0.07	0.22	0.0196	0.068	0.004	0.34	0.02	0.34	0.03		
PAPA 6-deep	3800	8.72	0.27	0.27	0.03	0.586	0.020	1.89	0.06			0.087	0.003
PAPA 7-deep	3800	4.15	0.14	0.12	0.012	0.335	0.011	1.02	0.04			0.047	0.002
WAST-shallow	1085	0.49	0.012	0.17	0.006	0.042	0.002	1.10	0.06	1.74	0.39	0.051	0.003
WAST-deep	3033	1.26	0.07	0.22	0.009	0.093	0.003	1.26	0.05	1.33	0.12	0.058	0.002
CAST-shallow	1000	0.71	0.024	0.34	0.015	0.043	0.003	1.36	0.05	1.45	0.19	0.063	0.002
CAST-deep	2400	2.57	0.10	0.53	0.04	0.175	0.010	0.72	0.02			0.033	0.001
EAST-shallow	1705	1.66	0.05	0.49	0.023	0.137	0.007	1.39	0.04	1.82	0.32	0.064	0.002
EAST-deep	2773	2.48	0.07	0.56	0.023	0.133	0.006	1.30	0.04	1.44	0.16	0.060	0.002
procedure blank*		0.05	0.006	0.0007	0.0005	0.003	0.007						

* in per sample

the data otained from the NABE station, which were obtained by the alpha counting technique, the rest of the ^{234}U and ^{235}U data were obtained by ICP-MS, and ^{238}U was calculated by the natural $^{235}U/^{238}U$ activity ratio of 0.046. A range of 0.3 to 0.8 grams of dry weight composited sediment trap material was analyzed. The analytical uncertainty of each measurement with propagated uncertainties in the 1-sigma counting statistics is in the range of 3% (^{235}U by ICP-MS technique) to 12% (Pa and Th isotopes by alpha counting technique, and ^{234}U by ICP-MS technique). The uncertainty is primarily due to small sample size and low concentration, and the practical limits of counting time. Procedural blank corrections are also included in Table 3.2. The blank corrections are between 0.5% to 9% for ^{230}Th, and 0.5% to 10% for ^{231}Pa. Uncertainties reported in each table were obtained by using a standard propagation of error calculation, including $\pm 1\sigma$ counting statistics and uncertainities in blank correction and detector efficiencies.

Table 3.3 lists the calculated results of this study. It includes the unsupported ^{230}Th and ^{231}Pa activities, the specific activities and fluxes of detrital uranium and authigenic uranium, and calculated $^{238}U/^{232}Th$, $^{234}U/^{238}U$ and $^{230}Th/^{232}Th$ activity ratios.

3.5.1. Unsupported Isotope Activities

Unsupported ^{230}Th and ^{231}Pa are those amounts of the ^{230}Th and ^{231}Pa that were scavenged directly from the water column. To be able to calculate the unsupported ^{230}Th and ^{231}Pa activities (designated by the notations $^{230}Th_{ex}$, $^{231}Pa_{ex}$ for convenience), i.e., scavenged ^{230}Th and ^{231}Pa activities, it is necessary to correct for the supported activities from uranium

Table 3.3 Calculated results of radionuclides for sediment trap samples

No.	Trap Sample	Total flux (g/m2/yr)	234U/238U	238U/232Th	230Th/232Th	authigenic U (dpm/g)	authigenic U flux (dpm/cm2/ka)
1	NABE 34-1000	18.28		1.64	3.27	0.24	0.44
2	NABE 34-2000	23.85	1.07	1.07	3.98	0.12	0.28
3	NABE 34-4000	21.38	1.01	0.93	9.66	0.06	0.14
4	NABE 48-1000	19.27	1.02	2.27	3.18	0.22	0.42
5	NABE 48-4000	25.21		1.57	10.88	0.17	0.42
6	PAPA 6-deep	7.19		7.00	31.50	1.67	1.20
7	PAPA 7-deep	30.81		8.50	33.78	0.92	2.85
8	PAPA^ 6/7-deep	19.95	1.43	6.59	32.11	1.27	2.09
9	WAST-shallow	66.87	1.06	5.73	2.13	0.97	6.46
10	WAST-deep	66.09	1.07	4.00	4.93	1.08	7.16
11	CAST-shallow	40.30		1.36	1.29	1.09	4.38
12	CAST-deep	34.73	1.30	2.83	4.05	0.30	1.03
13	EAST-shallow	32.59	1.09	2.32	2.58	1.00	3.25
14	EAST-deep	39.10			3.63	0.85	3.33

Table 3.3 (con't)

No.	detrial U (dpm/g)	Authigenic U %	230Thexo dpm/g	231Paex dpm/g	230Thex flux dpm/m2/yr	231Paex flux dpm/m2/y	(231Pa/230Th)ex
1	0.23	51	0.94	0.03	17.18	0.550	0.029 ± 0.004
2	0.35	25	1.75	0.06	41.74	1.431	0.036 ± 0.002
3	0.41	14	4.90	0.13	104.73	2.779	0.027 ± 0.002
4	0.12	65	0.48	0.02	9.25	0.385	0.051 ± 0.006
5	0.17	49	2.36	0.06	59.50	1.513	0.024 ± 0.002
6	0.22	89	8.50	0.58	61.12	4.170	0.068 ± 0.003
7	0.10	91	4.05	0.33	124.78	10.167	0.082 ± 0.004
8	0.16	88	6.10	0.44	95.51	7.409	0.073 ± 0.004
9	0.13	86	0.36	0.04	24.07	2.675	0.101 ± 0.005
10	0.18	80	1.08	0.08	71.38	5.287	0.078 ± 0.005
11	0.27	41	0.44	0.03	17.73	1.209	0.070 ± 0.005
12	0.42	72	2.15	0.16	70.07	5.557	0.072 ± 0.005
13	0.39	66	1.27	0.12	41.39	3.911	0.094 ± 0.006
14	0.45		2.03	0.11	79.37	4.301	0.055 ± 0.003

in the detrital minerals and from authigenic uranium derived from seawater from the measured ^{230}Th and ^{231}Pa activities (Table 3.2) in the sediment trap material. Since $^{238}U/^{232}Th$ activity ratios for most major minerals and pelagic marine sediments vary over a narrow range (0.8±0.2), the detrital uranium content is usually estimated by measuring ^{232}Th and $^{238}U/^{232}Th$ activity ratios (Anderson, 1982; and Anderson *et al.*, 1990 and 1992). The authigenic uranium content is usually calculated from the difference between the measured total uranium content and the detrital uranium content. For sediment trap samples analyzed here, authigenic uranium concentrations range from 0.06 to 1.67 dpm/g, which are approximately 14% to 91% of the total, measured uranium activity in the samples. Although most of the sediment trap materials contain a significant amount of authigenic U (Table 3.3) that is derived from seawater, the contributions of the decay products ^{230}Th and ^{231}Pa are always negligible because the samples are always too "young" to be corrected for any significant amount of the decay products of authigenic U (Anderson *et. al,* 1990). The detrital components of ^{230}Th and ^{231}Pa were calculated by assuming their activities to be in secular equilibrium with their U parents; thus, scavenged ^{230}Th and ^{231}Pa activities were calculated by using the difference between total ^{231}Pa and ^{230}Th activities and the activities of their respective parents. The estimations can be done with the following equations (Lao, 1991; and Anderson *et al.*, 1990):

$$^{230}Th_{ex} = {}^{230}Th_{m} - (0.8\pm0.2)^{232}Th_{m}, \quad (3\text{-}1)$$

$$^{231}Pa_{ex} = {}^{231}Pa_{m} - 0.046(0.8\pm0.2)^{232}Th_{m}, \text{ and} \quad (3\text{-}2)$$

$$\text{Authigenic U} = U_{m} - (0.8\pm0.2)^{232}Th_{m} \quad (3\text{-}3)$$

where all values are in activity units, "m" is the measured total activity in the sample, (0.8±0.2) is the ratio of $^{238}U/^{232}Th$, and 0.046 is the natural $^{235}U/^{238}U$ activity ratio. From the above equations, I calculated the uncertainties of unsupported activities of ^{230}Th and ^{231}Pa, and their propagated uncertainties are approximately 20%. Large uncertainties of calculated $^{230}Thex$ and $^{231}Paex$ are derived from the large uncertainty of the assumed $^{238}U/^{232}Th$ ratio.

Depth profiles of unsupported activities of ^{230}Th and ^{231}Pa at different stations always showed a similar pattern: lower activity levels for the shallower trap and higher activity levels for the deeper trap. The pattern of increasing activities with depth is expected, since both ^{230}Th and ^{231}Pa are produced throughout the water depth.

3.5.2. Authigenic Uranium and Particulate Uranium

The concentrations of detrital uranium (calculated by measuring ^{232}Th and assuming a constant $^{238}U/^{232}Th$ ratio of 0.8 ± 0.2 for the detrital phase), show an increase with depth for all stations. The authigenic uranium concentration in the samples from the PAPA and all the Arabian Sea stations, with the exception of the deep CAST trap, remarkably enough dominates almost 70% to 90% of the total uranium measured (Table 3.2). For three mooring sites from the Arabian Sea stations, the concentrations of authigenic U are higher in the shallowest trap sample and have lower concentrations in the deep trap samples. The NABE stations show a similar trend of decreasing in seawater-derived uranium activity with depth. This feature was observed at other stations in the open ocean (Anderson, 1982). The flux of authigenic

uranium decreases with depth, a trend clearly shown in the data from the stations of NABE. This decrease with depth is suggested as a reflection of the formation of authigenic uranium that must occur in surface water, then is remineralized in the water column; this authigenic uranium must be associated with very labile particle phases that would not remain for long periods of time when they reach the sediment surface (Anderson, 1982; Anderson *et al.*, 1990). The possible carrier phase of particulate authigenic uranium is believed to be organic matter. The $^{234}U/^{238}U$ ratios (Table 3.3) scatter compared to the seawater value for most of the samples; it is not possible to demonstrate whether there is a significant correlation between the $^{234}U/^{238}U$ ratios and the authigenic U contents because of the large counting errors that result from the low counting rate of ^{234}U by ICP-MS. In addition to the $^{234}U/^{238}U$ activity ratio, the $^{238}U/^{232}Th$ ratio is clearly greater than the value in the detrital phase (i.e., 0.6 to 1.0) (Table 3.3). This demonstrates that the particulate U at most sites is dominated by the authigenic source.

3.6 DISCUSSION

The essential tasks of this chapter are to examine the relationships between particle flux and the various indicators. How is the nuclide scavenging influenced by mean annual particle flux? Is the spatial variation in nuclide scavenging within an ocean basin (i.e., stronger scavenging at the ocean margins than in the open ocean) largely a result of the spatial variation in annual particle flux? How does scavenging removal compete with horizontal transport to cause fractionation between ^{231}Pa and ^{230}Th? Does the spatial contrast in the value of the $(^{231}Pa/^{230}Th)_{ex}$ ratio in the sediment

indicate a contrast in the scavenging rate in the overlying water column? To examine these questions, the correlation between mean annual particle flux and mean annual nuclide flux was examined. Compilation of all available data obtained from year-long deployment of sediment traps from this thesis work and other previous studies are included to establish better the influence of particulate material on nuclide scavenging. The mean annual total particle fluxes recorded in the sediment traps varied by a large range from ~1 to ~17 $g/cm^2/ka$. The geographic distributions cover a wide spatial range from an oligotrophic ocean to a margin ocean and the polar ocean. The locations and collection periods of all sediment traps are provided in Table 3.4. Fluxes of particulate material, fluxes of particulate radionuclides, and $(^{231}Pa/^{230}Th)_{ex}$ ratios are also shown in Table 3.4. The stations from NABE, the Arabian Sea, and PAPA were done within the scope of this thesis. For most of stations, all of the radionuclides were determined on the size fractions < 1 mm, and the flux of <1 mm material is taken to represent the total particulate flux. It is assumed that the concentrations of nuclides are negligible on the >1 mm particles. The flux of <1 mm particles are dominates total mass flux, ranging from 85% to 100% of the total mass flux (Figure 3.1).

The collections of sediment traps for PAPA6 and PAPA7 each covered one half of a year, and they were analyzed for nuclides and sedimentary components separately. The mean annual total mass flux, and the mean annual fluxes of nuclides and compositions at the PAPA station thus calculated based on the time-weighed fraction for each collection period. The reason for the calculation was to remove the effects of seasonal variations in nuclides and particle fluxes. This calculation is also done for the stations off the California coast (Lao, 1991) and the Nares Abyssal Plain (Fisher *et al.*,

Table 3.4 Compiled data for sediment trap samples

Trap Sample depth (cm)	Total flux (g/cm2/ka)	230Th)F/P	231Pa)F/P	231Pa/230Th)exo/0.093
NABE 34-1000	1.83	0.56	0.20	0.31
NABE 34-2000	2.39	0.80	0.30	0.38
NABE 34-4000	2.14	0.89	0.26	0.29
NABE 48-1000	1.93	0.32	0.14	0.55
NABE 48-4000	2.52	0.61	0.17	0.26
PAPA 6-deep	0.72	0.61	0.45	0.73
PAPA 7-deep	3.08	1.25	1.11	0.88
PAPA^ 6/7-deep	2.00	0.96	0.81	0.78
WAST-shallow	6.69	0.84	1.02	1.08
WAST-deep	6.61	0.89	0.72	0.84
CAST-shallow	4.03	0.67	0.50	0.75
CAST-deep	3.47	1.11	0.96	0.78
EAST-shallow	3.26	0.92	0.95	1.01
EAST-deep	3.91	1.09	0.64	0.59
Sargasso Sea	0.99	0.71	0.36	0.51
Lofoten Basin	2.12	0.81		
PAPA1-3 deep	4.60	0.98		
Panama Basin	9.60	1.50	2.49	1.66
Califonia-near shore 500	9.50	1.49	3.13	2.10
Califonia-near shore 1000	12.80	1.80	3.99	2.22
Califonia-near shore 2329	16.10	1.60	3.71	2.32
Califonia-midway 500	1.77	0.31	0.66	2.13
Califonia-midway 1750	4.90	0.71	1.72	2.42
Califonia-midway 2330	4.30	0.61	1.48	2.43
Bransfield Strait	11.00	1.32		
Nares Abys. Plain-deep	0.91	0.71		
Nares Abys. Plain	1.12	0.68		

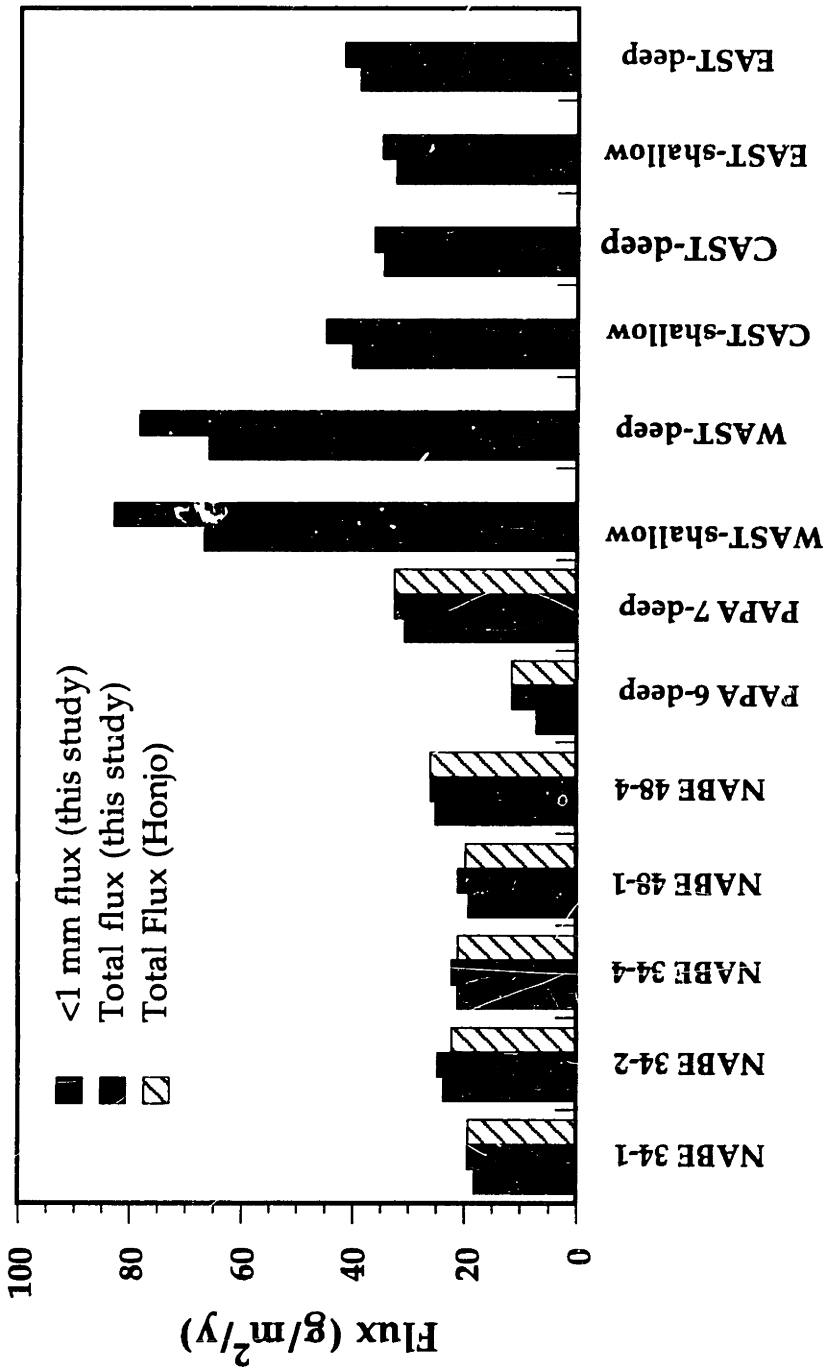

Figure 3.1 Comparsion of estimated mean annual flux

1988). In addition, PAPA1-3 data were taken from Bacon (unpublished data) and given in Table 3.4 for comparison. Sample materials from the Arabian Sea stations were only from half-year collections, but they were taken to represent the mean annual records and are included in the compiled data plots for discussion. The mean annual flux range (3 to 7 $g/cm^2/ka$) of these half-year collections is apparently higher than the mean annual flux (2.3 to 3.4 $g/cm^2/ka$) reported from the whole year collection (Nair *et al.*, unpublished); therefore, the fluxes might be under- or over-estimated because of seasonal variations.

3.6.1 Quantification of sediment trap efficiency with ^{230}Th and ^{231}Pa

For more than a decade, sediment traps have aided scientists in developing insights into the functioning of ocean systems. The trapping efficiency of a sediment trap is essential to know for quantifying the flux of particulate materials. The production of ^{230}Th in the water column occurs at a known rate because it is produced from the decay of uranium, an element with nearly constant concentration and uniform distribution in the ocean, at least through the Quaternary (Anderson, 1982); in addition, the residence time of ^{230}Th in the ocean is very short, in a range of ~20 to 40 years (Anderson *et al.*, 1983a and 1983b), as compared to its half-life of 75,200 years. Thus, ^{230}Th has been suggested as the best candidate for quantifying trapping efficiency (Brewer *et al.*, 1980).

By comparing the flux (F) of Th measured in collected sediment trap material to its production rate (P) from the overlying water column, the trapping efficiency would be determined (i.e., the trapping efficiency equals

F/P). The production (P) of ^{230}Th can be calculated by the formula $P^{230}Th$ =0.0026*Z, where Z is the water depth in meters, and P is in dpm/cm^2/ka. If there is no trapping error, F/P=1.

The above is based on the assumption that V=P, where V is the vertical flux of ^{230}Th scavenged from seawater, but this is subject to some uncertainties (Bacon *et al.*, 1985). The uncertainties arise from (1) the possible partitioning of ^{230}Th scavenging between vertical and horizontal pathways and (2) temporal variations in scavenging rate of ^{230}Th due, for example, to the seasonal variations in total particle flux. From the total fluxes of ^{230}Th collected in a PARFLUX-design sediment trap at 3200m in the Sargasso Sea, Bacon *et al* (1985) showed that the apparent trapping efficiency obtained for different two-month intervals varied from 25% to 101%. The data indicate, for the short term, that the production and removal of ^{230}Th are clearly not in balance. However, the seasonal bias may be removed, as suggested by Bacon *et al.* (1985), by averaging over annual, or longer, records of ^{230}Th in the trap to obtain the mean annual flux F of ^{230}Th. This is what I have done in the following.

Horizontal transport of ^{230}Th may occur; thus, the net horizontal transport (H) of ^{230}Th needs to be evaluated. It then becomes a problem to use the mass balance of ^{230}Th to examine both the trapping efficiency and the extent of the horizontal transport of ^{230}Th, which can not be solved uniquely. As previously suggested (Anderson *et al.*, 1983b; and Bacon *et al.*, 1985), to evaluate absolute trapping efficiency, one needs to combine information on $^{230}Th/^{231}Pa$ activity ratio both in the water column and in settling particulate matter at the site; [illegible]an calculate both the vertical flux V

and horizontal transport flux H by simultaneously satisfying oceanic material balances for ^{230}Th and ^{231}Pa (Bacon *et al.*, 1985):

$$H_{Th} + V_{Th} = P_{Th} \quad (3\text{-}4)$$

$$H_{Pa} + V_{Pa} = P_{Pa} \quad (3\text{-}5)$$

$$H_{Th} = R_h H_{Pa} \quad (3\text{-}6)$$

$$V_{Th} = R_0 V_{Pa} \quad (3\text{-}7)$$

This method was designed to estimate V and H that are independent of the fluxes measured by traps. The equations are based on mass balance, assuming that H is the horizontal flux from the ocean interior toward the margins of the basin, which causes an intensified scavenging at the margins. A flux of ^{230}Th, however, might occur in a particulate form from the opposite direction at the margins due to sediment resuspension at the margins and lateral spreading toward the ocean interior. In other words, the flux H should be evaluated to take into account all net effects of horizontal redistribution of the ^{230}Th production.

In equation (3-6), R_h is the $^{230}Th/^{231}Pa$ activity ratio in seawater (governing the horizontal transport), and R_0 (equation 3-7) is the $^{230}Th/^{231}Pa$ activity ratio in the settling particulate matter. The net flux H is taken to be positive for transport away from the ocean interior. The absolute trapping efficiency E is then given by

$$E = F/V = F/(P\text{-}H). \quad (3\text{-}8)$$

The R_h of the NABE 47-shallow and -deep stations were calculated from the measured values of $^{230}Th/^{231}Pa$ activity ratios in the water column

at depth of 1550 m and 2700 m. The measurements were done by A. Fleer (unpublished data). The value for the Sargasso Sea was taken from unpublished data of Bacon. Measurements are not available for the other stations in Table 3.4, so R_h was estimated by a best-fit of a third- order polynomial regression line (Figure 3.2) to the measured $^{231}Pa/^{230}Th$ ratio data from other stations where measurements were available. As shown in Figure 3.2, the $^{230}Th/^{231}Pa$ ratio increases with depth, and the ratio shows only slight variations, within a narrow envelop, at a given depth, even when the data are from different regions. The values of R_U and F for all stations were taken from the measured values in Table 3.4. The sources of the compiled data for R_U are indicated in Table 3.4. The required parameters to solve for both H and V for the ^{230}Th and ^{231}Pa of all traps, and the calculated results are summarized in Table 3.5. The sources of error are largely from the analytical errors of both ^{230}Th and ^{231}Pa measurements in the water column and in the particulate material. Since the concentrations of both nuclides in the two phases are low, the analytical results would therefore have a large error.

The calculated values of trapping efficiency E (i.e. F/V of ^{230}Th) range from 0.3 to 1.4 (Table 3.5 and Figure 3.3). If E values is close to 1, it can be concluded that the sediment trap performed well in measuring the flux of particulate materials. Within a deviation of ±30%, this result was found for all of the PARFLUX sediment traps at the deeper depths for the NABE 34 and 48, PAPA, Sargasso Sea, and all Arabian Sea stations. The shallow traps (~1000 m or shallower) showed a tendency toward undertrapping. Most of the shallow traps, even as deep as ~1000 m, show clearly the imbalance between production and removal of ^{230}Th. The sediment traps used for this

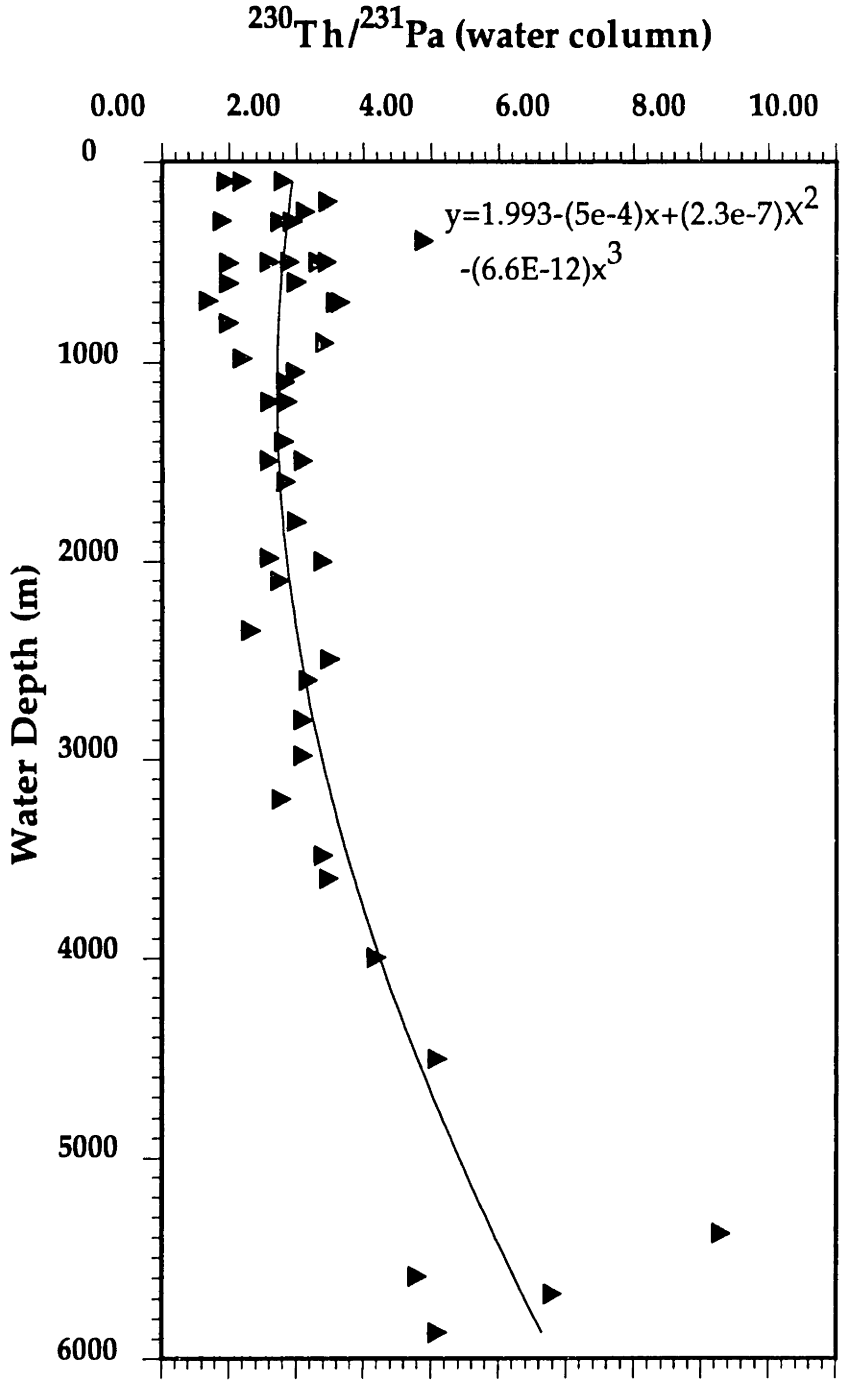

Figure 3.2 Summary of some available $^{230}Th/^{231}Pa$ activity ratios measured in water column

Table 3.5 Model results of the sediment trap efficiency

No.	Trap Sample	Trap depth (m)	P(Th) (dpm/m2/y)	P(Pa) (dpm/m2/y)	Rv(Th/Pa) Particulate	Rh (Th/Pa) Total in seawater
1	NABE 34-1000	1159	30.48	2.80	34.48	1.71
2	NABE 34-2000	1981	52.10	4.79	27.78	1.85
3	NABE 34-4000	4478	117.77	10.84	37.04	3.77
4	NABE 48-1000	1110	29.19	2.69	19.61	1.71
5	NABE 48-4000	3734	97.31	8.99	41.67	2.99
6	PAPA^ 6/7-deep	3800	99.94	9.20	13.70	3.05
7	WAST-shallow	1085	28.54	2.63	9.90	1.71
8	WAST-deep	3033	79.77	7.34	12.82	2.41
9	CAST-shallow	1000	26.30	2.42	14.29	1.72
10	CAST-deep	2400	63.12	5.81	13.89	2.03
11	EAST-shallow	1705	44.84	4.13	10.64	1.78
12	EAST-deep	2773	72.93	6.71	18.18	2.23
13	Sargasso Sea	3200	84.16	7.74	21.28	2.53
14	Panama Basin	2590	68.12	6.27	6.48	2.13
15	Califonia-near shore 500	500	13.15	1.21	5.12	1.80
16	Califonia-near shore 1000	1000	26.30	2.42	4.84	1.72
17	Califonia-near shore 2329	2329	61.25	5.64	4.71	1.99
18	Califonia-midway 500	500	13.15	1.21	5.05	1.80
19	Califonia-midway 1750	1750	46.03	4.24	4.44	1.79
20	Califonia-midway 2330	2329	61.25	5.64	4.42	1.99

Table 3.5 (con't)

No.	V(Pa) (dpm/m2/y)	V(Th) (dpm/m2/y)	V/P)Pa	V/P)Th	F/V)Th (E)Th	F/P)Th	Total flux eff.-corrected	Notes
1	0.78	27.03	0.28	0.89	0.63	0.56	2.89	Rh*
2	1.67	46.31	0.35	0.89	0.90	0.80	2.65	Rh*
3	2.31	85.62	0.21	0.73	1.22	0.89	1.75	Rh*
4	1.37	26.94	0.51	0.92	0.35	0.32	5.56	measured Rh from 2770 m A. Fleer
5	1.82	75.89	0.20	0.78	0.78	0.61	3.22	measured Rh from 1550 m A. Fleer
6	6.75	92.48	0.73	0.93	1.04	0.96	1.92	Rh*
7	2.94	29.07	1.12	1.02	0.82	0.84	8.11	Rh*
8	5.96	76.46	0.81	0.96	0.94	0.90	7.04	Rh*
9	1.76	25.17	0.73	0.96	0.70	0.67	5.76	Rh*
10	4.33	60.12	0.75	0.95	1.17	1.11	2.98	Rh*
11	4.23	45.02	1.02	1.00	0.92	0.92	3.56	Rh*
12	3.63	66.06	0.54	0.91	1.20	1.09	3.25	Rh*
13	3.44	73.29	0.44	0.87	0.82	0.71	1.21	Rh*, Rv:Bacon, unpublished
14	12.58	81.54	2.01	1.20	1.25	1.50	7.66	Rh*, Rv:Bacon, unpublished
15	3.30	16.92	2.73	1.29	1.16	1.49	8.20	Rh*, Rv: Lao, 1991
16	7.09	34.32	2.93	1.30	1.38	1.80	9.28	Rh*, Rv: Lao, 1991
17	18.41	86.69	3.27	1.42	1.13	1.60	14.24	Rh*, Rv: Lao, 1991
18	3.38	17.05	2.79	1.30	0.24	0.31	7.40	Rh*, Rv: Lao, 1991
19	14.49	64.36	3.42	1.40	0.51	0.71	9.65	Rh*, Rv: Lao, 1991
20	20.60	91.07	3.66	1.49	0.41	0.61	10.48	Rh*, Rv: Lao, 1991

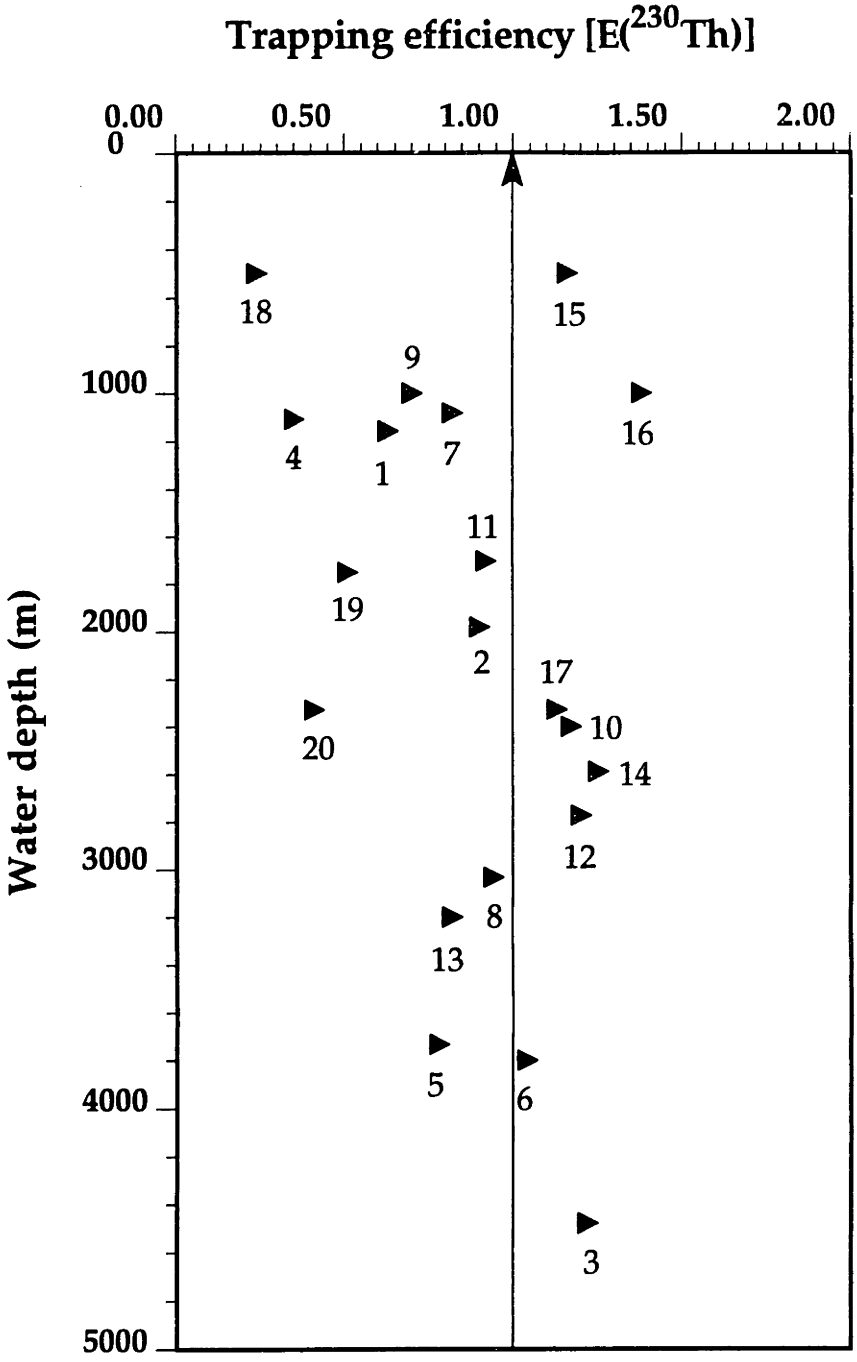

Figure 3.3 The estimated trapping efficiency [E(^{230}Th)] versus trap depth. The numbers are same as those in Table 3.5

study show a tendency of increasing in trapping efficiency with water depth for almost of stations. The potential problems due to swimmers and hydrodynamic bias have been suggested to influence significantly the records in shallow trap collections, but to influence to a lesser degree records in deeper traps (Gardner, 1980; 1985; Lee *et al.*, 1988; U. S. JGOFS Report, 1989; Busseler, 1991).

The trapping efficiency of the off-California nearshore deepest trap indicates overtrapping. Sediment traps deployed in margin areas might have collected some resuspended and laterally advected slope sediments, thus providing another source of ^{230}Th in addition to that scavenged from the overlying water column. From the calculations shown from equation (3-4) to (3-8), the data clearly suggest that the sediment trap performed unreliably in measuring the particle fluxes in the NABE 34 and 48-shallow traps, and the station off-California midway.

The data from the PAPA station was derived from time-weighted mean annual flux from two half-year collections PAPA6 and PAPA7. Comparing this time-weighed mean annual ^{230}Th flux F to its production rate P yields 0.96, a value comparable to a previous analysis result of 0.98 from the same site (Bacon, unpublished data). The two estimates come from different time periods that showed different values of total mass flux (two-fold difference in total mass flux between the two periods). This indicates that the scavenging efficiency of ^{230}Th is so strong that its scavenging rate is independent of total mass flux from the overlying water column. This indicates also that the interannual variations in the ^{230}Th flux may be small even though the variations in mass flux can be large. The absolute trapping efficiency of the traps, however, during the collection period of PAPA1-3 is

not known. Finally, the trapping efficiency of the traps off the California coast was estimated independently by comparing the F/P of ^{230}Th for the deepest trap to the F/P data of the core top (Lao, 1991); their data (0.66 for the traps of the off-California nearshore, and 0.17 for the trap off the California midway) were significantly lower than the calculations shown here. The average E value for all traps is 0.87 ± 0.32 (n=20), but the average E for all deep PARFLUX traps is 1.00 ± 0.05 (1 standard error of the mean, n=9). This indicates that the PARFLUX traps deployments are very reliable for the deep water particle collection.

As mentioned earlier, F/P of ^{230}Th was initially used for the estimation of apparent trapping efficiency (Brewer *et al.*, 1980). By comparing the measured flux of ^{230}Th integrated over collection period to the rate of production in the overlying water column, the apparent trapping efficiency for all traps were calculated. The F/P values of ^{230}Th are listed in Table 3.5 also for comparison with the absolute trapping efficiency based on F/V values of ^{230}Th. In general, the apparent trapping efficiency based on F/P values of ^{230}Th shows similar patterns for all traps used for this study.

3.6.2 Quantification of Particulate Radioisotope Flux

Since the F/P ratio is used to examine the scavenging efficiency of radionuclides by the settling particles, corrections for trapping error must be made to provide better quantification of the scavenging efficiency of radionuclides and their adsorbers and better understanding of the scavenging behaviors of both ^{230}Th and ^{231}Pa. The trapping efficiency corrected-mass flux will be used in the following discussion.

As indicated in Table 3.5, after correction for trapping efficiency, the total mass fluxes of particulate material at the NABE 34 station showed a smaller mass range than those at the NABE 48 station. The range of mass fluxes in the NABE stations and both the CAST and EAST stations varies from ~2 to ~6 $g/cm^2/ka$, whereas the total mass fluxes of the two WAST traps range from 7 to 8 $g/cm^2/ka$. There is a decreasing trend in the corrected- total mass flux with depth for stations in the open ocean, but an increasing trend with depth for those stations at the margins. Total mass flux of open ocean stations such as the NABE, Arabian EAST and CAST, PAPA, Sargasso Sea, and Nares Abyssal Plain stations ranges from 1 to 6 $g/cm^2/ka$, and in the ocean margin area and high production regions such as Panama Basin and off California nearshore stations it is a few times higher. A station from the polar ocean, the Lofoten Basin (not corrected for trapping efficiency), has a total mass flux similar to the open ocean stations. The lowest flux shown in Table 3.4 occurs at shallow depth over the Nares Abyssal Plain, and the highest flux is in the deepest trap at the margin site off California nearshore. The total mass flux of the sediment traps corrected for trapping efficiency in Table 3.5 ranges from ~1 to ~14 $g/cm^2/ka$.

3.6.2-a The value of V/P for ^{230}Th

The ratio of vertical flux of ^{230}Th (and ^{231}Pa) to its production rate (V/P) is used to quantify the scavenging efficiency of radionuclides by the settling particles. Although V/P provides better quantification of the scavenging efficiency of radionuclides and their adsorbers, F/P values were calculated and listed in Table 3.5 for comparison. The V/P values for ^{230}Th

(Table 3. 5) indicate that nearly all of ^{230}Th production in the water column is removed by the vertical particulate flux for the Arabian Sea stations, and at least 90% of ^{230}Th production is removed by the vertical particulate flux for the Sargasso Sea and shallow depths of the NABE 34 and NABE 48 stations. This indicates that almost all of the ^{230}Th produced in the water column is removed into the underlying seafloor for those stations. The deeper NABE stations show a lesser extent of vertical scavenging, but still have at least 70% of ^{230}Th production from overlying water removed. The remaining ^{230}Th seems to be carried off horizontally to sites of high particulate flux or ocean margins. The vertical flux of ^{230}Th for the Panama Basin station and for the California coast stations showed fluxes greater than ^{230}Th production in the water column by approximately 20%, and 30% to 50%, respectively. This provides evidence that the excess of ^{230}Th is being taken up at these regions. Very similar conclusions also have been reached from data from the Pacific (Anderson *et al.*, 1983 a & b). By comparing, the F/P values of ^{230}Th show a larger deviation from 1, but the balance between production and removal of ^{230}Th still holds reasonably well for most of stations. For those stations with a deviation larger than 30%, reflect mainly trapping errors.

The V/P values were used to account for the difference in water depth that results from the linear proportion of production to water depth. Thus the question of whether the mean annual nuclide flux corresponds to the mean annual total mass flux can be examined. Figure 3.4 a and b are the plots for the trapping efficiency-corrected mean annual particle flux versus the values of V/P for ^{230}Th and the mean annual particle flux versus the values of F/P for ^{230}Th. It illustrates how the scavenging efficiency of ^{230}Th is

related to particulate flux for both plots. The mean annual fluxes of ^{230}Th are well correlated with mean annual total mass fluxes. A simple linear relationship of V/P ratios for ^{230}Th with trapping efficiency-corrected total mass flux was found (Figure 3.4-a). The regression line can be represented by the following equation for the total mass flux from <1 g/cm^2/ka up to 14 g/cm^2/ka: Y = 0.73 + 0.06 X; where Y is the V/P ratio for ^{230}Th, and X is the total mass flux. The correlation coefficient R is 0.88. A similar regression line for the relationship between mean annual particle flux versus the values of F/P for ^{230}Th was also found (Figure 3.4-b).

When the fluxes of $^{230}Th_{ex}$ and $^{231}Pa_{ex}$ in sediment traps are less than their rates of production in the overlying water column, lateral transport or other processes may be removing portions of the ^{230}Th and ^{231}Pa (Anderson, *et al.*, 1983a). Since each data point in Table 3.4 represents a year-long composited record at a site, and the trap deployments covered a large range in total mass flux, a global-average mass balance of ^{230}Th can be estimated by averaging all available V/P data. The result gives an average value of 1.06 ± 0.05 (1 standard error of the mean, n=20), indicating that, on a global scale, there is a good balance between production and removal.

3.6.2-b Is ^{230}Th flux constant?

Although there is a definite trend in the composited data of V/P ratios (also F/P ratios in Figure 3.4-b) for ^{230}Th with total mass flux, with V/P <1 in areas of low mass flux and V/P > 1 in areas of high mass flux, the slope of the regression line is shallow (Figure 3.4-a). The data indicate that while total mass flux varies 14 fold between low- and high-productivity regions, the

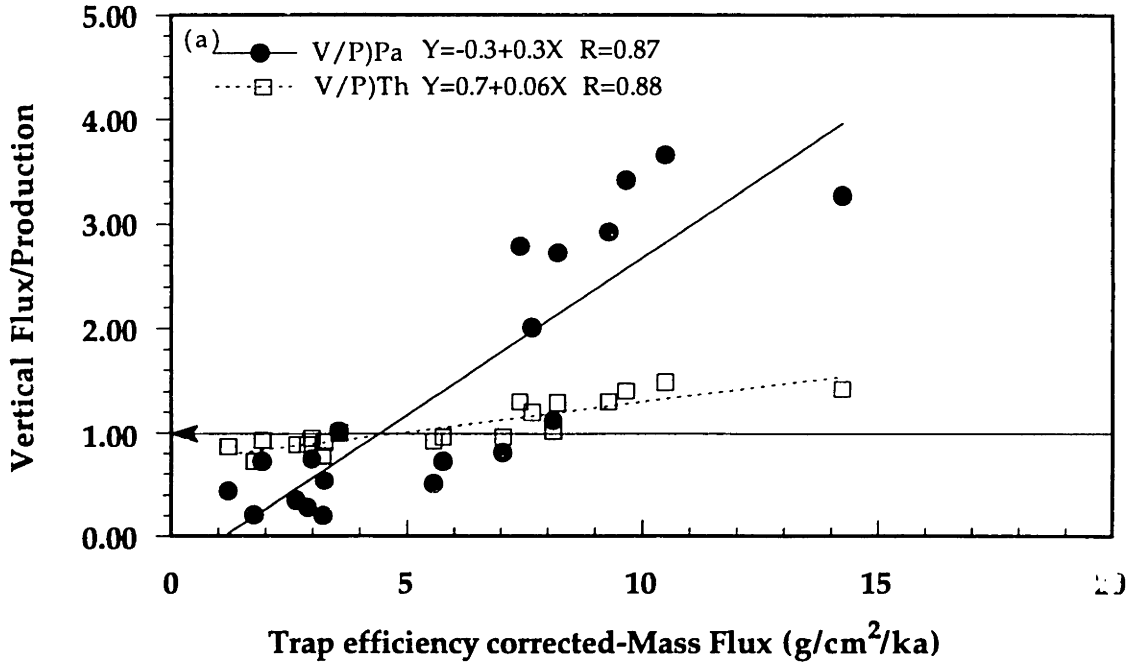

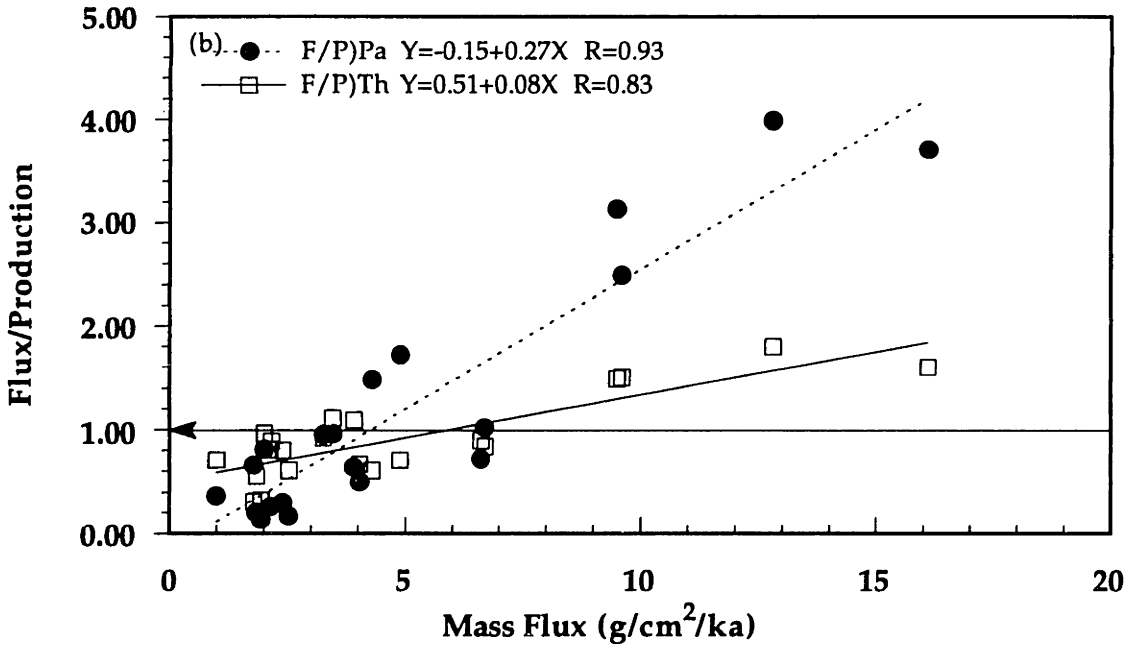

Figure 3.4 (a) V/P)^{230}Th and V/P)^{231}Pa versus trap efficiency-corrected mass flux; (b) F/P)^{230}Th and F/P)^{231}Pa versus mass flux.

accompanying flux of ^{230}Th varies only two times. A V/P ratio greater than one is an expression of the so-called "boundary scavenging" phenomenon. For most of the V/P values for ^{230}Th, which are close to one, the effect of "boundary scavenging" on ^{230}Th appears comparatively small as shown in Tables 3.4 and 3.5, and Figure 3.4-a. At the lowest mass fluxes of ~ 1 g/cm^2/ka (Sargasso Sea), close to 90% of ^{230}Th production was found in the vertical flux. At the site of the lowest scavenging efficiency of ^{230}Th, more than 70% of ^{230}Th production was still sedimented out to the underlying seafloor, whereas in the higher flux regions (Panama Basin and California margin), the ^{230}Th flux exceeds production rate by no more than 50%, and even this value may be biased toward the high side because of resuspension.

A similar conclusion has been derived from theoretical considerations. The extent of boundary scavenging depends primarily on the relative time scales of scavenging and lateral mixing (Bacon, 1988; Anderson *et al.*, 1990). The time scale for lateral mixing depends on the rate of lateral mixing and the distance over which lateral transport occurs. Using a one-dimensional horizontal diffusion model, Anderson *et al.*, (1990) pointed out that for a typical ocean basin with a half width of 3000 km and an isopycnal diffusivity of 3x10^7 cm^2/s, the boundary scavenging effect will be minor for elements with residence times of less than 95 years. The residence time of ^{230}Th with respect to chemical scavenging has been estimated at 30 to 50 years (Brewer *et al.*, 1980; Anderson *et al.*, 1983), which suggests that boundary scavenging should have a minor impact on what is measured in the open ocean and margin areas. From a simple box model, Bacon (1988) concluded that less than 15% of the ^{230}Th produced in open ocean waters is scavenged in margin areas.

Tne extent of "horizontal transport " of ^{230}Th might be used to "fine-tune" the ^{230}Th fluxes; the data shown in Tables 3.4 and 3.5, and Figure 3.4-a indicated that the effect of particle flux variations on the ^{230}Th flux might be at most 30%. The ^{230}Th data from Table 3.5 and Figure 3.4-a, therefore, suggest that the assumption of a ^{230}Th rain rate equal to the integrated production in the overlying water column is, in most instances, correct within about 30%, and probably better. Thomson and his colleagues (1993) reported a similar conclusion recently.

In conclusion, the assumption that ^{230}Th flux to the seafloor is constant and close to the rate of production in the overlying water column is well supported by annual flux measurements obtained from sediment traps deployed in areas spanning a wide range of total settling fluxes. For most of the deep-sea, the sedimentation flux has been estimated within a range of 1 to 3 g/cm^2/ka; the application of the "^{230}Th-normalized flux method" to estimate the variation of the paleo-particle rain rate can be used perfectly well since the entire flux of ^{230}Th production is scavenged downward vertically in such a mass flux range. In regions with extremely high particle flux, although the absolute values of paleoflux might be underestimated by as much as 10% to 30%, the application of the ^{230}Th-normalization flux method to obtain the variation of paleoflux with time should be distorted less by this effect.

I conclude, therefore, that the large variations of F/P of ^{230}Th reported from sediments from one up to as much as ten in those margin sediments (Mangini and Diester-Haass, 1983), in SEEP-I &II (Anderson *et al.*, 1991), and the western and the eastern equatorial Atlantic sediments (Francois, *et al.*, 1991) must be due to sediment redistribution.

3.6.2-c The V/P values for ^{231}Pa

The V/P values show a strong tendency for significant horizontal transport of ^{231}Pa from the open ocean to regions of higher particle flux (Table 3.5). For ^{231}Pa, the partitioning of the removal flux is the reverse in comparison to that of ^{230}Th, with only one-fifth of the production in open ocean sites being carried downward by settling particles and the rest being taken up at the ocean margins or other regions with high particulate flux.

The relationship between the V/P and trapping efficiency-corrected total mass flux for ^{231}Pa can also be represented by a linear regression (Figure 3.4-a). It is clearly indicated in Figure 3.4 that there is a strong dependence of the V/P values of ^{231}Pa on total mass flux. In low particle flux regions, traps collected flux with a much lower value than production rate for ^{231}Pa in the overlying water column; while in areas of higher mass flux or margins, traps collected flux with a much higher value of F/P. While total mass flux collected by traps varies 14-fold between low- and high-productivity regions, the accompanying flux of ^{231}Pa varies up to more than one order of magnitude, from a deficit of as low as about 30% in oligotrophic regions to an excess of more than 4 times greater in high particle regions and margin areas. This shows that the extent of horizontal transport for ^{231}Pa is much greater than it is for ^{230}Th.

Results of the compiled data set suggest that particle flux is the major factor influencing removal of the nuclides ^{230}Th and ^{231}Pa from seawater. The scavenging rate of ^{230}Th apparently fluctuates less in relation to the flux of particulate materials; whereas ^{231}Pa is very sensitive in relation to the flux

of particulate materials. The hypothesis of a constant flux of ^{230}Th therefore holds as a good approximation for the ^{230}Th-normalized flux model.

3.6.3. Particulate $(^{231}Pa/^{230}Th)_{ex}$ ratios in sediment traps

Since the vertical flux of ^{230}Th fluctuates much less than the vertical flux of ^{231}Pa in response to variations in the particle flux (Figure 3.4), a higher ratio of $(^{231}Pa/^{230}Th)_{ex}$ should reflect the higher particle rain rates. Data from sediment traps deployed for a year or longer in the deep sea do show this phenomenon (Figure 3.5 a and b). Higher unsupported $(^{231}Pa/^{230}Th)_{ex}$ ratios, more than two times higher than the theoretical production ratio of 0.093 (Table 3.5 and Figure 3.5a), occurred in regions of higher particle flux such as ocean margins and high production areas (e.g., the Panama Basin and off the California coast); whereas lower ratios, as low as one-fourth of the theoretical ratio, occurred in regions of lower particle flux such as open ocean gyres (e.g., the Sargasso Sea, the northern Atlantic Ocean). The dependence of $(^{231}Pa/^{230}Th)_{ex}$ ratios on the total flux is strong, as indicated by the slope of the regression line (Figure 3.5a). The slope shows the$(^{231}Pa/^{230}Th)_{ex}$ ratio to be approximately 14 times with the variations in total particle flux. While total mass flux collected by traps varies 16-fold between low- and high-productivity regions, the accompanying ratio of $(^{231}Pa/^{230}Th)_{ex}$ varies from as low as 30% of the theoretical ratio in oligotrophic regions to an excess of about 2.5 times of 0.093 in high particle flux regions. This reflects the large amount of horizontal transport of ^{231}Pa from low flux regions to high flux regions.

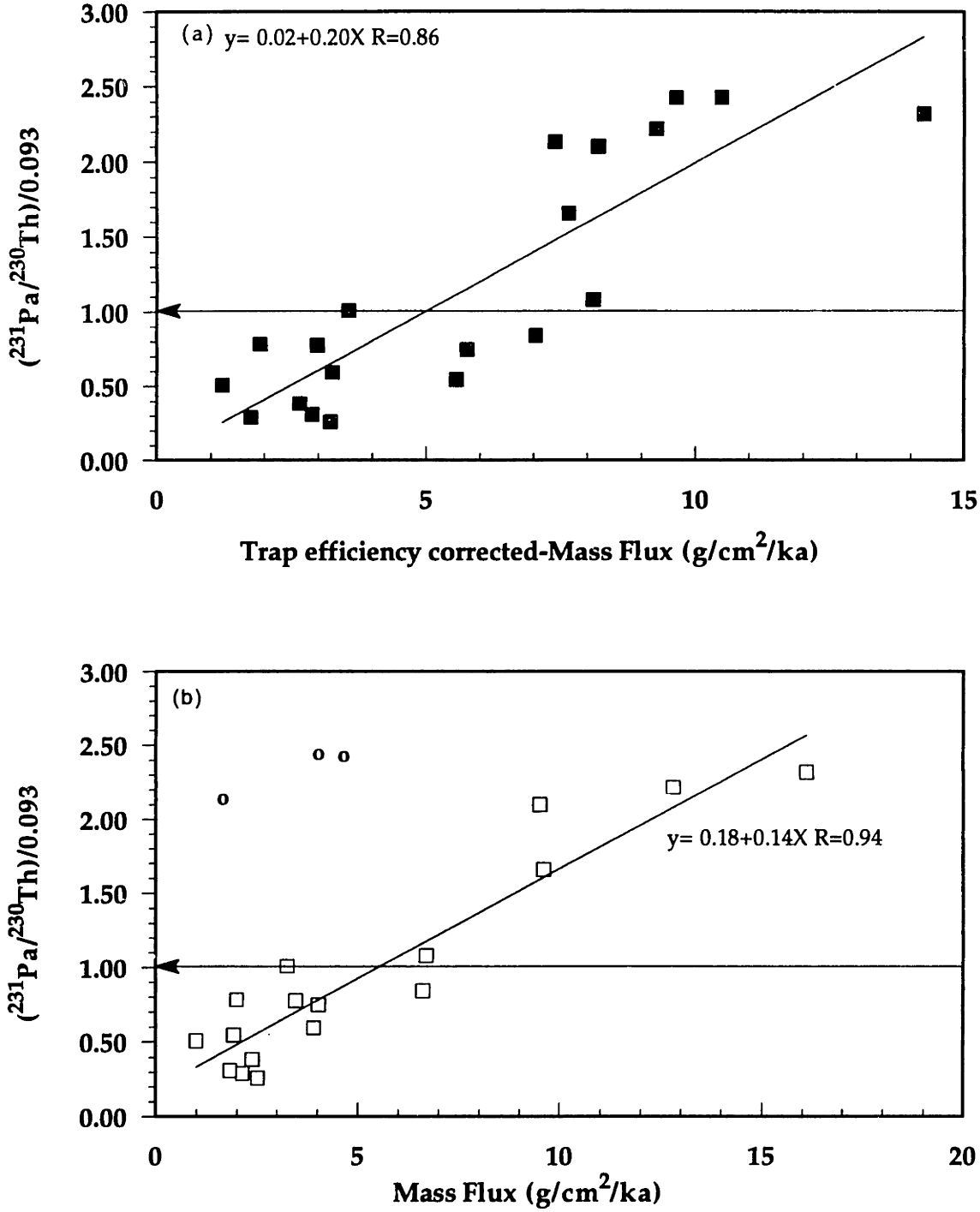

Figure 3.5 Pa/Th)/0.093 versus (a) trap efficiency corrected-mass flux and (b) mass flux. Symbols (o) on figure (b) are data from the California-midway traps, which are not included in the regression line.

3.6.4 Does the composition of particles affect the relationship between particle flux and nuclide flux and the $(^{231}Pa/^{230}Th)_{ex}$ ratio?

Boundary scavenging is the term used to describe the phenomenon of more enhanced chemical scavenging at the ocean margins than in the ocean interior (Spencer *et al.*, 1981). Although many previous workers have found this phenomenon to occur for particle reactive chemical substances in different regions (Bacon et al., 1976; Nozaki *et al.*, 1981; Spencer *et al.*, 1981; Anderson *et al.*, 1983 a&b; Lao *et al.*, 1993), the controlling mechanisms are not well understood. Higher total flux of particular matter certainly contributes to a higher $(^{231}Pa/^{230}Th)_{ex}$ ratio, as demonstrated above (Table 3.5 and Figure 3.5) and in other works (Taguchi *et al.*, 1989; Anderson *et al.*, 1990; Lao, 1991). Other factors such as the chemical composition of particulate matter, ocean mixing rate, and residence time of the scavenged elements (Anderson *et al.*, 1983b; Bacon, 1988; and Anderson *et al.*, 1990) have also been suggested as potentially important factors. In the following section, I discuss how the particle composition may cause deviations from the simple relationship of $(^{231}Pa/^{230}Th)_{ex}$ ratio to total particle flux. The quality of particles, and whether the change in quality of particles during their transportation and transformation, controls the fractionation between ^{231}Pa and ^{230}Th in different ocean regions are important issues to examine.

Partitioning of particle-reactive metals between particles and solutions is often described by a distribution coefficient (K_d), defined as

$$K_d = [M]_p/[M]_d,$$

where $[M]_p$ is the activity in the solid phase (in dpm/g of particle) and $[M]_d$ is the activity in the solution (in dpm/g of solution). In an attempt to identify

possible differences in the scavenging properties of different particulate carrier phases for both ^{231}Pa and ^{230}Th, the K_ds of ^{230}Th and ^{231}Pa for each of these phases should be examined. Unfortunately, field data is very limited. For now, I will provide two types of indirect ways to examine the empirical relations of V/P of both ^{231}Pa and ^{230}Th, and of the $(^{231}Pa/^{230}Th)_{ex}$ ratio, with the deposition rate of a component of interest in particulate material. First, the empirical relation of the nuclides with the four major components of settling particles, carbonate, biogenic opal, organic carbon, and terrigenous materials, were examined and the results are shown in Table 3.6. Figure 3.6 a-d shows the correlation of V/P of both ^{231}Pa and ^{230}Th with the trap efficiency corrected-flux of carbonate, organic carbon, opal, and terrigenous carrier phases. Figure 3.7 a-d gives the correlation of the $(^{231}Pa/^{230}Th)_{ex}$ ratio compared with the flux of the major carrier phases. No significant correlations are observed, suggesting that no carrier phase of carbonate, opal, organic matter, or terrigenous material alone can control chiefly the affinity of both ^{230}Th and ^{231}Pa to settling particles. These observations show inconsistent patterns compared with previous studies. The previous studies (as described below) on particulate materials or on surface sediments, however, did not obtain a uniform conclusion about the effect of particle composition on scavenging behavior of nuclides.

Secondly, since the flux of each particle component in Figure 3.7 represents the variation in its concentration and the total particle flux at the site, the control by composition can not be decoupled entirely from the influence of total flux as used in Figures 3.6 and 3.7. The logical idea is to examine whether the concentration of sedimentary components for those data points with a higher particle flux range in the Figure 3.5 do show any

Table 3.6 Concentration and flux of components of sediment trap samples

Trap Sample depth (cm)	Total flux (g/m2/yr)	carbonate %	opal %	%Corg *	lithogenic%	Carbonate flux (g/m2/y)	Opal flux (g/m2/y)	Corg flux** (g/m2/y)	Lithogenic flux (g/m2/y)
NABE 34-1000	18.28	70.05	7.29	21.93	0.73	12.81	1.33	4.01	0.13
NABE 34-2000	23.85	70.20	8.36	10.7	10.74	16.74	1.99	2.55	2.56
NABE 34-4000	21.38	68.80	9.49	9.5	12.21	14.71	2.03	2.03	2.61
NABE 48-1000	19.27	61.05	17.80	15.94	5.21	11.76	3.43	3.07	1.00
NABE 48-4000	25.21	60.10	23.79	9.58	6.53	15.15	6.00	2.42	1.65
PAPA 6-deep	7.19	35.70	47.50	15.03	1.77	2.57	3.42	1.08	0.13
PAPA 7-deep	30.81	43.80	44.75			13.49	13.79		
PAPA^ 6/7-deep	19.95	40.08	46.01	15.03	-1.12	8.00	9.18	3.00	-0.22
WAST-shallow	66.87	58.90	22.51			39.39	15.05		
WAST-deep	66.09	54.10	5.44			35.75	3.60		
CAST-shallow	40.30	53.50	6.30	42.03	-1.82	21.56	2.54	16.94	-0.73
CAST-deep	34.73	63.40	5.63	32.6	-1.63	22.02	1.96	11.32	-0.57
EAST-shallow	32.59	49.20	10.54			16.03	3.43		
EAST-deep	39.10	43.40	1.82			16.97	0.71		
Brainsfield Strait	107.70								

* percentage of organic matter, which is 2.5 times of percentage of organic carbon in samples

** flux of organic matter in the samples

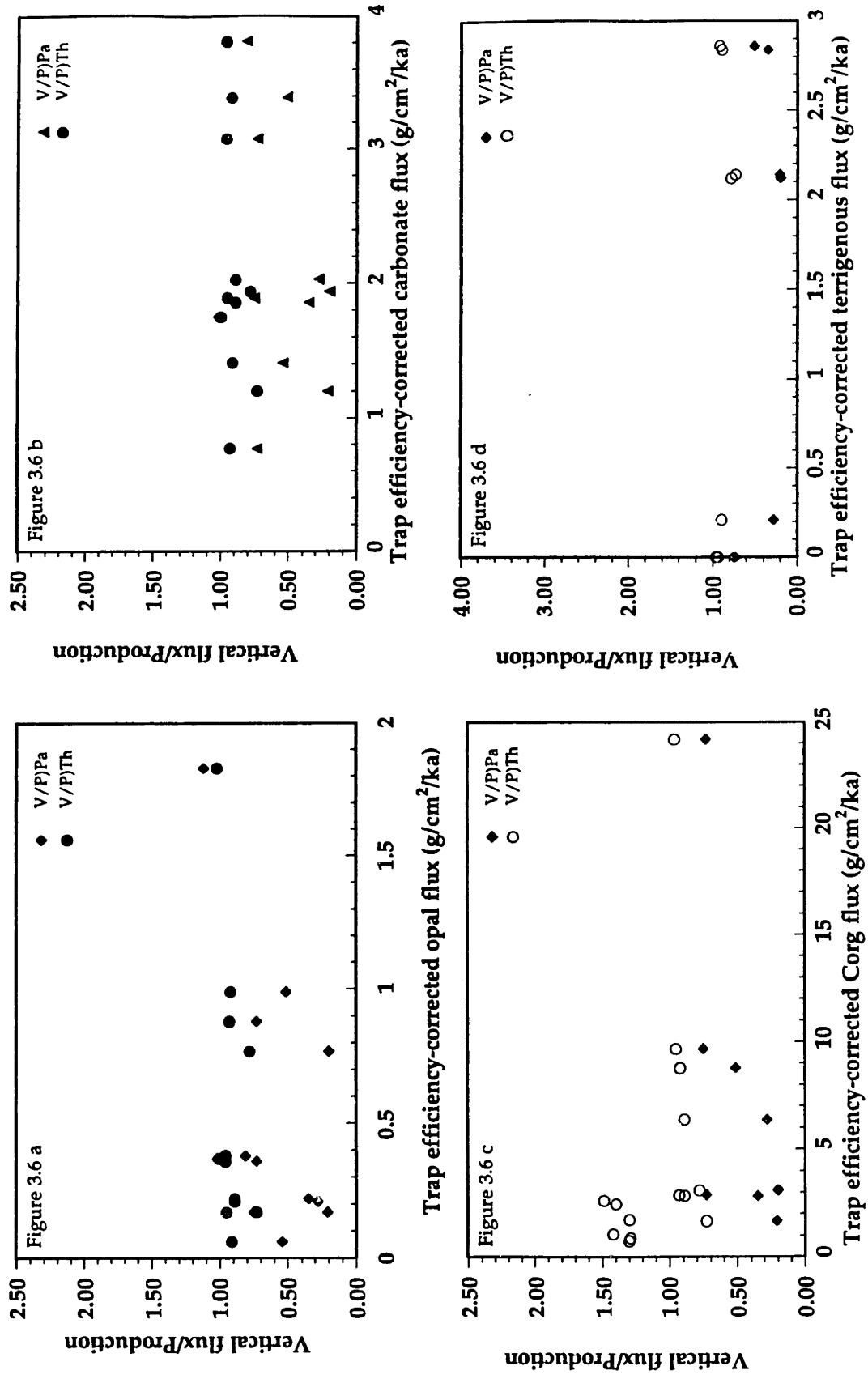

Figure 3.6 The vertical flux/production ratio of ^{230}Th and ^{231}Pa versus trap efficiency corrected-flux of (a) opal, (b) carbonate, (c) organic matter, and (d) terrigenous.

definite trend in terms of the correlation between the $(^{231}Pa/^{230}Th)_{ex}$ ratio and the concentration of sedimentary components. In the following, I examine the relation of the deviations from the best-fit regression line as shown in Figure 3.5 (the $(^{231}Pa/^{230}Th)_{ex}$ ratio to its production ratio of 0.093 versus total mass flux) with the concentration of each component to evaluate whether there is any definite trend. The results are given in Figure 3.8 a-d. I particularly emphasize discussion of the relationship of activity ratio to biogenic opal, because it was hypothesized previously that biogenic opal is a specific particulate phase causing enhanced scavenging in high production regions.

It has been proposed by Demaster (1979) and Kumar *et al.* (1993) that the extremely high flux of biogenic silica quantitatively strips dissolved ^{230}Th and ^{231}Pa and that this accounts for the high activity ratio to the Antarctic sediments. In high production regions (the Gulf of Alaska and the northern North Pacific Ocean and off the California coast), Taguchi and his colleagues (1989) found a relatively high correlation of F/P for ^{231}Pa with opal flux in sediment traps and thus suggested that the surface biogenic opal production is responsible for the fractionation between ^{230}Th and ^{231}Pa. However, as shown in Figure 3.8 a, I can not find a definite relationship with opal in samples I have analyzed. These results therefore do not support the hypothesis. The strong correlations found by Taguchi and his colleagues (1989) might be due to the influence of total mass flux rather than by the concentration itself. In addition, most of sediment traps used by Taguchi and his colleagues (1989) were only deployed a short period of time which may

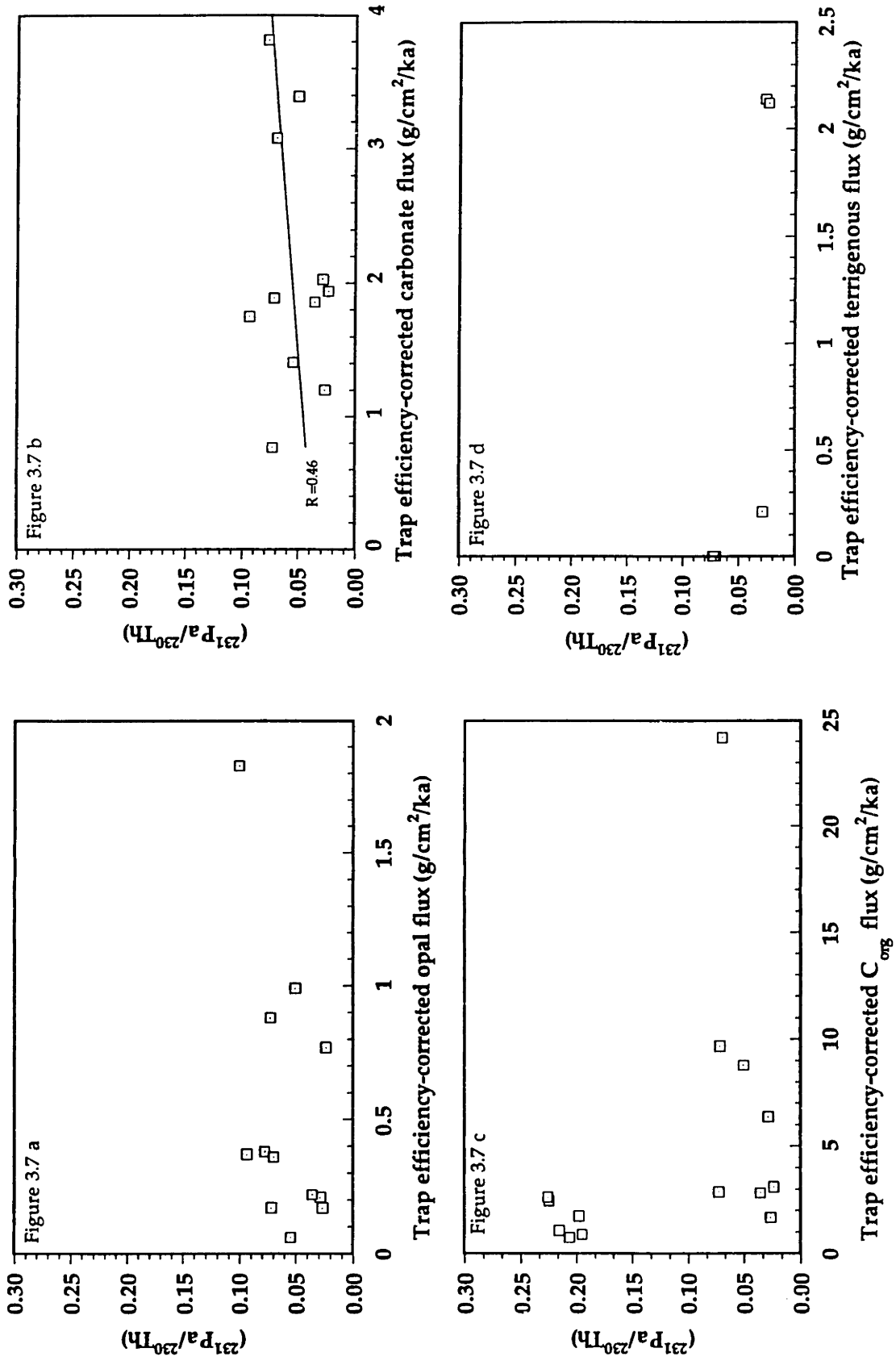

Figure 3.7 The $^{231}Pa/^{230}Th$ activity ratio versus trap efficiency corrected-flux of (a) opal, (b) carbonate, (c) organic matter, and (d) terrigenous.

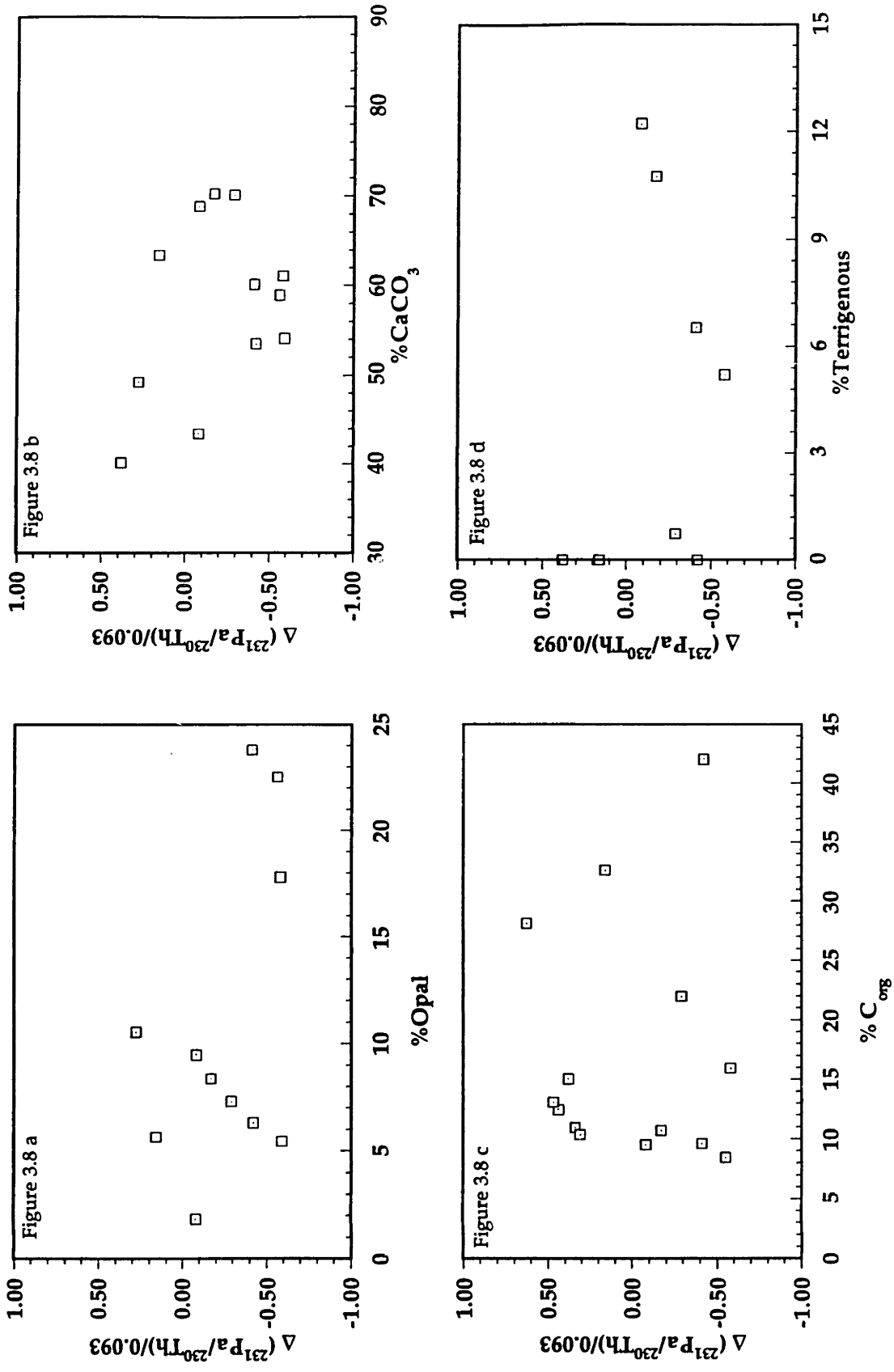

Figure 3.8 Deviations of the $^{231}Pa/^{230}Th$ activity ratio over 0.093 versus (a) %opal, (b) %carbonate, (c) %organic matter, and (d) %terrigenous.

cause a largely seasonal bias to the records; also there were no estimations or corrections of their traps for the trapping efficiency. On the other hand, there only a subset of the sediment trap samples used in Figure 3.5 have biogenic opal data; thus the data may not be completely representive. In addition, since the materials of sediment traps were composited for all annual collections, I perhaps average in actually observing relationships that exist.

However, these results seem to agree with an direct measurement of the adsorption of ^{230}Th and ^{231}Pa on the silica phase which was performed recently in a laboratory experiment by Anderson *et al.* (1992). In their laboratory study, batch experiments were conducted by adding spikes of ^{234}Th and ^{233}Pa radiotracers to suspensions (~0.5 mg/l) of various particle types in synthetic seawater and in 0.2-μm-filtered coastal seawater at constant temperature, salinity and pH. Solid phases in the experiments were hematite (α-Fe_2O_3), MnO_2-coated XRD resin, γ-Al_2O_3, silica gel and interfacial sediments from Buzzards Bay, MA. At predetermined times, aliquots of the suspensions were flitered (0.2-μm Nucleopore), and ^{234}Th and ^{233}Pa activities were measured in the filter-retained particles and in the filtrate. Their experiment results showed that the measured K_d values for Th and Pa on different particle types ranged from 10^5 to 10^8, indicating that different solid phases have different affinities for the two elements. Of particular importance, the ratio of the K_d values for Th and Pa, defined as the fractionation factor $f = K_d^{Th}/K_d^{Pa}$, also varied significantly for the different phases. Fractionation factors of f for hematite (2.1), silica (1.1), and MnO_2 (0.8) indicate these phases do not fractionate substantially for Th and Pa. By comparison, large fractionation factors were observed for Al_2O_3 (12.5) and natural sediments (8.9), indicating that these phases preferentially adsorb Th

over Pa (Anderson *et al.*, 1992). Of particular interest, the relation between the deviations of activity ratio over 0.093 versus the percentage of terrigenous materials for my samples (Figure 3.8 b) do show some degree of correlation between the two parameters, indicating that the terrigenous materials might cause some degree of the fractionation between ^{230}Th and ^{231}Pa, in agreement with the results shown by Anderson *et al* (1992), but this concept needs to be refined.

Other particle phases were also examined. Taguchi *et al.*, (1989) found a weak correlation between F/P for ^{231}Pa of the settling particles and organic carbon and clay r=0.6 for both), but no correlation with MnO_2 and $CaCO_3$ phases (r<0.5). In Figure 3.8, my data also do not show any correlation of the deviations of $(^{231}Pa/^{230}Th)_{ex}$ ratio over 0.093 with $CaCO_3$ and organic carbon phases. Any of these observations include in this study, however, may be insufficient to discuss the fractionation factor because the interaction between particle composition and nuclide scavenging behavior is very complicated, and because the data set is limited. In addition to these complexities, the effect scavenging efficiency will need to compete against the effect of horizontal transport, and the effect of mass redistribution within an ocean basin for both ^{230}Th and ^{231}Pa.

The role of the specific particulate phase MnO_2 coating on particles in preferential scavenging of ^{231}Pa over ^{230}Th in ocean margins was strongly suggested in previous works (Spencer *et al.*, 1981; Anderson *et al.* 1983b). In the Panama and Guatemala Basins, a value of fractionation factor of $f_{Th/Pa}$ ~1 was found, whereas a value of $f_{Th/Pa}$ ~ 10 was found in the open ocean gyres in the North Atlantic Ocean. It was concluded that particles at ocean margins may be different from open ocean particles so that the adsorption no longer

favors ^{230}Th over ^{231}Pa (Anderson *et al.*, 1983b). Conversely, the boundary scavenging phenomenon due to the specific particulate phase MnO_2 was not found in the Middle-Atlantic Bight (MAB) (Anderson *et al.*, 1992), and the fractionation between ^{231}Pa and ^{230}Th was not found in the laboratory studys (Anderson *et al.*, 1992) either.

Other particulate phases such as Ba (barite) and Al (Al_2O_3) were also suggested as important carriers of ^{231}Pa and ^{230}Th, and they may be factors causing the fractionation between ^{231}Pa and ^{230}Th (Lao *et al.*, 1993). Given the correlation between the $(^{231}Pa/^{230}Th)_{ex}$ ratio with the opal or Ba concentration in the surface sediments or in settling particulates, some authors have thus suggested that we can use the $(^{231}Pa/^{230}Th)_{ex}$ ratio as an index of surface production (Taguchi *et al.*, 1989; Lao *et al.*, 1992).

Apparently, we expect that the quality and quantity of settling particles to be related to the fractionation between ^{231}Pa and ^{230}Th, but all the field and laboratory studies discussed above do not give a definite conclusion in terms of the particle composition controlling the fractionation between ^{231}Pa and ^{230}Th. Caution should be extended to suggestion that the $(^{231}Pa/^{230}Th)_{ex}{}^{o}$ ratio can be used as a primary production index. More data is needed to confirm the hypothesis. To be able to examine whether the particle composition, or which particle composition, causes the fractionation of ^{231}Pa and ^{230}Th, and causes the enhanced scavenging in the high production and ocean margins, further work needs to be done to fully understand the role of individual particulate phases. Until then, it is impossible to predict a fundamental principle from which to derive how the extent of scavenging of ^{231}Pa and ^{230}Th will be affected by a particular element or composition. At least, however, we do demonstrate that the total

mass flux certainly affects the scavenging rates of ^{231}Pa and ^{230}Th, but to a much weaker extent for ^{230}Th, and that the mass flux strongly controls the fractionation between ^{231}Pa and ^{230}Th.

3.6.5 Implications for the ^{230}Th-normalized flux method

3.6.5-a The method and its assumptions

As mentioned previously, the production of ^{230}Th in the water column occurs at an exactly known rate and its residence time is very short. This allows us to make two assumptions: negligible amounts of ^{230}Th decay before sedimentation, and all of the ^{230}Th produced in a basin is sedimented out in that basin, not advected away to be preferentially scavenged at boundaries or ocean margins. The latter is proved in a basin wide data set in the Atlantic Ocean sediments (Chapter 4 in this thesis). There is, moreover, a large fraction of total ^{230}Th that is scavenged *in situ* from the overlying water column, and only contains a small fraction of detrital ^{230}Th, which can be corrected by simply subtracting the concentration of U. As a consequence, excess ^{230}Th activity in settling particulates is related inversely to total mass flux, and excess ^{230}Th can be used as a reference against which the flux of other sedimentary components can be estimated:

$$^{230}Th_{ex}{}^{o}=\beta.z/F. \qquad (3\text{-}9)$$

To be able to apply this method, the concentration of U and the sediment chronology are required for correction of detrital ^{230}Th and for decay correction. In an independently dated sediment (using ^{18}O or ^{14}C chronologies), decay-corrected ^{230}Th activity profiles can be used then to

provide high resolution, point-by-point estimates of past rain rates (Bacon, 1984) by rearranging (3-9), i.e.,

$$F=\beta.z/^{230}Th_{ex}{}^{o}. \qquad (3\text{-}10)$$

From (3-10), the ^{230}Th-normalized flux of any sedimentary component can be obtained after multiplying F by the weight fraction of the sediment constituent of interest (f_i), ie.,

$$F_i=f_i\beta.z/^{230}Th_{ex}{}^{o} \qquad (3\text{-}11)$$

F_i can be interpreted as a record of the pelagic rain rate of the sedimentary constituent i. β is the production rate from the uranium decay in the water column, i.e. 0.00263 dpm/cm^3/ka.

3.6.5-b Advantages and problems

Since the accumulation of ^{230}Th in the sediments is dependent only on the depth of the overlying water column (P(^{230}Th) =0.0026*Z), this simple relationship enables one to evaluate the rate at which other species are removed from the water column and to distinguish pelagic rain rates from sediment accumulation rates. The latter is controlled by bottom current activity as well as by the primary pelagic settling flux reaching the seafloor. In other words, the procedure tends to correct for post-deposition sediment redistribution and focusing. This is the major advantage of the ^{230}Th-normalized flux method. The redistribution of the sediments after deposition will affect the flux of ^{230}Th in a particular sediment core. If a bottom current focuses sediments eroded from a large area to a single site, the

measured surface inventory of ^{230}Th will be larger than the water column source. Suman and Bacon (1989) argued that even in drift deposits, where sediment accumulation is dominated by bottom current transport, the ^{230}Th-normalized flux still retains information on regional pelagic fluxes. Downslope transport may, however, present a greater problem, because it carries sediment initially deposited at significantly shallower depths. This problem can be significant at a site under a rise. Even in the unrealistic "worse case" in which all the material originated from the top of the rise, it was argued that the normalized fluxes would overestimate the true pelagic fluxes by only ~10%, and even less if more sediment came from the lower part of the rise (Francois *et al.*, 1990). Following the reasonably similar model calculation as that for downslope transportation, lateral transport would bring the material which characteristized high concentration of ^{230}Th, then the normalized fluxes would underestimate the true pelagic rate (Francois *et al.*, 1990). These two processes as discussed above would have less of an affect on the $(^{231}Pa/^{230}Th)_{ex}$ ratio, since both ^{231}Pa and ^{230}Th are produced under the same proportion of $\beta.z$.

Sediment focusing is a common redistribution process on the seafloor. If sediment drifts consist of redeposited material eroded from other sites, the records would be mixtures of materials of all ages; therefore, sediment focusing could lead to misinterpretation of the removal of the nuclides and their adsorbers in the overlying water column. If the focusing material is fresh, the material may have little effect on the normalized fluxes (and the $(^{231}Pa/^{230}Th)_{ex}$ ratio) if the foreign material has a similar constitution as the sediment in the host site. Another type of sediment redistribution process is the result of transport of aged, eroded sediment to a site. On one hand, this

might overestimate the normalized fluxes because the aged material with lower activity of ^{230}Th would dilute the activity of ^{230}Th at the host site; on the other hand, the ($^{231}Pa/^{230}Th$) ratio would be lower.

The ^{230}Th-normalized flux method will be subject to some uncertainties under three possible violations of the assumptions:non-linear adsorption of ^{230}Th with depth; significant horizontal transport away from open ocean or preferential scavenging of ^{230}Th at ocean margins; and enhanced scavenging of ^{230}Th on to particles in the nepheloid layer after resuspension and before redeposition. Using the sediment trap data as calculated above for F, V, and H to production P for ^{230}Th, the first two conditions are proved not to be significant violations of the assumptions.

In the model, sediment redistribution is traced using $^{230}Th_{ex}{}^{o}$ for a bulk phase; however, differentiation between individual components is not considered. Possible biases include fractionation by sediment component type (carbonate vs. non-carbonate) and fractionation by size class. The trace metal or components calculations made by the ^{230}Th-normalized flux method as applied to flux estimation could be invalidated if any of the following is true to a large extent: a flux of dissolved metal or a sedimentary component exists across the sediment interface involved with authigenic mineral formation; or the ^{230}Th or specific trace metals or sedimentary component are remobilized after deposition. If the "quality" of particles changes spatially, $^{230}Th_{ex}{}^{o}$ accumulation rates could become non-linear with depth and dependent on location and time. The fraction of ^{230}Th transported to the sediments on organic matter or $CaCO_3$, which subsequently dissolves, can either adsorb on to other sediment particles or can migrate through the pore waters back into seawater. ^{230}Th released from the sediments after carbonate dissolution

causes the model to overestimate the non-carbonate flux while redeposition of ^{230}Th results in the model underestimating the absolute carbonate flux. The ^{230}Th-normalized flux method will only provide information of a net rain rate after dissolution; thus, for sediments that contain variable carbonate concentrations, or sediment cores below lysocline, the records of the normalized flux of carbonate can not be interpreted simply in terms of production. A higher $^{231}Pa_{ex}/^{230}Th_{ex}$ ratio may add confirmation of higher rain rates (and thus higher efficiency for the scavenging of particle-reactive metals) from the overlying water column even though the biogenic adsorbers are subject to dissolution.

The second possibility is that ^{230}Th should be preferentially adsorbed to smaller particles because of their larger surface to volume ratio. In such case, winnowing of fine particles would change ^{230}Th activity of the site for resuspension and deposition independent of the rain rate of particles at these sites. Does winnowing create district redeposition regions, those with more large particles depleted in ^{230}Th and those with predominately smaller particles enriched in ^{230}Th? Recently, Thomson *et al.*, (1993), compared the activities of $^{230}Th_{ex}$ and the weight percentages of different size classes in the surface mixed layers of core tops. Size fractions (four size classes: >400, 400-20, 20-5, and <5 μm) of the surface mixed layer material showed that the two cores experienced similar fluxes of the material in the 400- to 20-μm size range, but the more rapidly accumulated core had a much larger fine (<5 μm) component. The specific activities of the four different size fractions of the two cores are identical, so that the greater mass and ^{230}Th fluxes to the more rapidly accumulating core are predominately due to its greater <5 μm flux.

Size fraction might fractionate the ^{231}Pa, and it might fractionate differently for ^{231}Pa than for ^{230}Th. Further work need to be done.

3.7 CONCLUSIONS AND FUTURE STUDIES

The investigations of sediment traps, including 26 traps which had been deployed for approximately one year or longer and providing diverse geographic coverage, provided information about the variations of radionuclides ^{230}Th and ^{231}Pa in the particulate materials, and the fractionation between ^{230}Th and ^{231}Pa.

By applying the available measured data of $(^{231}Pa/^{230}Th)_{ex}$ in the water columns to all of those trap stations and using the measured data from the collected materials from the sediment traps, I have provided quantitative estimates of trapping efficiency for all deployed sediment traps used for this study. The results demonstrated that all of the deeper traps are reliable for the particle flux; while all of the shallow traps showed undertrapping. The sediment traps used for this study showed a tendency of increasing in trapping efficiency with water depth for almost all of stations.

The results of the investigations of the sediment trap materials shows two major facts:1) particle flux is the major factor influence removal of the nuclides ^{230}Th and ^{231}Pa from seawater; 2) the scavenging rate of ^{230}Th apparently fluctuate less in relation to the flux of particulate materials; whereas ^{231}Pa is very sensitive in relation to the flux of particulate materials. These results demonstrated two important concepts: 1) the assumption of a constant flux of ^{230}Th holds as a good approximation for the ^{230}Th-

normalized flux methods; 2) particulate $(^{231}Pa/^{230}Th)_{ex}$ ratio is strongly dependent on the mass flux. Thus the two concepts can be used together for reconstruction of paleo-particle flux in the past ocean, and applied for paleoceanographic studies.

The particle components could influence the fractionation between ^{230}Th and ^{231}Pa; however, all field and laboratory studies do not reach a universal conclusion. Biogenic opal was hypothesized as an important factor causing the preferential scavenging of ^{231}Pa over ^{230}Th in ocean margins and high production regions; however, the trap results in this study do not support the scenario. Further studies either through field data or laboratory experiments in determinations of the fractionation factor are needed to confirm. Different fractionation between ^{231}Pa and ^{230}Th results from different size fraction should also be examined in future study.

CHAPTER 4

BASIN-WIDE VARIATIONS IN CHEMICAL SCAVENGING OF ^{231}PA AND ^{230}TH WITHIN THE ATLANTIC OCEAN SINCE THE LAST GLACIAL MAXIMUM

4.1 INTRODUCTION

Yang *et al.* (1986) published a map of the Pacific Ocean in which contours of the unsupported ^{230}Th/^{231}Pa ratios of surface sediment suggested that all margins are important boundary sinks for ^{231}Pa. However, many of the ^{231}Pa values used to construct their map were assumed or inferred, from ^{231}Pa contents of sediments in other regions. Additional information about which margins actually act as important boundary sinks was provided by Anderson *et al.* (1991) and Lao (1991) who recently published their ^{231}Pa/^{230}Th data from ocean margin sediments collected off North and South America, from the Bering Sea, and from the northwest Pacific. Their data eliminates some of the uncertainty in the Pacific map by Yang *et al.* (1986). The combined data sets illustrate which margins are important boundary sinks for ^{231}Pa and ^{230}Th in the Pacific Ocean.

A similar map has not been constructed for the Atlantic Ocean. For this chapter, I measured ^{231}Pa and ^{230}Th in a number of well-dated deep-sea sediment cores collected from the Atlantic Ocean. I also compiled all available data in the literature from Atlantic cores with reasonably well-defined

stratigraphy and combined it with my data to construct a map similar to the one available for the Pacific. The purpose, first of all, is to examine questions for the Holocene Atlantic Ocean similar to those asked about the Pacific Ocean data (Anderson *et al.*, 1983a and b, 1990, 1991; Yang *et al.*, 1986; Shimmield and Price, 1988, 1989; Lao, 1991): Where does the boundary scavenging of ^{231}Pa or ^{230}Th occur in the Atlantic Ocean? What factors control the distribution patterns of chemical fractionation between ^{230}Th and ^{231}Pa in the Atlantic Ocean? From the distribution of boundary scavenging of Pa and Th, we may gain insights on the distribution or flux of other reactive elements or trace metals .

The second purpose is to compare the distribution patterns of $(^{231}Pa/^{230}Th)_{ex^0}$ ratio between the Atlantic and Pacific. It is interesting to make such a comparison, because the ocean processes are considered to be dynamically different between the two oceans. As I will show later by a simple mass balance model, the advection by ocean circulation, which in previous studies is usually assumed to have a negligible effect, is an important factor to cause the fractionation between ^{231}Pa and ^{230}Th in the Atlantic Ocean. I also quantify the influence by advection resulting from the thermohaline circulation on the fractionation of the two nuclides. Furthermore, I provide a simple box model to demonstrate that export flux from the Atlantic by ocean advection is an important role to account for the budget of ^{231}Pa in deep sea sediments located beneath the Southern Ocean.

I have also constructed a $^{231}Pa/^{230}Th$ map for the Last Glacial Maximum (LGM) in the Atlantic Ocean to examine the differences between the LGM and the Holocene. By comparing these two maps, I hope to answer the following questions: Has the intensity of scavenging changed significantly with time, particularly between extreme conditions represented by the LGM and the

Holocene? What changes in ocean conditions and processes can respond to changes in the redistribution patterns of $^{231}Pa/^{230}Th$ between these extremes? What is the effect of the climatically controlled variations in the sedimentation?

Furthermore, variations in sedimentation rate have been known for a long time to be related to climate changes. For instance, the biogenic components of deep-sea sediments can record changes in production and oceanic circulation related to climate changes; the terrigenous input might record changes in sea-level, humidity and aridity, and intensity and direction of winds. These are two major components in the Atlantic pelagic sediments; thus, we need to examine what the distribution patterns of the sedimentary components in the Atlantic Ocean are, and how their changes in flux relate to variations in climate.

4.2 METHODS

All sorts of lateral transport processes may influence the removal of ^{231}Pa and cause the fractionation between it and ^{230}Th within an ocean basin; therefore, a large number of cores would be required to obtain complete representation of different scavenging conditions in the whole Atlantic Ocean. Given the limitations of stratigraphic databases, time and funding, however, a modest number of cores were selected and previously reported data with good quality of their stratigraphic data were compiled together for Holocene and LGM distribution maps of unsupported $^{231}Pa/^{230}Th$ activity ratio in the Atlantic Ocean. The data discussed in this chapter should be considered to serve for an initial investigation into the scavenging characteristics of ^{230}Th and ^{231}Pa in the Atlantic Ocean. These cores were selected because of their quality and available data on stratigraphy.

For my experiments, I selected twenty-eight deep sea cores from the Atlantic Ocean for analysis of uranium-series nuclides in order to accomplish the goals as proposed above. The core locations are given in Figure 4.1 and listed in Table 4.1. The cores that I selected are a subset of those used for mapping Cd/Ca and isotope $\delta^{13}C$ by Boyle (1992), who lists the original sources of the stratigraphic information. Since the differences between LGM and the Holocene are specifically my interests in this study, I sampled only the two sections of the sediments corresponding to these two time intervals for the uranium-series radionuclide analyses. I also determined carbonate content in these two sections.

4.3 RESULTS

In order to examine the chemical scavenging of ^{231}Pa and ^{230}Th, which is a reflection of the flux of particulate materials in the ocean, I used many well-dated deep-sea cores distributed over the Atlantic Ocean basin. The analytical results of ^{231}Pa, Th and U isotopes for the Holocene and LGM sections are shown in Tables 4.2 and 4.3. The unsupported initial (decay-corrected) concentrations of ^{231}Pa and ^{230}Th (Table 4.4) were calculated as follows.

$$^{230}Th_{ex}{}^{o} = \{^{230}Th_m - 1.14^* (0.8\pm0.2)\ ^{232}Th_m - [1.14^* (^{238}U_m - (0.8\pm0.2)^{232}Th_m (1- e^{-\lambda_{230}t})]\} * e^{\lambda_{230}t} \quad (4\text{-}1)$$

$$^{231}Pa_{ex}{}^{o} = \{^{231}Pa_m - 0.046^* (0.8\pm0.2)\ ^{232}Th_m - 0.046^* [(^{238}U_m - (0.8\pm0.2)^{232}Th_m (1- e^{-\lambda_{231}t})]\} e^{\lambda_{231}t} \quad (4\text{-}2)$$

The equations above, which estimate the quantities of ^{230}Th and ^{231}Pa scavenged from seawater (denoted as $^{230}Th_{ex}$ and $^{231}Pa_{ex}$), were drived by subtracting the supported components from the decay of the detrital uranium

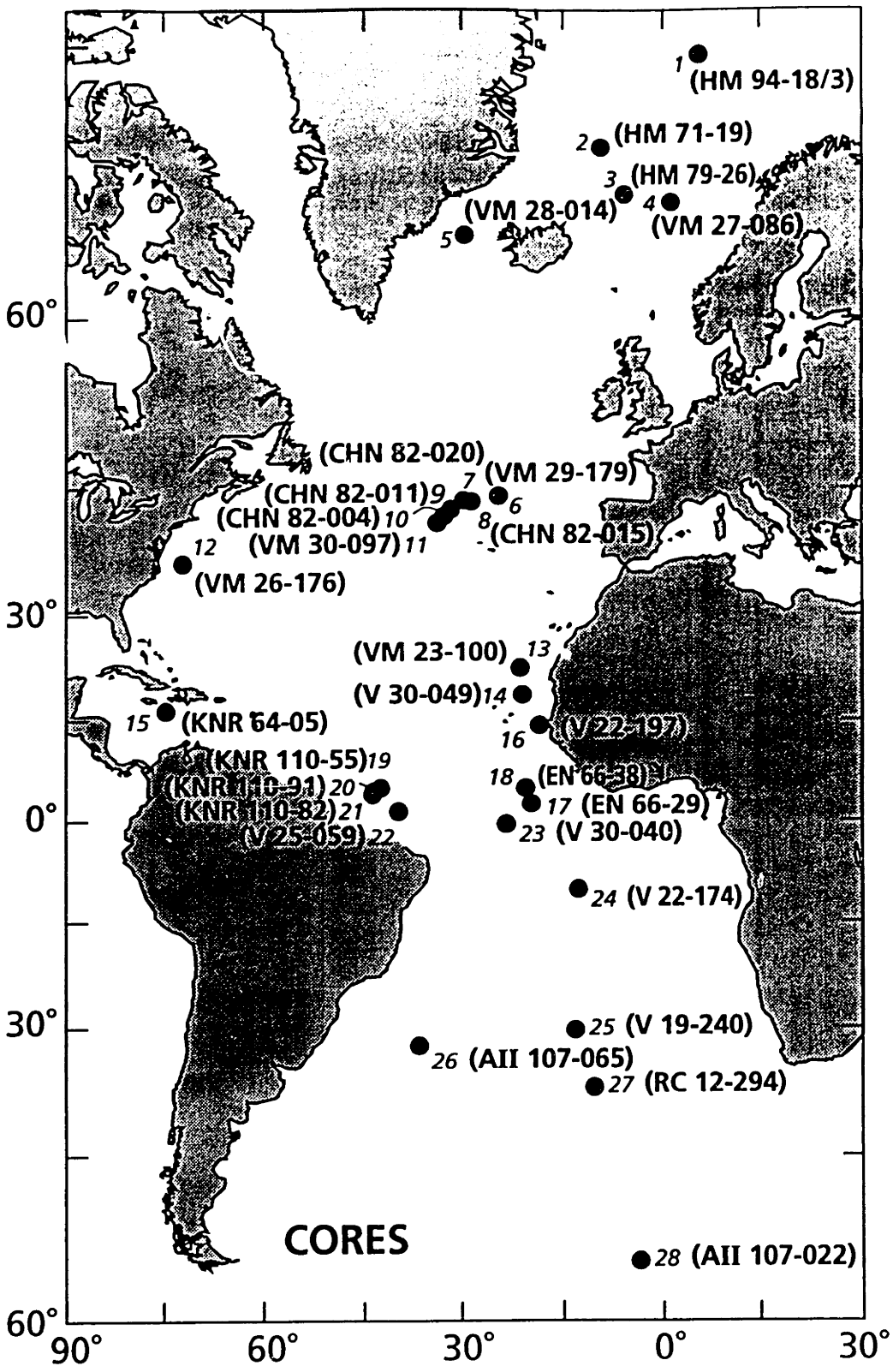

Figure 4.1 The map of selected cores from the Atlantic Ocean. See Table 4.1 for details.

Table 4.1 Locations of selected sediment cores in the Atlantic Ocean

Core	Latitude	Longitude	Water Depth(m)	Depth of LGM(cm)	Depth of Holocene (cm)	Core No. on Map
	High Latitude Northern Atlantic					
HM 94-18/3	73.30N	05.41E	2469	35.5	0	1
HM 71-19	69.29N	09.31W	2210	50	0	2
HM 79-26	66.54N	05.56W	3312	70	0	3
VM 27-086	66.36N	01.07E	2900	60	9	4
VM 28-014	64.47N	29.34W	1855	190	13	5
	The Northern Atlantic (20 - 60N)					
VM 29-179	44.00N	24.32W	3371	80	16	6
CHN 82-020	43.30N	29.52W	3070	62 ~ 69.5	4 ~ 6	7
CHN 82-015	43.22N	28.14W	2153	29-37	3 ~ 4	8
CHN 82-011	42.23N	31.48W	3209	69.5 - 71.5	3.5 - 5	9
CHN 82-004	41.43N	32.51W	3427	56-71	2 ~ 4	10
VM 30-097	41.00N	33.56W	3371	130-169	5 ~ 16	11
VM 26-176	36.00N	72.00W	3942	358	8 ~ 10	12
VM 23-100	22.41N	21.18W	4579	35-60	10 ~ 20	13
	Equatorial Atlantic (20N - 20S)					
VM 30-049	18.26N	21.05W	3093	62-84	10 ~ 15	14
KNR 64-051	16.31N	74.48W	3047	38-42	6 ~ 7.5	15
VM 22-197	14.10N	18.35W	3167	133	25	16
EN 66-29	02.28'N	19.46W	5104	34 ~ 47	2 ~ 12	17
EN 66-38	04.55N	20.30W	2931	24.5 ~ 34.5	2.5 ~ 9.5	18
KNR110-55	04.57N	42.54W	4556	51 ~ 58.5	4 ~ 17	19
KNR110-91	04.46N	43.18W	3810	72	0	20
KNR110-82	04.20N	43.29W	2816	53 ~ 64	0 ~ 13	21
VM 25-059	01.22N	39.29W	3824	60	8	22
VM 30-040	00.12S	23.08W	3706	45	10	23
VM 22-174	10.04S	12.49W	2630	49	8	24
	The Southern Atlantic (20S - 60S)					
VM 19-240	30.35S	13.17W	3103	80	20	25
AII 107-065	32.02S	36.11W	2795	33-45	3 ~ 4	26
RC 12-294	37.16S	10.06W	3308	45	10	27
AII 107-022	54.48S	3.20W	2768	66-70	3 ~ 4	28

Table 4.2: Analytical results of radionuclides for the Holocene Atlantic sediments

Cores of HL	Sample depth	230Th		232Th		231Pa		238U		235U		234U	
	(cm)	dpm/g	std.dev.	dpm/g	std.dev.	dpm/g	std.dev.	dpm/g	std.dev.	dpm/g	std.dev.	dpm/g	std.dev.
HM 94-18/3	0	7.98	0.28	1.66	0.05	0.36	0.02	1.09	0.01	0.047	0.002	1.24	0.03
HM 71-19	0	4.32	0.15	0.90	0.03	0.31	0.02	0.65	0.02	0.028	0.001	0.77	0.01
HM 79-26	0	5.97	0.05	0.93	0.03	0.41	0.02	0.60	0.02	0.028	0.001	0.72	0.01
VM 27-086	9	4.10	0.06	0.58	0.02	0.34	0.02	0.44	0.01	0.0212	0.0004	0.59	0.03
VM 28-014	13	3.69	0.08	0.40	0.02	0.38	0.01	0.30	0.01	0.0143	0.0003	0.38	0.04
VM 29-179	16	5.49	0.12	0.28	0.00	0.24	0.01	0.18	0.01	0.0092	0.0004	0.27	0.01
CHN 82-020	4~6	6.48	0.29	0.35	0.02	0.33	0.01	0.30	0.01	0.011	0.001	0.34	0.01
CHN 82-015	3~4	3.28	0.23	0.35	0.01	0.22	0.01	0.28	0.03	0.013	0.001	0.31	0.01
CHN 82-011	3.5~5	5.92	0.14	0.45	0.01	0.31	0.02	0.29	0.01	0.013	0.001	0.31	0.02
CHN 82-004	2~4	6.42	0.10	0.57	0.02	0.41	0.03	0.27	0.02	0.012	0.001	0.31	0.03
VM 30-097	5~16	1.86	0.05	1.16	0.02	0.37	0.01	0.60	0.01	0.0272	0.0003	0.71	0.06
VM 26-176	8~10	5.22	0.08	2.05	0.01	0.31	0.02	1.54	0.04	0.071	0.001	1.97	0.05
VM 23-100	10	8.83	0.23	0.83	0.01	0.32	0.01	0.53	0.01	0.026	0.005	0.77	0.01
V 30-049	10~15	5.73	0.13	0.75	0.01	0.45	0.01	0.58	0.01	0.025	0.001	0.71	0.05
KNR 64-05	6~7.5	3.77	0.08	0.60	0.03	0.20	0.01	0.45	0.02	0.020	0.001	0.46	0.02
V 22-197	25	8.07	0.11	1.57	0.02	0.42	0.02	1.59	0.02	0.071	0.001	2.18	0.04
EN 66-29	2~12	12.79	0.30	1.05	0.06	0.60	0.03	0.46	0.03	0.021	0.001	0.50	0.03
EN 66-38	2.5~9.5	6.98	0.26	0.62	0.03	0.35	0.02	0.49	0.02	0.0204	0.0003	0.45	0.02
KNR110-55	4~17	10.17	0.39	1.80	0.01	0.52	0.03	0.84	0.02	0.038	0.001	0.91	0.06
KNR110-91	0	8.89	0.17	3.21	0.04	0.27	0.02	0.67	0.05	0.0313	0.0004	0.82	0.06
KNR110-82	0~13	6.56	0.19	0.81	0.06	0.30	0.02	0.68	0.03	0.031	0.001	0.72	0.04
V 25-059	8	7.09	0.19	0.59	0.01	0.30	0.01	0.31	0.01	0.0144	0.0001	0.43	0.01
V 30-040	15	7.47	0.08	0.31	0.01	0.30	0.01	0.16	0.01	0.0081	0.0003	0.25	0.03
V 22-174	8	9.12	0.11	0.17	0.00	0.46	0.01	0.23	0.01	0.0096	0.0002	0.29	0.01
V 19-240	20	6.27	0.06	0.38	0.00	0.25	0.01	0.28	0.01	0.0121	0.0002	0.35	0.01
AII 107-065	3~4	8.45	0.13	0.39	0.02	0.41	0.03	0.43	0.02	0.020	0.001	0.43	0.02
RC 12-294	10	8.15	0.12	0.38	0.00	0.36	0.02	0.31	0.01	0.0128	0.0003	0.33	0.01
AII 107-022	3~4	6.00	0.07	0.18	0.01	1.37	0.08	0.40	0.02	0.019	0.001	0.49	0.03

Table 4.3: Analytical results of radionuclides for the LGM Atlantic sediments

LGM Cores	Sample depth	230Th		232Th		231Pa		238U		235U		234U	
	(cm)	dpm/g	std.dev.	dpm/g	std.dev.	dpm/g	std.dev.	dpm/g	std.dev.	dpm/g	std.dev.	dpm/g	std.dev.
HM 94-18/3	35.5	4.47	0.16	2.68	0.88	0.17	0.01	1.59	0.02	0.072	0.002	1.82	0.03
HM 71-19	50	3.23	0.11	2.54	0.09	0.16	0.01	1.52	0.01	0.074	0.002	1.88	0.03
HM 79-26	70	4.22	0.07	2.48	0.06	0.20	0.01	1.46	0.03	0.067	0.002	1.75	0.03
VM 27-086	60	2.82	0.05	2.88	0.07	0.14	0.01	1.72	0.03	0.080	0.001	1.92	0.07
VM 28-014	190	2.17	0.03	1.43	0.03			0.91	0.01	0.040	0.001	1.05	0.05
VM 29-179	80~89	17.00	0.56	1.42	0.02	0.22	0.01	0.30	0.01	0.014	0.001	0.36	0.04
CHN 82-020	62~69.5	2.14	0.10	2.29	0.07	0.089	0.004	1.13	0.03	0.052	0.002	1.18	0.06
CHN 82-015	29~31	1.72	0.05	1.18	0.01	0.12	0.01	0.63	0.02	0.0280	0.0004	0.63	0.01
CHN 82-011	69.5~71.5	4.40	0.16	1.33	0.03	0.17	0.01	0.67	0.01	0.032	0.001	0.70	0.03
CHN 82-004	60~62	3.43	0.18	1.38	0.08	0.13	0.01	0.63	0.03	0.027	0.001	0.60	0.04
VM 30-097	133~159	6.29	0.22	1.18	0.02	0.27	0.01	3.30	0.03	0.149	0.009	4.58	0.23
VM 26-176	358	2.39	0.06	2.84	0.01	0.104	0.004	1.94	0.03	0.087	0.001	2.34	0.05
VM 14-001													
VM 23-100	50	6.47	0.12	0.90	0.02	0.20	0.01	0.64	0.02	0.029	0.007	0.83	0.03
V 30-049	63~80	4.79	0.16	1.13	0.02	0.24	0.01	1.05	0.01	0.049	0.002	1.47	0.02
KNR 64-05	37.5~39.5	3.52	0.10	0.87	0.05	1.04	0.03	0.68	0.03	0.031	0.001	0.70	0.04
V 22-197	133	5.18	0.07	2.21	0.06	0.43	0.02	4.44	0.08	0.206	0.006	6.14	0.21
EN 66-29	34~47	17.11	0.79	2.19	0.08	0.71	0.03	1.07	0.04	0.049	0.001	1.11	0.07
EN 66-38	24.5~34	5.79	0.20	1.61	0.09	0.64	0.05	0.91	0.03	0.042	0.001	0.97	0.03
KNR110-55	51~58.5	7.62	0.27	2.95	0.01	0.05	0.04	1.47	0.02	0.064	0.002	1.38	0.03
KNR110-91	49~50	6.31	0.22	2.26	0.07	0.29	0.02	0.70	0.09	0.032	0.001	1.55	0.06
KNR110-82	53~64	4.75	0.27	2.36	0.06	0.31	0.02	1.52	0.04	0.057	0.001	1.32	0.05
V 25-059	60	5.73	0.11	1.36	0.02	0.36	0.02	0.62	0.01	0.0282	0.0004	0.81	0.01
V 30-040	50	5.79	0.14	0.98	0.01	0.32	0.02	0.47	0.01	0.0210	0.0004	0.58	0.03
V 22-174	49	8.60	0.07	0.307	0.002	0.27	0.01	0.206	0.004	0.0087	0.0004	0.31	0.01
V 19-240	80	5.51	0.10	0.56	0.01	0.22	0.01	0.76	0.01	0.034	0.001	1.01	0.03
AII 107-065	35.5~37.5	7.82	0.41	1.42	0.11	0.22	0.01	0.57	0.02	0.026	0.001	0.62	0.02
RC 12-294	45	5.93	0.17	0.63	0.01	0.21	0.01	0.323	0.004	0.0137	0.0003	0.38	0.01
AII 107-022	66~69	8.76	0.32	1.05	0.08	0.82	0.07	0.57	0.03	0.025	0.001	0.57	0.08

Table 4.4: Unsupported intial radionuclide activities for the Holocene Atlantic sediments

Cores	230Thexo dpm/g	231Paexo dpm/g	Pa/Thexo dpm/g	detrial 238U dpm/g	Authigenic 238U dpm/g	234U/238U	238U/232Th	230Thexo/232Th
HM 94-18/3	6.89	0.31	0.045	1.33	-0.24	1.14	0.66	4.15
HM 71-19	3.67	0.28	0.077	0.72	-0.07	1.18	0.72	4.08
HM 79-26	5.37	0.38	0.071	0.74	-0.14	1.20	0.65	5.77
VM 27-086	3.66	0.32	0.087	0.46	-0.02	1.34	0.76	6.31
VM 28-014	3.39	0.37	0.108	0.32	-0.02	1.27	0.75	8.48
VM 29-179	5.31	0.23	0.044	0.22	-0.04	1.50	0.64	18.96
CHN 82-020	6.18	0.32	0.052	0.28	0.02	1.13	0.86	17.66
CHN 82-015	3.00	0.21	0.069	0.28	0.00	1.11	0.80	8.57
CHN 82-011	5.63	0.30	0.053	0.36	-0.07	1.07	0.64	12.51
CHN 82-004	6.15	0.40	0.065	0.46	-0.19	1.15	0.47	10.79
VM 30-097	1.26	0.34	0.272	0.93	-0.33	1.18	0.52	1.09
VM 26-176	3.68	0.24	0.066	1.64	-0.10	1.28	0.75	1.79
VM 23-100	8.30	0.29	0.035	0.66	-0.14	1.46	0.63	9.99
VM 30-049	5.15	0.42	0.082	0.60	-0.02	1.22	0.77	6.85
KNR 64-05	3.32	0.18	0.054	0.48	-0.04	1.04	0.74	5.50
VM 22-197	6.82	0.35	0.051	1.26	0.33	1.37	1.01	4.34
EN 66-29	12.33	0.58	0.047	0.84	-0.38	1.09	0.44	11.75
EN 66-38	6.49	0.33	0.051	0.50	0.00	0.91	0.79	10.43
KNR110-55	9.33	0.49	0.052	1.44	-0.60	1.08	0.47	5.19
KNR110-91	8.22	0.24	0.029	2.57	-1.90	1.23	0.21	2.56
KNR110-82	5.88	0.27	0.046	0.65	0.03	1.06	0.84	7.28
VM 25-059	6.78	0.28	0.042	0.47	-0.16	1.39	0.53	11.49
VM 30-040	7.31	0.30	0.040	0.25	-0.08	1.56	0.53	23.80
VM22-174	8.98	0.45	0.050	0.14	0.10	1.24	1.37	52.51
VM19-240	5.98	0.24	0.040	0.30	-0.02	1.24	0.74	15.71
AII 107-065	8.14	0.39	0.048	0.31	0.12	1.00	1.11	20.87
RC 12-294	7.85	0.35	0.045	0.31	0.00	1.07	0.80	20.48
AII 107-022	5.85	1.35	0.231	0.15	0.26	1.22	2.22	32.14

and from the ingrowth of the authigenic uranium. The activities of the scavenged ^{230}Th and ^{231}Pa components then were corrected for their decay loss. The constant 0.8± 0.2 is the value of the $^{238}U/^{232}Th$ ratio of the average crust (Anderson, 1982; Anderson *et al.*, 1990), i.e., the $^{238}U/^{232}Th$ ratio of the sediment detrital phase. The constant 1.14 is the seawater isotopic composition of $^{234}U/^{238}U$, and 0.046 is the natural abundance of $^{235}U/^{238}U$ in activity units. The decay constants of ^{230}Th and ^{231}Pa are λ_{230} and λ_{231}. The ages (t) of the sediment samples used for decay-correction of ^{230}Th and ^{231}Pa were based on the chronologies of the cores given in Table 4.1 for the transect samples. The ages of the core-top sediments were assumed zero age, and the LGM samples were assigned an age of 18 ka.

Since the variations in Pa/Th ratio between the Holocene and the LGM are specific interests for this study, one section within each of these two time intervals of the cores was carefully sampled for analyses of radioisotopes and sediment components. The stratigraphic framework is essential to this work, and has been on careful handling in the samples' selections. As mentioned, the stratigraphic data were provided in Boyle (1992). However, as Boyle (1992) pointed out "because many cores have been heavily sampled, it is not always possible to make paleochemical analyses at the glacial maximum because of the lack of core sample. For this reason, one should not over-interpret fine points of this data set; only large-scale signals confirmed by nearby samples and sites should be considered seriously." To resolve this complication for fine scale discussion, a subcore within each core should be drilled (Broecker, personal communication); however, this is not plactically possible to request sample materials.

For convenience, hereafter, "Pa/Th" will be used throughout the text to designate the ratio $(^{231}Pa/^{230}Th)_{ex^0}$ except when further differentiation is necessary. This decay-corrected ratio is truly representative of the scavenging fractionation between ^{230}Th and ^{231}Pa at the time they deposit onto the seafloor.

The Holocene Pa/Th ratios of the cores from the whole Atlantic Ocean are shown in a map (Figure 4.2). The data includes measurements from this thesis work (Table 4.4) and those available in the literature (Table 4.5). The cores cover geographic regions from the open ocean abyssal sediments to the Mid-Atlantic Ridge (MAR) sediments, to the flanks of the MAR sediments, to the high latitudes in both the northern and southern Atlantic oceans, and to ocean margins with different characteristics (strictly speaking, the margins referred to here and previously in the literature mean the areas of the edges of the ocean basins). The data from 63 cores are included in the Holocene Atlantic map.

4.4 DISCUSSION

4.4.1. Chemical fractionation between ^{231}Pa and ^{230}Th in the Holocene Atlantic sediments

In this section, first, I show the distribution patterns of ^{231}Pa relative to ^{230}Th (presented by the Pa/Th ratio) for the Holocene Atlantic sediments; second, I discuss the "boundary scavenging" within the Atlantic basin; then, I discuss those anomalous features in terms of deposition conditions. This study emphasizes the process of locating the regions of enrichment or depletion of ^{231}Pa relative to the uniform scavenging efficiency of ^{230}Th on a basin-wide scale. The geographic distribution of this enrichment or depletion reflects the

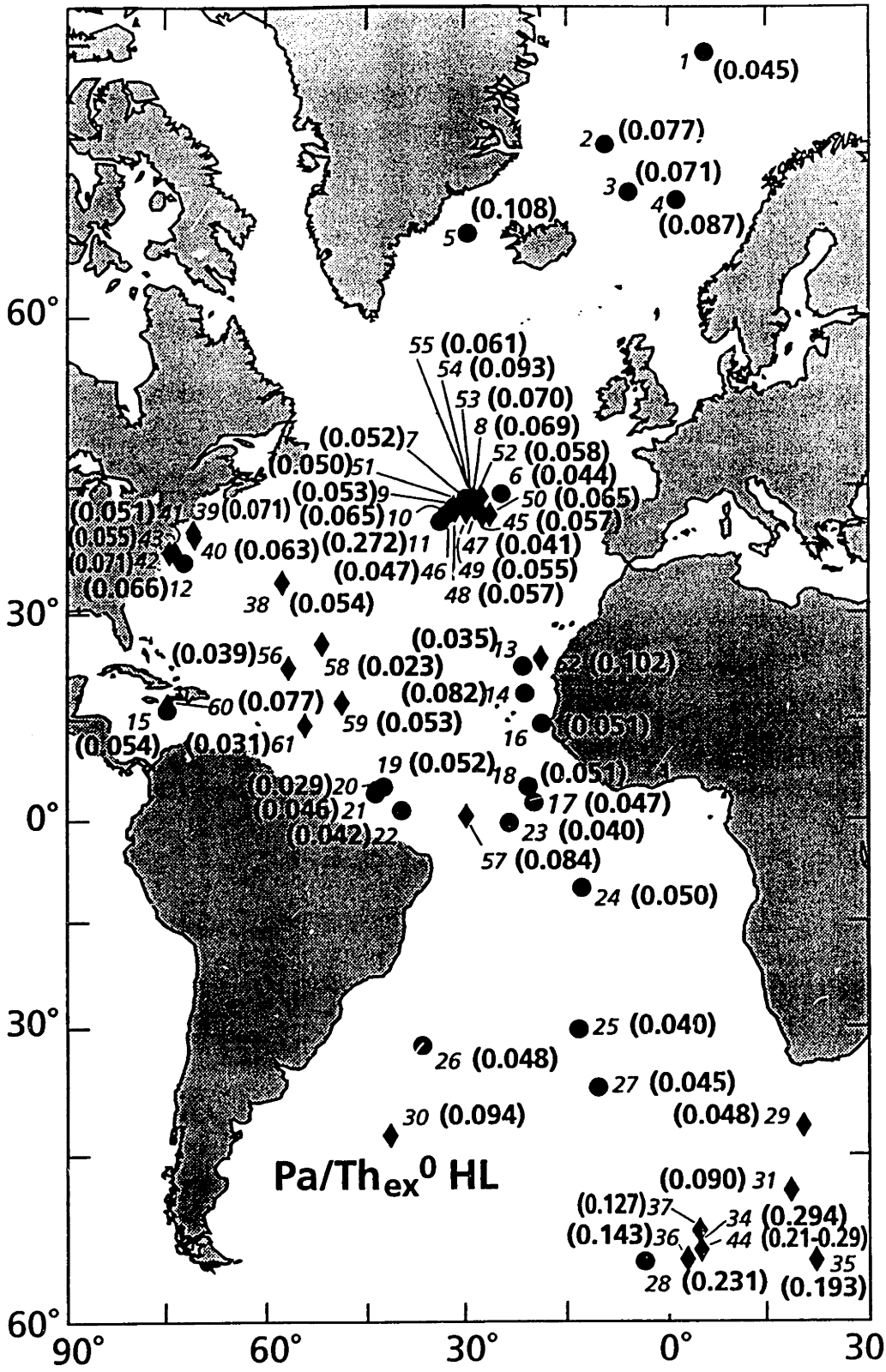

Figure 4.2 The map of decay-corrected unsupported $^{231}Pa/^{230}Th$ ratio (Pa/Th_{ex}^{0}) of the Holocene Atlantic Ocean.

Table 4.5 Compiled data of 231Pa/230Th ratios of Holocene Atlantic sediments

Core	Latitude	Longitude	Pa/Th Holocene	Pa/Th LGM	# on the map	data sources	Notes HL sample
AII 76-3	41o33'S	20o12'E	0.048		#29	DeMaster, 1979	0-1 cm
RC 15-101	42o59'S	41o34'W	0.094		#30	DeMaster, 1979	4-7 cm
VM 29-105	48o05'S	18o41'E	0.090	0.084	#31	DeMaster, 1979	3-6 cm
AII 76-16	53o00'S	35o38E	0.123		#32	DeMaster, 1979	0-1 cm
RC 17-58	53o31'S	36o38'E	0.111		#33	DeMaster, 1979	7-9 cm
RC 13-259	53o33'S	04o56'E	0.294		#34	DeMaster, 1979	5-8 cm
RC 11-76	54o23'S	22o08'W	0.193	0.169	#35	DeMaster, 1979	10-13 cm
RC 13-255	54o35'S	02o54'E	0.143	0.294	#36	DeMaster, 1979	4-7 cm
RC 13-271	59o39'S	04o31'E	0.127	0.127	#37	DeMaster, 1979	14-16 cm
GPC 5	33o41'N	57o37'W	0.054	0.049	#38	Bacon&Rosholt, 1982	32 cm
OCE 152-BC8	39o46.5'N	70o58'W	0.071		#39	Anderson et al, 1991	0-0.5 cm
OCE 152-BC5	39o08'N	70o56'W	0.063		#40	Anderson et al, 1991	0-0.5 cm
EN 179-BC7	37o25'N	73o49.4'W	0.051		#41	Anderson et al, 1991	0-1 cm
EN 179-BC4	37o32'N	74o02'W	0.071		#42	Anderson et al, 1991	1-2 cm
EN 187-BC6	37o24'N	73o50'W	0.055		#43	Anderson et al, 1991	0-1 cm
RC 13-259	53o33'S	04o56'E	0.21-0.29	0.12-0.13	#44	Kumar et al, 1993	
CHN 82-23	41o38'N	27o20'W	0.057		#45	Ku et al., 1972	0-5 cm
CHN 82-24	41o43'N	32o51'W	0.047		#46	Ku et al., 1972	0-5 cm
CHN 82-25	42o19'N	28o35'W	0.041		#47	Ku et al., 1972	0-6 cm
CHN 82-26	42o10'N	31o38'W	0.057		#48	Ku et al., 1972	0-10 cm
CHN 82-28	42o00'N	29o54'W	0.055		#49	Ku et al., 1972	0-10 cm
CHN 82-30	41o51'N	26o28'W	0.065		#50	Ku et al., 1972	0-10 cm
CHN 82-31	42o23'N	31o48'W	0.050		#51	Ku et al., 1972	0-10 cm
CHN 82-32	43o45'N	27o47'W	0.058		#52	Ku et al., 1972	0-10 cm
CHN 82-33	42o29'N	28o40'W	0.070		#53	Ku et al., 1972	0-10 cm
CHN 82-41	43o22'N	28o14'W	0.093		#54	Ku et al., 1972	0-10 cm
CHN82-42	43o20'N	28o05'W	0.061		#55	Ku et al., 1972	0-10 cm
AII 42-41	22o14'N	56o39'W	0.039		#56	Ku et al., 1972	0-5 cm
V 9-97	00o23'N	29o52'W	0.084		#57	Ku 1966	5-8 cm
V 10-95	26o31'N	51o47'W	0.023		#58	Ku 1966	0-6 cm
V 16-21	17o17'N	48o28'W	0.053		#59	Ku 1966	2-10 cm
V 12-122	17o00'N	74o24'W	0.077		#60	Ku 1966	10-15 cm
CH 75-2-8	14o1'N	54o1'W	0.031		#61	Anderson et al.,1983	2-4 cm
Core 12310	23o30'N	18o43'w	0.102		#62	Mangini & Diester-H	

combined effects of the geographic variations in the extent of particle flux (i.e., scavenging intensity) and the extent of horizontal transport of ^{231}Pa in the Atlantic Ocean during the Holocene.

The Pa/Th activity ratio of production from uranium in the water column is at a fixed value of 0.093 because of the fixed abundance of $^{235}U/^{238}U$ (the progenitors of ^{231}Pa and ^{230}Th, respectively) in the ocean. Sediment values deviating from this value imply differential deposition of the two nuclides from the water column to the seafloor. Since the deposition rate of ^{230}Th in most of the ocean is balanced by its production from the overlying water column, the Pa/Th ratio is used to evaluate the extent of the fractionation between these two elements, thus revealing the regions of the enrichment or depletion of ^{231}Pa relative to ^{230}Th. In sediments, if a Pa/Th ratio is greater than the production rate ratio of 0.093, this implies the site is a "enriched" ^{231}Pa relative to ^{230}Th, i.e., the site receives an extra amount of ^{231}Pa in addition to production from the overlying water column. Conversely, if the ratio is less than 0.093, the site is "depleted", i.e., a certain fraction of ^{231}Pa produced in the overlying water column is laterally transported to other areas in the ocean.

Boundary scavenging is the phenomenon influencing the distribution and flux of chemically reactive substances in the oceanic water column (Anderson *et al.*, 1983, 1990; Nozaki and Nakanishi, 1985; Yang *et al.*, 1986; Lao, 1991). Within an ocean basin, boundary scavenging occurs due to regional differences in scavenging intensity, particle composition, the residence time of the element, and the rate of lateral mixing in the deep sea (Bacon, 1988). Since ^{231}Pa is a "boundary scavenging"- sensitive element, the distribution pattern of the Pa/Th ratio should reflect the regional extent of "boundary scavenging". In the following, the statistics of the compiled Atlantic core top data are calculated and

shown in Table 4.6. For discussion in the following, "enriched", "depleted", and "boundary scavenging" will represent a region of Pa/Th ratio greater than production rate ratio of 0.093, less than 0.093, and a Pa/Th ratio above the mean value of the grouped region.

First of all, the map presented in Figure 4.2 clearly indicates that fractionation of ^{230}Th and ^{231}Pa occurs within the whole Atlantic Ocean. The real variability is seen as "scatter" within the basin-wide distributions (Figure 4.2), so I could not contour the Pa/Th ratio for the Atlantic map as was done for the Pacific map by Yang *et al.* (1986). In general, the Atlantic map of Pa/Th ratio is featureless in the distribution patterns. The one striking fact is that most of the Pa/Th ratios in the Holocene Atlantic Ocean are lower than the production rate ratio of 0.093, implying that most of the ocean floor in the Atlantic is Pa depleted. The Southern Ocean (Atlantic sector) is the only region that displays higher values of Pa/Th ratio than the production rate ratio. The extensive areas of Pa/Th ratios that exceed the production rate ratio seen in ocean margins on the Pacific map (Yang *et al.*, 1986; Anderson *et al.*, 1990; Lao, 1991) are not observed in the Atlantic.

Within different geographic divisions, the nature of boundary scavenging of ^{231}Pa can be revealed by comparing the Pa/Th ratio at each single site to the arithmetic mean (m) of the division as shown in Table 4.6. In Table 4.6, the Atlantic Ocean is divided into several geographic divisions by latitude: the North Atlantic (north of 20°N), the Tropical Atlantic (20°N to 20°S), the South Atlantic (20°S to 45°S), and the Antarctic Atlantic sector (south of 45°S). The compiled data is plotted as a histogram graph and shown in Figure 4.3. The figure illustrates the large-scale mass imbalance between ^{231}Pa and ^{230}Th in sediments north of 45°S.

Table 4.6 Statistics of the 231Pa/230Th ratio of the Holocene Atlantic sediments

Pa/Th Cell	Cell mid-point	N of 20N	20N-20S	20S-45S	S. of 45S	N of 45S	All Atlantic
<0.025	0.0125	1	0	0	0	1	1
0.025-0.05	0.0375	6	7	4	0	17	17
0.05-0.075	0.0625	20	5	0	0	25	25
0.075-0.10	0.0875	3	3	1	1	7	8
0.10-0.125	0.1125	2	0	0	2	2	4
0.125-0.15	0.1375	0	0	0	2	0	2
>0.15-0.294	0.222	1	0	0	4	0	4
Mean (m) ± std. error of mean		0.061±0.003	0.053±0.004	0.055±0.009	0.174±0.022	0.058±0.0025	0.078±0.007

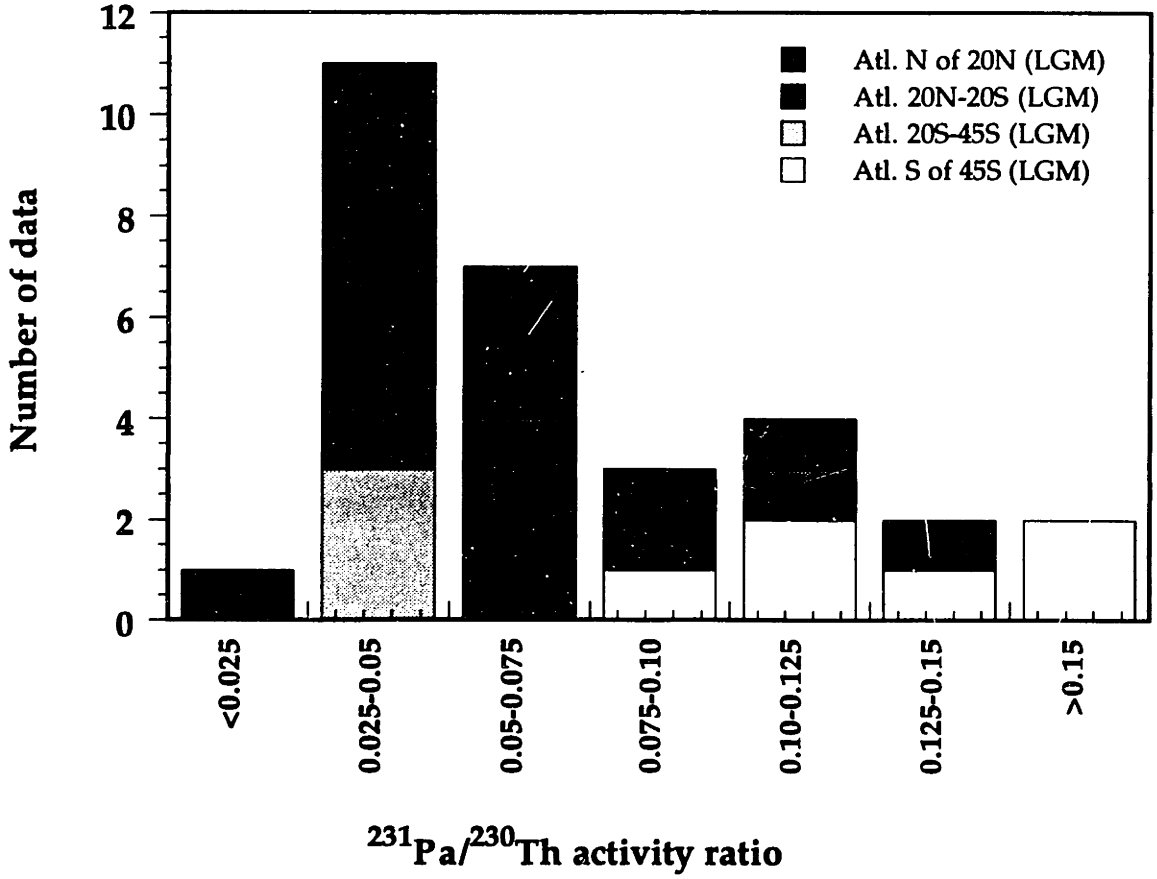

Figure 4.3 Summary of unsupported $^{231}Pa/^{230}Th$ ratios measured in the Holocene Atlantic sediments

The arithmetic mean Pa/Th ratio from cores north of 45°S in the Atlantic was calculated to identify regions of boundary scavenging of ^{231}Pa in the Atlantic Ocean. The mean value is 0.058 ± 0.005 (2 sigma of the standard error of the mean); it is close to each mean value (m) of the three divisions (the North, the Tropical, and the South Atlantic). By taking two sigma, the "normal" range of the Pa/Th ratio can be defined as 0.053 to 0.063. Values north of 45°S that are higher than this range may indicate regions of the boundary scavenging of Pa, and such areas are discussed below.

Significant boundary scavenging of ^{231}Pa is found in the polar region. Four cores (numbers 2-5 on the map) between 64°N and 70°N show Pa/Th ratios ranging from ~0.07 to ~0.11, significantly higher than the mean. The excess ^{230}Th activities range from 3.39 to 5.37 dpm/g (Table 4.4) in the Holocene sections of these cores, which is in agreement with the reported data in the sediments of the Norwegian Sea by Scholten *et al.*, (1990). The ^{230}Th-normalized total flux is higher in this region compared to some other regions in the Atlantic Ocean (Table 4.7), supporting the relatively higher Pa/Th ratios as a result of the higher flux of particles in the water column. It is interesting that the inventories of normalized-excess ^{210}Pb (i.e., normalized to the ^{210}P[illegible]cavenging from the overlying water column), an element with similar particle reactivity to ^{231}Pa in the water column (Bacon, 1988), also shows higher values for surface sediments in the region (Cochran *et al.*, 1990). The normalized excess ^{210}Pb inventories, on average, were found to be considerably greater than or equal to 100 per cent in the high-latitude sediments (north of 50°N). This suggests the enhanced boundary scavenging effect of reactive elements in this region. The higher inventories of normalized-excess ^{210}Pb were interpreted as the result of high productivity and particle flux (Cochran *et al.*, 1990). The Pa/Th ratios in the

region, however, still remain slightly less than the production ratios, implying that even here some ^{231}Pa from the production in the overlying water column has been transported elsewhere.

Higher values than the mean (0.058± 0.005) are found in two cores (#14 and #62) from the eastern Atlantic margin off northwest Africa, an area that has extremely high primary production in today's surface ocean (>100 $gC/m^2/yr$, according to Berger *et al.*, 1989). This suggests that the high production resulting from the higher upwelling intensity in the region (Mangini and Diester-Haass, 1983) may be responsible for the significant boundary scavenging of Pa. The core # 62(M12310) shows a Pa/Th ratio even higher than 0.093. The values of other cores in the region, however, are close to the mean value, so the picture of boundary scavenging effect even here is not entirely consistent.

For the cluster of cores from the MAR and its flanks (numbers 6 to 11, and 45 to 55 in Figure 4.2), the average Pa/Th ratio is 0.059± 0.006. This is close to the mean value and suggests that boundary scavenging is not significant for the MAR and its flanks. However, the range is fairly large (0.041 to 0.093). It was found to be a deficit area also for normalized-excess ^{210}Pb inventories of the surface sediments in the mid-latitude North Atlantic (Cochran *et al.*, 1990). In this region, the primary production is characterized by a large spring bloom triggered by thermal stratification (Sancetta, 1992). According to Berger *et al.* (1987), primary production is within the 45 $gC/m^2/yr$ contour. This is a moderate to high primary production in the Atlantic Ocean.

One core (number 11:V30-97) showed extremely abnormal Pa/Th ratio almost three times higher than the production rate ratio. The data seems odd compared to other data nearby in the region, but it does not seem to be the result

Table 4.7: Sediment composition, 230Th-normalized paleoflux, and (Pa/Th)exo/0.093 ratio for the Atlantic sediments

Cores	%CaCO3 Holocene	%CaCO3 LGM	%Opal Holocene	%Opal LGM	%Terrigenous Holocene	%Terrigenous LGM	%Non-CaCO3 Holocene	%Non-CaCO3 LGM
HM 94-18/3	38.80	10.00			61.20	90.00	61.20	90.00
HM 71-19	56.10	8.70			43.90	91.30	43.90	91.30
HM 79-26	57.20	11.90	2.90	2.20	39.90	85.90	42.80	88.10
VM 27-086	62.60	9.50			37.40	90.50	37.40	90.50
VM 28-014	62.60	13.40	6.27	7.45	31.13	79.15	37.40	86.60
VM 29-179	91.75	49.70			8.25	50.30	8.25	50.30
CHN 82-020	90.60	40.60			9.40	59.40	9.40	59.40
CHN 82-015	84.20	49.50			15.80	50.50	15.80	50.50
CHN 82-011	86.00	43.60			14.00	56.40	14.00	56.40
CHN 82-004	88.30	42.00	1.09	3.26	10.61	54.74	11.70	58.00
VM 30-097	85.10	49.65			14.90	50.35	14.90	50.35
VM 26-176	23.90	11.70	4.57	4.18	71.53	84.12	76.10	88.30
VM 23-100	68.50	67.85			31.50	32.15	31.50	32.15
V 30-049	68.60	54.60			31.40	45.40	31.40	45.40
KNR 64-05	75.15	64.10			24.85	35.90	24.85	35.90
V 22-197	39.20	16.90	3.23	3.66	57.57	79.44	60.80	83.10
EN 66-29	71.30	21.25			28.70	78.75	28.70	78.75
EN 66-38	77.60	50.20	5.80	2.07	16.60	47.73	22.40	49.80
KNR110-55	49.00	20.30			51.00	79.70	51.00	79.70
KNR110-91	59.90	22.60	2.23		37.87	77.40	40.10	77.40
KNR110-82	72.40	27.40			27.60	72.60	27.60	72.60
V 25-059	83.40	63.30			16.60	36.70	16.60	36.70
V 30-040	91.25	71.25			8.75	28.75	8.75	28.75
V 22-174	93.45	94.00	0.95	0.81	5.60	5.19	6.55	6.00
V 19-240	84.90	82.60	2.17	2.21	12.93	15.19	15.10	17.40
AII 107-065	89.80	59.50	0.81	2.57	9.39	37.93	10.20	40.50
RC 12-294	81.10	76.80	1.91	1.90	16.99	21.30	18.90	23.20
AII 107-022	5.80	7.90			94.20	92.10	94.20	92.10

Table 4.7 (con't)

Cores	(Pa/Th)/0.093 Holocene	(Pa/Th)/0.093 LGM	Total flux Holocene	Total flux LGM	CaCO3 flux Holocene	CaCO3 flux LGM	Non-CaCO3 flux Holocene	Non-CaCO3 flux LGM
HM 94-18/3	0.483	0.462	0.942	1.909	0.37	0.19	0.58	1.72
HM 71-19	0.817	0.648	1.584	2.882	0.89	0.25	0.70	2.63
HM 79-26	0.757	0.635	1.622	2.671	0.93	0.32	0.69	2.35
VM 27-086	0.927	0.676	2.084	5.892	1.30	0.56	0.78	5.33
VM 28-014	1.149		1.439	3.268	0.90	0.44	0.54	2.83
VM 29-179	0.463	0.163	1.670	0.450	1.53	0.22	0.14	0.23
CHN 82-020	0.549	0.483	1.306	6.775	1.18	2.75	0.12	4.02
CHN 82-015	0.734	1.153	1.887	4.415	1.59	2.19	0.30	2.23
CHN 82-011	0.561	0.474	1.499	1.920	1.29	0.84	0.21	1.08
CHN 82-004	0.688	0.492	1.466	2.729	1.29	1.15	0.17	1.58
VM 30-097	2.896	0.525	7.036	1.575	5.99	0.78	1.05	0.79
VM 26-176	0.698	0.498	2.818	19.524	0.67	2.28	2.14	17.24
VM 23-100	0.377	0.376	1.450	1.751	0.99	1.19	0.46	0.56
V 30-049	0.877	0.685	1.580	1.791	1.08	0.98	0.50	0.81
KNR 64-05	0.579	4.682	2.411	2.390	1.81	1.53	0.60	0.86
V 22-197	0.544	1.481	1.221	2.557	0.48	0.43	0.74	2.13
EN 66-29	0.499	0.539	1.088	0.709	0.78	0.15	0.31	0.56
EN 66-38	0.540	1.617	1.188	1.339	0.92	0.67	0.27	0.67
KNR110-55	0.554	0.000	1.284	1.651	0.63	0.34	0.65	1.32
KNR110-91	0.309	0.607	1.219	1.514	0.73	0.34	0.49	1.17
KNR110-82	0.494	1.013	1.260	1.943	0.91	0.53	0.35	1.41
V 25-059	0.445	0.858	1.483	1.667	1.24	1.06	0.25	0.61
V 30-040	0.431	0.746	1.334	1.553	1.22	1.11	0.12	0.45
V 22-174	0.531	0.410	0.770	0.698	0.72	0.66	0.05	0.04
V 19-240	0.428	0.499	1.354	1.389	1.16	1.15	0.21	0.24
AII 107-065	0.514	0.349	0.903	0.860	0.81	0.51	0.09	0.35
RC 12-294	0.476	0.453	1.109	1.316	0.90	1.01	0.21	0.31
AII 107-022	2.453	1.285	1.244	0.753	0.07	0.06	1.17	0.69

* 230Th-normalized paleoflux is in g/cm2/ka

of an artificial effect. Core top loss or a mix-up of the aged section of the core should cause the Pa/Th ratio to be lower rather than higher because the half-life of ^{231}Pa (32.5 ka) is shorter than that of ^{230}Th (75.2 ka). The proximity to the Mid-Atlantic Ridge suggests the possibility that this sample might reflect enhanced scavenging by metalliferous particles, as observed in the Pacific (Shimmield and Price, 1988 and 1989); however, the Mg/Fe ratio was not found to be abnormal for the core top sample by Boyle (personal communication). Thus at the moment, I can not provide a reasonable explanation.

In the Middle-Atlantic Bight, the data from core V26-176 (core #12, this study) and several cores from Anderson *et al.*, (1992) have Pa/Th ratio ranging from 0.05 to 0.07, with an average value of 0.063 ± 0.016 (2 times of standard error of the mean). This is indistinguishable from the Atlantic mean north of 45°S, indicating that the Middle Atlantic Bight is not a margin for the enhanced boundary scavenging of ^{231}Pa. This was found to be true for ^{210}Pb also (Anderson *et al.*, 1988; Biscaye *et al.*, 1988). The consistently lower unsupported Pa/Th activity ratio than their production ratio is in contrast to the typical feature found at other margins in the Pacific, where Pa/Th ratio ranges from 0.2 to 0.3 (Anderson *et al.* , 1992).

Cores from the margins of the western tropical Atlantic also are abnormal because their Pa/Th ratios range from ~0.03 to ~0.05, which is much lower than the production rate ratio of 0.093, and also significantly lower than the mean value. The lowest value for the Pa/Th ratio is seen in the region of the central subtropical Atlantic Ocean where the lowest primary production occurs (Berger *et al.*, 1987). A lower ^{230}Th-normalized total flux in these cores is also seen and supports the low-level particle flux through the water column, causing the inefficiency of scavenging of the radionuclides in the region. The lower Pa/Th

ratio is a typical open ocean value, and Pa must be laterally transported to other regions.

The northern-most core (#1, HM 94-18/3, 74°N) exhibits a lower Pa/Th ratio than the mean value for the Holocene section. It appears that ^{231}Pa in the polar region is removed to the seafloor by downward sinking particle flux at the site at a rate that is only half of its production in the overlying water column, so the remaining ^{231}Pa should have been transported laterally to elsewhere in the ocean. A lower scavenging efficiency in the polar region might be seen as a consequence of unusually low levels of organic production and flux of particles through the water column because of ice cover and the long polar night. The lower scavenging efficiency is also supported by the lower ^{230}Th-normalized total flux in the sample (Table 4.7), and the low content of opal in a nearby core. The inefficiency of scavenging of reactive elements is also observed from sediments in the Arctic Ocean by Ku and Broecker (1967), and in a later work from the same basin by Finkel *et al.* (1977). It was also demonstrated by the relatively high ^{231}Pa and ^{230}Th isotope activities in water column profiles over the Alpha ridge in the Arctic Ocean by Bacon *et al.* (1989). The observations of lower scavenging efficiency may imply a net export of these reactive radionuclides to the North Atlantic (Ku and Broecker, 1967; Bacon *et al.*, 1989).

In contrast, the arithmetic mean is 0.174 ± 0.044 (2 sigma) for the cores from the Antarctic Ocean (Atlantic sector) (Table 4.6). The Pa/Th ratio is on average three-fold higher than the mean value of the cores from north of 45°S in the Atlantic Ocean. Thus the Southern Ocean (Atlantic sector) is the only region where the Pa/Th ratio appears consistently higher than the production ratio 0.093. This is consistent in all the observations in the Southern Ocean around today's Polar Front (DeMaster, 1979; Kumar *et al.*, 1993; Yu, *et al.*, 1990; Chapter 5

in this thesis). High siliceous productivity and opal burial rate is associated clearly with the Polar Front in the Antarctic (DeMaster, 1979; Burckle and Cirilli, 1987; Charles *et al.*, 1991; Mortlock *et al.*, 1991; Chapter 5 in this thesis); however, north of the front, the siliceous production and burial rates drop greatly. Whether the higher ratios indicating enhanced scavenging of ^{231}Pa over ^{230}Th from the water column are due to extremely high siliceous production in the overlying water column or other mechanisms is still unconfirmed. In any case the Southern Ocean sediments seem to act as a major sink for ^{231}Pa which is otherwise deficient in the whole Atlantic north of 45°S.

In conclusion, even though significant boundary scavenging of ^{231}Pa resulting from a higher particle flux, either lithogenic or biogenic, or both within the Atlantic Ocean north of 45°S may occur, the Pa/Th ratio from most regions is lower than the production rate ratio. This implies ^{231}Pa depletion in the North Atlantic sediments. The question is:where does the "missing" ^{231}Pa end up? Since the Antarctic sediments are the only region of ^{231}Pa enrichment, it must be that the ^{231}Pa in the North Atlantic Ocean has been exported by advection to the South Atlantic Ocean, and then to the Antarctic. This is the first report of this striking feature. In the following, a simple mass balance of ^{231}Pa across 25°N of the Atlantic Ocean is pursued to examine whether the circulation is indeed sufficient to account for this inferred export.

4.4.2 Export of ^{231}Pa and ^{230}Th from the North Atlantic across 25°N

The statistics in Figure 4.3 show that the Pa/Th ratio in Atlantic Ocean surface sediments north of 45°S is usually little more than half the production rate ratio. This implies that the balance between oceanic production and

deposition of ^{231}Pa does not hold for this ocean. The question is:where could the "missing ^{231}Pa" go?

The North Atlantic Ocean has been widely regarded as an important region in terms of its large-scale circulation, consisting of both horizontal, wind-driven gyre circulation and vertically overturning thermohaline-driven circulation. Both circulations act in concert to transport heat (Hall and Bryden, 1982), and CO_2 (Brewer *et al.*, 1989) to latitudes where disequilibrium with the atmosphere occurs. Considering this same driving force of the ocean advection, I hypothesize that the "missing ^{231}Pa" in the North Atlantic Ocean is exported from the North Atlantic to the South Atlantic; eventually, it must also be further exported from the South Atlantic to the Southern Ocean to accumulate in the Antarctic sediments.

In what follows, I examine the mass balance between the production rate and the sedimentation plus the net export for both ^{231}Pa and ^{230}Th in the North Atlantic Ocean. I chose 25°N as the boundary because estimation of the variation of mean meridional volume transport with depth has been computed at the 25°N section by Hall and Bryden (1982; data source listed in their Table 5) to estimate the net heat transport in the 25°N latitude section. I make specific use of these mean meridional volume transports of water and combine the total ^{230}Th and ^{231}Pa activity profiles (Figures 4.4 and 4.5) in the water column from the North Atlantic Ocean to calculate the northward and southward advective flux of nuclides across this section. For simplification, I divide the ^{231}Pa and ^{230}Th activity depth profiles, and water mass transport profile into only two layers: shallow (0 to 1050 m) and deep (>1050 m to bottom). Each layer has an average tracer concentration C and net depth-integrated water transport.

The steady-state mass balances of ^{231}Pa and ^{230}Th are as follows:

$$\Sigma P = S + E, \qquad (4\text{-}3)$$

where ΣP is the integrated production rate from the decay of uranium for the entire ocean north of 25°N for each tracer, S is the sedimentation rate for each tracer, and E is the net export flux of each tracer across the 25°N boundary section. Integrated production can be calculated as follows:

$$\Sigma P \text{ (in dpm/s)}$$

$$= P^* V'$$

$$= C_U * \lambda * f * V' \qquad (4\text{-}4)$$

where C_U =uranium concentration in seawater, i.e., 3.3 μg/l (Turekian and Chan, 1971; Chen *et al.*, 1986);

λ = decay constant of tracer;

f = activity ratio of $^{234}U/^{238}U$ in seawater, i.e., 1.15 for ^{230}Th calculations, or

f = activity ratio of $^{235}U/^{238}U$ in seawater, i.e., 0.046 for ^{231}Pa calculations,

V' = total water volume between 25°N and 90°N latitude of the Atlantic Ocean (Table4.8).

The water volume of the Atlantic Ocean was calculated using the "AVS" program provided by Dr. Bill Jenkins of the Woods Hole Oceanographic Institution. The volume estimates were made by discrete integration of 5 minute resolution topographic data base dbdb5 for the Atlantic. The program results and sums are listed on Table 4.8.

Export is computed from the volume transports and concentration, as indicated previously.

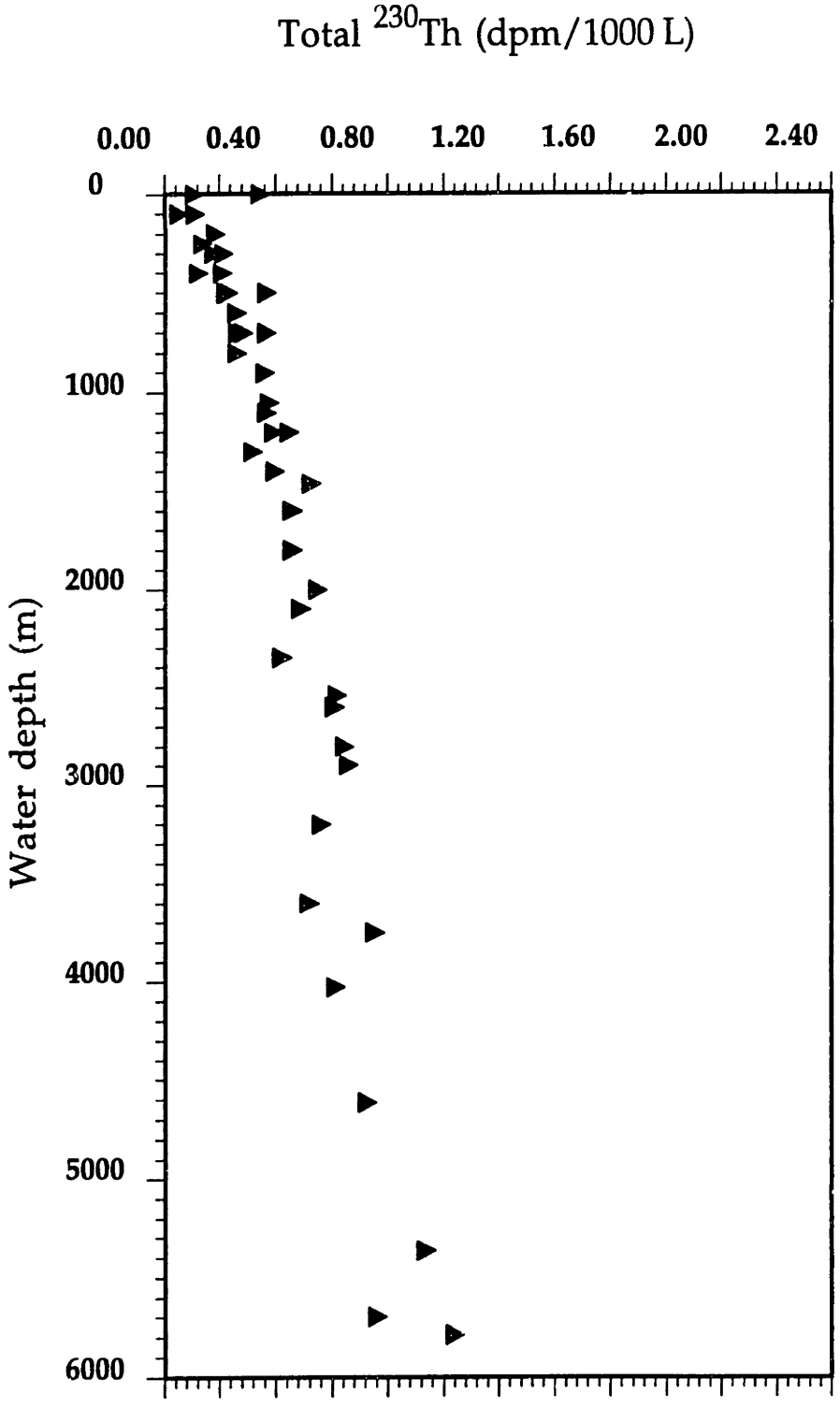

Figure 4.4 ^{230}Th distributions measured in ocean-water profiles by alpha-counting. Data are taken from Bacon (unpublished) and Cochran *et al.* (1987).

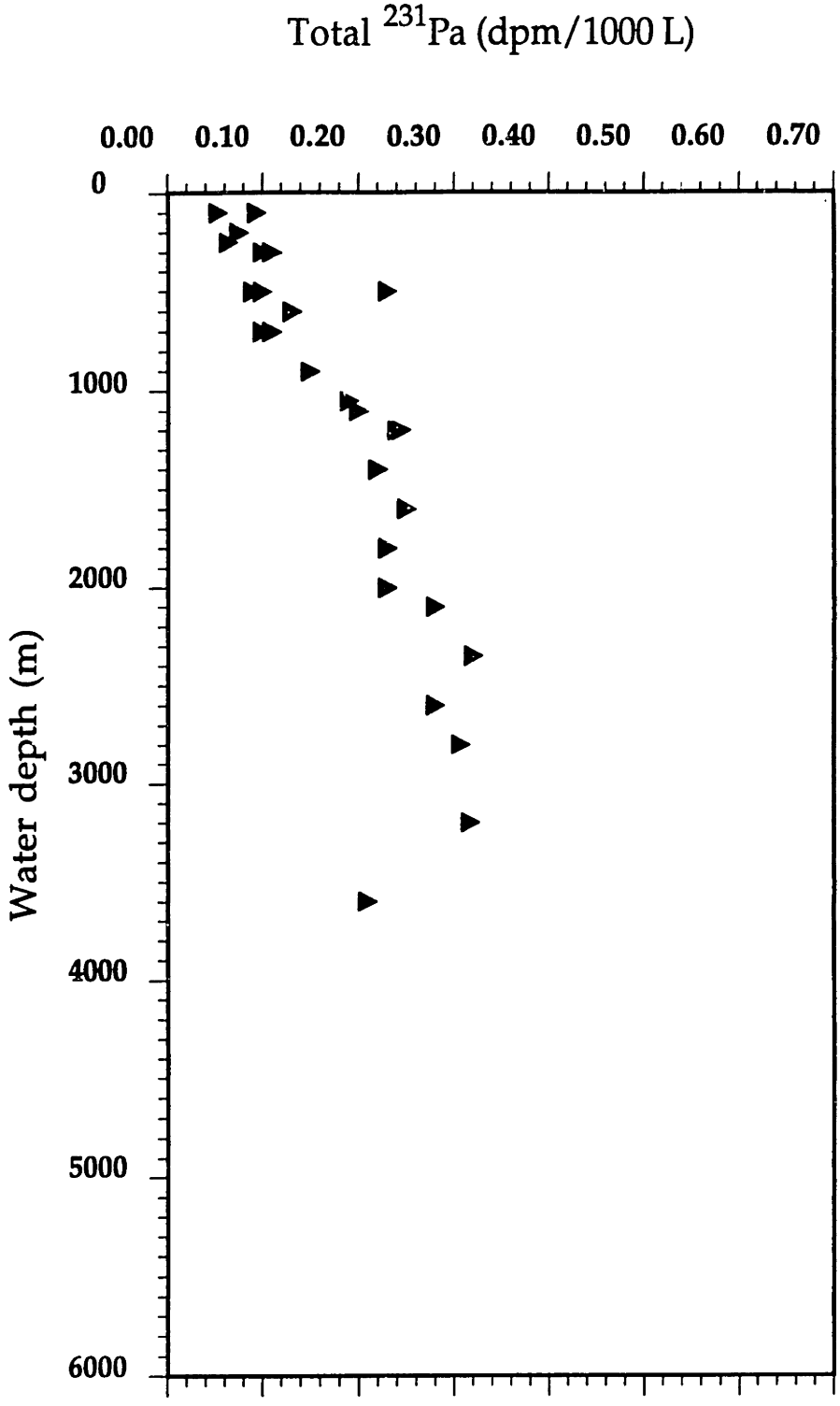

Figure 4.5 ^{231}Pa distributions measured in ocean-water profiles by alpha-counting. Data are taken from Bacon (unpublished).

Table 4.8: Summary results of the mean Atlantic Ocean Volume from AVS program

Latitude oN	Mean Area 10E12 m2	Volume 10E15 m3	Latitude oS	Mean Area 10E12 m2	Volume 10E15 m3
0 - 25	14.7	61.09	0 - 25	15.3	64.80
25 - 35	7.2	30.99	25 - 35	7.1	26.74
35 - 45	6.1	22.27	35 - 45	8.0	33.18
45 - 55	4.4	11.26	45 - 55	7.2	25.57
55 - 65	4.0	6.53	55 - 65	5.8	23.6
65 - 90	4.2	6.21	65 - 90		
Total	40.7	138.35	Total	43.4	173.89

$$E = C_s^* v_s + C_d^* v_d \quad (4\text{-}5)$$

In equation 4-5, C_s and C_d are average concentrations of the shallow and deep layers, and v_s and v_d are mean meridional volume transports in the shallow and deep layers. The concentrations C are all measurable quantities. The data of total ^{230}Th and ^{231}Pa in the water column were taken from the unpublished data of Bacon and Fleer (Figures 4.4 and 4.5) and data of Cochran *et al.* (1987). The mean meridional volume transport with depth is taken from the estimation by Hall and Bryden (1982). Broad features of the volume transports with depth have indicated that there are a net volume transport to the south in the deep layer and to the north in the shallow layer. The activities of ^{231}Pa and ^{230}Th in the water column show higher concentrations at deeper depth and lower concentrations at shallower depth; thus, a net flux of ^{231}Pa and ^{230}Th must be transported southward in the Atlantic Ocean. Table 4.9 summarizes the quantities used in the calculations.

The results (Table 4.9) support my proposed hypothesis of the advective flux of ^{231}Pa and ^{230}Th from the North to the South Atlantic, indicating that as much as 50% of the ^{231}Pa production, but only about 10% of the ^{230}Th production, is exported by ocean circulation from the North Atlantic Ocean across 25°N. The estimated magnitude of export for ^{231}Pa is close to the amount of ^{231}Pa deficit in the open ocean water column, which was previously considered laterally transported from the open ocean to the ocean margin. If these estimations of export of both ^{231}Pa and ^{230}Th are right, then there will be about 50% of ^{231}Pa and 90% of ^{230}Th production remaining for deposition to sediments. The Pa/Th ratio in the North Atlantic sediments should be expected to average 0.053 ± 0.016 (1 sigma). This is very close to the actually observed arithmetic mean Pa/Th ratio of 0.061 ± 0.006 (2 sigma) north of 25°N. The large

error (~30%) of estimation is seen as the result of the estimation error from the water mass transport (~25%, according to Hall and Bryden, 1982), the water volume north of 25°N based on the topographic data (~6%), and the analytical error of concentrations of tracers (ranging from <10% to 15%). It is obvious that the database is very small, and the assumption of homogeneous distribution for each tracer within a single box would be oversimplication; so the quantitative conclusion based on it must be regarded as a first approximation. However, it seems there can be little doubt about the basic conclusion.

As we can see in Figure 4.2, within the estimation error (1 sigma), the estimation result for the sedimentation ratio of Pa/Th is consistent with the observations of the deposition rate ratio of Pa/Th in the North Atlantic sediments, which range from 0.3 to 0.7 for most of the sediments covering the Atlantic Ocean seafloor. The above calculation, most emphatically, does not mean that the ocean marginal boundary scavenging effect is negligible. The internal-basin redistribution still must be found within the basin north of 25°N in the Atlantic Ocean; however, the exported fractions of ^{231}Pa and ^{230}Th are shown to be important contributions to the final redistribution of Pa/Th deposition ratios as seen for all Atlantic sediments. This result is important evidence that the advection effect by ocean circulation in the North Atlantic significantly influences the mass balance of nuclides within an ocean basin, and significantly influences the ratio observed in the sediments. The effect can not be ignored when sediment data are interpreted.

One question can be asked now: the export of ^{231}Pa from the Atlantic Ocean to the Southern Ocean result in horizontal gradient of ^{231}Pa in water column from the North Atlantic to the Southern Ocean?

Table 4.9 The simple mass balance model for 231Pa and 230Th in the Atlantic Ocean

Model's Input/Output	**Unit**	**231Pa**	**230Th**
Cs (0 - 1050 m)	dpm/m3	0.11	0.30
Cd (1051 - bottom)	dpm/m3	0.26	0.65
Vs (Sum Transport)	10E6 m3/s	19.26	19.26
Vd (Sum Transport)	10E6 m3/s	-19.17	-19.17
E (Net advection)	10E6 dpm/s	-2.87	-6.70
P (Integrated production)	10E6 dpm/s	5.88	63.54
% Net advection flux	%	49	10.5
% Sedimentation flux	%	51	89
Mean sedimentation Pa/Th			0.053 ± 0.016
Mean Pa/Th of 25N Atlantic core tops			0.061 ± 0.003

1. See text for detailed explanation of input/output parameters
2. The negative sign represents a southward transport,
   while the positive sign represents a northward transport across 25N

The only available data for ^{230}Th and ^{231}Pa in the water column of the Southern Ocean were reported recently by Rutgers Van Der Loeff and Berger (1993); however, the data are stiking. Vertical profiles of dissolved and particulate ^{230}Th and ^{231}Pa were obtained across the Antarctic Circumpolar Current (ACC) in the southern Atlantic. North of the Polar Front, dissolved and total ^{230}Th increase with depth; ^{230}Th concentrations increase three-fold across the Polar Front; while the concentrations of ^{231}Pa change little with depth and latitude across the ACC (Rutgers Van Der Loeff and Berger, 1993). As a consequence, the Pa/Th ratio in the water column decreases toward the south, but it remains far above the production ratio of 0.093. Although the Pa/Th ratio higher than the production rate ratio, the range of ratios falls within the same range as we typical observed in Figure 3.2. The concentrations of ^{230}Th and ^{231}Pa are in the same ranges of those observed in Figures 4.4 and 4.5, suggesting there is no significant horizontal gradient in ^{230}Th and ^{231}Pa concentration in the water column. These data suggested a controversial feature that I would expect regarding to the export flux of ^{231}Pa from the Atlantic OCean. One possible explanation is that the export ^{231}Pa from the Atlantic Ocean is stripped very rapidly when it reaches to the region of the Polar Front Zone (PFZ) because of highly scavenging efficiency due to either the intensity of particle flux or due to biogenic silicate phase or due to combination of both. In other word, the residence time of ^{231}Pa must be very short in this specific region across the Subtropical Convergence (STC, ~45°S) to the Polar Front Zone (PFZ). Future study of measuring Pa and Th in water column and in collected materials with sediment trap across the STC to the PFZ must be performed to confirm the scavenging phenomena of both nuclides. Before that, I propose the following explanation. To be able to obtain a large contrast in preferential deposition of ^{231}Pa between north and south in the Atlantic sediments, two principle factors must be involved. Firstly, there must be

more intense scavenging from the water in the Southern Ocean. Secondly, there must be sufficient time available for the transport from north to south Atlantic to take place before the reactive elements are scavenged, i.e., the scavenging residence time must be larger than the mixing time from the north to the south Atlantic Ocean. Although the exact residence times for both ^{231}Pa and ocean mixing are not known in the Atlantic Ocean, the average residence time of water in the deep Atlantic is probably longer than that of ^{230}Th and shorter than that of ^{231}Pa to be able to export ^{231}Pa from the north Atlantic to the Southern Ocean. Once reaching the Southern Ocean, the residence time of ^{231}Pa must be very short due to the possible reasons as discussed above. The large difference in distribution patterns of Pa/Th ratio between the Atlantic and Pacific Oceans is probably a result of the largely relative residence time of deep water within the Pacific and its larger size compared to that within Atlantic Ocean.

4.4.3 The mass balance of ^{231}Pa in Holocene Antarctic sediments

The above calculation demonstrated that transport of ^{231}Pa by the meridional circulation in the Atlantic is sufficient to account for the ^{231}Pa deficit observed in North Atlantic sediments. Because the South Atlantic sediments north of 45°S are also ^{231}Pa depleted, there must be additional export from the South Atlantic, and all of this ^{231}Pa must enter the circumpolar region. Now, the question is left whether the budget can be balanced between the deposition rate of ^{231}Pa in the Antarctic sediments and the production rate of ^{231}Pa in the Antarctic overlying water plus the export of ^{231}Pa from the Atlantic Ocean. In other words, is the Southern Ocean the only site to trap all of this excess ^{231}Pa, or

is a portion of it further transport northward into the Pacific and Indian Oceans after it enters the Antarctic Circumpolar Current.

A simple box model serves for the first order approximation in examining the mass balance of ^{231}Pa in the Antarctic sediments. The diagram is shown in Figure 4.6. In the model, for simplification, I assume that the system of the Southern Ocean has stabilized so that gain just balances loss. The decay loss of ^{231}Pa in the water is negligible. The input of ^{231}Pa into the Southern Ocean box is assumed to be the production from the uranium decay in the overlying water column plus the export from the North Atlantic Ocean. The output is deposition to the seafloor and the further export north into the Indian or Pacific Ocean..

I further assume that the export flux of ^{230}Th toward to the Southern Ocean is negligible. Then, since the depositon rate of ^{230}Th almost equals to the production rate from the uranium decay in the overlying water column, the deposition rate of ^{231}Pa in the Antarctic sediments can be estimated by taking the mean value of Pa/Th in the entire Antarctic sediments multiplied by the sum of the production rate of ^{230}Th in the entire Southern Ocean.

The mass balance of ^{231}Pa for the Holocene is given in Figure 4.6. The results show clearly that, within the uncertainties, the deposition of ^{231}Pa in Antarctic sediments is sufficient to balance both the Antarctic production and ^{231}Pa which is exported from the Atlantic Ocean. Within the uncertainties, there is no further export into the Indian or Pacific Ocean. This indicates that the Pa/Th deposited ratio in the Antarctic sediments should be controlled not only by the scavenging rate but also by the advective transport from the Atlantic. It is

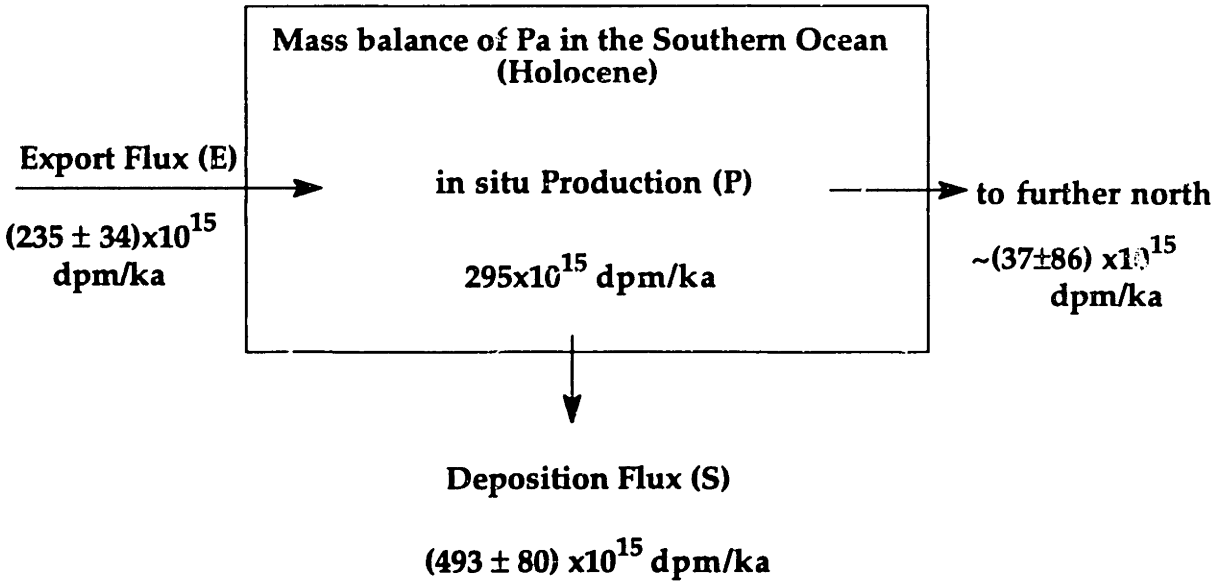

Input/Output	North of 45°S Atlantic	Southern Ocean
Production ^{231}Pa (dpm/ka)	631x10^{15}	295 x10^{15}
Production ^{230}Th (dpm/ka)	6813x10^{15}	3186x10^{15}
Deposition (dpm/Ka)	(395 ± 68)x10^{15} (2 sigma)	(493 ± 80)x10^{15}* (2 sigma)
Volume (m^3)	263x10^{15}	123x10^{15}**
Export flux (dpm/ka)	(235±68)x10^{15} (2 sigma)	(37 ± 86)x10^{15} (2 sigam)
Mean Pa/Th ratio	0.058 ±0.005 (n=52, 2 sigma)	0.155 ± 0.024 # (n=21, 2 sigma)

* Deposition of ^{231}Pa in the Southern Ocean=(Pa/Th) xProduction(^{230}Th) x Volume
** from Warren and Wunsch (1987)
# Mean Pa/Th from all available data in the Holocene Southern Ocean

Figure 4.6 Diagram of the mass balance of ^{231}Pa in the Holocene Southern Ocean.

important to keep this in mind when variations in the Pa/Th ratio in the Antarctic sediments with time are interpreted.

4.4.4 LGM/Holocene changes in the Pa/Th distribution in Atlantic sediments

During the Late Quaternary climate cycles, the ocean system has been affected in many ways. For instance, dramatic changes in oceanic circulation patterns and extent, and carbon system chemistry have been found to occur (Boyle and Keigwin, 1982, 1987; Curry and Lohman, 1983, 1990; Duplessy *et al.*, 1988; Curry *et al.*, 1988; Broecker *et al.*, 1990). The fluctuations in sea level must have changed the input of terrigenous materials (Damuth, 1977; Milliman *et al.*, 1975); the ice sheets at high latitudes must have varied the discharge of the ice-rafted debris (Ruddiman, 1971); and the changes in wind intensity and direction must have changed the transport of the eolian materials into the ocean (Kolla *et al.*, 1979). Because oceanic distribution of reactive nuclides is largely governed by scavenging by sinking particles and lateral transport within an ocean basin, these factors are reflected in the nuclide distributions in the sediments. Ultimately, it may become possible to use the nuclide distribution to deduce changes in particle flux or lateral transport from the sedimentary record.

In Chapter 3, I demonstrated from the results of year-long deployment of sediment traps that the scavenging efficiency of these nuclides and the fractionation between the two nuclides are largely controlled by the intensity of particle flux. Chemical composition of the settling particles could also influence the relative distribution of the two nuclides (e.g., due to preferential uptake of ^{231}Pa by Mn oxide or biogenic opal), but this factor is still poorly understood. Besides the particle flux and chemical composition of a particle, a simple steady-

state one box model, as shown in section 4.4.2, suggested another mechanism to influence the fractionation of ^{231}Pa and ^{230}Th. The model examined the mass balance of ^{231}Pa and ^{230}Th north of the 25°N, and it was shown that the reactive nuclides (in particular ^{231}Pa) are influenced strongly by oceanic advection. The dramatic changes in oceanic circulation patterns during the glacial - interglacial climate cycles, as many works have suggested, thus may affect the distribution pattern and boundary scavenging of these reactive nuclides as well. For these reasons, I focus in this section and in the following section on how changes in oceanic condition (particularly under extremely different conditions representative of the LGM and the Holocene) might have impacted the fractionation between ^{231}Pa and ^{230}Th. Careful mapping of the Pa/Th ratio from the Holocene and LGM over the entire Atlantic Ocean may provide insight into how the ocean system has changed.

LGM data for ^{231}Pa, Th and U isotopes are listed in Table 4.3, and the calculated results are given in Table 4.10. A map of Pa/Th ratio for the LGM sediments, similar to the Holocene map of the Pa/Th ratios, was constructed (Figure 4.7). For easier comparison of the changes in Pa/Th ratios and other sediment components between the LGM and the Holocene, the notation $(Pa/Th)_{G/H}$ ratio is introduced:

$$(Pa/Th)_{G/H} = (Pa/Th)_{LGM}/(Pa/Th)_{HL} \qquad (4\text{-}6)$$

where $(Pa/Th)_{LGM}$ and $(Pa/Th)_{HL}$ are the Pa/Th ratios in the LGM and the Holocene sediments. The $(Pa/Th)_{LGM}$ ratios and $(Pa/Th)_{HL}$ ratios are taken from Tables 4.4 and 4.10. Table 4.11 summarizes the $(Pa/Th)_{G/H}$ ratios. These ratios are decay-corrected to the time of deposition.

First of all, the LGM Atlantic map shows similar distribution patterns as the Holocene map in terms of enrichment and depletion of ^{231}Pa. The major site of ^{231}Pa enrichment still occurs in the Southern Ocean; the other regions are still ^{231}Pa depleted. The statistics of the LGM data are also calculated and listed in Table 4.12 and shown in Figure 4.8 as a histogram. By comparing the Pa/Th ratio in each individual core to the arithmetic mean (0.062 ± 0.012, 2 sigma) for all cores from north of 45°S in the Atlantic Ocean, the nature or pattern of boundary scavening of ^{231}Pa and ^{230}Th can be revealed for the LGM Atlantic Ocean. The LGM data reveals that the variations in Pa/Th ratio have a larger range compared to the that of the Holocene. It is worthwhile to notice (Figure 4.7) that the boundary scavenging effect appears in the northernmost margin off Africa, which is a region of dramatic increase in primary production during the glacial periods (Sarnthein et al., 1988). Boundary scavenging is also seen for the two cores (#21 and #22) from the western equatorial Atlantic. The rest of the regions north of 45°S in Atlantic Ocean clearly display no significant boundary scavenging of ^{231}Pa during the LGM.

A map of the LGM/Holocene ration of Pa/Th ratio, similar to the Holocene map of the Pa/Th ratios, are also plotted in Figure 4.9. The values of the arithmetic mean in each division are also compared to those during the Holocene (Tables 4.6 and 4.12). The major changes in the distribution features of Pa/Th between the LGM and the Holocene are as follows: 1) the arithmetic mean of Pa/Th ratio for the North Atlantic and South Atlantic Oceans slightly decreased; 2) in both the eastern and western equatorial Atlantic Ocean, the scavenged ratio of Pa/Th was higher during the LGM; in addition to this, one core from the Caribbean Sea (KNR 64-05) also had higher Pa/Th ratio during the

Table 4.10: Unsupported initial radionuclide activities of the LGM Atlantic sediments

Cores	230Thex	231Paex	230Thexo	231Paexo	Detrial 238U	Authigenic 238U	Pa/Th)exo	234U/238U	238U/232Th	230Thexo/232Th
	dpm/g	dpm/g	dpm/g	dpm/g	dpm/g	dpm/g				
HM 94-18/3	2.88	0.10	3.40	0.15	2.14	-0.55	0.043	1.14	0.59	1.08
HM 71-19	1.71	0.08	2.02	0.12	2.03	-0.51	0.061	1.23	0.60	0.67
HM 79-26	2.76	0.13	3.26	0.19	1.98	-0.52	0.060	1.20	0.59	1.11
VM 27-086	1.10	0.06	1.29	0.08	2.30	-0.58	0.064	1.11	0.60	0.38
VM 28-014	1.27		1.49		1.14	-0.24		1.16	0.63	0.89
VM 29-179	16.70	0.21	19.71	0.30	1.14	-0.84	0.015	1.18	0.21	11.73
CHN 82-020	1.01	0.04	1.19	0.05	1.83	-0.70	0.045	1.05	0.49	0.44
CHN 82-015	1.09	0.10	1.28	0.14	0.95	-0.32	0.108	1.00	0.53	0.92
CHN 82-011	3.73	0.13	4.40	0.20	1.07	-0.39	0.045	1.04	0.51	2.80
CHN 82-004	2.80	0.10	3.30	0.15	1.10	-0.47	0.046	0.94	0.46	2.03
VM 30-097	4.77	0.19	5.63	0.28	0.95	0.65	0.049	1.39	2.79	4.04
VM 26-176	0.45	0.02	0.53	0.02	2.27	-0.33	0.047	1.21	0.68	0.16
VM 23-100	5.83	0.17	6.88	0.24	0.72	-0.08	0.035	1.29	0.71	6.50
V 30-049	3.85	0.20	4.54	0.29	0.90	0.04	0.064	1.39	0.94	3.42
KNR 64-05	2.84	1.01	3.35	1.48	0.70	-0.02	0.440	1.04	0.78	3.27
V 22-197	2.76	0.31	3.26	0.45	1.77	0.74	0.139	1.38	2.01	1.25
EN 66-29	16.04	0.66	18.92	0.96	1.76	-0.68	0.051	1.03	0.49	7.31
EN 66-38	4.88	0.60	5.75	0.87	1.29	-0.37	0.152	1.07	0.57	3.03
KNR110-55	6.15		7.26		2.36	-0.89	0.000	0.94	0.50	2.08
KNR110-91	5.61	0.26	6.62	0.38	1.81	-1.11	0.057	2.21	0.31	2.48
KNR110-82	3.23	0.25	3.81	0.36	1.89	-0.37	0.095	0.87	0.64	1.37
V 25-059	5.11	0.33	6.03	0.49	1.09	-0.47	0.081	1.31	0.45	3.76
V 30-040	5.32	0.30	6.28	0.44	0.78	-0.31	0.070	1.23	0.48	5.43
V 22-174	8.40	0.26	9.91	0.38	0.25	-0.04	0.039	1.49	0.67	27.35
V 19-240	4.98	0.19	5.88	0.28	0.45	0.09	0.047	1.33	1.36	8.91
AII 107-065	7.25	0.19	8.55	0.28	1.14	-0.56	0.033	1.08	0.40	5.10
RC 12-294	5.60	0.19	6.61	0.28	0.50	-0.18	0.043	1.16	0.52	8.95
AII 107-022	8.19	0.80	9.66	1.17	0.84	-0.27	0.121	0.96	0.54	7.78

Table 4.11: LGM/Holocene changes in 230Th-normalized paleoflux and Pa/Th)exo ratio of the Atlantic sediments

Cores	(Pa/Th)exo LGM/Holocene	Total flux LGM/Holocene	%CaCO3 LGM/Holocene	CaCO3 flux LGM/Holocene	Terrigenous flux LGM/Holocene	Non-CaCO3 flux LGM/Holocene
HM 94-18/3	0.96	2.03	0.26	0.52	2.98	2.98
HM 71-19	0.79	1.82	0.16	0.28	3.78	3.78
HM 79-26	0.84	1.65	0.21	0.34	3.54	3.39
VM 27-086	0.73	2.83	0.15	0.43	6.84	6.84
VM 28-014		2.27	0.21	0.49	5.77	5.26
VM 29-179	0.35	0.27	0.54	0.15	1.64	1.64
CHN 82-020	0.88	5.19	0.45	2.32	32.77	32.77
CHN 82-015	1.57	2.34	0.59	1.38	7.48	7.48
CHN 82-011	0.85	1.28	0.51	0.65	5.16	5.16
CHN 82-004	0.71	1.86	0.48	0.89	9.61	9.23
VM 30-097	0.18	0.22	0.58	0.13	0.76	0.76
VM 26-176	0.71	6.93	0.49	3.39	8.15	8.04
VM 23-100	1.00	1.21	0.99	1.20	1.23	1.23
V 30-049	0.78	1.13	0.80	0.90	1.64	1.64
KNR 64-05	8.08	0.99	0.85	0.85	1.43	1.43
V 22-197	2.72	2.09	0.43	0.90	2.89	2.86
EN 66-29	1.08	0.65	0.30	0.19	1.79	1.79
EN 66-38	3.00	1.13	0.65	0.73	3.24	2.51
KNR110-55	0.00	1.29	0.41	0.53	2.01	2.01
KNR110-91	1.96	1.24	0.38	0.47	2.54	2.40
KNR110-82	2.05	1.54	0.38	0.58	4.06	4.06
V 25-059	1.93	1.12	0.76	0.85	2.48	2.48
V 30-040	1.73	1.16	0.78	0.91	3.83	3.83
V 22-174	0.77	0.91	1.01	0.91	0.84	0.83
V 19-240	1.17	1.02	0.97	0.99	1.20	1.17
AII 107-065	0.68	0.95	0.66	0.63	3.85	3.78
RC 12-294	0.95	1.19	0.95	1.12	1.49	1.46
AII 107-022	0.52	0.61	1.36	0.82	0.59	0.59

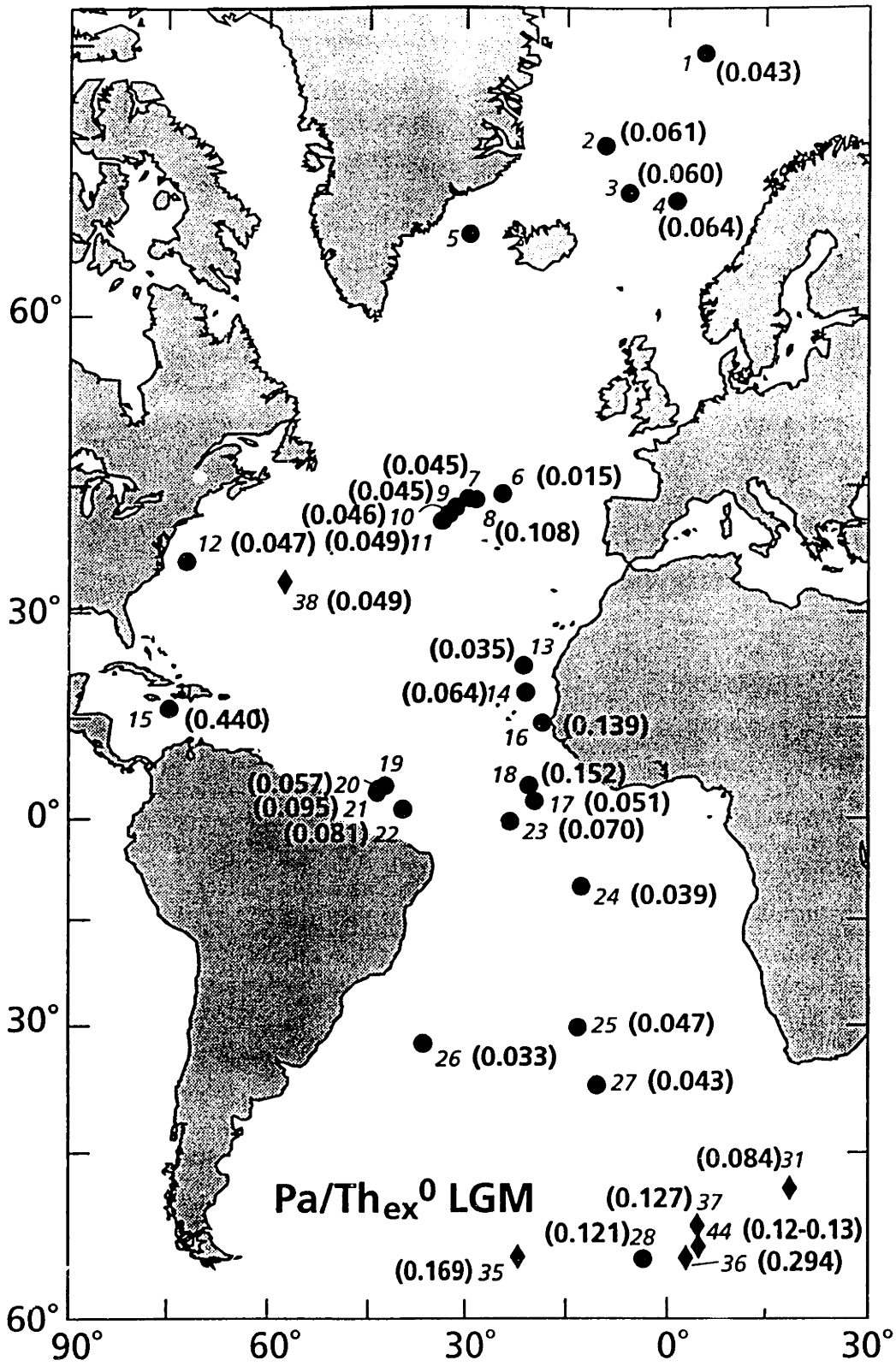

Figure 4.7 The map of decay-corrected unsupported $^{231}Pa/^{230}Th$ ratio (Pa/Th_{ex}^{0}) of the Last Glacial Maximum (LGM) Atlantic Ocean.

Table 4.12 Statistics of the 231Pa/230Th ratio of the LGM Atlantic sediments

Pa/Th Cell	Cell mid-point	N of 20N	20N-20S	20S-45S	S. of 45S	N of 45S	All Atlantic
<0.025	0.0125	1	0	0	0	1	1
0.025-0.05	0.0375	7	1	3	0	11	11
0.05-0.075	0.0625	3	4	0	0	7	7
0.075-0.10	0.0875	0	2	0	1	2	3
0.10-0.125	0.1125	1	1	0	2	2	4
0.125-0.15	0.1375	0	1	0	1	1	2
>0.15-0.294	0.222	0	0	0	2	0	2
Mean (m) ± std error of mean		0.0515±0.021	0.083±0.012	0.041±0.003	0.154±0.027	0.062±0.012	0.064±0.007

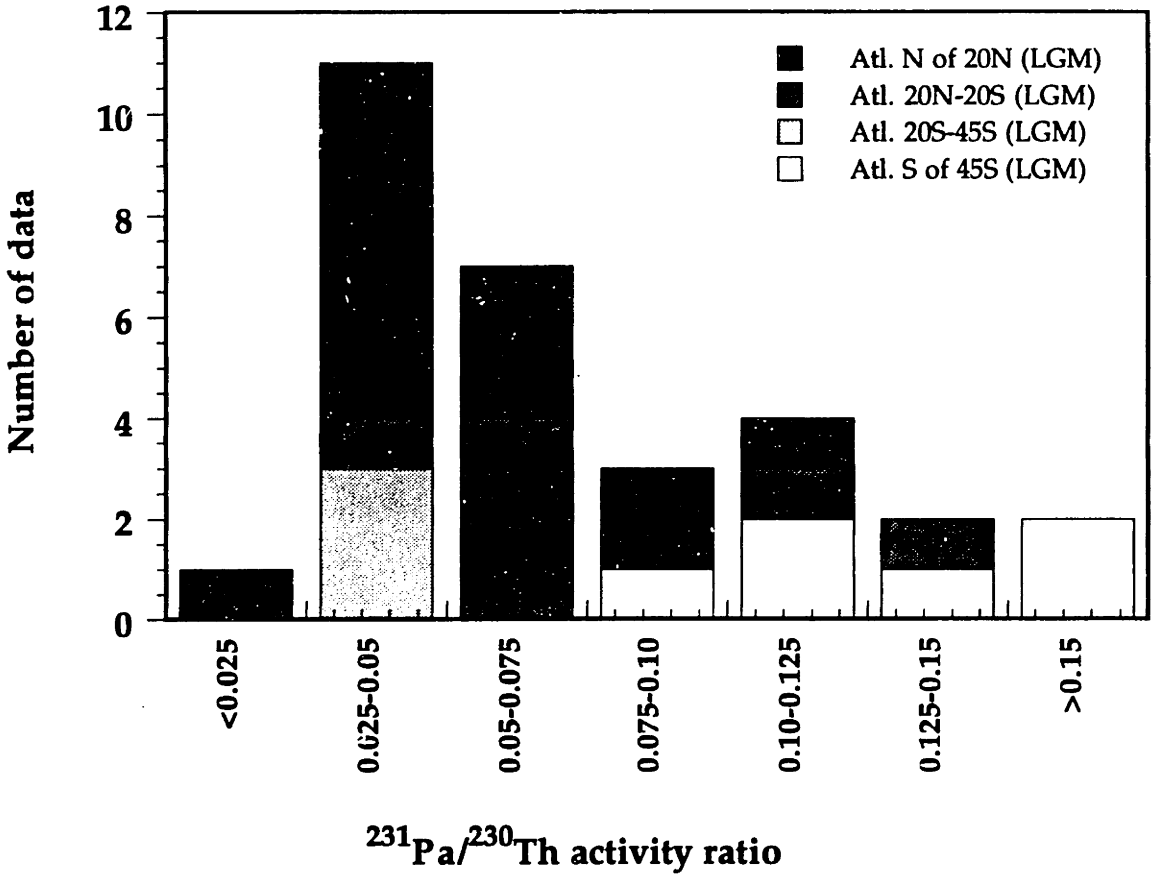

Figure 4.8 Summary of unsupported $^{231}Pa/^{230}Th$ ratios measured in the Last Glacial Maximum Atlantic sediments

LGM; and 3) the preferential scavenging of ^{231}Pa over ^{230}Th in the Antarctic Ocean was less during the LGM.

If advection has truly affected the ^{231}Pa and ^{230}Th mass balance as the model has shown (section 4.4.2) in the Holocene Atlantic, the changes in ocean circulation patterns and intensity during the glacial time might have accompanied variations in the distribution of $(Pa/Th)_{G/H}$. Now, the question can be asked whether the sluggishness of the southward-flowing NADW (North Atlantic Deep Water) decreased the export of ^{231}Pa and ^{230}Th from the Atlantic to the Southern Ocean.

In the following, I use the same box model used for the Holocene to examine the mass balance of ^{231}Pa in the Southern Ocean during the LGM. The purpose is to examine the question whether the sluggish advection of NADW during the LGM (Boyle and Keigwin, 1982, 1987; Oppo and Fairbanks, 1987; Duplessy *et al.*, 1988; Curry and Lohman, 1983, 1990) would decrease the export of ^{231}Pa from the North Atlantic, and it would be an important cause of the variations in Pa/Th ratio in the Antarctic sediments. The estimation is based on the same production rate of ^{231}Pa and ^{230}Th in both the North Atlantic and the Southern Ocean, and the deposition rate of ^{231}Pa for both divisions are determined by the Pa/Th deposition ratios during the LGM. Following the same calculation as that for the Holocene box model, the results indicated in Figure 4.10 suggest that the export flux of ^{231}Pa and the deposition rate of ^{231}Pa in the Antarctic sediments are almost the same within the 2 times of standard devision of the mean during the LGM. The result shows that the depostion of ^{231}Pa into the Antarctic sediments is still enough to account for all excess ^{231}Pa exported from the North Atlantic, and there is no significant amount of ^{231}Pa exported further northward. However, the result is somehow striking, because the export

of ^{231}Pa from the Atlantic and deposition rate of ^{231}Pa in the Southern Ocean sediments suffer no changes even though the ocean conditions are thought to be extremely different between the glacial and interglacial climates. The higher production during the LGM induced by the increasing intensity of upwelling (Sarnthein *et al.*, 1987, 1988; Mix, 1988) might have resulted in higher surface scavenging intensity and thus been strong enough to cause higher scavenging efficiency of ^{231}Pa in the equatorial Atlantic where ^{231}Pa was supposed to increase in the glacial North Atlantic. All of these variations in intensity and patterns of ocean circulation along with the internal basin redistribution (i.e., open ocean gyre and the margins) might have caused the decreased Pa/Th ratios in the North Atlantic, increased Pa/Th in the tropical Atlantic, and decreased Pa/Th ratio in the Southern Atlantic Ocean during the LGM (Figure 4.9). Since the export to the Southern Ocean is a net effect of scavenging by particles and advection by different patterns of water circulations in the Atlantic Ocean, the small difference between the LGM and the Holocene in terms of the ^{231}Pa mass balance in the Southern Ocean may indicate that combination of those effects are a real reflection of little change in terms of the ^{231}Pa budget in the Southern Ocean, or it may indicate that the rough scale of mass balance I calculated would not be able to decouple the effects. A fine scale of budget must be examined to not erase the signal of boundary scavenging in the Southern Ocean. In any case, this implies that the downcore variations in Pa/Th ratio reflect variations not only in particle flux (i.e., production), but also in the intensity or pattern of the thermohaline circulation.

In conclusion, the advection effect seems to be a very important factor controlling the fractionation between ^{231}Pa and ^{230}Th in the Southern Ocean

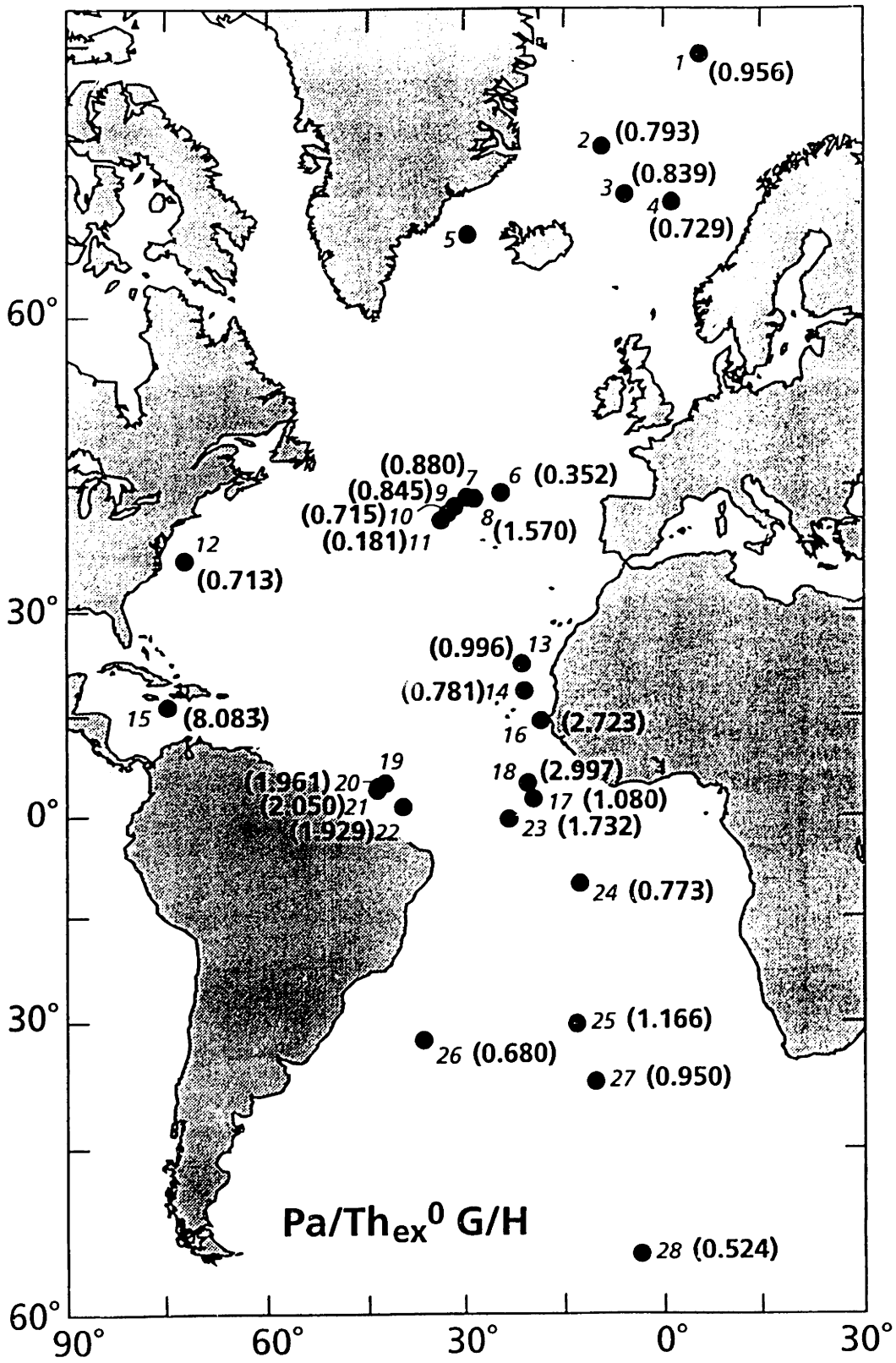

Figure 4.9 The map of LGM/Holocene ratio of the decay-corrected unsupported $^{231}Pa/^{230}Th$ ratio (Pa/Th_{ex}^{0}) in the Atlantic Ocean.

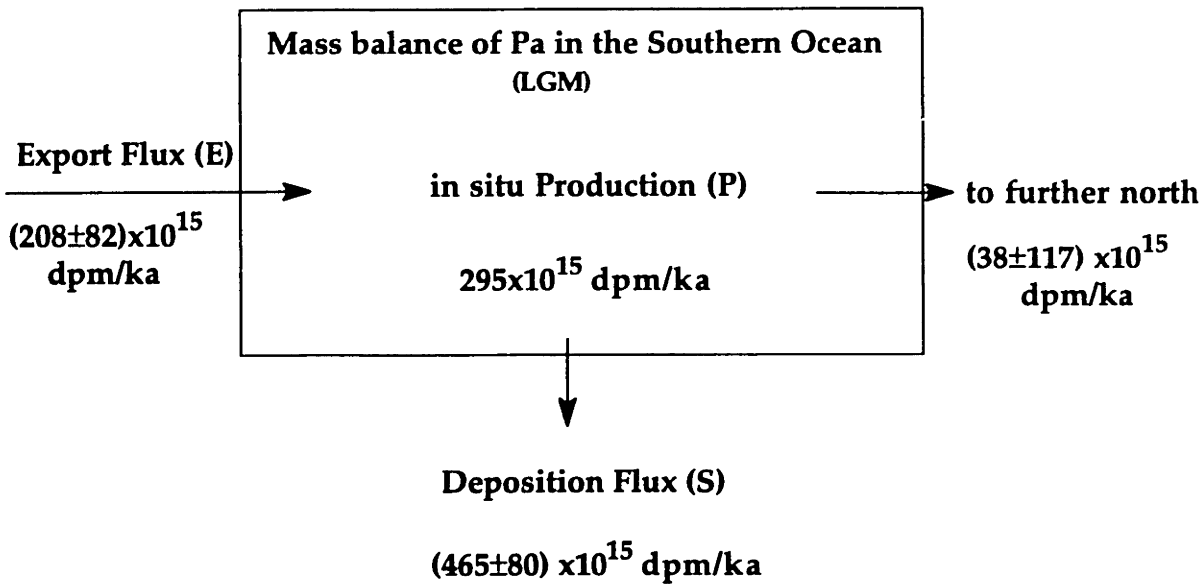

Input/Output	North of 45°S Atlantic	Southern Ocean
Production ^{231}Pa (dpm/ka)	631 x10^{15}	295 x10^{15}
Production ^{230}Th (dpm/ka)	6813x10^{15}	3186x10^{15}
Deposition (dpm/Ka)	(423±82)x10^{15} (2 sigma)	(465±80)x10^{15} (2 sigma)
Volume (m^3)	263 x10^{15}	123x10^{15}**
Export flux (dpm/ka)	(208±82)x10^{15} (2 sigma)	(38±117)x10^{15} (2 sigam)
Mean Pa/Th ratio	0.062 ±0.006 (n=52, 2 sigma)	0.146±0.013 # (n=16, 2 sigma)

* Deposition of ^{231}Pa in the Southern Ocean=(Pa/Th) x Production(^{230}Th) x Volume
** from Warren and Wunsch (1987)
# Mean Pa/Th from all available data in the LGM Southern Ocean

Figure 4.10 Diagram of the mass balance of ^{231}Pa in the LGM Southern Ocean.

and the depostion rate ratio of Pa/Th in the Southern Ocean. This factor must be considered in the interpretation of downcore variations in Pa/Th.

4.4.5. Changes in the flux of sedimentary components between LGM and Holocene

As mentioned earlier, deep-sea sedimentation rates vary with climate. Since carbonate and terrigenous phases are two major components of the cores studied in this chapter, the following discussion will focus on the interpretation of the variations in these two components.

Measurements of %carbonate and %non-carbonate for both LGM and the Holocene section samples are presented in Table 4.7, and are plotted in Figure 4.11 and 4.12. The comparison between LGM and the Holocene is shown in Table 4.11. All cores except AII 107-22 show lower $CaCO_3$ flux during the LGM. The amplitude of the reduction, however, varies from core to core, ranging from five times to minor amplitude changes (Table 4.11). A core in the Norwegian Sea appears to have the highest amplitude of change; while most of the cores are reduced by about a factor of two. By examining the ^{230}Th-normalized total flux, carbonate flux, and non-carbonate flux (largely a terrigenous flux) in Table 4.11 and Figure 4.13, the comparisons of the glacial and interglacial sedimentation fluxes show remarkable regularity. With few exceptions, total flux was higher, non-carbonate flux was higher, but carbonate flux was lower during the LGM.

Factors controlling the calcium carbonate content of the deep-sea sediments are supply of biogenic carbonate, loss by dissolution, and dilution by non-carbonate phases. Each process may contribute to the climatically controlled

fluctuations in the carbonate content of deep-sea sediments at individual sites. Based on measurements during the GEOSECS expeditions, the relationship between the carbonate ion content of deep water and the depth of the lysoclines for calcite and aragonite in the open ocean were established by Broecker and Takahashi (1978). The regional average lysocline depths drawn from their data occur at 4800 m, 4700 m, 4800 m, and 4300 m for the 42°N MAR, 20°N MAR, the North American Basin, and the equatorial Atlantic, respectively (the data was taken from Table 1 of Bacon, 1984). Atlantic waters at present become undersaturated with respect to calcite between 4,000 and 5,000 m (Takahashi, 1975). Luz and Shackleton (1975), on the basis of their study of eastern equatorial Pacific cores, concluded that for depths at or above the regional lysocline, dissolution does not play an important role in the glacial/interglacial fluctuations of carbonate content. Since most cores used for this study were collected from 2000 m to 4000 m, which is above the lysocline, the fluctuation in carbonate content for most cores used in this study should be the least affected by carbonate dissolution. This conclusion was substantiated in many previous works (Bacon, 1984; Curry and Lohaman, 1986; Francois *et al.*, 1990).

Although recent works have indicated that even at depths well above the lysocline a significant amount of carbonate dissolution may occur by reaction of the carbonate in the sediment with metabolically produced CO_2 (Emerson and Bender, 1981), the percent carbonate plots for the cores selected in this thesis were considered to be principally due to variation in supply of carbonate or dilution by non-carbonate. In order to evaluate the effect of each process, I calculated the rain rates of the carbonate and terrigenious materials in sediments. For several cores, I also determined the content of biogenic opal, but for the rest of the cores I took non-carbonate to consist entirely of terrigenous phase.

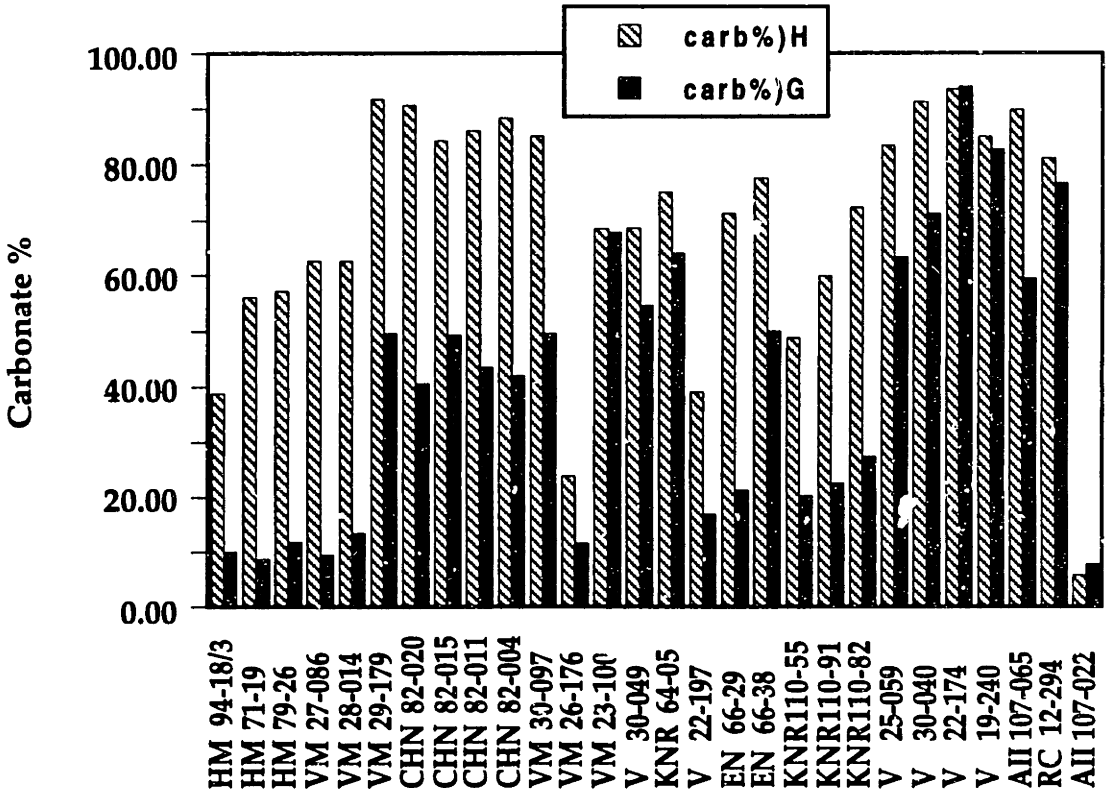

Figure 4.11 %Carbonate for both the LGM and Holocene sections in the Atlantic sediments

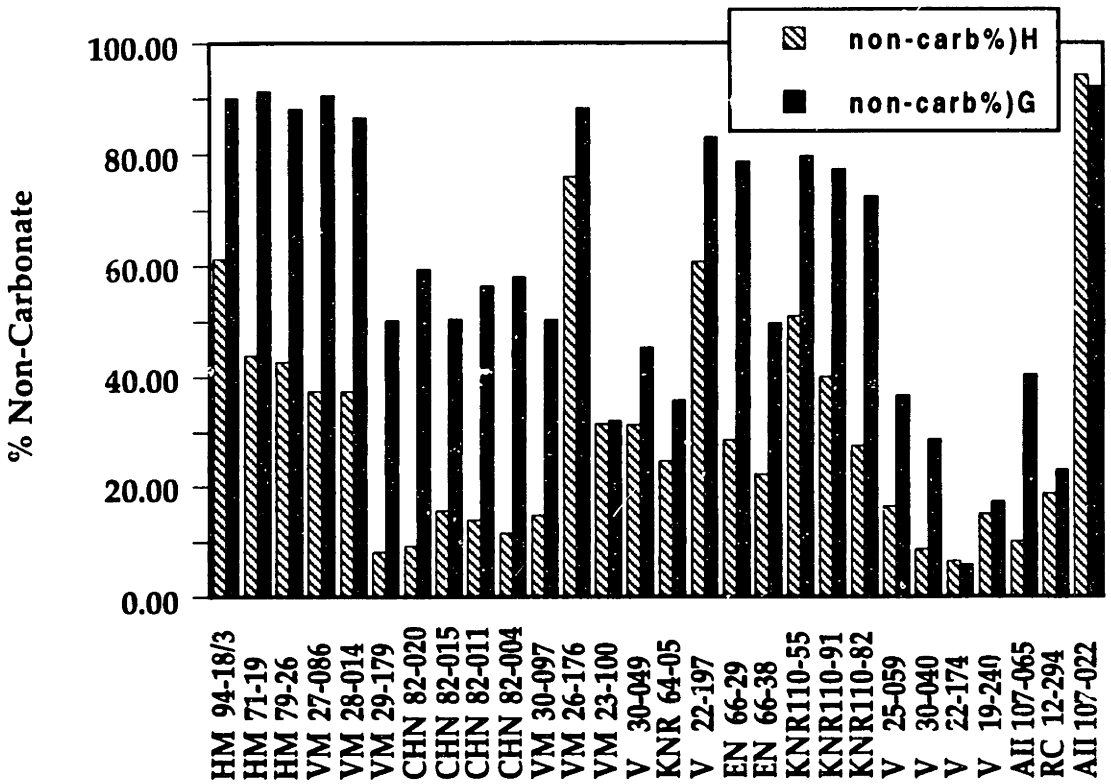

Figure 4.12 %Non-carbonate for both the LGM and Holocene sections in the Atlantic sediments

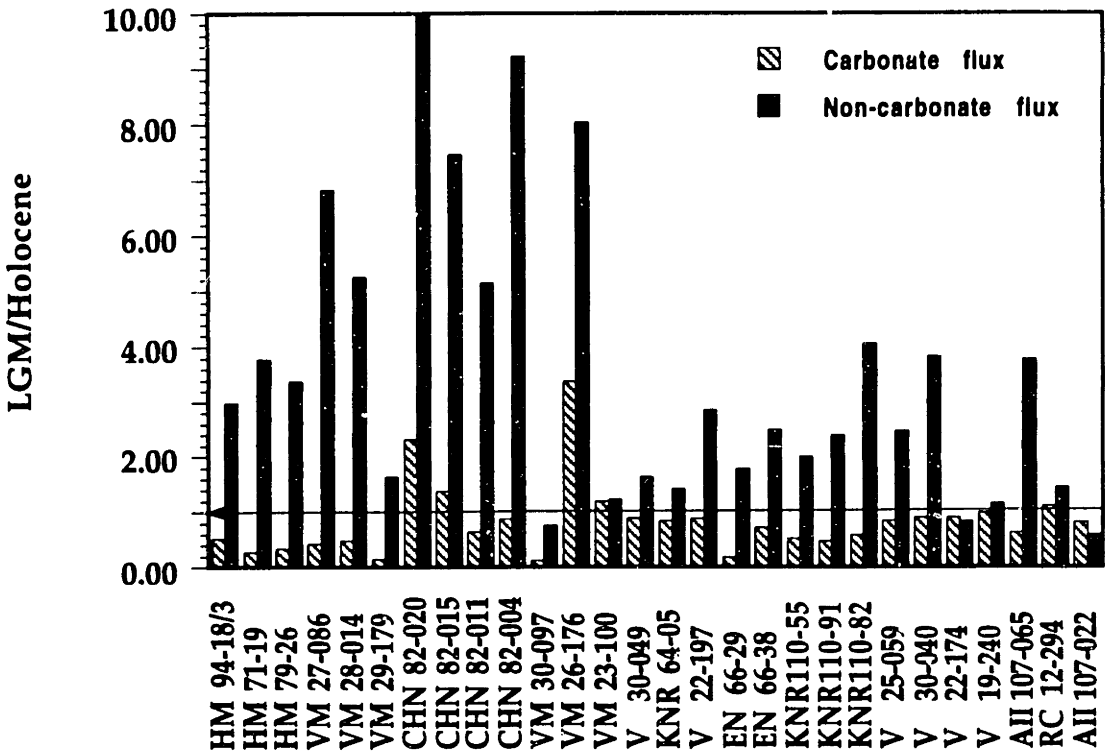

Figure 4.13 The LGM/Holocene ratio of the ^{230}Th-normalized carbonate and non-carbonate flux for the Atlantic sediments

The fluxes of sediment components are normalized to the ^{230}Th activity in the sediment (i.e., ^{230}Th-normalized flux method).

$$\text{Carbonate flux} = \beta\ (f/^{230}Th_{ex}{}^{o}) \qquad (4\text{-}7)$$

and

$$\text{Non-carbonate flux} = \beta\ [(1\text{-}f)/^{230}Th_{ex}{}^{o}], \qquad (4\text{-}8)$$

where $^{230}Th_{ex}{}^{o}$ is in excess and has been decay-corrected; f is the fraction of carbonate; β is the known flux of ^{230}Th, which is controlled by the uranium content of seawater and is a linearly increasing function of water depth Z:

$$\beta\ (dpm/cm^2/ka) = 0.00263\ Z\ (m). \qquad (4\text{-}9)$$

As pointed out in Chapter 3, the ^{230}Th-normalization method is used to obtain the vertical settling of particulates and tends to corrrect for redistribution of sediment on the bottom. Since it is not possible to rule out dissolution (e.g., carbonate dissolution for carbonate flux) entirely, carbonate flux refers to the net carbonate production minus dissolution.

Both ^{230}Th-normalized carbonate and non-carbonate flux for the Holocene and the LGM samples from the Atlantic Ocean are presented in Table 4.7. Comparisons of the LGM and the Holocene changes are plotted in Figure 4.13. The changes in carbonate flux (Figure 4.13) between LGM and the Holocene bear some similarities to those patterns observed in changes in carbonate content (Figure 4.11). Most cores show a lower in carbonate flux during the LGM. This finding is consistent with previously reported carbonate accumulation rates in the Atlantic sediments by Turekian (1965), Bacon (1984), and Curry and Lohman (1986, 1990). The changes in ^{230}Th-normalized non-carbonate flux, however,

appear to be several times higher during the LGM (Figure 4.13). This finding is also in agreement with previous observations by Bacon (1984), Curry and Lohmann (1986, 1990), and Francois and Bacon (1991). Results from both the ^{230}Th-normalized carbonate and non-carbonate flux thus suggest that the carbonate content in all the cores I selected from the Atlantic Ocean have been altered to a large extent by changes in the input rate of non-carbonate components (Figures 4.11 and 4.12). In addition, the reduction in ^{230}Th-normalized carbonate flux suggests a decrease in carbonate production from the surface water.

The dilution effect of the non-carbonate input on the carbonate content shows that during the Holocene, the non-carbonate input contributes less to the dilution of the carbonate content than during LGM. This supports the conclusion of a number of authors that the carbonate fluctuations in Atlantic cores are controlled largely by the variable dilution effect of non-carbonate input (Broecker *et al.*, 1958; Ruddiman, 1971; Bacon, 1984; Curry and Lohamn, 1986, 1990).

Although the variations of carbonate and non-carbonate flux exhibit regularity of changes between the LGM and the Holocene [illegible] most of the cores from the Atlantic Ocean for this study, the fluctuation [illegible] va[illegible] region to region. For individuate sites, I discuss the variations in flu[illegible]en glacial and Holocene periods in the following paragraphs.

The cores from the high latitudes in the North Atlantic have a large amplitude changes in carbonate flux that is a factor of two between the LGM and the Holocene. Since the cores are well above the average lysocline depth and within the region of low production due to ice cover, their lower carbonate flux in the LGM relative to the Holocene could imply a much lower carbonate input.

The non-carbonate flux, conversely, was much greater during the LGM. If the carbonate flux contains a fraction of detrital carbonate, then the increase in the non-carbonate phase could contribute to the increase in carbonate flux. This obviously is not the case in these cores. Thus, the lower carbonate flux implies a lower biogenic carbonate production in the overlying water column. If this suggestion is right, then the increase in carbonate production during glacial time would cause lower alkalinity and lower CO_2 in the atmosphere during the LGM. Several possible mechanisms could account for the higher non-carbonate flux during the LGM. It could be the result of an increase in ice-rafted debris (as suggested by Ruddiman, 1971), increase in terrigenous input due to a lower sea level lower, increase in eolian transport due to wind patterns (as suggested by Kolla *et al.*, 1979 and Leinen *et al.*, 1985), or all of these possibilities together.

Four cores selected show patterns of LGM/Holocene changes in carbonate flux that are anomalous compared to the general patterns seen in most of the other cores. Two cores (CHN 82-20 and CHN 82-15) are from about 42°N to 43°N in the Atlantic, where is a region found to have massive discharges of ice-rafted debris due to iceberg melting (when the ice front reaches its maximum seaward position), which are called "Heinrich layers" (Bond *et al.*, 1992; Broecker *et al.*, 1992; Heinrich, 1988). The first two "Heinrich layers", from radiocarbon dating, occurred at ~14,300 and ~21,000 years ago (Bond *et al.*, 1992; Broecker *et al.*, 1992; Heinrich, 1988). These two layers may have been picked up in some of the selected cores between the latitude 43°N to 55°N, which is the region where these events are distributed, for the LGM sections used for nuclide measurements. The bioturbation by benthic organisms can increase the possibility of mixing of the different time zones in the sediment sections. The extremely low concentrations of ^{230}Th and ^{231}Pa activities in samples may be indicative of these layers,

because their scavenging activities in the water column can be diluted due to massive discharges of detrital material. I suspect that this may be the case for the LGM sections of the two cores from about 42°N Atlantic, resulting in the higher carbonate and non-carbonate LGM flux compared to the Holocene flux. To be able to prove this explanation, additional measurements such as Mg/Ca ratios of the samples would need to be carried out (Francois and Bacon, 1994).

One core off Chesapeake bay (V26-176) also exhibited an increase of both carbonate and non-carbonate flux during the LGM, which may result from the increasing terrigenous input during the LGM, which may also input large amounts of detrital carbonate.

In this work, results of variations in the changes of non-carbonate flux between the LGM and the Holocene in the Atlantic show a consistent unique trend of the LGM having higher input flux compared to the flux during the Holocene. The terrigenous materials are the major phase of the non-carbonate sedimentary component since biogenic silica makes up only a few percent of the non-carbonate phase. The observations of higher input of terrigenous materials into the deep sea during the LGM are in agreement with other works in the Atlantic Ocean (Bacon, 1984; Curry and Lohman, 1986; Francois and Bacon, 1991). The high input of terrigenous materials into the deep sea during the LGM most likely indicates that when the sea level was low, rivers flowed across the continental shelves, which were above sea level, and discharged their load directly into deep water. Higher erosion rates in the northern latitudes must have also increased the load of many rivers fed directly by glaciers, whereas at low latitudes, intensification of the trade winds and more arid conditions in western tropical Africa resulted in large amounts of eolian transport.

4.5 CONCLUSIONS

A Pa/Th map for the Holocene in the Atlantic Ocean has revealed that large-scale fractionation between ^{231}Pa and ^{230}Th occurs in sediments. A unique feature of the Pa/Th distribution pattern is that the Southern Ocean (Atlantic sector) is the only region that displays consistently higher values of Pa/Th ratio than the production rate ratio of 0.093, i.e. ^{231}Pa enrichment; while the rest of the seafloor north of 45°S in the Atlantic shows depletion of ^{231}Pa. Although boundary scavenging is hinted at in some places, the Atlantic Ocean does not show the stong pattern of scavenging of ^{231}Pa relative to ^{230}Th on the ocean margins seen in the Pacific Ocean.

A simple mass balance model across the North Atlantic Ocean north of 25°N has quantified the influence of advection resulting from the thermohaline circulation on the fractionation of ^{231}Pa and ^{230}Th. This is an important factor controlling the distribution patterns of Pa/Th in the Atlantic Ocean. The model result shows that almost half of ^{231}Pa, while only 10% of ^{230}Th, produced from uranium decay in the water column in the North Atlantic Ocean is exported toward the South Atlantic and accumulates in the Southern Ocean sediments.

A simple box model also has demonstrated that the amount of exported ^{231}Pa from the North Atlantic Ocean plus *in situ* ^{231}Pa production in the water column can balance the deposition rate of ^{231}Pa in the sediments of the Southern Ocean. This is found for both the Last Glacial Maximum and the Holocene. In other words, the export of ^{231}Pa from the North Atlantic Ocean play an important role to control the budget of ^{231}Pa in the Southern Ocean. Consequently, this implies that the variations in Pa/Th ratio reflect variations not

only in particle flux (i.e., production), but also in the intensity or pattern of the thermohaline circulation. This is found to be true for the changes in Pa/Th ratios of the sediments beneath the Southern Ocean between the Last Glacial Maximum and the Holocene.

Finally, the changes in distribution patterns of Pa/Th ratio and the flux or the distribution patterns of the sedimentary components (carbonate and terrigenous materials) in the Atlantic Ocean are found to relate to variations in the glacial-interglacial climate cycle.

CHAPTER 5

VARIATIONS IN ^{231}PA, ^{230}TH, AND SEDIMENT FLUXES ACROSS THE FRONTAL ZONES IN THE SOUTHERN INDIAN OCEAN AND CHANGES SINCE THE LAST GLACIAL MAXIMUM

5.1 INTRODUCTION

In this chapter, I present the characteristics of the ^{231}Pa/^{230}Th ratio, and sedimentary particle flux in the southern Indian Ocean, and discuss how these characteristics might have changed between the Last Glacial Maximum (LGM) and the Holocene. The reasons for doing such work are discussed below.

5.1.1 Why do we care to reconstruct past changes in particle fluxes in the Southern Ocean?

Since the discovery of that atmospheric pCO_2 during the last glacial maximum was approximately 80 µatm lower than the pre-industrial level (Berner *et al.*, 1979; Delmas *et al.*, 1980; Neftel *et al.*, 1982), extensive efforts have been directed towards understanding which alternations in the biogeochemistry or circulation of the ocean were responsible for this change in atmospheric composition. Many models or scenarios have focussed on the role of high-latitude surface waters. The studies of Sarmiento and Toggweiler (1984), Siegenthaler and Wenk (1984), and Knox and McElory (1984) suggest that increased nutrient utilization by plankton or reduced vertical mixing in high-latitude surface waters could have lowered their surface water ΣCO_2, and thus

have lowered the pCO_2 of the glacial atmosphere. Geochemical indicators of overall productivity and nutrient utilization efficiency are equivocal about glacial-interglacial changes. Several such indicators, including $\delta^{13}C$, Cd/Ca ratio, $\delta^{15}N$, Ge/Si ratio, and opal burial rate have been applied. The change in calcium carbonate chemistry, by altering the distribution of carbonate ion in the ocean or changes in carbonate productivity, also attracted attention because it contributes to the changes in alkalinity in the ocean and would affect the pCO_2 (Broecker and Peng, 1989; Curry and Lohmann, 1990; Howard and Prell, 1992). In this chapter, both carbonate and biogenic opal were thus determined in selected cores to examine the changes in carbonate and biogenic opal preservation between the LGM and the Holocene.

Additional motivation is to evaluate the latitudinal variability in biogenic and non-biogenic particle fluxes in the southern Indian Ocean. Several dynamic oceanographic fronts extend roughly east-west across the southern Indian Ocean separating various water masses in this region. The main hydrographic fronts, the Subtropical Convergence (STC), the Subantarctic Front (SAF), and the Antarctic Polar Front (APF), are well-defined in the surface water of this region. At present, APF is a boundary with steep temperature, nutrient, and productivity gradients in the upper ocean column. There are also a marked lithogenic changes associated with the front, with calcareous oozes to the north and biosiliceous oozes to the south (Burckle and Cirilli, 1987; Morley, 1989; Froelich *et al.*, 1991). Thus, the sediment functions as an indicator of the latitudinal migration of the APF in the past.

5.1.2 Why do ^{231}Pa, ^{230}Th, $(^{231}Pa/^{230}Th)_{ex}{}^{o}$ measurements?

The investigations from sediment traps and water columns (see Chapter 3) have shown that first, ^{230}Th flux to the sefloor nearly equals the production rate in the overlying water column for entire ocean; thus it can be a reference for particle rain rate. Secondly, the extent of fractionation between ^{231}Pa and ^{230}Th could reflect a broad distribution pattern of particle flux and provide insight into changes in relative particle fluxes in different regions; thus, the $(^{231}Pa/^{230}Th)_{ex}{}^{o}$ ratio can provide an additional tool to confirm the pattern from $^{230}Th_{ex}{}^{o}$-normalized flux at a site.

In addition, since redistribution of ^{231}Pa in an ocean basin is also controlled by the extent of its lateral transport as well as by scavenging intensity, $(^{231}Pa/^{230}Th)_{ex}{}^{o}$ ratio can reveal the regional contrasts of deficit and excess of ^{231}Pa in terms of mass balance. It is of special interest to examine $(^{231}Pa/^{230}Th)_{ex}{}^{o}$ fluctuation at fronts corresponding to large variations in the flux of particles. Are high scavenging rates of ^{231}Pa and ^{230}Th due to high surface production? Can they provide us tools to identify and even quantify past changes in productivity? In this chapter, a transect cores in the region were selected to observe the response to the variations; core MD88-773 (52° 90'S, 109.8° E, water depth of 2460 m) was chosen to observe the variation with time. Moreover, since MD88-773 core is beneath immediately south of today's APF, the records of the variations in sedimentary fluxes and nuclide ratios can avoid systematic variations in glacial-interglacial cycles of movements in front position and their impact on the interpretation of the tim variations in the chemical properties and biogenic particle records (see the text in the later sections).

5.2 DEEP-SEA SEDIMENT SAMPLES

5.2.1 Core locations and physical setting in the region

The samples analyzed in this study came from trigger cores and piston cores (Eltanin cores, Antarctic Core Facility, Department of Geology, Florida State University) from a region between 28° and 62° S. Core locations are listed in Table 5.1 and shown in Figure 5.1. Waters between 40° S and the Antarctic continent can be divided into several well-defined circumpolar zones. North of the STC is the characteristic oligotrophic subtropical water, and the STC acts as a boundary to separate it from the subantarctic water. The APF is the boundary between the subantarctic water and the Antarctic water. The Subantarctic Front Zone (SAFZ) is defined as the region between the STC and APF. The PFZ (Polar Front Zone) is defined as the region which includes the APF and immediately south of the APF. The locations of the fronts are identified by their steep temperature or salinity gradients. During austral summer, the APF in the Indian Ocean sector of the Southern Ocean generally coincides with the 5° C surface isotherm, and during the austral winter, it coincides with the position of the 2-4° C surface isotherms. The position of the STC is marked at the surface by the 10° C to 14° C surface isotherms in winter, and the 14 °C to 18° C isotherms in summer (Deacon, 1982; Gordon, 1972; Gordon *et al.*, 1974; Edwards and Emery, 1982). The locations of the fronts in the Indian sector, according to Gordon (1972) and Edwards and Emery (1982), are 42° S (varying from 42° S to 44° S), 46° S (varying from 46° S to 48°S) and 51.7° S (varying from 50° S to 53° S) for the STC, SAF, and APF, respectively. The range of variation is due to the seasonal variations. Generally, the nutrient concentration is high and uniform in the waters south of the APF, but north of APF, the water shows greater variation in nutrients and temperature.

Table 5.1 Locations of selected sediment cores in the southern Indian Ocean

Core	*	LAT. (S)	LONG. (E)	Water Depth(m)	Depth (cm) Holocene	Depth (cm) LGM	Strat. Method	References **	LGM sample depth (cm)
E48-13	PC	28.31	93.30	3380	2 - 4	100-120	O-18	L	103/105 & 115/117
E48-11	TC	29.40	97.32	3462	4 - 6	30 - 40	O-18	E	30 - 40
E45-9	TC	29.49	102.14	4549	0 - 1				
E48-27	TC	38.33	79.54	3285	5 - 7	50-65	O-18	E	50 - 65
E48-22	TC	39.54	85.25	3378	5 - 7	60-85	Biostrat/O-18	E, H, K=M	60 - 85
E45-24	TC	40.09	104.11	4048	0 - 1				
E48-3	TC	41.01	100.01	3930	3 - 5	20-40	Biostrat	E, K=M	20 - 40
E45-27	TC	43.19	105.33	3776	5 - 7	30-40	Biostrat	E, K=M	31/33& 37/39
E45-29	TC	44.53	106.31	3863	7 - 9	45-65	O-18/DIAT.	B, C	45/47& 63/65
E45-79	TC	45.03	114.22	4079	4 - 6	25-50	DIAT./O-18	C, H	26/28 & 43/45
E45-74	TC	47.33	114.26	3744	4 - 6	20-40	DIAT./O-18	C, G, J, M	22/24 & 36/38
E45-71	TC	48.02	114.29	3658	5 - 7	40 - 48	DIAT.	C	41/43 & 46/48
E45-32	TC	50.31	109.35	3115	0 - 1				
E50-8	PC	50.56	104.55	3227	0 - 2	160 - 180	DIAT.	C	160 - 180
E49-6	TC	51.00	109.59	3326	1 - 3	40 - 48	DIAT.	C	42 - 48
E45-64	TC	52.29	114.05	3823	3 - 5	140 - 160	DIAT.	C	144/146 & 157/159
E45-63	TC	53.26	114.15	3915	2 - 4	140 - 160	DIAT.	C	142/144 & 157/159
E49-8	PC	55.04	110.01	3693	2 - 4	100 - 120	DIAT.	C	104/106 &118/120
E49-29	TC	57.06	94.57	4237	bag	40 - 48	DIAT.	C	42/44 & 46/48
E50-13	TC	60.00	105.00	4209	6 - 8	40 - 48	DIAT.	C	40 - 48
E45-47	TC	60.45	114.14	4291	0 - 1				
E50-17	TC	62.00	120.03	4081	3 - 5	90 - 100	DIAT.	C	92/94 & 97/99

*TC, core top from trigger core; PC, core top from piston core; all LGM samples were taken from piston cores.

**B=Charles, et al., 1991; C=Francois, et al., 1993; E=Prell et al., 1980; G=Williams and Keany, 1978; H=Williams et al., 1985; J=Shemesh et al., 1989; K=Williams, 1976; L=Mar. Micropal.1, 1976; M=Corliss, 1979.

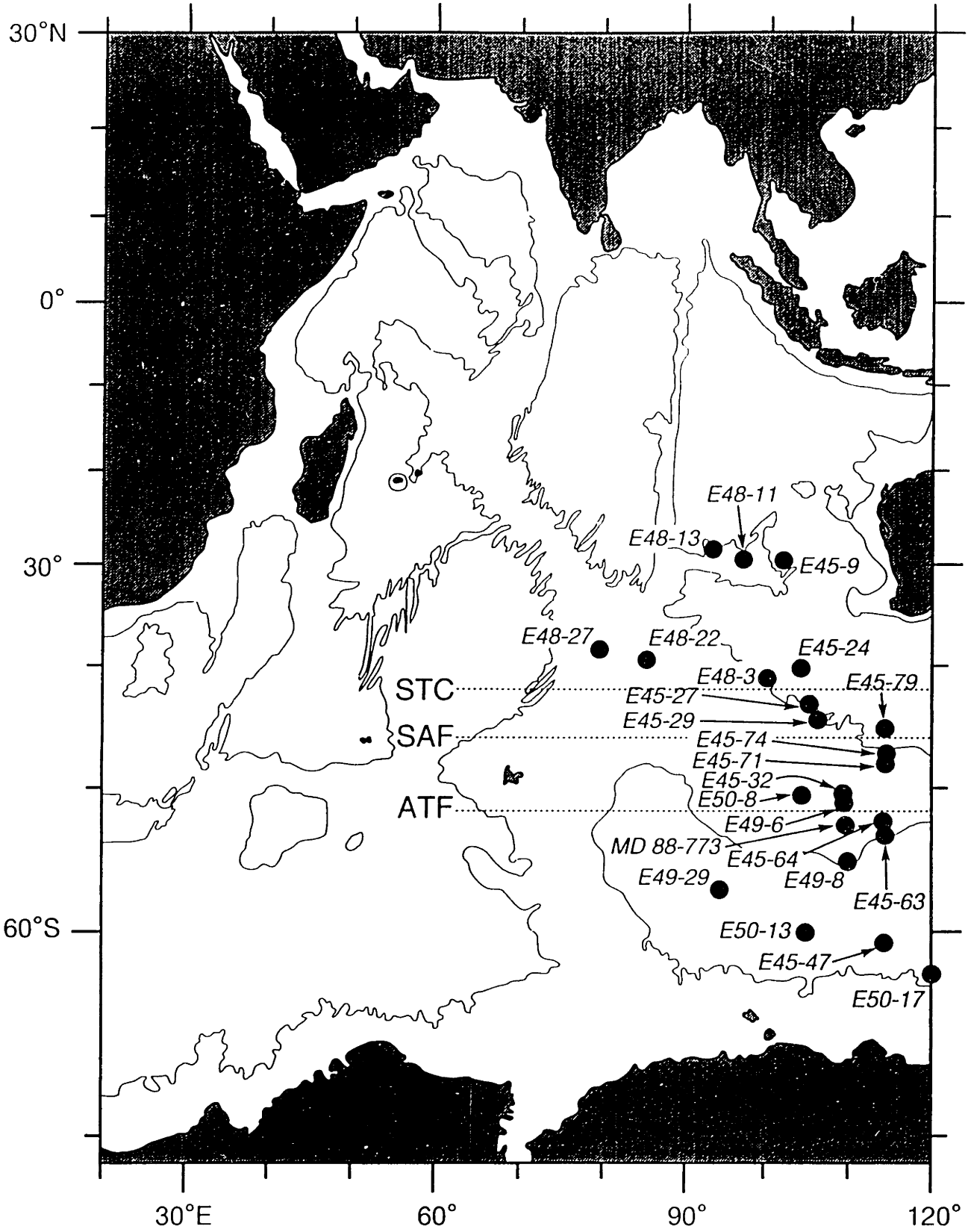

Figure 5.1 The map of selected cores from the southern Indian Ocean. Th locations of the fronts (STC=Subtropical Convergence, SAF=Subantarctic Front, and APF=Antarctic Polar Front) in this study region are also indicated.

5.2.2 Stratigraphy and sample selection

Twenty-two deep-sea cores in the Southern Indian Ocean were selected for this study. Sediment samples were taken from core tops and last glacial maximum (LGM) levels to assess changes in the intensity and latitudinal distribution of radionuclides and particle rain rates during two time intervals. Core tops were assumed to be Holocene in age. Two depths of samples within the LGM level (17 ka to 23 ka) were taken and made up into a homogeneous sample to represent the LGM level in each core. LGM depths in cores, also indicated in Table 5.1, were established either from their $\delta\,^{18}O$ records or diatom stratigraphies (Burckle and Cooke, 1982; Burckle, 1982; Burckle *et al.*, 1987). The stratigraphies of these samples were provided mainly by Dr. Burckle at LDEO. Many of these cores were also analyzed for $\delta\,^{15}N$ by Francois and Altabet (1992); the micropaleontological techniques for identifying the Holocene and LGM ages were described in detail in a published paper by Francois and Altabet (1992). In these samples, I analyzed ^{231}Pa, and Th and U isotopes. Percentages of opal and carbonate in the sediment samples were also determined; I calculated their fluxes, including terrigenous flux, by normalizing their contents to the unsupported initial ^{230}Th concentration.

5.2.3 Downcore profile on the APF in the southeastern Indian Ocean

The percentage of carbonate was measured in addition to the radionuclide contents. The core is from the location underlying immediately south of the present-day Polar Front (APF) in the southeastern Indian Ocean. The sample materials and the chronology data of core MD88-773 were kindly provided by

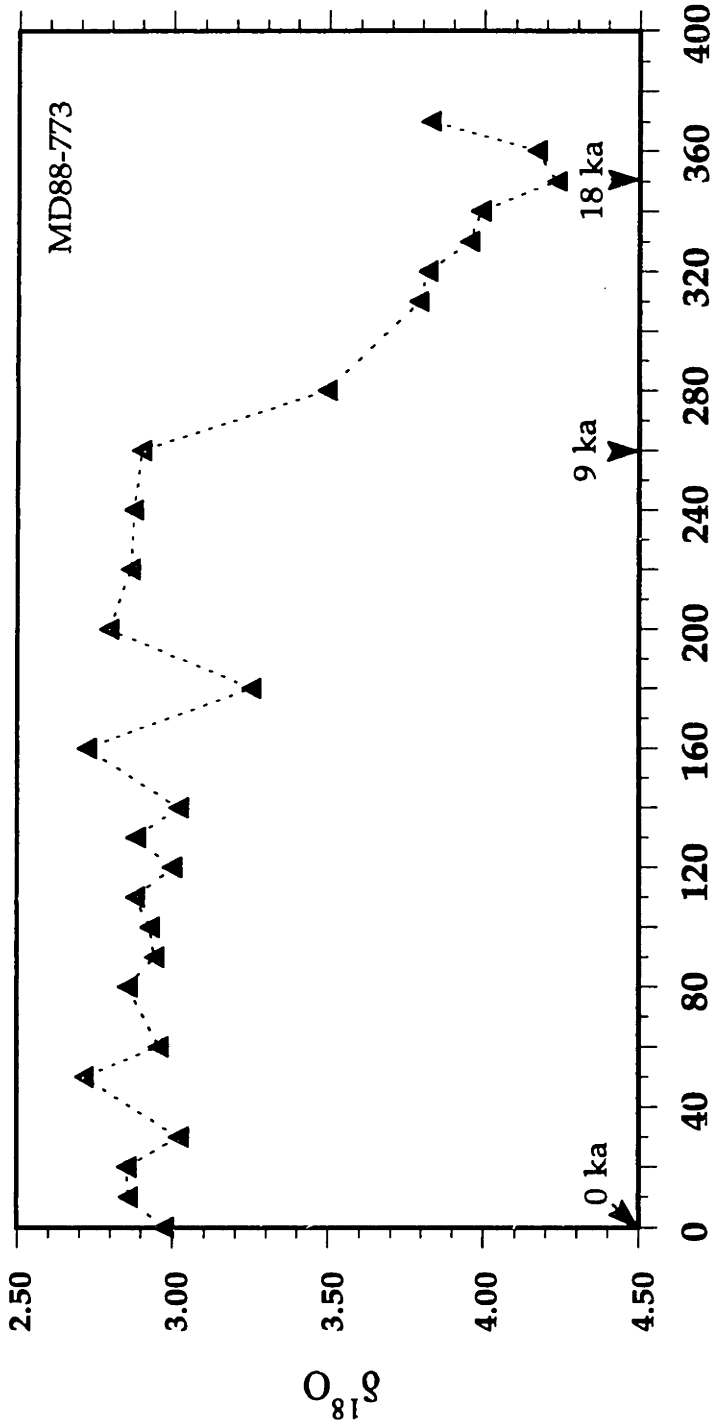

Figure 5.2 Oxygen isotope chronology of the core MD88-773. Data were provided by Dr. L. D. Labeyrie at Gif-sur-Yvette, France

Dr. Laurent D. Labeyrie of Gif-sur-Yvette, France. The chronology of MD88-773 was determined by Labeyrie from $\delta\,^{18}O$ stratigraphy (Figure 5.2). There were eighteen samples from the core top through the LGM sections, which I analyzed. The results are discussed in association with data from the transect to examine the latitudinal variations and time variations of Th and U isotopes, ^{231}Pa, and fluxes of major sedimentary components. The depth-time model results for establishing ages of MD88-773 were obtained by assigning the core depths 0 cm, 260 cm, and 350 cm as ages of 0 ka, 9 ka, and 18 ka, respectively. Between these depth, linear interpolation was used.

5.3. RESULTS

Radiochemical data are given in Tables 5.2 through 5.4. Decay-corrected unsupported radioactivities and the radioactive disequilibrium relationships for these samples are shown in Tables 5.5 and Table 5.6. The features of the radionuclide results are described as follows.

5.3.1 Uranium contents of the transect samples

As shown in Table 5.2, for the Holocene sections of the samples near the Antarctic continent, uranium concentrations are remarkably high. Lithogenic materials contribute a large fraction of the detrital uranium present in these samples, since their $^{238}U/^{232}Th$ activity ratios displayed an average crustal abundance of ^{238}U and ^{232}Th. The component of uranium which derived from seawater is estimated by measuring ^{232}Th and $^{238}U/^{232}Th$ activity ratios; the

Table 5.2: Measured radioisotopes of the Holocene transect sections from the southern Indian Ocean

Core	LAT.	LONG.	Depth (m)	Th230 (dpm/g)	Th232 (dpm/g)	Pa231 (dpm/g)	U234 (dpm/g)	U235 (dpm/g)	U238 (dpm/g)
E48-13	28.31	93.30	3380	15.14	0.25	0.38	0.24	6.90E-03	0.15
E48-11	29.40	97.32	3462	6.60	0.79	0.65		1.85E-02	0.40
E45-9	29.49		4549	14.57	0.25	0.36	0.24	8.90E-03	0.19
E48-27	38.33	79.54	3285	10.20	0.18	0.75	0.15	5.66E-03	0.12
E48-22	39.54	85.25	3378	8.93	0.17	0.56	0.18	6.16E-03	0.13
E45-24	40.09		4048	9.49	0.30	0.40	0.14	5.00E-03	0.11
E48-3	41.01	100.01	3930	17.46	0.26	0.82	0.13	6.06E-03	0.13
E45-27	43.19	105.33	3776	10.01	0.12	0.58	0.11	5.00E-03	0.11
E45-29	44.53	106.31	3863	14.85	0.13	0.69	0.15	5.80E-03	0.13
E45-79	45.03	114.22	4079	17.70	0.36	0.89	0.17	6.90E-03	0.15
E45-74	47.33	114.26	3744	11.94	0.17	0.91	0.36	1.28E-02	0.28
E45-71	48.02	114.29	3658	11.71	0.08	0.76	0.14	5.90E-03	0.13
E45-32	50.31		3115	7.16	0.17	1.10	0.31	1.90E-02	0.41
E50-8	50.56	104.55	3227	4.16	0.66	0.24	1.01	4.19E-02	0.91
E49-6	51.00	109.59	3326	9.50	0.13	1.15	0.45	1.83E-02	0.40
E45-64	52.29	114.05	3823	9.70	0.11	1.33	0.51	2.10E-02	0.46
E45-63	53.26	114.15	3915	9.46	0.16	1.30	0.60	2.21E-02	0.48
E49-8	55.04	110.01	3693	6.73	0.57	0.91	0.67	2.35E-02	0.51
E49-29	57.06	94.57	4237	11.17	1.47	1.12	0.78	3.55E-02	0.77
E50-13	60.00	105.00	4209	4.43	0.44	0.10		1.06E-02	0.23
E45-47	60.45		4291	4.27	3.69	0.25	1.06	6.00E-02	1.30
E50-17	62.00	120.03	4081	9.10	3.53	1.64	0.96	5.42E-02	1.18

Table 5.3: Measured radioisotopes of the LGM transect sections from the southern Indian Ocean

Core	LAT.	LONG.	Depth (m)	Th230 (dpm/g)	Th232 (dpm/g)	Pa231 (dpm/g)	U234 (dpm/g)	U235 (dpm/g)	U238 (dpm/g)
E48-13	28.31	93.30	3380	0.52	0.16	0.02	0.14	6.00E-03	0.13
E48-11	29.40	97.32	3462	0.38	0.18	0.02		7.41E-03	0.16
E45-9	29.49		4549	n.d.	n.d.	n.d.	n.d.	n.d.	n.d.
E48-27	38.33	79.54	3285	7.91	0.34	0.39	0.16	6.39E-03	0.14
E48-22	39.54	85.25	3378	7.09	0.20	0.33	0.13	5.92E-03	0.13
E45-24	40.09		4048	n.d.	n.d.	n.d.	n.d.	n.d.	n.d.
E48-3	41.01	100.01	3930	2.96	0.35	0.05	0.14	6.12E-03	0.13
E45-27	43.19	105.33	3776	13.27	0.60	0.73	0.21	9.50E-03	0.21
E45-29	44.53	106.31	3863	13.69	0.50	0.99	0.31	1.39E-02	0.30
E45-79	45.03	114.22	4079	17.00	0.63	1.06	0.31	1.39E-02	0.30
E45-74	47.33	114.26	3744	13.60	0.64	0.72	0.33	2.20E-02	0.48
E45-71	48.02	114.29	3658	7.82	0.34	0.44	0.25	9.40E-03	0.20
E45-32	50.31		3115	n.d.	n.d.	n.d.	n.d.	n.d.	n.d.
E50-8	50.56	104.55	3227	9.61	2.76		2.80	1.30E-01	2.82
E49-6	51.00	109.59	3326	4.71	0.67	0.49	0.45	1.97E-02	0.43
E45-64	52.29	114.05	3823	8.21	0.68	0.87	0.78	2.90E-02	0.63
E45-63	53.26	114.15	3915	6.84	0.64	0.95	0.67	3.38E-02	0.73
E49-8	55.04	110.01	3693	8.31	0.45	1.08	1.20	4.50E-02	0.98
E49-29	57.06	94.57	4237	4.18	0.75	0.20	0.57	2.64E-02	0.57
E50-13	60.00	105.00	4209	11.75	2.89	0.99	0.87	3.87E-02	0.84
E45-47	60.45		4291	n.d.	n.d.	n.d.	n.d.	n.d.	n.d.
E50-17	62.00	120.03	4081	6.24	4.46	0.53	1.12	5.59E-02	1.22

Table 5.4: Analytical results of radionuclides in core MD88-773

Depth	Age	230Th		232Th		231Pa		238U		235U		234U	
cm	ka	dpm/g	std.dev.	dpm/g	std.dev.	dpm/g	std.dev.	dpm/g	std.dev.	dpm/g	std.dev.	dpm/g	std.dev.
10	**0.35**	6.46	0.19	0.162	0.009	1.254	0.028	0.430	0.006	0.022	0.003	n.d.	
28	**0.97**	5.80	0.19	0.137	0.007	0.86	0.01	0.398	0.003	0.0204	0.0004	n.d.	
47	**1.63**	6.42	0.13	0.136	0.007	1.02	0.04	0.397	0.009	0.0185	0.0004	0.70	0.03
68	**2.35**	7.03	0.21	0.160	0.004	1.24	0.04	0.426	0.007	0.021	0.001	0.74	0.01
98	**3.39**	6.05	0.13	0.155	0.004	1.13	0.03	0.438	0.005	0.019	0.001	0.68	0.06
128	**4.43**	6.08	0.16	0.149	0.003	1.152	0.029	0.397	0.008	0.0182	0.0004	0.74	0.03
158	**5.47**	6.41	0.27	0.160	0.004	1.00	0.02	0.361	0.004	0.0164	0.0004	0.61	0.02
190	**6.58**	4.60	0.09	0.126	0.004	0.99	0.02	0.331	0.010	0.0158	0.0004	n.d.	
268	**9.80**	6.48	0.12	0.247	0.005	1.21	0.04	0.571	0.010	0.0254	0.0004	0.84	0.01
299	**12.90**	3.93	0.09	0.248	0.006	0.85	0.02	0.448	0.009	0.021	0.001	0.73	0.01
309	**13.90**	3.41	0.07	0.188	0.004	lost		0.376	0.006	0.018	0.001	0.70	0.01
329	**15.90**	4.22	0.05	0.312	0.015	0.74	0.01	0.467	0.006	0.0216	0.0004	0.60	0.01
350	**18.00**	5.45	0.08	0.437	0.021	0.95	0.03	0.690	0.010	0.033	0.001	1.04	0.02
368	**19.80**	6.01	0.13	0.916	0.013	0.905	0.022	1.223	0.019	0.057	0.002	1.67	0.10
388	**21.80**	7.43	0.08	0.833	0.046	0.825	0.021	1.954	0.021	0.084	0.001	2.60	0.06
415	**24.50**	6.82	0.16	0.875	0.021	1.12	0.04	2.465	0.037	0.109	0.024	3.63	0.09
455	**28.50**	6.35	0.16	0.919	0.012	0.91	0.02	1.950	0.047	0.096	0.002	3.02	0.04
485	**31.50**	6.11	0.12	0.705	0.007	0.96	0.03	1.775	0.030	0.081	0.002	2.55	0.07

Table 5.5: Calculated data of the radioisotopes for the Holocene and the LGM transect samples

Core	Th230exo dpm/g HL	231Paexo dpm/g HL	230Thexo/232Th HL	234U/238U HL	238U/232Th HL	231Pa/230Thex0 HL	Authigenic U dpm/g HL
E48-13	14.94	0.37	59.76	1.60	0.60	0.025	-0.05
E48-11	5.96	0.62	7.52		0.51	0.104	-0.23
E45-9	14.37	0.35	58.19	1.24	0.78	0.024	0.00
E48-27	10.06	0.74	56.19	1.23	0.69	0.074	-0.02
E48-22	8.79	0.56	50.52	1.31	0.77	0.063	-0.01
E45-24	9.25	0.39	31.26	1.29	0.37	0.042	-0.13
E48-3	17.25	0.81	65.84	1.02	0.50	0.047	-0.08
E45-27	9.91	0.58	81.25	1.01	0.89	0.058	0.01
E45-29	14.75	0.69	112.56	1.19	0.96	0.046	0.02
E45-79	17.41	0.88	48.22	1.13	0.42	0.050	-0.14
E45-74	11.80	0.90	68.62	1.29	1.62	0.077	0.14
E45-71	11.65	0.76	149.33	1.09	1.64	0.065	0.07
E45-32	7.02	1.09	40.35	0.75	2.37	0.156	0.27
E50-8	3.63	0.21	5.52	1.11	1.38	0.058	0.38
E49-6	9.39	1.15	70.63	1.12	2.99	0.122	0.29
E45-64	9.62	1.33	91.58	1.12	4.35	0.138	0.37
E45-63	9.33	1.29	58.88	1.25	3.03	0.139	0.35
E49-8	6.27	0.89	11.03	1.31	0.90	0.142	0.05
E49-29	9.99	1.07	6.80	1.01	0.52	0.107	-0.40
E50-13	4.07	0.09	9.20		0.52	0.021	-0.12
E45-47	1.32	0.11	0.36	0.81	0.35	0.083	-1.65
E50-17	6.28	1.51	1.78	0.81	0.33	0.241	-1.64

Table 5.5 (Con't)

Core	Th230ex0 dpm/g LGM	231Paex0 dpm/g LGM	230Thex/232Th LGM	234U/238U LGM	238U/232Th LGM	231Pa/230Thex0 LGM	Authigenic U dpm/g LGM
E48-13	0.47	0.03	2.90	1.07	0.81	0.057	0.00
E48-11	0.28	0.02	1.56	0.00	0.89	0.069	0.02
E45-9							
E48-27	9.01	0.55	26.49	1.12	0.41	0.061	-0.13
E48-22	8.18	0.47	40.68	1.00	0.64	0.058	-0.03
E45-24							
E48-3	3.16	0.05	9.03	1.05	0.38	0.017	-0.15
E45-27	15.10	1.04	25.33	1.02	0.35	0.069	-0.27
E45-29	15.68	1.42	31.36	1.03	0.60	0.091	-0.10
E45-79	19.46	1.52	30.82	1.03	0.48	0.078	-0.20
E45-74	15.45	1.02	24.29	0.69	0.75	0.066	-0.03
E45-71	8.91	0.63	26.12	1.22	0.60	0.070	-0.07
E45-32							
E50-8	8.74		3.17	0.99	1.02		0.61
E49-6	4.93	0.68	7.38	1.05	0.64	0.138	-0.11
E45-64	9.05	1.24	13.30	1.23	0.93	0.137	0.09
E45-63	7.47	1.36	11.67	0.91	1.15	0.181	0.22
E49-8	9.38	1.56	20.65	1.23	2.15	0.166	0.62
E49-29	4.22	0.25	5.59	0.99	0.76	0.060	-0.03
E50-13	11.14	1.30	3.86	1.03	0.29	0.116	-1.47
E45-47							
E50-17	3.15	0.54	0.71	0.92	0.27	0.170	-2.35

Table 5.6 Calculated results of radionuclides and measured components results in core MD88-773

Depth cm	Age ka	Authigenic U dpm/g	230Thex dpm/g	231Paex dpm/g	230Thexo dpm/g	231Paexo dpm/g	(231Pa/230Th)exo
10	**0.35**	0.30	6.32	1.25	6.34	1.26	0.198±0.008
28	**0.97**	0.29	5.69	0.85	5.74	0.87	0.152±0.005
47	**1.63**	0.29	6.31	1.02	6.40	1.05	0.164±0.007
68	**2.35**	0.30	6.89	1.23	7.05	1.29	0.183±0.008
98	**3.39**	0.31	5.91	1.12	6.10	1.20	0.197±0.007
128	**4.43**	0.28	5.95	1.15	6.20	1.25	0.202±0.008
158	**5.47**	0.23	6.27	0.99	6.59	1.10	0.167±0.008
190	**6.58**	0.23	4.49	0.98	4.77	1.12	0.235±0.007
268	**9.80**	0.37	6.25	1.20	6.84	1.45	0.212±0.008
299	**12.90**	0.25	3.70	0.84	4.17	1.09	0.261±0.009
309	**13.90**	0.23	3.23		3.67		
329	**15.90**	0.22	3.94	0.73	4.56	1.00	0.219±0.003
350	**18.00**	0.34	5.04	0.93	5.95	1.32	0.223±0.006
368	**19.80**	0.49	5.18	0.86	6.22	1.28	0.205±0.006
388	**21.80**	1.29	6.50	0.77	7.94	1.19	0.150±0.003
415	**24.50**	1.77	5.71	1.06	7.16	1.71	0.239±0.008
455	**28.50**	1.21	5.29	0.85	6.88	1.49	0.217±0.006
485	**31.50**	1.21	5.20	0.91	6.95	1.69	0.243±0.006

Table 5.6 (Con't)

Depth cm	Total flux (g/cm2/ka)	% carbonate	carbonate flux g/cm2/ka	non-carbonate flux g/cm2/ka
10	1.02	12.8	0.13	0.89
28	1.13	14.7	0.17	0.96
47	1.01	13.1	0.13	0.88
68	0.92	13.6	0.12	0.79
98	1.06	17.1	0.18	0.88
128	1.04	14.4	0.15	0.89
158	0.98	15.6	0.15	0.83
190	1.36	13.5	0.18	1.17
268	0.95	36.4	0.34	0.60
299	1.55	16.5	0.26	1.30
309	1.76	25.4	0.45	1.31
329	1.42	11.8	0.17	1.25
350	1.09	12.8	0.14	0.95
368	1.04	7.4	0.08	0.96
388	0.81	5.9	0.05	0.77
415	0.90	11.6	0.10	0.80
455	0.94	9.1	0.09	0.85
485	0.93	11.7	0.11	0.82

formula to compute the authigenic uranium is same as used in Chapter 3. The authigenic uranium activity is relatively higher in most of the sediment cores underlying the present-day position of the Polar Front Zone (Table 5.5). The authigenic uranium makes up 40% to 80% of the total uranium for the Holocene sections for these samples in PFZ.

For LGM sections, a higher value of total uranium is still found in the southernmost core; slightly higher values of total uranium are found in the LGM sections relative to the Holocene sections of the cores in the PFZ and SAFZ. The authigenic uranium of samples in the PFZ, however, shows a large scatter in the changes between the LGM and the Holocene.

5.3.2 Unsupported Activities of ^{230}Th and ^{231}Pa of the transect samples

The unsupported initial (decay-corrected) concentrations of ^{231}Pa and ^{230}Th were calculated using equations 4-1 and 4-2 in Chapter 4. The ages of sediment samples used for decay-correction of ^{230}Th and ^{231}Pa were based on the chronologies of the cores given in Table 5.1. The ages of the core-top were assigned as 0 ka, and the LGM level sediments were assigned 18 ka. Table 5.5 provides calculated results of decay/ingrowth-corrected scavenged ^{230}Th and ^{231}Pa, based on the above calculations for both Holocene and LGM sections. These values are the activity of these nuclides at the time the sediments were deposited. The unsupported activities of radionuclides on both Holocene and LGM transect samples display a random variation. The lower activity of $^{230}Th_{ex}{}^{0}$ is found at the PFZ for the Holocene transect. In contrast, the $^{231}Pa_{ex}{}^{0}$ activity is relatively higher in the cores from the PFZ for the Holocene sections. A peak of the $^{230}Th_{ex}{}^{0}$ activity is found to be coincidentally at the position of

SAFZ during the LGM; while peaks of $^{231}Pa_{ex}{}^{o}$ are found in both SAFZ and PFZ regions.

5.3.3 Radionuclide results from MD88-773

Total uranium and authigenic uranium of MD88-773 are plotted in Figure 5.3. A pronounced increase in total uranium is found starting at the LGM (18 ka) and still remains high during the late isotopic stage 3, while much lower activities are found during the deglacial and the Holocene. Detrital uranium in isotopic stage 2 and late stage 3 also show higher values than those during the Holocene; however, detrital uranium has contributed to only a small fraction of the total uranium, while the rest is authigenic, implies that uranium may have been added to the sediment as a result of reducing condition in the sediment (Cochran and Krishnaswami, 1980; Barnes and Cochran, 1990; Klinkhammer and Palmer, 1991). The calculated results of $^{230}Th_{ex}{}^{o}$ and $^{231}Pa_{ex}{}^{o}$ for MD88-773 are based on the chronologies given in Table 5.4 and the data shown in Table 5.6.

5.4 DISCUSSION

5.4.1 ^{230}Th-normalized paleoflux

5.4.1-a The ^{230}Th-normalized total flux for the Holocene transect samples

The ^{230}Th-normalized flux method is applied to reconstruct the particle flux in the present and past ocean. The equations (3-10 and 3-11) are used to compute the flux.

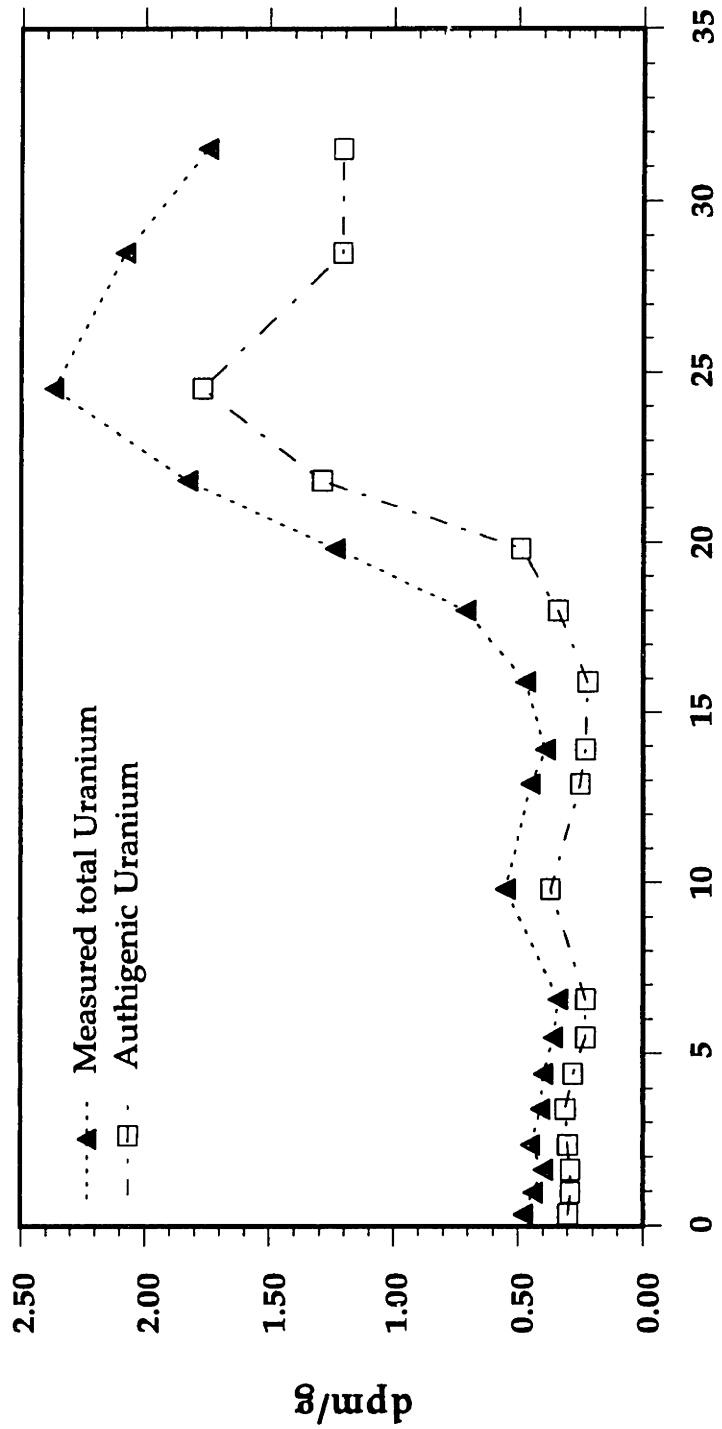

Figure 5.3 Total uranium and authigenic uranium versus age in core MD88-773. Authigenic uranium is calculated from equation (3-3).

The method tends to correct for post-depositional sediment redistribution, and provide information on net rain rate after dissolution. The flux, therefore, is interpretated as net rain rate after dissolution. These fluxes, it should be emphasized, are representative of pelagic rain rate rather than sediment accumulation rate; each data point represents a measurement of flux at that particular time. The latitudinal variations in ^{230}Th-normalized total flux for the Holocene and LGM sections of the transect samples selected for this study are plotted in Figures 5.4 a and b.

The values of total flux range from 0.6 to an extremely high value of 8.56 g/cm2/ka (Figure 5.4a). The extremely high value occurs in the E45-47 core top, which contains low activities of both ^{230}Th and ^{231}Pa. The core top was taken from a trigger core, which is believed to provide minimal disturbance, so contamination by older materials from the deeper sections of the core is a less plausible explanation for the extremely low activities of ^{230}Th and ^{231}Pa. Sediment composition in the E45-47 core top (Table 5.7) indicates that the high flux of this sample is mainly due to an extremely high flux of terrigenous materials; the flux values of opal and carbonate remain very low. The low concentrations of ^{230}Th and ^{231}Pa and extremely high terrigenous flux suggest a massive input of ice-rafted material from the continent. Comparatively high ^{230}Th-normalized total flux is also noticed in two other core tops (E50-8 and E50-13). The high flux seen in E50-13 might also be due to dilution by massive ice-rafted debris as seen in E45-47. Unlike the cores E45-47 and E50-13, the opal component of the E50-8 core top (immediately south of the APF at ca. 52° S, Gordon, 1982) constitutes a large portion of the sample. These two core tops (E50-8 and E50-13) were taken from piston cores, so they might be contaminated with older materials from the deeper core sections, however.

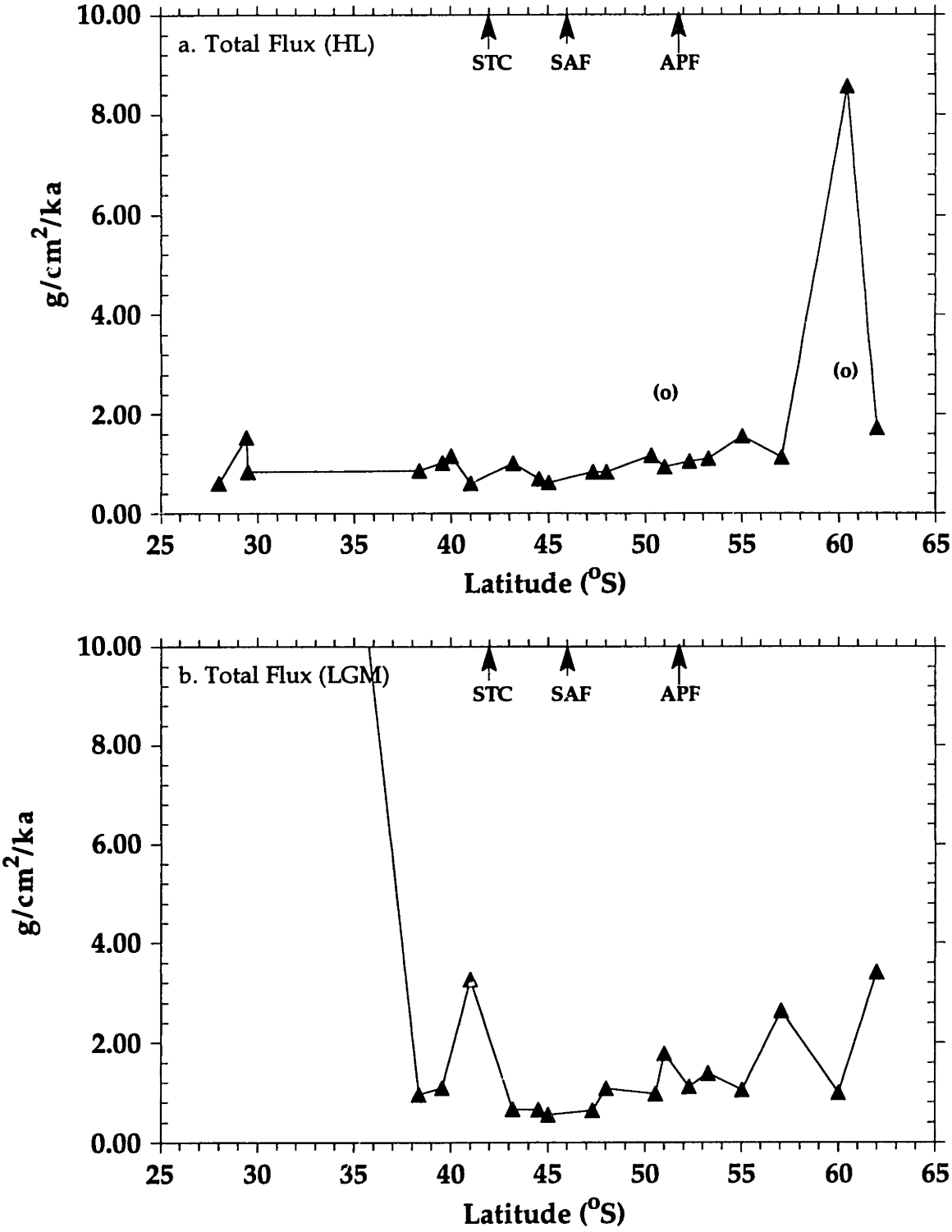

Figure 5.4 ^{230}Th-normalized total flux of the Holocene sections (a) and LGM sections (b) of the transect sediments from the southern Indian Ocean.

Table 5.7: Contents and 230Th-normalized fluxes of sediment components of transect samples

Core	LAT.	%Opal	% Carbonate	%Terrigenous	Opal flux g/cm2/ky	Carbonate flux g/cm2/ky	Terrigenous flux (g/cm2/ka)	Total Flux (g/cm2/ka)
		HL	HL	HL	HL	HL	HL	HL
E48-13	28.31	0.08	93.70	6.22	0.000	0.558	0.04	0.60
E48-11	29.40		93.30			1.425	0.10	1.53
E45-9	29.49	0.49	94.10	5.41	0.004	0.783	0.05	0.83
E48-27	38.33	1.33	92.70	5.97	0.011	0.796	0.05	0.86
E48-22	39.54	0.82	93.10	6.08	0.008	0.941	0.06	1.01
E45-24	40.09	1.62	91.80	6.58	0.019	1.056	0.08	1.15
E48-3	41.01	1.73	91.60	6.67	0.010	0.549	0.04	0.60
E45-27	43.19	1.18	86.60	12.22	0.012	0.868	0.12	1.00
E45-29	44.53	2.21	91.23	6.56	0.015	0.629	0.05	0.69
E45-79	45.03	3.15	88.60	8.25	0.019	0.546	0.05	0.62
E45-74	47.33	3.60	91.85	4.55	0.030	0.766	0.04	0.83
E45-71	48.02	3.75	91.60	4.65	0.031	0.757	0.04	0.83
E45-32	50.31	47.77	39.50	12.73	0.557	0.461	0.15	1.17
E50-8	50.56	44.25	17.65	38.10	1.033	0.412	0.89	2.33
E49-6	51.00	49.23	33.50	17.27	0.458	0.312	0.16	0.93
E45-64	52.29	62.40	11.75	25.85	0.652	0.123	0.27	1.05
E45-63	53.26	80.22	11.60	8.18	0.885	0.128	0.09	1.10
E49-8	55.04	57.13	0.60	42.27	0.884	0.009	0.65	1.55
E49-29	57.06	75.82	0.95	23.23	0.846	0.011	0.26	1.12
E50-13	60.00		6.15			0.167		2.72
E45-47	60.45	8.74	1.55	89.71	0.748	0.133	7.68	8.56
E50-17	62.00	31.36	5.45	63.20	0.536	0.093	1.08	1.71

Table 5.7 (con't)

Core	LAT.	%Opal	% Carbonate	Terrigenous%	Opal Flux (g/cm2/ka)	Carbonate flux (g/cm2/ka)	Terrigenous flux (g/cm2/Ka)	Total Flux (g/cm2/Ka)
		LGM	LGM	LGM	LGM	LGM	LGM	LGM
E48-13	28.31	0.04	95.17	4.79	0.008	18.142	0.91	19.06
E48-11	29.40	0.09	93.80	6.11	0.029	30.258	1.97	32.26
E45-9	29.49							
E48-27	38.33	2.80	88.57	8.63	0.027	0.849	0.08	0.96
E48-22	39.54	1.53	91.20	7.27	0.017	0.991	0.08	1.09
E45-24	40.09							
E48-3	41.01	2.92	91.95	5.13	0.096	3.008	0.17	3.27
E45-27	43.19	6.85	78.50	14.65	0.045	0.516	0.10	0.66
E45-29	44.53	14.34	62.43	23.23	0.093	0.404	0.15	0.65
E45-79	45.03	14.65	65.80	19.55	0.081	0.363	0.11	0.55
E45-74	47.33	17.25	67.60	15.15	0.110	0.431	0.10	0.64
E45-71	48.02	20.79	65.20	14.01	0.225	0.704	0.15	1.08
E45-32	50.31							
E50-8	50.56	95.00	5.00		0.922	0.049		0.97
E49-6	51.00	73.94	2.40	23.66	1.313	0.043	0.42	1.78
E45-64	52.29	60.96	1.00	38.04	0.678	0.011	0.42	1.11
E45-63	53.26	69.10	2.40	28.50	0.953	0.033	0.39	1.38
E49-8	55.04	48.65	2.35	49.00	0.504	0.024	0.51	1.04
E49-29	57.06	65.86	3.55	30.59	1.741	0.094	0.81	2.64
E50-13	60.00	47.42	2.00	50.58	0.471	0.020	0.50	0.99
E45-47	60.45							
E50-17	62.00	12.37	5.45	82.18	0.421	0.186	2.80	3.41

The ^{230}Th-normalized total flux in Holocene samples from the Polar Front Zone on average are higher than those in the SAFZ. The range of total flux (0.93 to 1.55 g/cm2/ka, if I exclude two extremely high values from the samples near the continent as mentioned above) in the PFZ is higher than that in the SAFZ and north of the STC (0.6 to 1.13 g/cm2/ka). Sediment composition in the PFZ indicates that biogenic opal contributes most of the total flux; while in the SAFZ and north of the STC, carbonate is the dominant component.

5.4.1-b The differences in the ^{230}Th-normalized total flux between the Holocene and the LGM of the transect samples

Data from LGM sections (Figure 5.4b) show that latitudinal features in all distribution patterns of total flux are similar to those in the Holocene data. The two northernmost LGM sections (cores E48-13 and E48-11) have abnormally high values of total flux. The two cores have no associated trigger cores (D. S. Cassidy, personal communication), as their recovery was not successful; thus, the two core tops were taken from the piston cores, so the values may be false because either an older sample was selected or the sample was contaminated with older material. These data will thus not be included in the discussion. The changes of ^{230}Th-normalized flux between LGM and Holocene samples are expressed as a ratio of LGM/Holocene (Table 5.8) and are plotted in Figure 5.5. With few exceptions, I found that the extent and patterns of total flux show no significant changes between the two time intervals.

5.4.1-c The latitudinal variations in extent of sediment focusing

Table 5.8: Changes of composition and 230Th-normalized fluxes between Holocene and LGM of transect sections

Core	LAT.	%Opal	% Carbonate	Opal Flux (g/cm2/ka)	Carbonate flux (g/cm2/ka)	Total Flux (g/cm2/Ka)	(231Pa/230Th)ex0
		LGM/HL	LGM/HL	LGM/HL	LGM/HL	LGM/HL	LGM/HL
E48-13	28.31	0.50	1.02	16.02	32.54	32.04	2.28
E48-11	29.40		1.01		21.23	21.12	0.67
E48-27	38.33	2.11	0.96	2.35	1.07	1.12	0.82
E48-22	39.54	1.87	0.98	2.01	1.05	1.08	0.92
E48-3	41.01	1.69	1.00	9.21	5.48	5.46	0.37
E45-27	43.19	5.81	0.91	3.81	0.60	0.66	1.19
E45-29	44.53	6.49	0.68	6.10	0.64	0.94	1.95
E45-79	45.03	4.65	0.74	4.16	0.66	0.89	1.55
E45-74	47.33	4.79	0.74	3.66	0.56	0.76	0.86
E45-71	48.02	5.54	0.71	7.25	0.93	1.31	1.08
E50-8	50.56	2.15	0.28	0.89	0.12	0.42	
E49-6	51.00	1.50	0.07	2.86	0.14	1.91	1.13
E45-64	52.29	0.98	0.09	1.04	0.09	1.06	0.99
E45-63	53.26	0.86	0.21	1.08	0.26	1.25	1.31
E49-8	55.04	0.85	3.92	0.57	2.62	0.67	1.17
E49-29	57.06	0.87	3.74	2.06	8.85	2.37	0.56
E50-13	60.00		0.33		0.12	0.37	5.53
E50-17	62.00	0.39	1.00	0.79	1.99	1.99	0.71

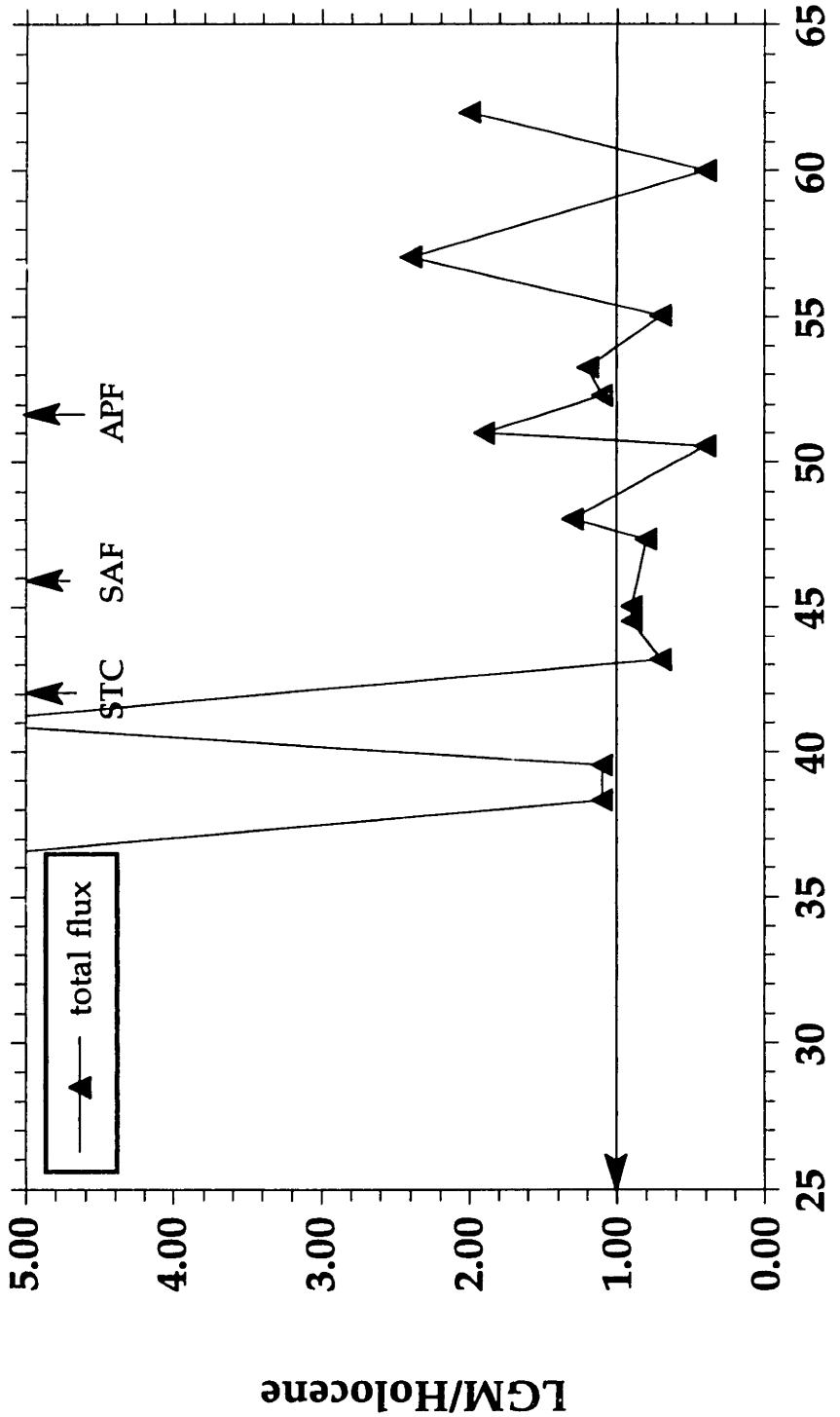

Figure 5.5 LGM/Holocene ratio of ^{230}Th-normalized total flux versus latitude for the transect samples in the southern Indian Ocean.

Sediment redistribution by bottom currents is common and can lead to errors in flux estimates based on sediment accumulation rates. As proposed, ^{230}Th-normalized flux estimation can correct the error which results from such sediment redistribution processes. In the following, I will compare the sediment mass accumulation rate with the ^{230}Th-normalized total flux to examine whether sediment redistribution significantly affects the traditional estimation of sediment accumulation rate in this region.

Sediment mass accumulation rate (MAR) can be calculated from the assigned chronology and bulk sediment density. I used the average sedimentation rate between the Holocene and LGM sections, assuming the time interval to be 18 ka. Dry bulk sediment density (ρ) is estimated from the following relationship between %$CaCO_3$ and dry bulk density as determined by Froelich *et al.* (1991) for southern ocean sediments:

$$\rho = 5.313e\text{-}5[CaCO_3]^2 + 9.346e\text{-}4[CaCO_3] + 0.3367 \qquad (5\text{-}4)$$

The comparison between MAR and ^{230}Th-normalized total flux is shown in Figure 5.6. Although there is a large uncertainty from the estimation of sedimentation rate, it is still obvious that the two records of MAR and ^{230}Th-normalized total flux show a dramatic difference in the area between 48° S and 57° S. Sediment mass accumulation rate is 1.5- to 2.5-fold higher than ^{230}Th-normalized total flux in this region. The neighboring areas north of the PFZ and further southward did not show significant differences between the two records. This same feature has been seen in the SW Indian Ocean by Francois et al. (1993) and in the Equatorial Atlantic (Francois et al., 1990). Based on same approach as I have shown above, Francois et al., (1993) argue that the sediment redistribution

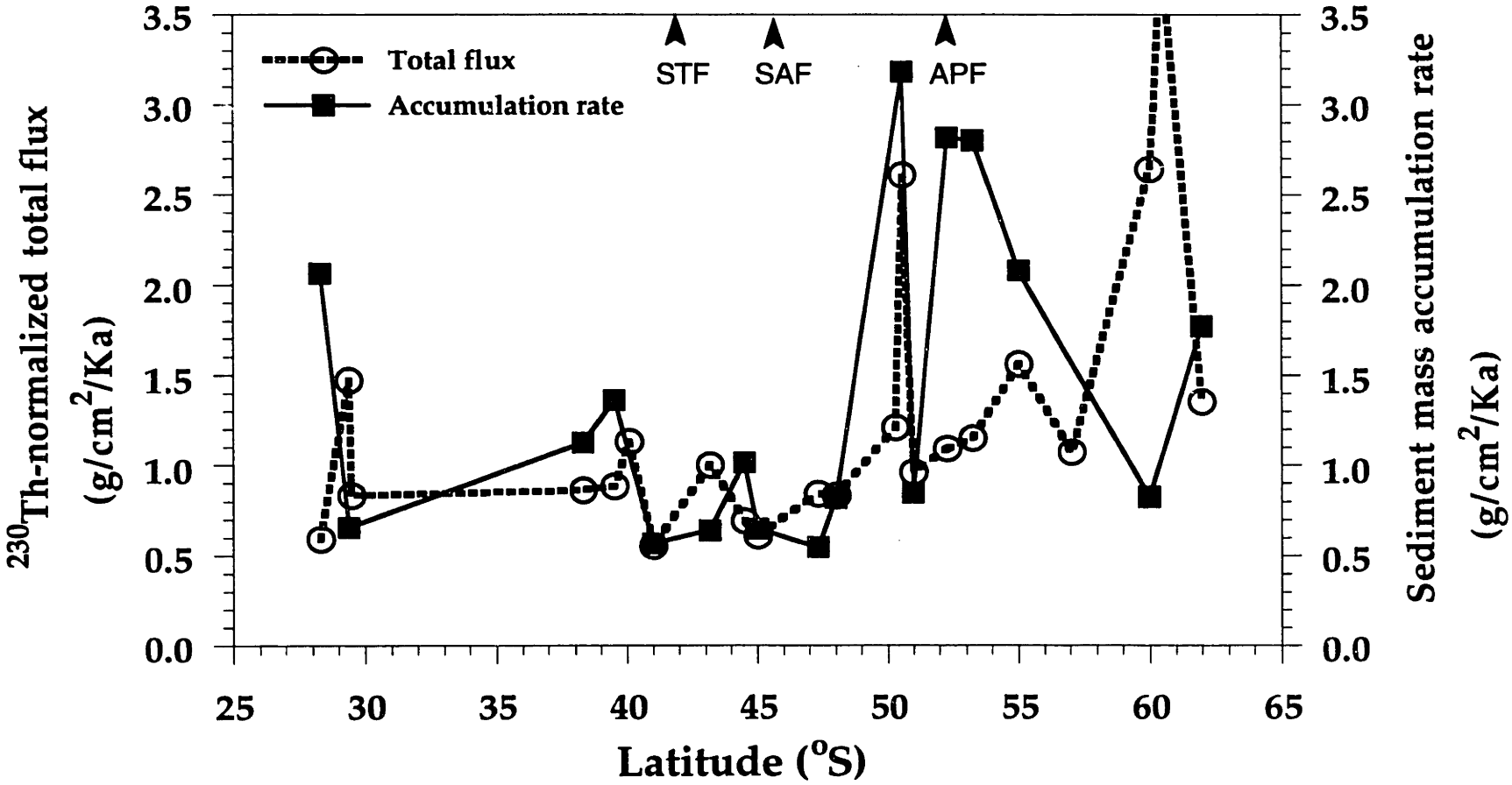

Figure 5.6 Comparison between the ^{230}Th-normalized total flux and the sediment mass accumulation rate for the Holocene transect samples in the southern Indian Ocean.

processes are especially significant in the Southern Ocean because of the presence normalized total flux show a dramatic difference in the area between 48° S and 57° S. Sediment mass accumulation rate is 1.5- to 2.5-fold higher than ^{230}Th-normalized total flux in this region. The neighboring areas north of the PFZ and further southward did not show significant differences between the two records. This same feature has been seen in the SW Indian Ocean by Francois et al. (1993) and in the Equatorial Atlantic (Francois et al., 1990). Based on same approach as I have shown above, Francois et al., (1993) argue that the sediment redistribution processes are especially significant in the Southern Ocean because of the presence of relatively strong abyssal currents associated with the Antarctic Circumpolar Current and Antarctic Bottom Water. High bottom water velocities responsible for the presence of scour zones was suggested by Watkins and Kennett (1972) and Anderson (1990). Sediment winnowed from these areas is eventually deposited in regions of lower current intensity, where sediment accumulation must be in excess of the vertical particle flux originating from surface water. This example illustrates the value of normalizing the accumulation rate of elements, nuclides, or solid phases to a tracer such as ^{230}Th whose known source permits lateral redistribution to be identified and regional burial rates to be evaluated.

5.4.1-d Change in the focusing factor with time

With the MD88-773 core, I can examine variations of sediment focusing with time. Suman and Bacon (1989) define a focusing factor (ψ) as the ratio of ^{230}Th accumulated on the seafloor to ^{230}Th produced in the overlying water column during a time interval:

$$\psi = \frac{1}{\beta Z (t1-t2)} \int_{r2}^{r1} ex[230Th]o\rho \, dr \qquad (5\text{-}5)$$

where $_{ex}[230Th]o$ is the activity of the decay- and ingrowth-corrected excess ^{230}Th in the sediment, r is depth in the core, and t is the age of horizon r. The values ρ, β, and z are dry bulk density, production factor of ^{230}Th in the overlying water column, and water depth, respectively.

Application of equation (5-5) to different sections of core MD88-773 (Table 5.9) indicates that the amount of ^{230}Th which accumulated at the coring location exceed that which was produced in the overlying water column by a factor four during isotopic stage 3 and by as much as a factor about ten during the Holocene, confirming that a large fraction of the sediment reaching the coring site during these periods was brought by syndepositional redistribution processes. This observation in MD88-773 from the southeastern Indian Ocean is in agreement with those in the southwestern Indian Ocean by Francois et al. (1993). During isotopic stage 2, ψ is relatively less than during isotopic stage 3 and the Holocene.

5.4.2 Variations in $(^{231}Pa/^{230}Th)_{ex}{}^{o}$ ratio

In this section, the latitudinal variations in the $(^{231}Pa/^{230}Th)_{ex}{}^{o}$ ratio from the Holocene and LGM sections of the transect samples are discussed. First, I will describe variation in $(^{231}Pa/^{230}Th)_{ex}{}^{o}$ and discuss the factors causing the fractionation between the two reactive nuclides in this study region. The changes in $(^{231}Pa/^{230}Th)_{ex}{}^{o}$ ratio between LGM and the Holocene and the possible reasons for the change will be discussed. Finally, I offer the study of a downcore

Table 5.9 Calculation of focusing factor for core MD88-773

Depth cm	Age ka	density g/cm3	[230Th] dpm/g	230Th accumulation dpm/cm2	230Th production dpm/cm2	Focusing Factor
0-268	0-9.80	0.36	6.23±0.21	601.07±20.26	63.40	9.5±0.3
268-415	9.80-24.50	0.38	5.42±0.59	302.76±32.96	95.11	3.2±0.3
415-485	24.50-31.50	0.35	7.00±0.07	171.50±1.72	45.29	3.79±0.04

profile (MD88-773) immediately south of the APF in the southeastern Indian Ocean to examine the time variations in the $(^{231}Pa/^{230}Th)_{ex}{}^{o}$.

5.4.2-a Latitudinal variations in $(^{231}Pa/^{230}Th)_{ex}{}^{o}$ ratios from the Holocene sections of the transect sediments

Results of $(^{231}Pa/^{230}Th)_{ex}{}^{o}$ ratios for transect samples are presented in Table 5.5. In Figures 5.7a and b are latitudinal variations for both the Holocene and LGM sections. One particularly interesting feature I found was that the ratios from north and south of the APF show a contrasting pattern. The $(^{231}Pa/^{230}Th)_{ex}{}^{o}$ ratios of the Holocene transect samples on the APF and south of the APF (ca. 50° S to 57° S in latitude) are substantially higher than the production ratio (0.093), and range from 0.107 to 0.156, with two exceptions from the uncertain core tops (E50-8 and E50-13). The $(^{231}Pa/^{230}Th)_{ex}{}^{o}$ ratios of the Holocene transect samples north of the APF (0.024 to 0.077), including sediments north of the STC and in the SAFZ, are lower than the production ratio of 0.093. One exception is found in the E48-11 core top but the value is only slightly higher. On average, the $(^{231}Pa/^{230}Th)_{ex}{}^{o}$ ratio of the cores (average ratio is 0.134 ± 0.006, 1 standard deviation of the mean) on the APF and south of the APF is about 2.6-fold higher than that of the cores (average ratio is 0.052 ± 0.005, 1 standard deviation of the mean) north of the APF (Table 5.10). One extremely high value is also found in the southernmost core E50-17 (Table 5.5).

The low values of the $(^{231}Pa/^{230}Th)_{ex}{}^{o}$ ratios from the sediments north of the STC and the SAFZ (Figure 5.7a) are comparable to those found in the sediments from the central equatorial Pacific and Atlantic oceans, the East Pacific Rise, the Mid-Atlantic Ridge, and the typical open ocean gyres (Anderson *et al.*,

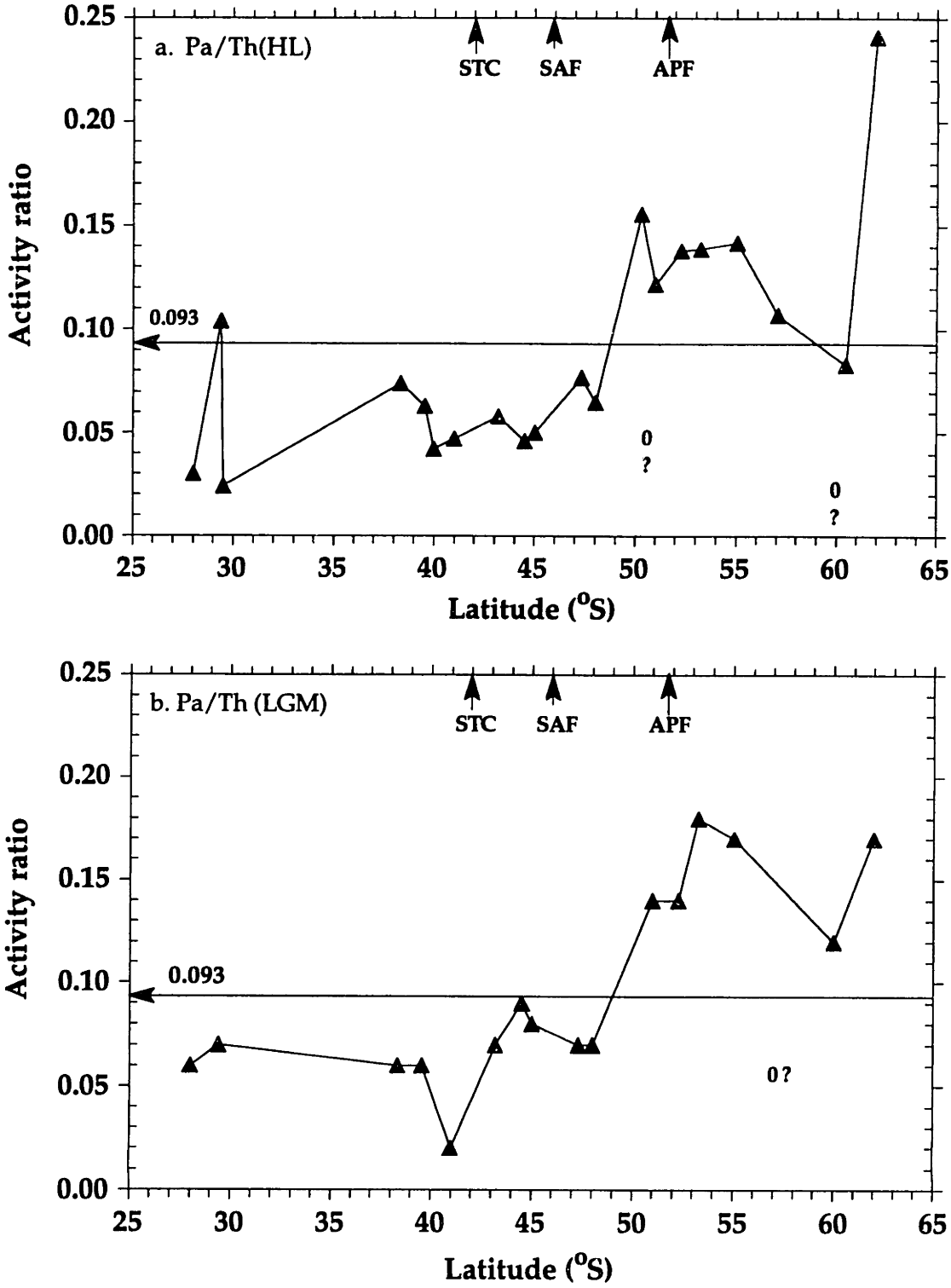

Figure 5.7 The $(^{231}Pa/^{230}Th)_{ex}{}^{o}$ activity ratio of the Holocene sections (a) and LGM sections (b) of the transect samples from the southern Indian Ocean.

Table 5.10: Average values of 230Th-normalized fluxes and (231Pa/230Th)ex0 ratio for the transect samples

Region	Total flux Holocene	Non-Carbonate flux Holocene	(231Pa/230Th)ex0 Holocene	Total flux LGM	Non-Carbonate flux LGM	(231Pa/230Th)ex0 LGM
PFZ	1.15 ± 0.08 (n=6)	1.03 ± 0.11 (n=6)	0.134 ± 0.006 (n=6)	1.32 ± 0.15 (n=4)	1.11 ± 0.07 (n=4)	0.158 ± 0.008 (n=4)
SAFZ	0.82 ± 0.05 (n=11)	0.071 ± 0.007 (n=11)	0.052 ± 0.005 (n=11)	1.11 ± 0.30 (n=8)	0.21 ± 0.03 (n=8)	0.065 ± 0.007 (n=8)
PFZ/SAFZ	1.40	14.54	2.58	1.54	5.29	2.42

1983a and 1990; Yang *et al.*, 1986; Lao, 1991; the Atlantic data in Chapter 4). Higher $(^{231}Pa/^{230}Th)_{ex}{}^{o}$ ratios in samples on the APF and south of the APF are similar to those found in recently reported data of the Holocene sediments from the Atlantic sectors in the Southern Ocean (Kumar *et al.*, 1993) and from the SW Indian Ocean (Francois *et al.*, 1993), but the $(^{231}Pa/^{230}Th)_{ex}{}^{o}$ ratios are relatively lower than those reported data from the Atlantic sector in the Southern Ocean by DeMaster (1979) and the typical Pacific Ocean margins by Anderson *et al.*, (1983b and 1990), and Lao (1991).

5.4.2-b The causes for the latitudinal variations in $(^{231}Pa/^{230}Th)_{ex}{}^{o}$ ratio of the Holocene transect samples

The conditions and processes that lead to the fractionation between ^{231}Pa and ^{230}Th have been discussed extensively in Chapters 3 and 4. In general, the reactivity of each element toward scavenging by particles (often expressed as residence time with respect to scavenging), the magnitude of the particle flux in each region, and the lateral mixing rate in the ocean are believed to be the major controlling factors. The question thus is whether a contrast in $(^{231}Pa/^{230}Th)_{ex}{}^{o}$ ratios between SAFZ and PFZ implies the different magnitude of particulate flux between the two regions.

By examining the ^{230}Th-normalized total flux from the Holocene sections of the transect data in this study, I found that the average total flux north of the APF is 0.82 ± 0.05 g/cm2/ka, while south of the APF, it is 1.15 ± 0.08 g/cm2/ka (Table 5.10). This indicates that the total flux in the PFZ is only 40% higher that in the SAFZ; while the $(^{231}Pa/^{230}Th)_{ex}{}^{o}$ ratio in the PFZ is a factor of 2.6 times higher than that to the north of the APF. It appears clearly that the difference of

^{230}Th-normalized total flux between north of the APF and PFZ is small, which presumably indicates that the particle fluxes in the overlying water column in both regions are of similar magnitude. In addition, a sample with higher total flux does not always, as one would expect, correspond to a higher $(^{231}Pa/^{230}Th)_{ex}{}^{o}$ ratio. These suggest that the oceanic conditions in this study region are complicated, and the total particle flux in the water column is not the only factor which controls $(^{231}Pa/^{230}Th)_{ex}{}^{o}$ ratio. Factors such as particle composition or other processes might play key roles in causing the contrast between the two regions (Figure 5.7a).

Particle composition is believed to control some degree of the fractionation between ^{231}Pa and ^{230}Th, although a unique conclusion is yet to be reached. An obvious change in composition of sediments across the APF in the Southern Ocean is the southward increase in opal content and decrease in carbonate content (Figures 5.8 and 5.9). In the Holocene sections of the transect cores, opal dominates in the PFZ samples, whereas carbonate dominates composition in samples north of the APF. This implies that under relatively constant ^{230}Th-normalized total flux in both regions, the opal component seems responsible for the preferential scavenging of ^{231}Pa than ^{230}Th in the PFZ; on the other hand, the carbonate seems unlikely to influence the fractionation between the two nuclides. On the other hand, it is clearly shown in Table 5.10 that the difference in average non-carbonate flux between north of the APF and PFZ is large while the fractionation between ^{231}Pa and ^{230}Th is great.

An affinity of ^{231}Pa for biogenic opal was suggested by Taguchi *et al.* (1989). DeMaster (1979) also suggested that biogenic opal might effectively strip the reactive nuclides such as ^{231}Pa, ^{230}Th, and ^{210}Pb, causing high inventories of these nuclides to deposit onto the seafloor. In addition, the result from one

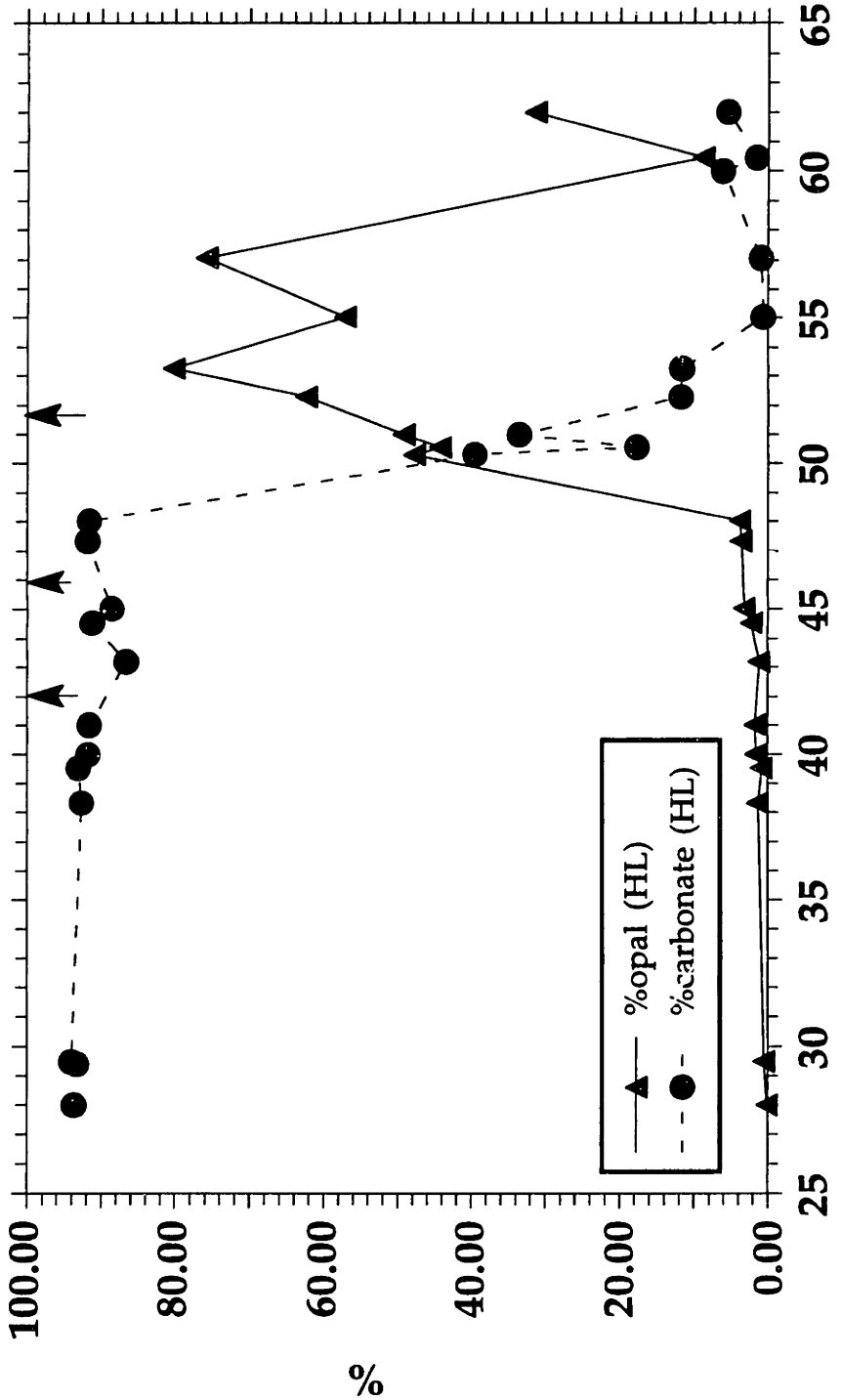

Figure 5.8 %Opal and %carbonate versus latitude for the Holocene transect sections in the southern Indian Ocean. Arrows denote (left to right) the approximate positions of the STC, SAF, and APF.

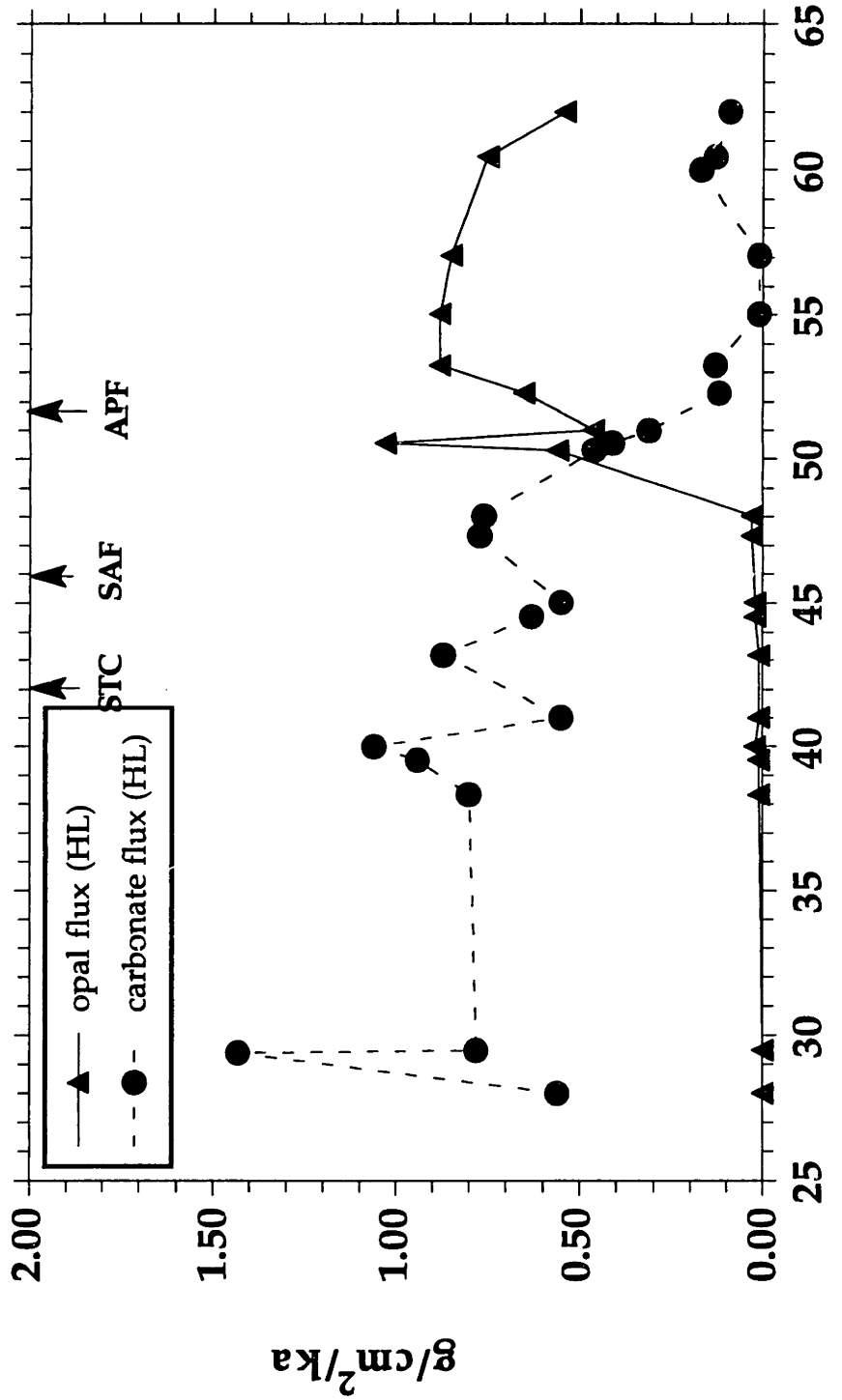

Figure 5.9 ^{230}Th-normalized opal and carbonate flux versus latitude for the Holocene transect sections in the southern Indian Ocean.

laboratory experiment showed that the Al_2O_3 phase gave a higher fractionation factor between ^{231}Pa and ^{230}Th (Anderson et al., 1992). Although a conclusion that is globally consistent about how the particle composition affects the affinity of reactive radionuclides such as ^{230}Th and ^{231}Pa can not be reached from sediment trap experiments and other sediment observations, the biogenic silica might be an important phase for stripping ^{230}Th and ^{231}Pa in the PFZ, since the opal is a dominant component in terms of total bulk sediment or surface particle material. Now, the question we are left with is: where do es excess ^{231}Pa in the PFZ come from?

The lateral transport of ^{231}Pa may be the explanation for the contrast in $(^{231}Pa/^{230}Th)_{ex}{}^{o}$ ratios of the sediments between north of the APF and the PFZ. Model results have suggested that the lateral transport of ^{230}Th is comparatively small, but large for ^{231}Pa (Bacon, 1988; Anderson et al., 1990; Chapter 4.4.3 in this thesis). A $(^{231}Pa/^{230}Th)_{ex}{}^{o}$ ratio that is lower than the production rate ratio implies that some fraction of ^{231}Pa in the water column has been laterally transported to another region; whereas, a $(^{231}Pa/^{230}Th)_{ex}{}^{o}$ higher than its production rate ratio implies addition of ^{231}Pa from another region. The $(^{231}Pa/^{230}Th)_{ex}{}^{o}$ ratio lower than 0.093 north of the APF, but the ratio higher than 0.093 south of the APF thus indicates that a portion of the ^{231}Pa production in the SAF and the STC is laterally transported out, thus causing the deficit in these regions. The laterally transported ^{231}Pa would then be deposited to the seafloor underlying the sediments of the present-day APF and south of the APF, and cause the excess ^{231}Pa in that region. An additional source is the export flux of Pa from Atlantic Ocean (Chapter 4.4.3).

Data from LGM sections show latitudinal features in distribution patterns of the $(^{231}Pa/^{230}Th)_{ex}{}^{o}$ ratios similar to those in the Holocene sections (Figures

5.7a and b). The amplitude of the variations for the average $(^{231}Pa/^{230}Th)_{ex}{}^{o}$ ratios in the PFZ and SAFZ are almost the same (within the error of 1 standard deviation) as for those in the Holocene sections (Table 5.10). This suggests that scavenging efficiency of both nuclides and the extent of fractionation between ^{231}Pa and ^{230}Th were of the same magnitude during the LGM as during the Holocene. This implies that the intensity of particle flux along with the degree of the lateral transportation of ^{231}Pa from SAFZ and north of the STC to the PFZ remains similar for both time intervals.

5.4.2.-c A downcore profile of $(^{231}Pa/^{230}Th)_{ex}{}^{o}$ ratios and particle fluxes south of the APF

The downcore $(^{231}Pa/^{230}Th)_{ex}{}^{o}$ ratio profile from MD88-773 (Figure 5.10) provides insight about temporal variations in the extent of fractionation between ^{231}Pa and ^{230}Th. Theoretically, the $(^{231}Pa/^{230}Th)_{ex}{}^{o}$ ratio should be a function of age only because of the constancy of the $^{235}U/^{238}U$ ratio in seawater (Rosholt et al., 1961; Sackett, 1964), and it should show an exponential decrease corresponding to a 57,200-year half-life. As seen in the downcore profile, however, there are several maxima and minima throughout the core from the Holocene to late isotopic stage 3, indicating variations in the degree of differential transport of the nuclides in the marine environment. Maximum $(^{231}Pa/^{230}Th)_{ex}{}^{o}$ ratios are found in the deglaciation (12.9 ka to 15.9 ka), while the lowest values are found during isotopic stage 2 (~21.8 ka) and late Holocene.

In these results, the first striking feature I noticed is that the $(^{231}Pa/^{230}Th)_{ex}{}^{o}$ ratios for all points in the profile are well above the seawater

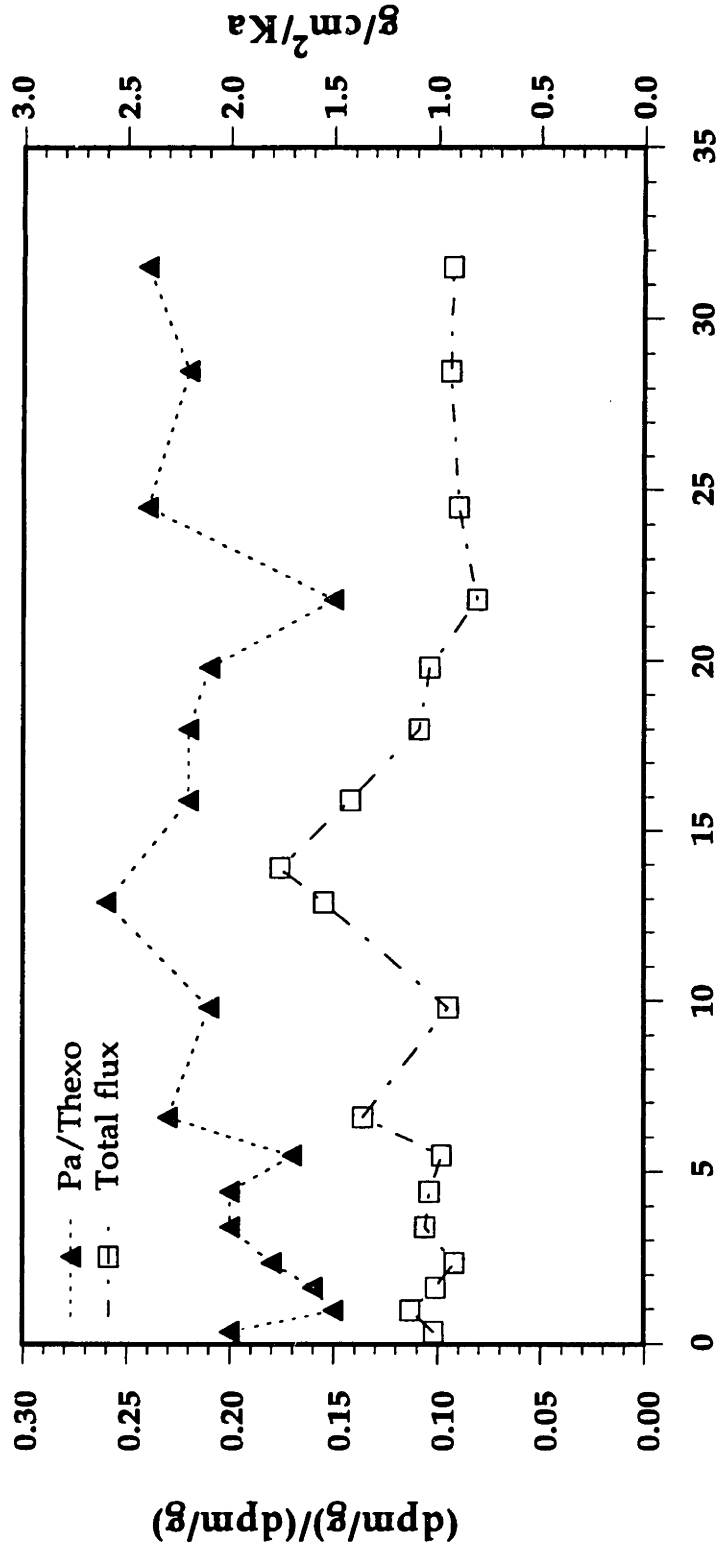

Figure 5.10 $(^{231}Pa/^{230}Th)_{ex}^{o}$ and ^{230}Th-normalized total flux versus age in the MD88-773.

production ratio of 0.093, even the minimum values. The highest value of 0.28 is three times higher than the production rate ratio. This implies a much higher particle flux in the PFZ of the Antarctic Ocean. The minimum value is at least 60% higher than the production rate ratio. All of these $(^{231}Pa/^{230}Th)_{ex}{}^{o}$ ratios of the downcore profile are within the range of values from the near-by transect samples. The comparison in $(^{231}Pa/^{230}Th)_{ex}{}^{o}$ between the Holocene and isotopic stage 2 is similar to that reported from a core north of the APF in the southwest Indian Ocean (Francois et al., 1993) but is in contrast to that data from a core south of the APF in the Atlantic sector (Kumar, et al., 1993) which shows a glacial reduction in $(^{231}Pa/^{230}Th)_{ex}{}^{o}$ ratio by almost two times compared to the late Holocene. The variations in the $(^{231}Pa/^{230}Th)_{ex}{}^{o}$ ratio are correlated well with the downcore variations in ^{230}Th-normalized total flux (Figure 5.10). Since the opal content dominants the total flux in this region, the time variations in $(^{231}Pa/^{230}Th)_{ex}{}^{o}$ ratio and ^{230} Th-normalized total flux imply the variations of the biogenic opal production in the surface water as well (see discussion in 5.4.3 also). The relative constancy of $(^{231}Pa/^{230}Th)_{ex}{}^{o}$ ratios and ^{230}Th-normalized total flux between the Holocene and the isotopic stage 2 supports the observations in the Holocene and LGM sectios of the transect samples, which suggest that there was no significant change in particle flux in this region during the LGM. In contrast, the higher $(^{231}Pa/^{230}Th)_{ex}{}^{o}$ ratio associates with a higher ^{230}Th-normalized total flux during the deglaciation (ca. 15 ka) could reflect either a higher particle flux in the overlying water column or a higher degree of horizontal transport.

5.4.3 Interpretation of the latitudinal variations in ^{230}Th-normalized opal flux

Measured percentages of opal and carbonate, and results for the ^{230}Th-normalized total, opal, carbonate, and terrigenious fluxes in the Holocene and LGM sections of the cores from the transect are presented in Tables 5.7 and 5.8. The Holocene results are plotted in Figures 5.8 and 5.9.

5.4.3-a *Latitudinal distribution patterns of opal content and ^{230}Th-normalized opal flux during the Holocene*

The Holocene opal content distribution (Figure 5.8) shows two contrasting regions. Core tops from the present Antarctic Polar Front (APF) and from south of the APF to 60° S have substantially higher opal content (45 to 80% opal) than those immediately north of the APF, which have almost minor levels (<5% opal). Latitudinal variations in ^{230}Th-normalized opal flux (Figure 5.9) show the same distribution pattern. The high opal flux for the Holocene sections in the PFZ ranges from ~0.5 to ~1.0 g/cm^2/ka, whereas the low opal flux for the Holocene sections north of the APF is <0.03 g/cm^2/ka.

Previously published opal accumulation rates in the Atlantic sector of the Southern Ocean by Mortlock et al. (1991) and Charles et al. (1991), and in the Indian sector by Charles et al. (1991) parallel the pattern of latitudinal variations in this study, but are higher by as much as 10 times both north and south of the APF. This discrepency is also seen in other works (van Bennekom, 1988; Bareille, et al., 1991) when compared to ^{230}Th-normalized opal flux. The estimated results of ^{230}Th-normalized opal flux in this study are in agreement with the results from samples in the Atlantic sector by DeMaster (1979), who estimated the opal accumulation rate based on the sedimentation rates derived from a uranium series disequilibrium method. Under such magnitude of the biogenic

opal accumulation rate, DeMaster (1979) has concluded that the Antarctic Ocean seafloor is an important site in terms of the biogenic opal mass budget in the ocean.

Table 5.11 compares opal fluxes estimated by normalization to ^{230}Th with those by others based on the mass accumulation rate of opal. The disagreement between these estimates is largely the result of the syndepositional redistribution effects due to the influence of strong abyssal currents in the APF region, as discussed previously (Figure 5.6). As shown in Figure 5.6, the sediment focusing effect is significant.

From the sediment trap investigations of biogenic opal flux in the Southern Ocean (Atlantic sector), Abelmann and Gersonde (1991) estimated the annual flux of opal at 700 m in the PFZ to be 1.53 g/cm2/ka, and at a 4454-m trap in the Weddell sea to be about 0.4 g/cm2/ka. By comparing their trap results, it is clear that an order of magnitude difference in opal accumulation rates (data from Mortlock *et al.*, 1991 and Charles *et al.*, 1991) recorded in the sediments could not possiblly be due to biogenic opal production in the surface water; however, the ^{230}Th-normalized opal flux that I estimated for the cores across the APF in the Indian sector showed the same amount of opal flux as seen from the trap data. This indicates that ^{230}Th-normalized opal flux provides a better record of the magnitude of the biogenic opal production rate from the water column. The application of the rate of opal accumulation history in the sediments, thus, could have led to incorrect conclusions about the productivity changes between glaciation and interglaciation.

Table 5.11 Estimations of the biogenic opal flux

Reference	North of the APF* g/cm2/ka	South of the APF* g/cm2/ka	Notes
Van Bennekom (1988)	3.6	3.6	Atlantic sector, Holocene
DeMaster (1979)	0.1 - 1.5	0.1 - 1.5	Indian sector, Holocene
Bareille et al. (1991)	2.0 - 4.0	6.0 - 8.0	Indian sector, Holocene
Mortlock et al. (1991)	0.1 - 1.0	2.5 - 13.1	Atlantic sector, Holocene
	0.1 - 3.2	0.9 - 5.6	Atlantic sector, LGM
230Th-normalized opal flux	<0.01 - 0.03	0.46 - 1.03	Indian sector, Holocene
(Yu et al., 1992; this study)	0.01 - 0.23	1.47 - 1.74	Indian sector, LGM

*APF: Antarctic Polar Front

5.4.3-b The conditions and processes responsible for the latitudinal distribution patterns of opal

The record of the percentage of opal in the sediments is controlled by its production from the surface waters, its survival from dissolution in the water column and on the seafloor, and the dilution effect by other sedimentary components. The strong global undersaturation of the ocean with respect to opal implies that its dissolution rate should be unaffected by circulation changes- unlike calcium carbonate dissolution which is governed by a variable depth-dependent distribution of saturation states. The latitudinal variations in opal content of the transect samples are affected by all these factors, but to different extents in the different regions.

The contrast in opal content of sediments between PFZ and north of the APF is obvious. The low opal content north of the APF is largely due to the dilution by carbonates. In contrast, the extremely high opal content found in the PFZ sediments is a result of the high surface diatom production. First of all, the low diatom production in the SAFZ seems to be limited by available silica supply (Jacques, 1983). From the culture studies, Neori and Holm-Hansen (1982) and Fenner *et al.*, (1976) also found that the low optimum diatom growth rate is caused by inefficient phytosynthensis due to the effect of temperature. They found that most Antarctic phytoplankton enjoy optimum growth rates only within a narrow temperature range between 0.8 - 1.0° C and about 8° C; at temperature greater than 8° C, the rates dropped off sharply. Neori and Holm-Hansen (1982) concluded that in the presence of adequate light intensity and nutrient supply, Antarctic phytoplankton photosynthesis is limited by thermodynamic effects on metabolic processes.

The high diatom production in the PFZ is the result of a combination of features such as: 1) a large supply of silicate and other nutrients transported to the surface by vertical mixing (Gordon, 1986); 2) the melting ice, which lowers salinity and density of the surface water layer, producing a stratified water column; and 3) increased penetration of light into the water column which promotes surface water productivity for the PFZ (Smith and Nelson, 1985; Nelson et al., 1987). The stabilization of the surface layer has been suggested as a necessary precondition for intense diatom blooms, so high diatom production is often associated with the front system in the PFZ (Lutjeharms et al., 1985).

To have opal preserved in sediments, the signal of surface production needs to be able to survive dissolution. The opal dissolution rate is difficult to quantify. The question of whether or not variations in opal dissolution rate affect significantly the contrast between north of the APF and PFZ is also difficult to answer. The results from measurements of dissolved silica in pore water (Ledford-Hoffman et al., 1986; van Bennekom et al., 1988; DeMaster et al., 1990) and from incubation experiments (DeMaster et al., 1990) indicates that opal dissolution rate is highly variable in the surface sediments. These studies suggest that about one-third of the biogenic silica arriving at the seafloor in the Bransfield Strait is dissolved, and that more than 60% of the silica in the abyssal sediments and less than 60% of the silica beneath the PFZ within the Atlantic sector are dissolved. One estimation from a factor analysis of the Southern Ocean by Bareille et al. (1991) also suggests that about 40 to 70% of biogenic opal production is dissolved for the surface sediments north of 40° S. Although the extent of dissolution is apparently different in sediments from the PFZ and north of the APF, there is little doubt that surface-water diatom production is high in the PFZ compared to that north of the APF. The contrasting records of the

^{230}Th-normalized opal flux of the Holocene samples between the PFZ and north of the APF (Figure 5.9) also support this fact. Furthermore, the contrasting records from the $(^{231}Pa/^{230}Th)_{ex}{}^{o}$ ratios between the two regions provide another evidence to confirm the observations in records of the ^{230}Th-normalized opal flux.

Relatively low opal content is noticed also in the selected cores further south which are believed also to be due to lower diatom production. Treguer et al., (1983), however, have argued that low diatom productivity in the waters poleward can not be explained by a lack of silica only. The reasons for such low diatom productivity are not obvious, but it has been suggested that the availability of other micronutrients such as iron limits the growth of diatoms (Martin, 1990). Sea ice cover might play an important role in suppressing diatom productivity in the Southern Ocean (Krebs, 1977; Whitaker, 1982).

5.4.3-c Interpretation of ^{230}Th-normalized opal flux changes between LGM and the Holocene:

The changes of the $(^{231}Pa/^{230}Th)_{ex}{}^{o}$ ratio, and ^{230}Th-normalized fluxes (opal and carbonate) between LGM and the Holocene are presented as a (LGM/HL) ratio, and are plotted in Figures 5.11. A major feature observed in the transect samples is the much higher ^{230}Th-normalized opal flux north of the APF during the LGM (Figure 5.11). These results from the Indian sector parallel those observations made in the Atlantic and the Pacific sectors of the Southern Ocean (Froelich *et al.*, 1989; Mortlock *et al.*, 1991; Charles *et al.*, 1991). South of the APF, however, the differences are small and not systematic (Figure 5.11). Thus, I can

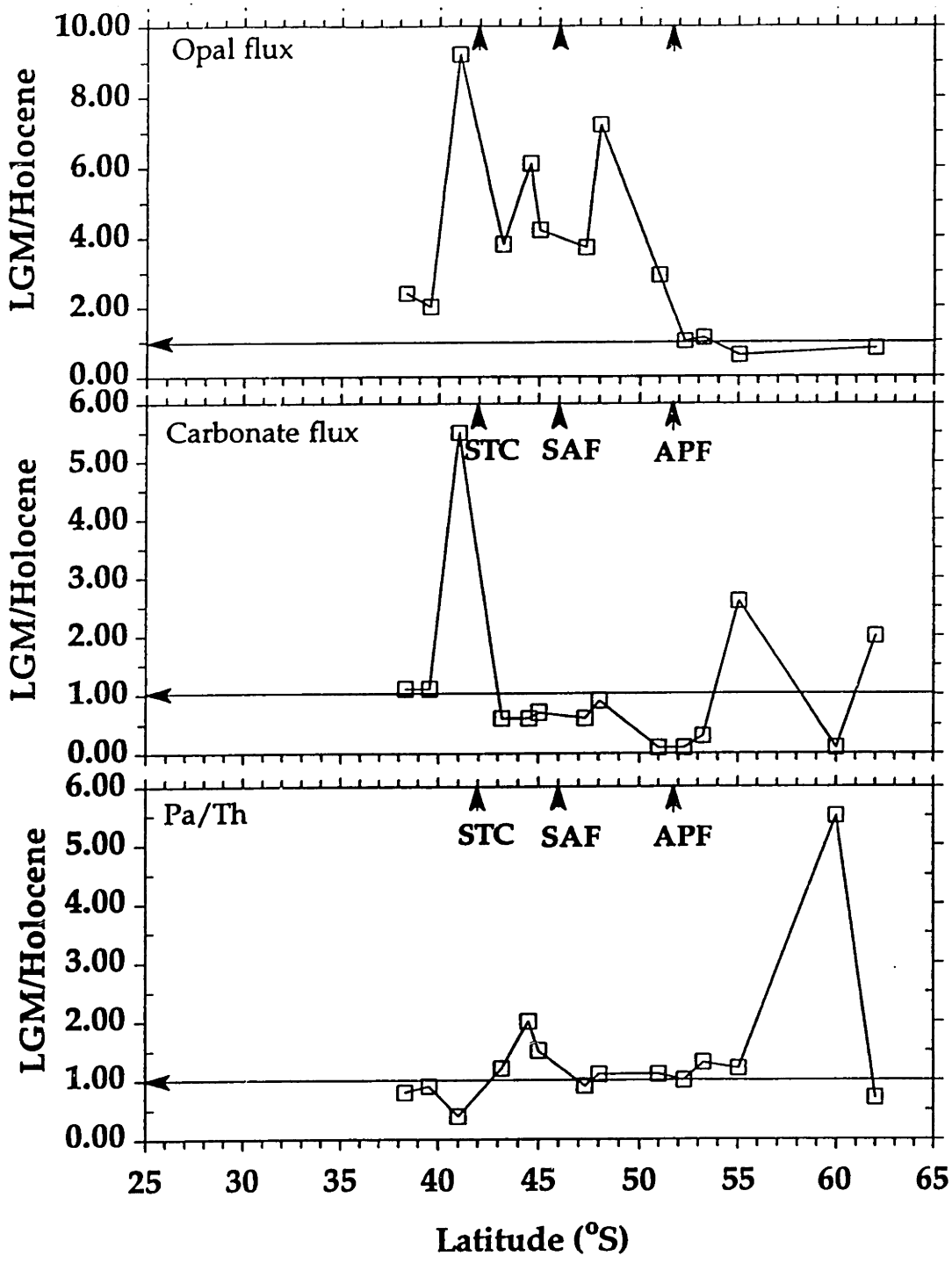

Figure 5.11 LGM/Holocene ratios of ^{230}Th-normalized opal flux, carbonate flux, and ^{231}Pa/^{230}Th ratio for the transect samples from the southern Indian Ocean.

not make the same conclusion as from previous works, which suggested a decrease in the glacial opal productivity south of the PFZ (Mortlock et al., 1991; Charles et al., 1991). My ^{230}Th-normalized opal flux data, however, should offer a better representation of the pelagic rain rate of opal, since the records of accumulation rate of opal in the sediments could be biased by sediment redistribution (as discussed in sections 5.4.1-c and 5.4.1-d).

Since the opal dissolution effect can modify the production record, and since the change of dissolution rate between the LGM and the Holcoene in this study region is not known, it is hard to draw a conclusion in terms of the LGM-Holocene changes of these opal records in the PFZ. In the following and later section (5.4.6), however, I hope to use the data of the $(^{231}Pa/^{230}Th)_{ex}{}^{o}$ ratios in MD88-773 downcore and transect sediments (Figures 5.10 and 5.11), and ^{230}Th-normalized total flux of the MD88-773 downcore (Figure 5.10) to comment on the question whether the production increased during the LGM.

From the Holocene data (Figures 5.7 and 5.9, sections 5.4.2-a and b, and 5.4.3-a), we have found that higher $(^{231}Pa/^{230}Th)_{ex}{}^{o}$ ratios correspond to higher ^{230}Th-normalized opal flux in the samples south of the APF. The data suggest that a portion of ^{231}Pa in the SAFZ and north of the STC might be transported laterally to the PFZ, where scavenging is enhanced by dominant biogenic opal phase. By examining the $(^{231}Pa/^{230}Th)_{ex}{}^{o}$ ratios in the samples, most of them (between the latitudes of 50°S to 55°S) show no significant change in the $(^{231}Pa/^{230}Th)_{ex}{}^{o}$ ratio between the LGM and the Holocene if I take the measurement errors into account (Figure 5.11). Although it is hard to estimate how much ^{231}Pa can be laterally transported from the SAFZ to the PFZ due to possible enhancement of scavenging when the silica front shifted northward, carbonate still dominates the bulk sediments in the SAFZ, indicating that the

shifting silica would not significantly change the scavenging efficiency of ^{231}Pa in PFZ during the LGM. The relative constancy of the $(^{231}Pa/^{230}Th)_{ex}{}^{o}$ ratios between the LGM and Holocene samples from the PFZ thus support the relative constancy of opal production during the LGM compared to the Holocene (Figure 5.11). Consequently, the inconsistent variations of ^{230}Th-normalized opal flux might be due to differential opal dissolution between LGM and the Holocene in each sample from the PFZ.

On the other hand, the changes I observed between the LGM and the Holocene sections of the cores from the SAFZ and north of the STC characterize higher percentages of opal, but lower percentages of carbonate during the LGM (Table 5.7). The ^{230}Th-normalized opal flux also shows higher glacial values in this region (Figure 5.11); this implies that the opal production in the surface water was higher in the region during the LGM. Since the opal content only contributes a minor component in the sediments of the SAFZ and north of the STC, the glacial age increase in ^{230}Th-normalized opal flux in the SAFZ might have resulted in little net production change when integrated over the whole Southern Ocean. In addition, today the 'silica front' where surface water silica concentrations (and opal burial in the underlying sediments) fall precipitously, coincides closely with the dynamic APF; thus the glacial-age northward shift of the "silica front" is the possible explanation for the changes of productivity to the south and north of the APF (see discussion in section 5.4.6).

5.4.3-d Impact of APF northward migration on the latitudinal distribution and magnitude of changes in opal flux

In the present-day Southern Ocean, higher levels of chlorophyll and plankton biomass are often associated with fronts (Steyaert, 1973; Plancke, 1977; Jacques and Minas, 1981; Allanson et al., 1981; Lutjeharms et al., 1985; Francois et al., 1993). The Antarctic Polar Front (APF) is the most stationary among the three ocean fronts in the Southern Ocean. Phytoplankton pigments are enhanced at these fronts (Lutjeharms et al., 1985; Bidigare et al., 1986) which possibly as a result of increased water column stability from sloping, isopycnal, or injection of nutrients into well-stratified subtropical waters and mixing by cross-frontal eddies (Pingree, 1978). As a consequence, the fronts create a region of enhanced flux to the seafloor in comparison to neighboring regions. The high $(^{231}Pa/^{230}Th)_{ex}{}^{o}$ ratio, coincidentally high ^{230}Th-normalized opal flux, and relatively high ^{230}Th-normalized total flux provide evidence for the enhanced flux to the seafloor.

Whether the ^{230}Th-normalized biogenic opal flux is directly related to the variations in hydrological conditions is not proved yet. However, the major producers of biogenic opal, diatoms and radiolarian, survive within a constrained environmental condition because of in addition to food supply, light, ice cover, and water stability, their metabolic processes are strongly controlled by temperature. As consequence, the "opal front" (a front acts like a transition between a diatomaceous-domain and a calcareous domain) is coincidendtal with today's APF position. Comparing the position of low-high transitions in opal and carbonate contents or ^{230}Th-normalized opal flux in both Holocene and LGM sections (Figures 5.8, 5.9, and 5.11) might indicate the migration of the fronts. Data in Figures 5.8, 5.9, and 5.11 show that the positions of the transition zone of high-low % opal or % carbonate or their ^{230}Th-normalized flux might vary from 3° to 5°. This is comparable to results deduced

from micropaleontological studies. Several micropaleontological studies have suggested that the position of the fronts in the southeastern Indian Ocean shifted northward by 4-10° latitude for STC, and 4-6° for APF (e.g. Be' and Duplessy, 1976; Prell et al., 1980; Burckle, 1984; Morley, 1989). Although there are some disagreements between different studies regarding the amplitude of the migration, they all show a significant glacial shift northward in the position of the fronts.

If northward migration of the hydrographic front system of the APF during the glacial times is true, the glacial opal flux increases in the SAFZ would not be due to the opal production changes, but it may be the result of the migration of the opal front. As seen in Table 5.7, however, the increase in glacial opal flux in the SAFZ due to the migration of the APF is small. In whole, the small increase in opal flux in the SAFZ accompanied with the inconsistent variations in glacial opal flux in the PFZ (Figure 5.11) imply little change in opal flux in the Southern Ocean.

5.4.3-e Did biological production change during LGM?

As discussed above, the ^{230}Th-normalized opal flux for transect samples give little evidence for production changes during the LGM compared to the Holocene in the Indian Sector in the Southern Ocean (see detail discussion in section 5.4.3-c). The downcore profile of the $(^{231}Pa/^{230}Th)_{ex}{}^{o}$ parallels perfectly with the time variation of the ^{230}Th-normalized total flux in the MD88-773 (Figure 5.10), and both profiles clearly show the relatively small changes between the isotopic stage 2 and the late Holocene. There profiles strongly suggest that the production changes between LGM (isotopic stage 2) and the late Holocene

must have been small in the Southern Ocean. Moreover, since the MD88-773 core already is situated underlying immediately south of the present-day APF, the complication due to the migration of the APF would not affect the conclusion. In conclusion, the production show little change during the LGM. In contrast, the pronounced high values of the $(^{231}Pa/^{230}Th)_{ex}{}^{o}$ ratio and coincidentally the pronounced high values of the ^{230}Th-normalized total flux were observed for the period during the deglaciation (ca.14ka to 15 ka) in the region.

Geochemical indicators of overall productivity are equivocal about net glacial-interglacial changes. The more depleted planktonic $\delta^{13}C$ of the glacial Antarctic sediments implies lower productivity (Labeyrie and Duplessy, 1985; Keigwin and Boyle, 1985; Charles and Fairbank, 1990); whereas planktonic Cd/Ca ratios suggest no net glacial-interglacial change (Boyle, 1988b; Keigwin and Boyle, 1989). Another line of evidence about the change in production comes from the transect $\delta^{15}N$ data. Analytical results of $\delta^{15}N$ were measured (by Francois and Altabet, 1992) for many of the same cores from the same transect samples I selected for the analyses of radionuclides and sedimentary components for this work. The available data for both LGM and the core tops, while principally from the samples between 45° S and 55° S, indicate that there was relatively little change in the magnitude of the decrease from $\delta^{15}N$ nutrient-depleted regions to the $\delta^{15}N$ nutrient -rich region. As proposed by Altabet and Francois (submitted, 1992), and Francois and Altabet (1992), the $\delta^{15}N$ of planktonic organic matter in surface water will increase with increasing nitrate depletion due to the preferential uptake of NO_3^- during photosynthesis process. Thus the small change in the latitudinal $\delta^{15}N$ gradient observed in core tops and glacial sediment sections also strongly argue against an increase in biological uptake of nitrate in the Southern Ocean as the main mechanism for lowering

glacial atmospheric CO_2. As a whole, both data from ^{230}Th-normalized opal flux and $(^{231}Pa/^{230}Th)_{ex}{}^{0}$ ratio for the transect samples and for the MD88-773 downcore, the $\delta^{15}N$ gradient observed in the Holocene and LGM transect samples, and Cd/Ca data in planktonic foraminifera would strongly argue against increased biological production in the Southern Ocean as the main mechanism for lowering glacial atmospheric CO_2.

5.4.4 Interpretations of ^{230}Th-normalized Carbonate flux

5.4.4-a Latitudinal variations of carbonate record, and changes between LGM and Holocene

The transect samples show that the %$CaCO_3$ in LGM sections is in general lower than that in the Holocene sections for the cores between 42° S and 55° S (Table 5.7 and Figure 5.12). The difference varies from 62% to 91% in the SAFZ and from 1% to 33% in the PFZ. With a precision in %$CaCO_3$ of about ± 1-5%, a difference of 30% carbonate is significant.

The pattern of %$CaCO_3$ recorded in sediments is a result of the balance of carbonate production, accumulation of non-carbonate sediments, and dissolution of carbonate. The systematic LGM-Holocene variations in the ^{230}Th-normalized carbonate flux, which is a quantitative value for the rain rate after accounting for the carbonate dissolution effect, do show the same patterns as the variations of carbonate content (Table 5.7 and Figures 5.11, 5.12, and 5.13). Although the percentage of non-carbonate also was higher during the LGM for the SAFZ and PFZ cores, the variations in ^{230}Th-normalized carbonate flux indicate that the %$CaCO_3$ cycles of the Southern Indian Ocean are not simply the result of

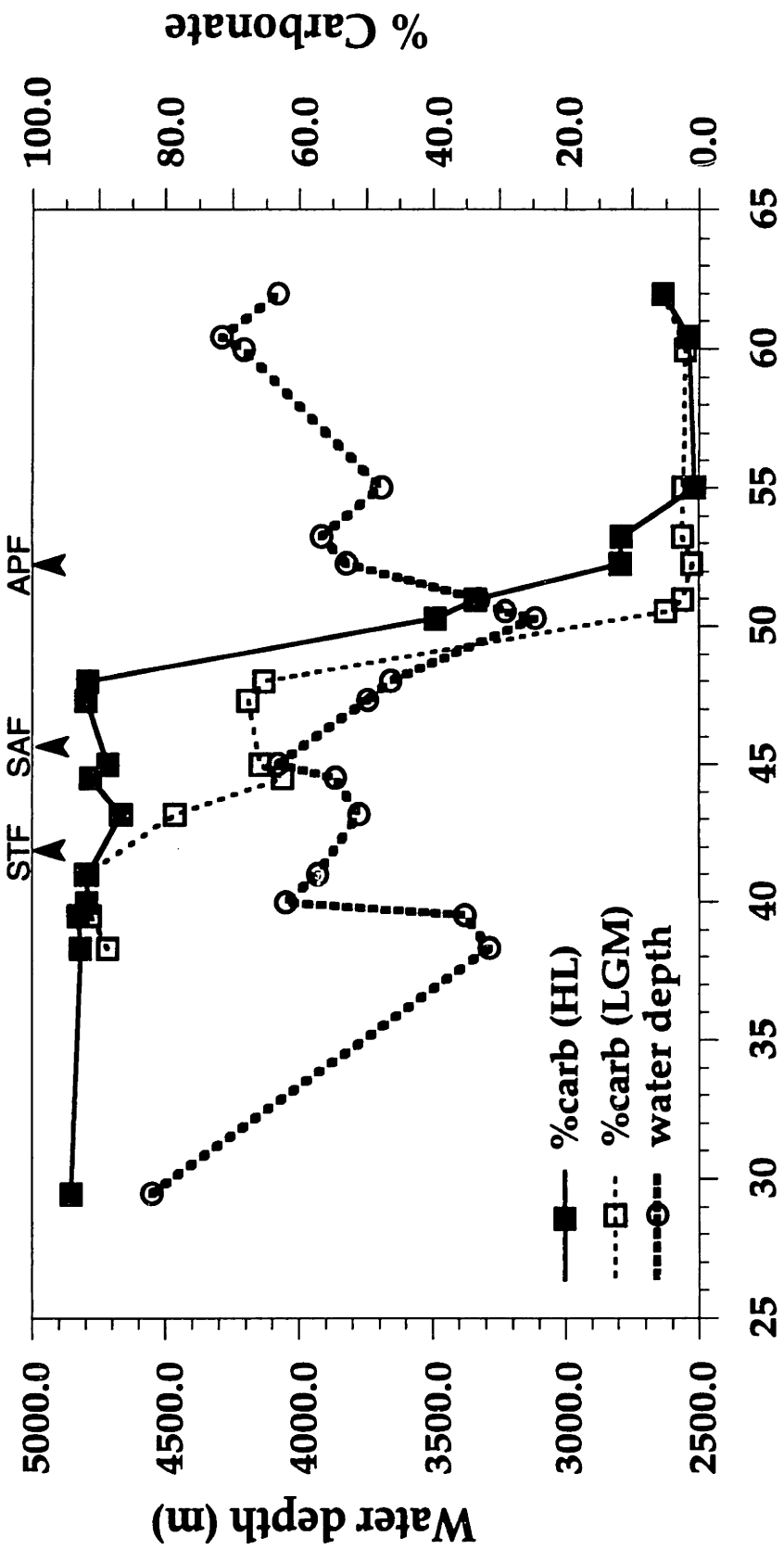

Figure 5.12 The water depth and %carbonate (both the LGM and Holocene) of the transect cores in the southern Indian Ocean.

dilution by terrigenious and biogenic opal sediments; they must be driven by changes in carbonate productivity or in preservation, or a combination of both.

The data of those cores from SAFZ between 42° S and 50°S or even more northward to 28° S shows %$CaCO_3$ for the Holocene sections >90% (Figure 5.12), even though all these cores are from water depths between 3200 m and 4550 m. For cores from 50°S to 55°S, even though they are from shallower depths (between 3100 m and 3900 m, in particular core E50-8 at 3100 m), %$CaCO_3$ is lower than in those cores from deeper depths. These patterns suggest two things. Firstly, carbonate production is higher in the region of 28°S to 50°S than in the region of 50°S to 55°S. Secondly, most of cores are above the lysocline depth which may be as deep as ~4000 m. The latter has been suggested by previous reports from Holocene profiles of calcium carbonate which indicated that the top of the calcite lysocline, a distinct decrease in %$CaCO_3$ with increasing water depth, lies at about 4300 m in this region (Kolla *et al.*, 1976; Lozano and Hay, 1976). Holocene core top distributions of forminiferal fragmentation also suggest that a distinct increase occurs from 4000 m down, placing the top of the forminiferal lysocline at this depth (Williams et al., 1985).

The high %$CaCO_3$ remains in the LGM sections in this region (62% to 95% for cores from 40° S to 50° S, see Figure 5.12), the lysocline depths should have been little variations, from the LGM to the Holocene. This seems to agree with the conclusion from Hay and his colleagues (1976) who have suggested that the site would have been above the lysocline continuously during at least the past 300,000 years. Since most of the cores (with the exception of E45-9, depth 4549m, and/or E45-79, E45-24, and those cores south 57° S) from the southern Indian Ocean for this study are above the regional sedimentary lysocline and the lysocline depth remains unchange over glacial to interglacial, the data of the

glacial reduction in carbonate content and ^{230}Th-normalized carbonate flux (ranging from 0.01 to 1.4 g/cm^2/ka for the Holocene sections, and 0.01 to 0.99 g/cm^2/ka for the LGM sections of the cores from 42° S to 50° S (Table 5.7 and Figure 5.13) thus are independent of the cores' depth. This implies that the reduction is the result of reductions in carbonate productivity. However, this suggestion is based on an assumption that there exists little carbonate dissolution above the lysocline depth, and the lysocline depth is at same depth for all of cores in this study region.

The similarity of glacial reduction in carbonate accumulation rate was also suggested as a reduction in carbonate productivity by Howard and Prell (1992) from the data in approximately the same region. They have argued that their cores are well-positioned to sense change of the regional lysocline through time, and lysocline depth during the isotopic stage 2 was about 600 m shallower than at present. They thus thought that the carbonate MAR variations in their records may be partly due to chemistry-driven lysocline variations, not changes in carbonate productivity in surface waters. If the carbonate dissolution increased during the LGM, as suggested by Howard and Prell (1992), the "true" carbonate rain rate from the surface water column must have exceeded those records based on the ^{230}Th-normalized carbonate flux (because the method only provides the records of the net rain rate after dissolution effect); thus, decrease in glacial carbonate production should be more than observed from the ^{230}Th-normalized carbonate flux.

5.4.4-b MD88-773 carbonate profiles provide evidence of carbonate production changes:

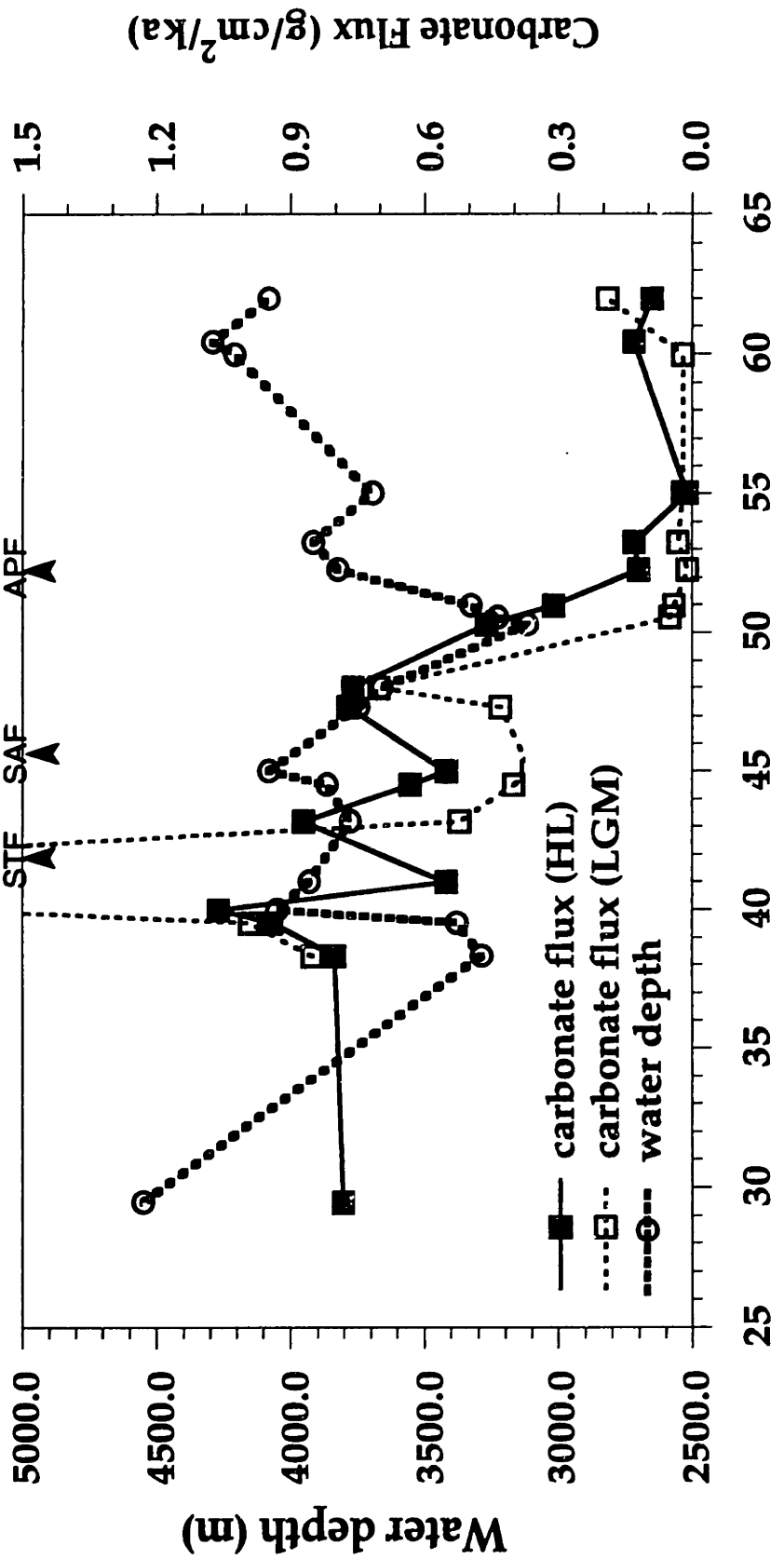

Figure 5.13 The water depth and carbonate flux (both the LGM and Holocene) of the transect cores in the southern Indian Ocean.

It is possible to deduce whether the ^{230}Th-normalized carbonate flux or carbonate accumulation rate during glaciation is due to reduction of carbonate production or partly due to lysocline variations. This is done by examining the downcore ^{230}Th-normalized carbonate flux profile of core MD88-773 to LGM-Holocene changes in carbonate flux in the northern APF. Core MD88-773 is from a water depth 2460 m, were above the lysocline and poleward of the present-day APF. Hay and his colleagues (1976) have suggested that the site would have been above the lysocline continuously during at least the past 300,000 years.

Estimates of changes in carbonate flux over the isotopic stage 3 for MD88-773 (Figure 5.14) show that isotopic stage 2 has an average carbonate flux of 0.08 g/cm2/ka, half the average for the late Holocene 0.16 g/cm2/ka, and almost six times less than the maximum peak for the deglaciation (15 ka, 0.48 g/cm2/ka). The similarity of the glacial-Holocene change in this shallow core to those from greater depths on the southern Indian Ocean (^{230}Th-normalized carbonate flux from this study or carbonate MAR from the cores of the Southern Indian Ridge by Howard and Prell, 1992) suggests that part of the glacial reduction in carbonate flux is independent of depth, thus implying in reductions in carbonate productivity. In addition, because MD88-773 is underline immediately south of today's APF, the effect of northward shifting (as discussed in the following section) opal-rich productivity regimes on carbonate records during the LGM is minimized.

5.4.4-c The effect of $CaCO_3$:C_{org}rain ratio on the interpretation of carbonate records

As discussed above, my data from the Southern Ocean indicate that calcium carbonate preservation, and probably carbonate production, were

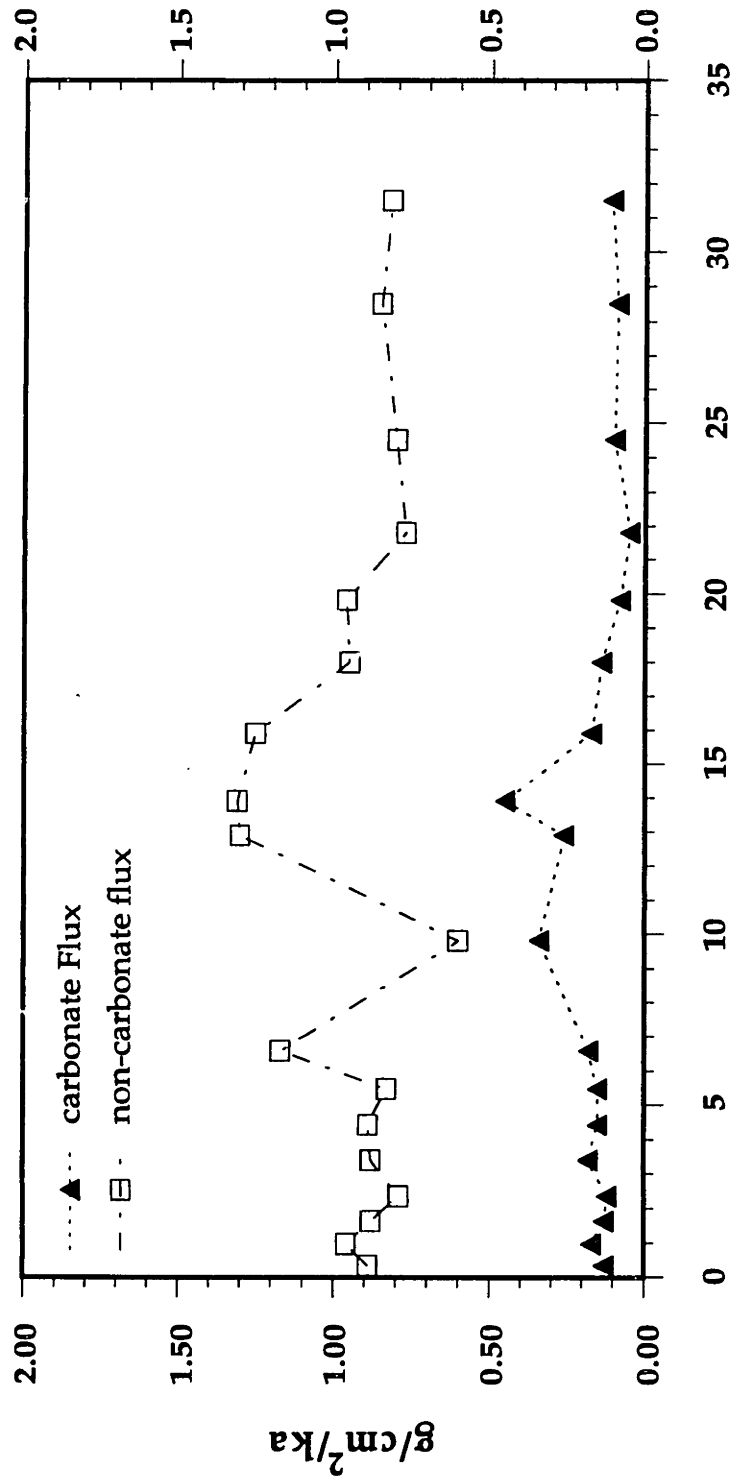

Figure 5.14 ^{230}Th-normalized carbonate and non-carbonate flux versus age in core MD88-773.

diminished during glacial intervals. The carbonate preservation, however, may be ambiguous because the glacial reduction in the $CaCO_3:C_{org}$ ratio of the particle rain may drive changes in dissolution within the sediments (Archer, 1991). The ^{230}Th-normalized opal flux records (Figure 5.11) suggest a glacial increase of opal between the present day's APF and the SAF, impling a higher glacial opal production and thus a higher glacial surface productivity in the SAFZ. These data, coupled with the significantly lower carbonate flux (Figure 5.11) imply that glacial $CaCO_3:C_{org}$ rain rate was lower than at present. Consequently, the reduction of the glacial carbonate flux (discussion in 5.4.4-c) or carbonate accumulation rate (Howard and Prell, 1992) might not be necessarily due to the reduction of carbonate productivity but due to the increase of dissolution. The decrease in the $CaCO_3:C_{org}$ rain ratio and enhanced dissolution would affect the shallow depth core the same as (or even more than) deeper cores; this could be the reason we have the same carbonate flux variations for the shallow MD88-773 core and for those deeper cores as well.

The APF position is believed to have migrated northward over the study sites during the glacial stages of the past 500,000 years (See section 5.4.6). This migration would add another complication to the variation of the carbonate system, because today's APF position is also a boundary between a carbonate-enriched and opal-enriched region; the shifting of the position of the boundary might have caused a change in the $CaCO_3:C_{org}$ ratio, which may be a result of the shifting of the domains from calcareous to siliceous sediments. Since the APF sediments might have sifted northward during the glacial, the $CaCO_3:C_{org}$ rain ratio might have decreased, resulting in an increase in the dissolution of carbonate during the glacial intervals rather than a change in carbonate production.

REFERENCES

Abelmann A. and R. Gersonde (1991) Biosiliceous particle flux in the Southern Ocean. *Mar. Chem.*, **35**, 503-536.

Anderson, R. F. (1982) Concentration, vertical flux, and remineralization of particlate uranium in seawater. *Geochim. Cosmochim. Acta*, **46**, 1293-1299.

Anderson, R. F., and A. P. Fleer (1982) Determination of natural actinides and plutonium in marine particulate material. *Analy. Chem.*, **54**, 1142-1147.

Anderson, R. F., M. P. Bacon, and P. G. Brewer (1983a) Removal of ^{230}Th and ^{231}Pa at ocean margins. *Earth Planet. Sci. Lett.*, **66**, 73-90.

Anderson, R. F., M. P. Bacon, and P. G. Brewer (1983b) Removal of ^{230}Th and ^{231}Pa from the open ocean. *Earth Planet. Sci. Lett.*, **62**, 7-23.

Anderson R. F., M. Q. Fleisher, P. E. Biscaye and N. Kumar (1991) Anomalous boundary scavenging in the Middle Atlantic Bight:evidence from ^{230}Th, ^{231}Pa, ^{10}Be, and ^{210}Pb. *Contin. Shelf Res.* SEEP-II volume.

Anderson, R. F., Y. Lao, W. S. Broecker, S. E. Trumore, H. J. Hofmann, and W. Wolfli (1990) Boundary scavenging in the Pacific Ocean: a comparison of ^{10}Be and ^{231}Pa. *Earth Planet. Sci. Lett.*, **96**, 287-304.

Anderson, R. F., A. P. LeHuray, M. Q. Fleisher, and J. W. Murray (1989) Uranium deposition in Saanich Inlet sediments, Vancouver Island. *Geochim. Cosmochim. Acta*, **53**, 2205-2213.

Bacon, M. P. (1984) Glacial to interglacial changes in carbonate and clay sedimentation in the Atlantic Ocean estimated from ^{230}Th measurements. *Isotope Geosci.*, 2, 97-111.

Bacon, M. P. (1988) Tracers of chemical scavenging in the ocean: boundary effects and large-scale chemical fractionation. *Philosoph. Trans. Roy. Soc. London* **A, 320**, 187-200.

Bacon, M. P., and J. N. Rosholt (1982) Accumulation rates of Th-230, Pa-231, and some trasition metals on the Bermuda Rise. *Geochim. Cosmochim. Acta*, **46**.

Bacon, M. P., C.-A. Huh, A. P. Fleer, and W. G. Deuser (1985) Seasonality in the flux of natural radionuclides and plutonium in the deep Sargasso Sea. *Deep-Sea Res.*, **32**, 273-286.

Bacon M. P., D. W. Spencer, and P. G. Brewer (1976) $^{210}Pb/^{226}Ra$ and $^{210}Po/^{210}Pb$ disequilibria in seawater and suspended particulate matter. *Earth Planet. Sci. Lett.*, **32**, 277-296.

Bard, E., L.D. Labeyrie, M.Arnold, M. Labracherie, J.-J. Pichon, J. Duprat and J.-C. Duplessy (1989) AMS C-14 ages measured in deep-sea cores from the southern ocean: implications for sedimentation rates during isotope stage 2. *Quat. Res.*, **31**, 309-317.

Bareille, G., M. Labracherie, L. Labeyrie, J.-J. Pichon, and J.-L. Turon (1991) Biogenic silica accumulation rate during the Holicene in the southeastern Indian Ocean. *Mar. Chem.*, **35**, 537-551.

Barnola, J. M., D. Raynaud, Y. S. Korotkevich, and C. Lorius (1987) Vostok ice core provides 160,000-year record of atmospheric CO_2. *Nature*, **329**, 408-414.

Be, A.W.H. and J.-C. Duplessy (1976) Subtropical convergence fluctuations and Quaternary climates in the middle latitudes of the Indian Ocean. *Science*, **194**, 419-422.

Berger, A. (1978) Long-term variationsof caloric insolation resulting from the Earth's orbital elemetns. *Quat. Res.*, **9**, 139-167.

Berger, W. H., and R. S. Keir (1984) Glacial-Holocene changes in atmosphere CO_2 and the deep-see record. pp. 337-351, **In**: J. E. Hanse, and T. Takahashi (eds), *Climate Processes and Climate Sensitivity* (Geophy. Monogr. Ser. 29). AGU, Washington, D. C.

Berger, W. H., V. S. Smetacek, G. Wefer (1989) Ocean productivity and paleoproductivity-An overview. In: Productivity of the Ocean:Present and Past. John Wiley and Sons.

Biscaye, P. E., and S. Eittreim (1977) Suspendedparticulate loads and transport in the nepheloid layer of the abysal Alantic Ocean. *Mar. Geol.*, **23**, 155-172.

Bond G., W. Broecker, S. Johnsen, J. McManus, L. Labeyrie, J. Jouzel and G. Bonani (1993) Correlations between climate records from North Atlantic sediments and Greenland ice. *Nature*, **365**, 143-147.

Boyle, E. A. (1988) Vertical oceanic nutrient fractionation and glacial/interglacial CO_2 cycles. *Nature*, **331**, 55-56.

Boyle, E. A. (1988) The role of vertical chemical fractionation in controlling late Quaternary atmospheric carbon dioxide. *J. Geophys. Res.*, **93**, 15701-15715.

Boyle, E.A. (1992) Cadmium and $\delta^{13}C$ paleochemical ocean distributions during the stage 2 glacial maximum. *Annu. Rev. Earth Planet. Sci.*, **20**, 245-287.

Boyle, E. A., S. S. Huested and S. P. Jones (1981) On the distribution of copper, nickel and cadmium in surface waters of the North Atlantic and North Pacific oceans. *J. Geophys. Res.*, **86**, 8048-8066.

Boyle, E. A., and L. Keigwin (1987) North Atlantic thermohaline circulation during the past 20,000 years linked to high-latitude surface temperature. *Nature*, **330**, 35-40.

Boyle, E. A., and L.D. Keigwin (1982) Deep circulation of the North Atlantic over the last 200,000 years: geochemical evidence. *Science*, **218**, 784-787.

Brewer, P. G., C. Goyet, and D. Dyrssen (1989) Carbon dioxide transport by ocean currents at 25°N latiude in the Atlantic Ocean. *Science*, **246**, 477-479.

Brewer, P. G., Y. Nozaki, D. W. Spencer, A. P. Fleer (1980) Sediment trap experiment in the deep north Atlantic and elemental fluzes. *J. Mar. Res.*, **38**, 703-728.

Broecker, W. S. (1971) Glacial accumulation rates and glacial to interglacial changes in oceanic mixiing. In: K. K. Turekian (ed.), *The late Cenozoic glacial ages*. Yale University Press, New Haven, Conn., pp.239-265.

Broecker, W.S., G. Bond, M. Klas, G. Bonani and W. Wolfli (1990) *Paleoceanogr.*, **5**, 469-478.

Broecker, W. S., G. Bond, M. Klas, E. Clark and J. McManus (1992) Origin of the northern Atlantic's Heinrich events. *Climate Dynamics*, **6**, 265-273.

Broecker, W. S., and T.-H. Peng (1982) *Tracers in the Sea.* Palisades, New York: Lamont-Doherty Geological Observatory.

Broecker, W. S., and T.-H. Peng (1989) The cause of the glacial to interlacial atmospheric CO_2 change: A polar alkalinity hypothesis. *Global Biogeochem.Cycles* **3**, 215-240.

Broecker, W.S. and T. Takahashi (1978) The relationship between lysocline depth and in situ carbonate ion concentration. *Deep-Sea Res.*, **25**, 65-95.

Broecker, W.S., K.K. Turekian and B.C. Heezen (1958) The relation of deep sea sedimentation rates to variations in climate. *Am. J. Sci.*, **256**, 503-517.

Broecker, W. S., and J. Van Donk (1970) Insolation changes, ice volumes, and the ^{18}O record in deep-sea cores. *Rev. Geophys.*, **8**, 169-198.

Busseler K. (1991) Do upper ocean sediment traps accurately record particle flux? *Nature*, **353**, 420-423.

Buesseler, K. O., and J. E. Halverson (1987) The mass spectrometric determination of fallout ^{239}Pu and ^{240}Pu in marine samples. *J. Environ. Radioact.*, **5**, 425-444.

Burckle, L.H. (1984) Diatom distribution and paleoceanographic reconstruction in the southern ocean-present and last glacial maximum. *Mar. Micropaleontol.*, **9**, 241-261.

Burckle, L. D., and D. W. Cooke (1983) Late Pleistocene Eucampia antarctica abundance stratigraphy in the Atlantic sector of the Southern Ocean. *Micropaleontol.*, **29**, 6-10.

Burckle, L. D., D. B. Clarke, and N. J. Shackleton (1978) Isochronous last-abundant-appearance datum (LAAD) of the diatom *Hemidiscus karstenii* in the Subantarctic. *Geology*, **6**, 243-246.

Burckle, L. D., D. Robinson, and D. Cooke (1982) Reappraisal of sea-ice distribution in Atlantic and Pacific sectors of the Southern Ocean at 18,000 yr. B.P. *Nature*, **299**, 435-437.

Burckle, L.H. and J. Cirilli (1987) Origin of diaton ooze belt in the southern ocean: implications for late Quaternary paleoceanography. *Micropaeontol.*, **33**, 82-86.

Campana, J.E. (1980) Elementary theory of the quadrupole mass filter. *Intl. J. Mass Spectrom.* **33**, 101-117.

Charles, C. D., and R. G. Fairbanks (1990) Glacial to interglacial changes in the isotopic gradients of southern ocean surface water. **In:** U. Bleil and J. Thiede (eds.) *Geological History of the Polar Oceans: Arctic Versus Antarctic.* Kluwer Academic, Boston, Mass., 519-538.

Charles, C. D., R. G. Fairbanks (1992) Evidence from Southern Ocean sediments for the effect of North Atlantic Deep Water flux on climate. *Nature*, **335**, 416-419.

Charles, C. D., P. N. Froelich, M. A. Zibello, r. A. Mortlock, and J. J. Morley (1991) Biogenic opal in Southern Ocean sediments over the last 450,000

years: Implications for surface water chemisry and circulation. *Paleoceanogr.*, **6**, 697-728.

Chen, J. H., R. L. Edwarddwards, and G. J. Wasserburg (1986) ^{238}U, ^{234}U and ^{232}Th in seawater. *Earth Planet. Sci. Lett.*, **80**, 241-251.

CLIMAP Project Members (1976) The surface of the ice-age earth. *Science*, **191**, 1131-1137.

CLIMAP Project Members (1981) Maps of northern and southern hemisphere continental ice, sea ice and sea surface temperatures in Auguast for the modern and the last glacial maximun. *Geol. Soc. Am. Map Chart Ser., MC-36.*

Cochran, J.K. (1992) The oceanic chemistry of the uranium- and thorium-series nuclides. In: Ivanovich, M. and R.S. Harmon (eds.) *Uranium-Series Disequilibrium*. 2nd edition, Oxford, Clarendon Press, 334-395.

Cochran, J.K. and S. Krishnaswami (1980) Radium, thorium, uranium and Pb-210 in deep-sea sediments and sediment pore waters from the North Equatorial Pacific. *Am. J. Sci.*, **280**, 849-889.

Cochran, J. K., H. D. Livingston, d. J. Hirschberg, and L. D. Surprenant (1987) Natural and anthropogenic radionuclide distributions in the northwest Atlantic Ocean. *Earth Planet. Sci. Lett.*, **84**, 135-152.

Cochran, J. K., and J. K. Osmond (1976) Sedimentation patterns and accumulation rates in the Tasman Basin. *Deep-Sea Res.*, **23**, 193-210.

Cooke, D. W., and J. D. Hays (1982) Estimates of Antarctic ocean seasonal sea-ice cover during glacial inervals, **In:** C. Craddock (ed.) *Antarctic Geoscience*, pp. 1017-1025, University of Wisconsin Press, Madison.

Curry, W. B., and G. P. Lohmann (1983) Reduced advection into Atlantic Ocean deep eastern basins during last glaciation maximum. *Nature*, **306**, 577-580.

Curry, W. B., and G. P. Lohmann (1986) Late Quaternary carbonate sedimentation at the Sierra Leone Rise (eastern equatorial Atlantic Ocean). *Mar. Geol.*, **70**, 223-250.

Curry, W. B., and G. P. Lohmann (1990) Reconstructing past particle fluxes in the tropical Atlantic Ocean. *Paleoceanogr.*, **5**, 487-505.

Curry, W. B., J. C. Duplessy, L. D. Labeyrie and N. J. Shackleton (1988) Changes in the distribution of $\delta^{13}C$ of deep water ΣCO_2 between the last glaciation and the Holocene. *Paleoceaogr.*, **3**, 317-341.

Curry, W.B. and G.P. Lohmann (1990) Reconstructing past particle fluxes in the tropical Atlantic Ocean. *Paleoceanogr.*, **5**, 487-505.

Damuth, J. E. (1977) Late Quaternary sedimentation in the western equatorial Atlantic. *Geol. Soc. Amer. Bull.*, **88**, 695-710.

Date A. R. and A. L. Grey (1989) Applications of Inductively Coupled Plasma Mass Spectrometry. Blackie.

DeMaster, D.J. (1979) *The marine budgets of silica and 32-S.*. Ph.D. Thesis, Yale Univ., New Haven, 308pp.

DeMaster, D. J. (1981) The suppy and accumulation of silica in the marine environment. *Geoch. Cosmoch. Acta*, **45**, 1715-1732.

DeMaster, D.J., T.M. Nelson, S.L. Harden and C.A. Nittrouer (1991) The cycling and accumulation of silica in Antarctic deep-sea and continental shelf environments. *Mar. Chem.*, **35**, 489-502.

Duplessy, J. C., N. J. Shackleton, R. G. Fairbanks, L. Labeyrie, D. Oppo, and N. Kallel (1988) Deep water source variations during the last climatic variations andtheir impact on the global deep water circlation. *Paleoceanogr.*, **3**, 343-360.

Edwards, R. J., and W. J. Emery (1982) Australian Southern Ocean frontal structure during summer 1976-77, Aust. *J. Mar. Freshwater Res.*, **33**, 3-22.

Edwards R. L., J. H. Chen, T.-L. Ku, and G. J. Wasserburg (1987) Precise timing of the last interglacial period from mass spectrometric determination of Thorium-230 in corals. *Science*, **236**, 1547-1553.

Emreson, S. and Bender, M. (1981) Carbon fluxes at the sediment-water interface of the deep sea: calcium carbonate presrevation. *J. Mar. Res.*, **39**, 139-162.

Falkner K. K. (1989) *An investigation of the marine geochemistry of gold.* Doc. dissertation.

Falkner K. K. (1991) Characterization of marine particulate material by ICPMS.

Finkel, R, S. Krishnaswami and D.L. Clark (1977) ^{10}Be in Arctic Ocean sediments. *Earth Planet. Sci. Lett.*, **35**, 199-204.

Fisher, N. S., J. L. Cochran, S. Krishnaswami, and H. D. Livingston (1988) Predicting the oceanic flux of radionuclides on sinking biogenic debris. *Nature*, **335**, 622-625.

Fleer, A. P. (1992) Updated determination of particulate and dissolved thorium-234. pp. 227-228, In: D. C. Hurd and D. W. Spencer (eds.), *Marine Particles: Analysis and Characterization* (Geophy. Monogr. Ser. 63). AGU, Washington, D. C.

Fleer, A. P., and M. P. Bacon (1984) Determination of lead-210 and polonium-210 in seaater and marine particulate matter. *Nucl. Instru. Methods Physics Res.*, **223**, 243-249.

Francois, R. and M.P. Bacon (1994) Heinrich events in the North Atlantic: radiochemical evidence. *Deep-Sea Res.* (in press)

Francois R., M. P. Bacon, M. Altabet, and L. D. Labeyrie (1993) Glacial/Interglacial changes in sediment rain rate in the SW Indian sector of subantarctic waters as recorded by ^{230}Th, ^{231}Pa, U and $\delta^{15}N$. *Plaeoceanogr.*, **8**, 611-629.

Froelich, P. N., R. A. Morlock, and A. Shemesh (1989) Inorganic germanium and silica in the Indian Ocean: biological fractionation during (Ge/Si) opal formation. *Global Biogeochem. Cycles* **3**, 79-88.

Froelich, P. N., et al. (1991) Biogenic opal and carbonate accumulation rates in the subantarctic South Alantic: the Late Neogene of Meteor Rise Site 704. *Proc. Ocean Drill. Program, Sci. Results*, **120**, 515-549.

Francois, R., M.A. Altabet and L.D. Burckle (1992) Glacial to interglacial changes in surface nitrate utilization in the Indian sector of the southern ocean as recorded by sediment $\delta^{15}N$. *Paleoceanogr.*, **7**, 589-606.

Francois, R., M. P. Bacon, and D. O. suman (1990) Thorium-230 profiling in deep-sea sediments: high-resolution records of flux and dissolution of carbonate in the equatorial Atlantic during the last 24,000 years. *Paleoceanogr.*, **5**, 761-787.

Francois, R., and M. P. Bacon (1991) Variations in terrigenous input into the deep equatorial Atlantic during the past 24,000 years. *Science*, **251**, 1473-1476.

Francois, R., M. P. Bacon, M. A. Altabet, and L. d. Labeyrie (1994) Glacial/interglacial changes in sediment rain rate in the S. W. Indian sector of subantarctic waters as recorded by ^{230}Th, ^{231}Pa, U and $\delta^{15}N$. *Paleoceanogr.* (accepted).

Francois R., M. P. Bacon, M. Altabet, and L. D. Labeyrie (1993) Glacial/Interglacial changes in sediment rain rate in the SW Indian sector

of subantarctic waters as recorded by ^{230}Th, ^{231}Pa, U and $\delta^{15}N$. *Plaeoceanogr.*, **8**, 611-629.

Gardner, W. D. (1980) Sediment trap dynamics and calibration: a laboratory evaluation. *J. Mar. Res.*, **38**:17-39.

Gardner, W. D. (1985) The effect of tilt on sediment trap efficiency. *Deep-Sea Res.*, **32**, 349-361.

Goldberg E. D. and M. Koide (1962) Geochronological studies of deep sea sediments by the ionium-thorium method. *Geichim. Cosmochim. Acta*, **26**, 417-450.

Gordon, A. L. (1972a) Introduction : Physical oceanography of the Southeast Indian Ocean. In: D. E. Hayes (ed.) *Anarctic Oceanology II: The Australian-New Zealand Sector, Antarct. Res.* Ser., **vol. 19**, 3-10, AGU, Washington D. C.

Gordon, A. L. (1972b) On the interaction of the Antarctic circmpolar current and the Macquarie ridge, In: D. E. Hayes (ed.) *Anarctic Oceanology II: The Australian-New Zealand Sector, Antarct. Res.* Ser., **vol. 19**, 71-78, AGU, Washington D. C.

Gordon, A. L. (1981) Seasonality of Southern Ocean sea ice. *J. Geophys. Res.*, **85**, 4193-4197.

Grousset, F., P. Buat-Menard, D. Boust, R.-C. Tian, S. Baudel, C. Pujol, C. Vergnaud-Grazzini (1989) Temporal changes of aeolian Saharan input in the Cape Verde abyssal plain since the last Glacial period. *Oceanologica Acta*, **11**, 177-185.

Grousset, F. E., L. Labeyrie, J. A. Sinko, M. Cremer, G. Bond, J. Duprat, E. Cortijo, and S. Huon (1993) Patterns of ice-rafted detritis in the glacial north Atlantic (40-55°N). *Paleoceanogr.*, **8**, 175-192.

Hall, M. M., and H. L. Bryden (1982) Direct setmates and mechanisms of ocean heat transport. *Deep-Sea Res.*, **29**, 339-359.

Hays, J. D. (1978) A review of the Late Quaternary climatic history of Antarctic sea. **In:** E. M. van Zinderen Bakker (ed.) *Antarctic Glacial History and World Paleoenvironments*, 57-71.

Hays, J. D., J. A. Lozano, N. J. Shackleton, and G. Irving (1976) Reconsturction of the Atlantic and western Indian Ocean sectors of the 18,000 B.P. Antarctic Ocean. In: R. M. Clines and J. D. Hays (eds.) Investigation of Late Quaternary Paleoceanography and Paleoclimatology. *Mem. Geol. Soc. Am.*, **145**, 337-372.

Heinrich, H. (1988) Origin and consequences of cyclic ice rafting in the northeast Atlantic Ocean during the past 130,000 years. *Quat. Res.*, **29**, 142-152.

Honjo S. (1980) Material fluxes and modes of sedimenatation in teh mesopelagic and bathpelagic zones. *J. Mar. Res.*, **38**, 53-97.

Honjo S and K. W. Doherty (1988) Large aperture time-series sediment traps; design objectives, construction and application. *Deep-Sea Res.*, **35**, 133-149.

Honjo S., S. J. Manganini, R. Krishfield (1989) Cruise report: JGOFS leg 1 International study of the North Atlantic Bloom. Technical Report, Woods Hole Oceanographic Institution.

Honjo S. and S. J. Manganini (1992) Biogenic particle fluxes at the 34N21W and 48N21W stations, 1989-1990: Methods and analytical data compilation. Technical Report, Woods Hole Oceanographic Institution.

Houk R. S. and J. J. Thompson (1988) Inductively Coupled Plasma Mass spectrometry. *Mass Spectrom Rev.*, **7**, 425-461.

Howard, W. R., and W. L. Prell (1992) Late Quaternary surface circulation of the southern ocean and its relationship to orbital variations. *Paleoceanogr.*, **7**, 79-117.

Hulmston P. and R. C. Hutton (1991) Analytical capabilities of electrothermal vaporization-Inductively Coupled Plasma Mass Spectrometry. *Spectroscopy*, **6**, 35-38.

Hurd, D. C., and F. Theyer (1975) Changes in the physical and chemical properties of biogenic silica. **In:** T. R. P. Gibbs (ed.) *Analy. Methods Oceanography, Adv. in Chem. Ser.* **147**, 211-239.

Jacques, G. (1983) Some ecophysiological aspects of the Antarctic phytoplankton. *Polar Biol.*, **2**, 27-33.

Jones, G. A., and P. Kaiteris (1983) A vacuum-gasometric technique for rapid and precise analysis of calcium carbonate in sediments and soils. *J. Sed. Petrol.*, **53**, 655-660.

Kallel, N., L. D. Labeyrie, A. Juillet-Leclerc, and J.-C. Duplessy (1988) A deep hydrological front between intermediate and deep-water masses in the glacial Indian Ocean. *Nature*, **333**, 651-655.

Keigwin, L. D., and E. A. Boyle (1989) Late Quaternary paleochemistry of high-laitude surface waters. *Palaeogeogr. Palaeoclimatol. Palaeoecol.*, **73**, 85-106.

Keir, R. S. (1988) On the late Pleistocene ocean geochemistry and circulation. *Paleoceonogr.*, **3**, 413-445.

Klinkhammer, G. and M. R. Palmer (1991) Uranium in the oceans: Where it goes and why? *Geochim. Cosmochim. Acta*, **55**, 1799-1806.

Knox, F. E., and M. McElroy (1984) Changes in atmospheric CO_2; influence of marine biota at high latitudes. *J. Geophys. Res.*, **89**, 4629-4637.

Koczy, F. F. (1961) Ratio of thorium-230 to thorium-232 in deep-sea sedimets. *Science*, **134**, 1978-1979.

Kolla, V., A.W.H. Be and P. Biscaye (1976) Calcium carbonate distribution in the surface sediments of the Indian Ocean. *J. Geophys. Res.*, **81**, 2605-2616.

Kolla, V., P. E. Biscaye, and A. F. Hanley (1979). Distribution of quartz in late Quaternary Atlantic sediments in relation to climate. *Quat. Res.*, **11**, 261-277.

Krebs, W.N. (1977) *Ecology and preservation of neritic marine diatoms, Arthur Harbor, Antarctica.* Ph.D. thesis, Univ. of California, Davis, 1-234.

Ku, T.-L. (1966) *Uranium Series Disequilibrium in Deep-sea Sediments,* Unpublished docoral dissertation, Columbia University, New York.

Ku, T.-L. (1976) The uranium-series methods of age determination. *Ann. Rev. Earth Planet. Sci.*, **4**, 347-379.

Ku, T.-L. and Broecker, W.S. (1967) Rates of sedimentation in the Arctic Ocean. *Prog. Oceanogr.*, **4**, 95-104.

Ku, T.-L., W.S. Broecker, and N. Opdyke (1968) Comparison of sedimentation rates measured by paleomagnetic and the ionium methods of age determination. *Earth Planet. Sci. Lett.*, 1-16.

Labeyrie, L.D., and J. C. Duplessy (1985) Changes in the oceanic $^{13}C/^{12}C$ ratio during the last 140,000 years: high-latitude surface water records. *Palaeogeogr., Palaeoclimatol., Palaeoecol.*, **50**, 217-240.

Lao, Y. (1991) *Transport and Burial Rates of ^{10}Be and ^{231}Pa in the Pacific Ocean*. Unpublished doctoral dissertation, Columbia University, New York.

Lao, Y., R. F. Anderson, W. S. Broecker (1992) Boundary scavenging and deep-sea sediment dating: constraints from excess ^{230}Th and ^{231}Pa. *Plaeoceanogr.* **8**:

Lao, Y., R. F. Anderson, W. S. Broecker, H. J. Hofmann, and W. Wolfli (1993) Particulate fluxes of ^{230}Th, ^{231}Pa, and ^{10}Be in the northeastern Pacific Ocean. *Geochim. Cosmochim. Acta*, **57**, 205-217.

Ledford-Hoffman, P. A., DeMaster, D. J., and Nittrouer, C. A. (1986) Biogenic silica accumulation in the Ross Sea and the importance of Antarctic continental shelf deposits in the marine silica budget. *Geochim. Cosmochim. Acta*, **50**, 2099-2110.

Lee, c., S. G. Wakeham and J. I. Hedges (1988) The measurement of oceanic particle flux- Are "swimmers" a problem? *Oceanogr.*, **2**, 34-36.

Leinen, M., D. Cwienk, G. H. Heath, P. E. Biscaye, V. Kolla, J. Thiede, and J. Dauphin (1986). Distribution of biogenic silica and quartz in recent deep sea sediments. *Geology*, **14**, 199-203.

Lisitzin, A. P. (1971) Sedimentation in the world ocean. *SEPM Spec. Pub.*, **17**, 218-241.

Lozano, J.A. and J.D. Hays (1976) Relationship of radiolarian assemblages to sediment types and physical oceanography in the Atlantic and western Indian Ocean sectors of the Antarctic Ocean, in R.M. Cline and J.D. Hays (eds.) *Investigation of Late Quaternary Paleoceanography and Paleoclimatology*, Geol. Soc. Am. Mem., **145**, 303-336.

Lutjeharms, J. R. E., N. M. Walters, and B. R. Allanson (1985) Oceanic frontal systems and biological enhancement, In: W. R. Siegfried, P. R. Condy, and R. M. Laws (eds) *Antarctic nutrient cycles and food webs*, pp.11-21, Springer-Verlag, New York.

Luz, B. and N.J. Shackleton (1975) CaCO3 solution in the tropical East Pacific during the past 130,000 years. In: W.V. Sliter, A.W.H. Be and W.H. Berger (eds.), *Dissolution of deep-sea Carbonates*. Sushman Found. Foram. Res., Spec. Publ., **13**, 142-150.

Mangini, A. and L. Diester-Haas (1983) Excess Th-230 in sediments off NW Africa traces upwelling in the past. In: *Coastal upwelling: its sedimentary records*, (ed. E. Suess and J. Thiede), pp:455-470. Plenum, New York.

Martin, J. H. (1990). Glacial-interglacial CO_2 change: the iron gypothesis. *Paleoceanogr.*, **5**, 1-15.

Melkert, M., G. Ganssen, W. Helder, and S. R. Troelstra (1992) Episodic preservatioin of pterood oozes in the deep Northeast Atlantic Ocean: Climatic change and hydrothermal activity. *Mar. Geol.*, **103**, 407-422.

Milliman, J. D., C. P. Summerhayes, and H. T. Barretto (1975) Quaternary sedimentation of the Amazon continental margin: a model. *Geol. Soc. Amer. Bull.*, **86**, 610-614.

Mix, A.C. (1989) Influence of productivity variations on long-trem atmospheric CO_2. *Nature*, **337**, 541-544.

Morlock, R. A., and P. N. Froelich (1989) A simple method for the rapid determination of biogenic opal in pelagic marine sediments. *Deep Sea Res.*, **36**, 1415-1426.

Morley, J. J. (1989). Variations in high-latitude oceanographic frontsin the southern Indian Ocean: An estimation based on faunal changes. *Paleoceanogr.*, **4**, 547-554.

Morley, J. J., and J. D. Hays (1983) Oceanographic conditions associated with high abundances of Radiolarian Cyclodophora davisiana. *Earth Planet. Sci. Lett.*, **66**, 63-72.

Mortlock, R. A., C. D. Charles, P. N. Froelich, M. A. Zibello, J. Saltzman, J. D. Hays, and L. H. Burchle (1991) Evidence for lower productivity in the Antarctic Ocean during the last glaciation. *Nature*, **351**, 220-223.

Muller P. J., and E. Suess (1979) Productivity, sedimentation rate and sedimentary organic matter in the oceans--I: organic carbon preservation. *Deep-sea Res.*, **26**, 1347-1362.

Nair R. R., V. Ittekkot, S. J. Manganini, V. Ramaswamy, B. Haake, E. T. Degens, B. N. Desal, and S. Honjo (unpublished?) Monsoon related particle fluxes to the deep Arabian Sea.

Neftel, A., H. Oeschger, T. Staffelbach, and B. Stauffer (1988) CO_2 record in the Byrd ice core 50,000-5,000 years BP. *Naure*, **331**, 609-611.

Nelson, D. M., and L. I. Gordon (1982) Production and pelagic dissolution of biogenic silica in the Southern Ocean. *Geochim Cosmochim. Acta*, **46**, 491-501.

Nelson, D. M., W. O. Smith, Jr., L. I. Gordon, and B. A. Huber (1987) Spring distributions of density, nutrients, and phytoplankton biomass in the ice edge zone of the Weddell-Scotia Sea. *J. Geophys. Res.*, **92**, 7181-7190.

Neori, A. and O. Holm-Hansen (1982) Effect of temperature on rate of photosynthesis in Antarctic phytoplankton. *Polar Biology*, **1**, 33-38.

Nozaki, Y. (1991) The systematic and kinetics of U/Th decay series nuclides in ocean water. *Rev. Aquat. Sci.*, 4:75-105.

Nozaki, Y., T. Nakanishi (1985) ^{231}Pa and ^{230}Th profiles in the open ocean water column. *Deep-Sea Res.*, **32**, 1209-1220.

Nozaki, Y. H., and H. Tsubota (1981) The water column distributions of thorium in the western North Pacific. *Earth Planet. Sci. Lett.*, **54**, 203-216.

Nozaki, Y., H.-S. Yang and M. Yamada (1987) Scavenging of thorium in the ocean. *J. Geophys. Res.*, **92**, 772-778.

Oppo, D. W., and R. G. Fairbanks (1987) Variability in the deep and intermediate water circulation of the Atlantic Ocean during the past 25,000 years: Northern hemisphere modulation of the Southern Ocean. *Earth Planet. Sci. Lett.*, **86**, 1-15.

Oppo, D. W., R. G. Fairbanks, A. L. Gordon, and N. J. shackleton (1990) Late Pleistocene Southern Ocean ^{13}C variability. *Paleoceanogr.*, **5**, 43-54.

Ostermann D. R., D. Karbott, and W. B. Curry (1990) Automated system to measure the carbonate concentration of sediments. Technical Report, Woods Hole Oceanographic Institution.

Park, Y.-H., L. Gamberoni, and E. Charriaud (1991) Frontal sturcture and transport of the Antarctic circumpolar current in the South Indian Ocean sector, 40-80°E. *Mar. Chem.*, **35**, 45-62.

Pichon, J.-J., L. D. Labeyrie, G. Bareille, M. Labracherie, J. Duprat, and J. Jouzel (1992) Surface water temperature changes in the high latitude of the southern hemisphere ovre the last glacial-interglacial cycle. *Paleoceanogr.*, **7**, 289-318.

Pingree, R.D. (1978) Cyclonic eddies and cross-frontal mixing. *J. Mar. Biol. Assoc. U.K.*, **58**, 955-963.

Plancke, J. (1977) Phytoplankton biomass and productivity in the subtropical convergence area and shelves of the western Indian subantactic islands, in *Adoptations within Antarctic Ecosystems*, Proceedings of the third SCAR Symposium on Antartic biology, 51-73.

Plank T. and J. Ludden (1994) Geochemistry of sediments in the argo Abyssal Plain at ODPSite 765: a continental margin reference section for sediment recycling in subduction zones. *Proc. ODP Sci. Results*, **123**: College Stateion, Texas. (in press)

Prell, W. L., W. H. Hutson, D. F. Williams, A. W. H. Be, K. Geitzenquer, and B. Molfino (1980) Surface circulation of the Indian Ocean during the last glacial maximum, approximately 18,000 yr B.P. *Quat. Res.*, **14**, 309-336.

Price Russ III G. and J. M. Bazan (1987) Isotopic ratio measurements with an inductively coupled plasma source mass spectrometer. *Spectrochimica Acta. 42B*, 49-62.

Rosholt, J. N., C. Emiliani, J. Geiss, F. F. Koczy, and P. J. Wangersky (1961) Absolute dating of deep-sea cores by the $^{231}Pa/^{230}Th$ method. *J. Geol.*, **69**, 162-185.

Ruddiman, W. F. (1977) Late Quaternary deposition of ice-rafted sand in the subpolar North Atlantic (lat 40 to 65°N). *Geol. Soc. Amer. Bull.*, **88**, 1813-1827.

Rutgers Van Der Loeff, M. M. and G. W. Berger (1993) Scavenging of ^{230}Th and ^{231}Pa near the Antarctic Polar Front in the South Atlantic. *Deep-Sea Res.*, **40**, 339-357.

Sachs, P.L., T.R. Hammar, and M.P. Bacon (1989) A Larg-volume, deep-sea submersible pumping system. (WHOI-89-55). (Technical Report). Woods Hole, Massachusetts: Woods Hole Oceanographic Institution.

Sackett, W. M. (1960) Protactinium-231 content of ocean water and sediments. *Science*, **132**, 1761-1762.

Sarmiento, J. L., and R. Toggweiler (1984) A new model for the role of the oceans in determining atmospheric pCO_2. *Nature*, **308**, 621-624.

Sarnthein M. and K. Winn (1988) Global variations of surface ocean productivity in low and mid latitudes: influence on CO2 reservoirs of the deep ocean and atmosphere during the last 21,000 years. *Paleoceanogr.*, **3**, 361-399.

Sarnthein, M., K. Winn, and R. Zahn (1987) Paleoproductivity of oceanic upwelling and the effect on atmospheric CO2 and climatic change during deglaciation times. pp. 311-337, **In:** W. H. Berger and L. D. Labeyrie (eds.), *Abrupt Climatic Change, Proceedings of the NATO/NSF A. R. W. Symposium at Biiers/Grenoble 1985.* Dordrecht, Holland: D. Reidel.

Sancetta, C. (1992) Primary production in the glacial North Atlantic and North Pacific oceans. Nature, 360, 249-251.

Scholten J. C., R. Botz, A. Mangini, H. Paetsch, P. Stoffers, and E. Vogelsang (1990) High resolution $^{230}Th_{ex}$ stratigraphy of sediments from high-latitude areas (Norweigan Sea, Fram Strait). *Earth Planet. Sci. Lett.*, **101**, 54-62.

Shaw T. J. and R. Francois (1991) A fast and sensitive ICP-MS assay for the determination of ^{230}Th in marine sediments. *Geochim. Cosmochim. Acta*, **55**, 2075-2078.

Shimmield, G. B., J. W. Murray, J. Thomson, M. P. Bacon, R. F. Anderson, and N. B. Price (1988) The distribution and behaviour of ^{230}Th and ^{231}Pa at an ocean margin, Baha California, Mexico. *Geoch. Cosmochim. Acta*, **50**, 2499-2507.

Shimmield, G. B., and N. B. Price (1988) The scavenging of U, ^{230}Th and ^{231}Pa during pulsed gydrothermal activity at 20°S, East Pacific Rise. *Geochim. Cosmochim. Acta*, **52**, 669-677.

Siegenthaler, U., and T. Wenk (1984) Rapid atmospheric CO_2 variations and ocean circulation. *Nature*, **308**, 624-626.

Sill C. W. (1978) Radiochemical determination of protactinium-231 in environmental and biological materials. *Analy. Chem.*, **50**, 1559-1571.

Smith, W.O. and D.M. Nelson (1985) Phytoplankton blooms produced by a receeding ice edge in the Ross Sea: spatial coherence with the density fields. *Science*, **227**, 163-166.

Spencer, D. W. (1972) GEOSECS II, the North Atlantic station: hydrographic features of oxygen and nutrients. *Earth Planet. Sci. Lett.*, **16**, 91-102.

Spencer, D. E., M. P. Bacon, P. G. Brewer (1981) Models of the distribution of ^{210}Pb in a section across the north equatorial Atlantic Ocean. *J. Mar. Res.*, **39**, 119-138.

Steyaert, J. (1973) Distribution of plankton diatoms along an African-Antarctic transect. *Invest. Pesq.*, **37**, 295-328.

Suman, D. O., and M. P. Bacon (1989) Variations. in Holocene sedimentation in the North American Basin determined from Th-230 measurements. *Deep-Sea Res.*, **36**, 869-878.

Taguchi, K., K. Harada, and S. Tsunogai (1989) Particulate removal of ^{230}Th and ^{231}Pa in the biologically productive northern North Pacific. *Earth Planet. Sci. Lett.*, **93**, 223-232.

Takahashi K. and S. Honjo (1989) Siliceous phytoplankton flux: interannual variability and response to hydrographic changes in the northeastern Pacific. In: Aspects of climate variability in the Pacific and western Americas, Peterson D. H. (ed.), Geophy. Monogr. 55, Amer. Geophys. Union, 151-160.

Thomson, J., S. Colley, R. Anderson, G. T. Cook, A. B. MacKenzie, and D. D. Harkness (1993) Holocene sediment fluxes in the Northeast Atlantic from $^{230}Th_{excess}$ and radiocarbon measurements. *Plaeoceanogr.* **8**, 631-650.

Thomson, J. and K.K. Turekian (1965) Some aspects of the geochemistry of marine sediments. In: J.P. Riley and G. Skirrow (eds.) *Chem. Oceanogr.*, **vol. 2**. Academic Press, New York, N.Y., pp. 81-126.

Toggweiler, J. R., and J. Sarmiento (1985) Glacial to interglacial changes in atmospheric carbon dioxide: the critical role of ocean surface water in high latitudes, **In:** E. T. Sundquist and W. S. Broecker (eds.) *The Carbon Cycle and Atmospheric CO2: Natural Variations Archean to Present.*, Geophys. Monogr. Ser., **32**, AGU, Washington, D. C., p.163-184.

Treguer, P., S. Gueneley and A. Kamatani (1988) Biogenic silica and particulate organic matter from the Indian sector of the Southern Ocean. *Mar. Chem.*, **23**, 167-180.

Turekian, K. K., and J. K. Cochran (1978) Marine chronologies with natural radionuclides. **In:** J. P. Riley and R. Chester (eds.), *Chemical Oceanography*, **vol. 7**, New York: Academic Press.

U. S. Global Ocean Flux Study (1989) Sediment trap technology and sampling.

U.S. JGOFS (1990). Isotopic Tracers in U.S. JGOFS. Reprot of a U.S. JGOFS workshop on radiochemistry held at Woods Hole, Massachusetts, 3 May-2 June, 1988. *U.S. JGOFS Planning Report*, **No. 12**, 116 pp.

Van Bennekom, A. J., G. W. Berger, S. J. Van der Gaast, and R. T. P. De Vries (1988) Primary productivity and the silica cycle in the Southern Ocean (Atlantic sector). *Palaeoeogr., Palaeoclimatol., Palaeoecol.*, **67**, 19-30.

Van der Loeff, M. M. R., and G. W. Berger (1991) Scavenging and particle flux: seasonal and regional variations in the Southern Ocean (Atlantic sector). *Mar. Chem.*, **35**, 553-568.

Wefer, G., E. Suess, W. balzer, G. Liebezeit, P. J. Muller, C. A. Ungerer, and W. Zenk (1982) Fluzesof biogenic components from sediment trap deployment in circumpolar waters of the Drake Passage. *Nature*, **299**, 145-147.

Wefer, G., G. Fischer, D. K. Futterer, and R. Gersonde (1988) Seasonal particle flux in the Bransfield Strait, Antarctica. *Deep-Sea Res.*, **35**, 891-898.

Whitaker, T.M. (1982) Primary production of phytoplankton off Sigey Island, South Orkneys, the Antarctic. *Proccedings of the Royal Society of London*, **B, 214**, 169-189.

Willians, D.f., D. Gribble, N. Healy-Williams and P. Leschak (1985) Dissolution and water-mass patterns in the Southeast Indian Ocean, Part II: the Pleistocene record from Brunhes to Matuyama age sediments. *Geol. Soc. Am. Bull.*, **96**, 190-202.

Yang, H.-S., Y. Nozaki, H. Sakai, and A. Masuda (1986) The distribution of ^{230}Th and ^{231}Pa in the deep-sea surface sediments of the Pacific Ocean. *Geochim. Cosmochim. Acta*, **50**, 81-99.

Yang, Y.-L., H. Elderfield, and M. Ivanovich (1990) Glacial to Holocene changes in carbonate and clay sedimentation in the equatorial Pacific Ocean estimated from thorium-230 profiles. *Paleoceanogr.*, **5**, 789-809.